BULGARIAN CHEMICAL COMMUNICATIONS

ANNIVERSARY

On the occasion of the 85th anniversary of Prof. Christo Boyadjiev

Eighty five years are the main part of human life. Prof. Christo Boyanov Boyadjiev started his scientific carreer in the Bulgarian Academy of Sciences before 60 years and 40 years of them he was a professor in the field of the chemical engineering. Before 65 years the first scientific paper by Prof. Christo B. Boyadjiev was published,

Later his scientific career and development are a sequence of the following stages.

His first research in the field of chemical engineering was on the hydrodynamics and mass transfer in a Venturi tube. Industrial equipment was built and applied for simultaneous capture of particulates and sulfur dioxide in waste gases, introduced in 1965 at the Copper Plant in Eliseina, Bulgaria.His start in theoretical research in the field of chemical engineering was in 1965, on hydrodynamics and mass transfer in flowing films. After successful cooperation in this field with V. Levich and V. Krylov from the Institute of Electrochemistry at the Soviet Academy of Sciences in Moscow he defended his PhD thesis in Bulgaria. After successful cooperation with V. Beschkov, V. Krylov and V. Levich many scientific papers were published, resulting in the monographs Chr. Boyadjiev, V. Beschkov, "Mass Transfer in Liquid Film Flows", Publ. House Bulg. Acad. Sci., Sofia, 1984 and Chr. Boyadjiev, V. Beschkov, "Mass transfer in moving fluid films", Ed. Mir, Moscow, 1988.

Prof. Chr. Boyadjiev was the founder of the scientific direction Process Systems Engineering (1976), as modeling of the set of processes in technological schemes (technologies). An interesting direction with its own mathematical (matrix) methods was developed. Large-scale research was conducted in the field of modeling and optimization of chemical-technological systems (ChTS): The following areas of this direction were developed: areas of impact and program for structural analysis of ChTS; decomposition method for optimization and software system for optimization of multi-range ChTS; optimal thermal integration and optimal synthesis of a system of heat exchangers; optimal schedules of multi-assortment ChTS; automated optimal design of multi-product ChTS; renovation of ChTS.

A theoretical research in the field of non-linear mass transfer and hydrodynamic stability started in 1983. The results were published in the monographs V. S. Krylov, Chr. Boyadjiev, "Non-Linear Mass Transfer", Institute of Thermophysics, Novsosibirsk, 1996 and Chr. Boyadjiev, V. N. Babak, "Non-Linear Mass Transfer and Hydrodynamic Stability", Elsevier, Amsterdam, 2000..

The wide base of used theoretical techniques became the basis of the monographs by Chr. Boyadjiev ″Modeling and Simulation in Chemical Engineering and Chemical Technology"(in Bulgarian), 1993; "Theoretical Chemical Engineering. Modeling and Simulation", Springer-Verlag, Berlin Heidelberg, 2010; and ,,Modeling and Simulation in Chemical Industry (in Bulgarian) 2017.

A new approach for modeling and simulation of mass transfer in column apparatus with creation of convective-diffusion and average-concentration models of processes of chemical reactions, absorption, adsorption and heterogeneous catalysis (2006). The results are published in the monographs by Chr. Boyadjiev, M. Doichinova, B. Boyadjiev, P. Popova-Krumova, "Modeling of Column Apparatus Processes", Springer-Verlag, Berlin Heidelberg, 2016, and by Chr. Boyadjiev, M. Doichinova, B. Boyadjiev, P. Popova-Krumova, "Modeling of Column Apparatus Processes" (Second edition), Springer-Verlag, Berlin Heidelberg, 2018.

A new approach for modeling and simulation of processes with unknown mechanism started in 2020. In one of the last works (Chr. Boyadjiev, A New Approach to Modeling and Simulation of Industrial

Processes, J. Eng. Thermophysics, 2021) the axiom "Quantitative descriptions of industrial processes are invariant by with regard to the measurement systems of quantities (of metric transformations) was formulated. According to Guchman's terminology, "metric transformations" are equivalent to "similar transformations", which he uses in proving his theorem "If the quantitative description of the process is invariant with respect to similar transformations, it can be represented as a power complex", i.e. product of the quantities on which the process depends, raised to degrees, which are determined by experimental data.

All these activities and achievements suggest high respect to the scientific contributions and skills of the jubilee. Let us congratulate and wish to Prof. Christo Boyadjiev good health and energy to follow his long and successful path in chemical engineering science.

From the Editorial Board of Bulgarian Chemical Communications

IN MEMORIAM
To the memory of Prof. DSc Boryan Radoev
(1941-2021)

This year we lost our eminent colleague and good friend Prof. Boryan P. Raodev. He was born in 1941 in Sofia. He was graduated in chemistry in the Faculty of Chemistry of the Sofia Unversity "St. Kliment Ohridski" in 1967 and he was immediately appointed as assistant professor in the Chair of Physico-chemistry in the same faculty. He defended a PhD thesis in 1974 on the subject of kinetics of thinning and deformation thin films stabilized by surfactants under the supervision of Prof. Ivan B. Ivanov. He was promoted as associate professor in the same Chair in 1981. He defended a DSc thesis in 1994 on:"Fluctuations and hydrodynamic interactions in dispersion systems" . In 1996 he was elected as Full Professor. Prof. DSc B. Radoev was a Head of the Chair of Physico-chemistry at the same Faculty of Chemistry in the period 2000/2004 and he has lead the Laboratory of Physico-chemistry of Surfaces and Dispersion Systems (2006-2011). He has been researcher in other European laboratories in Denmark, Germany and the Netherlands.He was a member of the German Kolloidgesellschaft and of the International Association of Colloids and Interface Science. He was also member of different scientific councils and governmental bodies in Bulgaria like the Higher Scientific Testimonial Commission to the Government of Bulgaria (1992-1997 and 2002-2005).

Dr. B. Radoev was introduced in scientific activity by Prof. Ivan B. Ivanov but his further scientific interests, approach and development were shaped under the influence of Academician A. Scheludko. Dr. Radoev started with the theoretical study of the dynamics and stability of foam films being his stable area of interest. Its further development focused on the effect of surfactants and the Marangoni effect on the films stability (in cooperation with Prof. Ivanov and Prof. E. Manev) has got broad recognition and initiated intensive research in different laboratories throughout the world.

The so-called theory of critical thicknesses was another lasting subject of research creativity for Prof. Radoev. He applied the stochastic approach to develop the fluctuation model of Scheludko-Vrij and to describe the evolution of non-stable modes (with Scheludko and Manev). Later this approach was applied to describe the stability of wetting liquid films on solid support. This theory enabled to confirm the existence of nano-sized bubbles on the interface between water and hydrophobic support (a work in cooperation with H. Schulze, Germany).

The problem with the dynamic wetting (or precisely the nature of hysteresis of the three-phase contact) was extension of these previous works. This subject found its practical development in flotation process (with Scheludko and Schulze).

The stochastic approach was applied independently for description of fluctuation waves on liquid surfaces, especially for solving the paradox of divergence of Fourier spectrum of capillary waves (with R. Tsekov).

In the last years the interests of Prof. Radoev were directed to the electrical properties of liquid surfaces. He formulated and developed the model of specific surface polarity (in the sense of Gibbs excess), solving the problem of the double electric layer generated by heterogeneous charged surface (with R. Slavchov).

He was an author and co-author of more than 120 papers, published in many prestigious international journals, like Advances in Colloid and Interface Science, Colloid and Polymer Science, Colloids and Surfaces A, International Journal of Multiphase Flow, International Journal of Quantum Chemistry, Journal of Colloid and Interface Science, Journal of the Chemical Society Faraday Transactions, Journal of Dispersion Science and Technology, Journal of Materials Science, Journal of Physical Chemistry A, Journal of Physics Condensed Matter, Kolloid Zeitschrift, Langmuir, Transactions of the Faraday Society, Zeitschrift für Physikalische Chemie, etc. He was an author of different chapter in specialized issues and collections published by Academic Press and Elsevier.

Prof. B. Radoev had very intensive teaching activity. He delivered lectures on colloidal chemistry in the Faculty of Chemistry in the University of Sofia for many years. He initiated and introduced many courses for MSc and PhD students on non-equilibrium thermodynamics, stochastic methods in natural sciences (with R. Tsekov), methods for production of dispersion systems, etc. He delivered lectures in other universities in Bulgaria.

He was very keen to work with students. He supervised the PhD theses of many students, later promoted as associate and full professors.

His original kind of thinking, high skills, broad scientific creativity and pedagogic talent will be remembered by his students and appreciated by his colleagues, co-workers and friends.

We shall remember Prof. Boryan Radoev as one of the most eminent Bulgarian scientist in the field of physical chemistry and as a best colleague and friend.

Venko Beschkov

A new analytical formula for calculating the energy gap value using the transmittance curve

H. Slimani[1,2*], N. Bessous[2]

[1]*University of El Oued, Faculty of Science, Department of Physics, El Oued, 39000, Algeria*
[2]*University of El Oued, Faculty of Technology, Department of Electrical Engineering, El Oued, 39000, Algeria*

This paper presents a new method to calculate the energy gap (E_g) value. The transmittance curve allows to define the E_g value. It is known that in a study, the calculation of the E_g may give a significant difference between two readings. These readings give a considerable overlap in the results to be analyzed, which is considered as a major drawback when different researchers' results are compared. The present paper proposes a new analytical model providing a unified formula to define the energy gap value. This new formula is based on logical analytical development and allows to guarantee the variation between the different energy gap values. As examples, thin films of zinc oxide (ZnO) and nickel oxide (NiO) on fluorine-doped tin oxides (FTO), used in photovoltaic system applications, are given.

Keywords: Ultraviolet-visible spectroscopy, energy gap, thin layer, analytical model, transmittance curve.

INTRODUCTION

A thin film is an entity with extremely small geometrical dimensions (thickness from a few tens of nm to a few μm). This explains why the physical features of these items are so important in surface interactions [1-7]. Moreover, this is the main reason why the physical properties of thin films significantly differ from those of other structures. In general, thin films are used in many applications such as photovoltaic systems, photocatalysis, optic systems, nano-electronics, etc. [8-14]. Microscopically, they consist of crystalline grains which are of the same order of magnitude as the thickness of the thin layer [15-17]. According to the literature, the thin layers have a microstructure in the form of columns with diameters ranging from 10 to 30 nm [18]. The orientation of the crystalline grains varies as a function of the angle between the plane of the substrate and the flow of molecules during the deposition [19-21].

The chemical and physical qualities of any material, as well as the physical conditions of deposition at each stage of the thin layer evolution have a huge impact on the microstructure of thin layers. In particular, the properties of a thin layer are very sensitive to the nature of the substrate on which it is located. This explains why layers of the same material and the same thickness may have substantially different physical properties on substrates of different types [22-24].

There are many techniques for deposition of thin layers on substrates [25-27]. The use of a technique depends on the properties of the deposited layers for a given application.

According to the theory of energy bands, there are three electrical states: metal, insulator and semiconductor. In the metal, the conduction band (CB) and the valence band (VB) are overlapping, which allows a free flow of the electrons. The semiconductor has a forbidden band that separates the VB and the CB, commonly called gap, and noted as E_g. The electrons cannot take the energies located in this band. They need to gain energy to get into the CB. For insulators the energy gap is larger than 4 eV, and at room temperature, the CB of an insulator is empty.

Glasses are common amorphous (not crystallized) materials, transparent in the visible range. They have a very high gap value and cannot conduct electric current (insulator).

However, semiconductors with a large gap (at least above 3.1 eV, corresponding to a wavelength of 400 nm) are theoretically transparent in the visible range. Thin layer deposition of this type of material ensures low absorption. The presence of admixtures, introducer by doping of the material, increases the number of free electrons.

Zinc oxide (ZnO) is a semiconductor of wide gap; it is transparent in the visible and in the near infrared range. It possesses a set of properties that allow its use in many applications [28-30]. It has very interesting electromechanical properties which allow its usage on a large scale as a transparent conductor in acoustic devices and in microwave delay lines, as piezoelectric materials, etc.

Different quantitative data are obtained by chemical analysis based on ultraviolet-visible (UV-Vis) spectroscopy. Transition metal ions, biological

---

* To whom all correspondence should be sent:
E-mail:slimani_hamza@yahoo.fr

macromolecules, highly conjugated organic compounds, etc., are used as dopants. UV-Vis spectroscopic measurements can also be performed in solids and in gases.

This technique is usually applied to molecules and/or inorganic complexes in solution. The perceived color of the chemical involved is directly affected by the absorption in the visible range. In addition, UV-Vis spectroscopy is very important for the quantitative measurements despite its limitations for sample identification. Furthermore, the absorbance measurements allow determining the analyte concentration. The characterization of the optical and/or the electronic properties of materials is usually based on their UV-Vis spectra [31-33].

The aim of this study is to find the E_g value in one step. As the transmittance curves in the materials yield a lot of information, the analytical model proposed here is based on the transmittance curve to easily calculate the E_g value. In addition, we carefully checked the values obtained with other results.

The novelty of this work is the development of an analytical model providing a new unified formula of E_g. This new formula will enable liable reading of the E_g for several samples. For this reason, test examples were considered which were based on the deposition and characterization of thin layers.

EXPERIMENTAL

Preparation of thin film samples

Before starting the development of the energy gap formula; we shall briefly present the experimental preparation of thin conductive and transparent layers of ZnO. Different solution concentrations were prepared by spray pyrolysis processing of glass substrates with fluorine-doped tin oxide (FTO). These films were obtained from a solution of zinc acetate dissolved in methanol at a fixed temperature (T=350°C) and with different concentrations of the solution in the range from 0.1 M to 0.5 M.

The different solution concentrations led to the variation of the structural and optical properties of these films.

The UV-Vis spectrophotometric measurements confirmed that good transparencies with a transmission of 70 - 85% in the visible range can be obtained. The values of the optical band gaps E_g deduced from the transmission UV-Vis spectra varied between 3.24eV and 3.43eV [34-36].

For this reason, our work focused on the calculation of the E_g value. Figure 1 shows the

transmission UV-Vis spectra of ZnO/FTO layers at different concentrations. It is clear that the energy gap will be different from one layer to another.
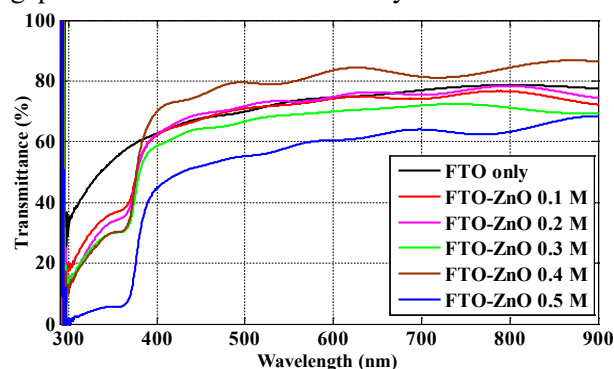

Fig. 1. Transmission spectra of ZnO/FTO samples for different molar concentrations.

Measurements

The fields of spectroscopy are generally distinguished according to the wavelength interval in which the measurements are made. The following characterization domains can be distinguished: ultraviolet-visible, infrared, microwave, etc.

In this case, we used a UV-Vis spectrophotometer, whereby we were able to plot curves representing the variation in the transmittance depending on the wavelength in the UV-Vis range of 300-900 nm (see Fig. 1). By exploiting these curves it is possible to estimate several quantities of the film such as thickness, optical characteristics, optical absorption threshold, absorption coefficient, width of the forbidden band and refractive index.

Our proposed approach here is to determine the energy gap value using the transmittance spectra. The next section will try to present the calculation in detail.

Analytical model of energy gap calculation

Everything in nature is subject to the laws that govern it. We therefore thought of a law to determine the energy gap (E_g) value based on the transmittance curves. There are some almost aligned points in the UV-Vis field that would build a straight line. The intersection between the line and the curve above is denotedas point B, and below is point A.

Theoretically, the line formed is parallel to the transmittance axis and perpendicular to the wavelength axis. But in reality the straight line is inclined, that is to say, $\lambda_B \neq \lambda_A$.

Point B is projected on the horizontal line which passes through point A; we denote this new point by C. Points B and C have the same wavelength λ_B

(see Fig. 2).

Some researchers in this field take the E_g in point B; but other researchers take it in point A [37-41]. This led us to develop a realistic formula for defining E_g and comparing the results obtained between the practical and the theoretical values.

The triangle ACB is right angled at C; we determined the center of gravity G of the triangle (see Fig. 2).
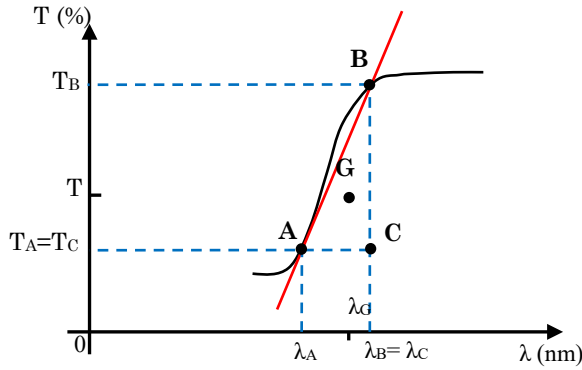

Fig. 2. Illustrative scheme of the transmission spectra.

According to Fig. 2, we assume that the points A, B, C of the triangle have equal masses m. By applying the law of the gravity center which is given by:

$$\overline{OG} = \frac{m\overline{OA} + m\overline{OB} + m\overline{OC}}{m + m + m} \quad (1)$$

or,

$$\overline{OG} = \frac{\overline{OA} + \overline{OB} + \overline{OC}}{3} \quad (2)$$

we can also write,

$$\overline{OA} = \lambda_A \times \vec{i} + T_A \times \vec{j} \quad (3)$$
$$\overline{OB} = \lambda_B \times \vec{i} + T_B \times \vec{j} \quad (4)$$
$$\overline{OC} = \lambda_B \times \vec{i} + T_A \times \vec{j} \quad (5)$$

so,

$$\overline{OG} = \frac{(\lambda_A + 2\lambda_B)}{3} \times \vec{i} + \frac{(2T_A + T_B)}{3} \times \vec{j} \quad (6)$$

We are interested in the part of the wave axis. The wavelength λ_G of the gravity center is written in this case as follows:

$$\lambda_G = \frac{(\lambda_A + 2\lambda_B)}{3} \quad (7)$$

It is known that:

$$E_g = \frac{1240}{\lambda} \quad (8).$$

According to equation (7) which defines the wavelength λ_G, we can extract the wavelength λ which is introduces in the calculation of E_g value

by:

$$\lambda = \lambda_G = \frac{(\lambda_A + 2\lambda_B)}{3} \quad (9)$$

so,

$$E_g = \frac{1240}{\lambda} = \frac{1240}{\frac{(\lambda_A + 2\lambda_B)}{3}} = \frac{3720}{(\lambda_A + 2\lambda_B)} \quad (10)$$

The final formula for determining the E_g value is:

$$E_g = \frac{3720}{(\lambda_A + 2\lambda_B)} \quad (11)$$

This method allows us to determine the energy gap (E_g) value based on the transmittance curve simply, efficiently and closer to the previous results.

We have demonstrated by mechanical laws at the beginning that we consider the selected points as mass centers and we have determined the center of mass of the proposed system in order to have a unified formula of the E_g.

It is important to facilitate the calculation of the E_g value in the subjects that use the transmittance curves in materials intendedfor photovoltaic systems or other uses.

The proposed analytical model based on the transmittance curve permits easy calculation of the E_g value. In addition, we have carefully checked the values obtained with other results. Equation (11) gives a new formula which was found according to well-defined steps.

Applying the new formula on a real example (ZnO /FTO)

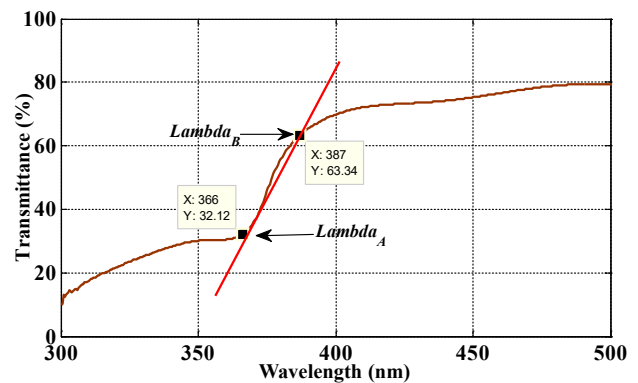In Fig. 3 we present the transmittance spectra of the ZnO/FTO films at a concentration of 0.4 M.

Fig. 3. Transmission shape of ZnO/FTO for 0.4 M concentration.

The band gap or energy gap (E_g) values of our ZnO/FTO layers are between 3.24 and 3.43 eV. According to Fig. 1, we can see a variation of the E_g value with the concentration of the solution. Forthe concentration of 0.4 M presented in Fig. 3;

the E_g value agrees with the literature value [34-36].

$$E_g = \frac{3720}{(366 + 2 \times (387))} = \frac{3720}{1140}$$

so,

$$E_g = 3.263 \ eV \ .$$

Note: In this occasion, we can define another formula that is based on the calculation of the average value of each E_g value, as follows:

$$E_{gA} = \frac{1240}{\lambda_A} \qquad (12)$$

and,

$$E_{gB} = \frac{1240}{\lambda_B} \qquad (13)$$

$$E_{g-Mean} = E_g = \frac{E_{gA} + E_{gA}}{2} \qquad (14)$$

or,

$$E_{g-Mean} = E_g = 620 \times \frac{(\lambda_A + \lambda_B)}{(\lambda_A \times \lambda_B)} \qquad (15)$$

In this case, we can find the E_g value as follows:

$$E_{g-Mean} = E_g = 620 \times \frac{(366 + 387)}{(366 \times 387)}$$

so,

$$E_{g-Mean} = E_g = 3.269 \ eV$$

It is clear that the two values are not equal (3.263 eV *vs.* 3.269 eV). For this reason, our analytical model shows a very good approximation when comparing with literature values[42-44].

Applying the new formula on a real example (NiO /FTO)

Before starting to calculate the energy gap based on the previous formula., we shall firstly indicate the experimental preparation of thin conductive and transparent layers of NiO. Different solution concentrations were prepared by spray pyrolysis processing on glass substrates with fluorine-doped tin oxide (FTO). These films were obtained from a solution of nickel nitrate in methanol at a fixed temperature (T =480°C) and with different concentrations(from 0.1 M to 0.5 M).

Fig. 4 shows the UV-Vis transmittance spectra of NiO/FTO layers at different concentrations. It is clear that the energy gap will be different from one layer to another.The band gap or energy gap (E_g) values of our NiO/FTO layers are between 3.38 eV and 3.74 eV. According to Fig. 4, there is a variation of the E_g value with the concentration of the solution.

For a concentration of 0.2 M presented in Fig. 4 (to the left); the E_g = 3.68 eV value agrees with the

402

literature value [45-47].

$$E_g = \frac{3720}{(319.3 + 2 \times (345.4))} = \frac{3720}{1010.1}$$
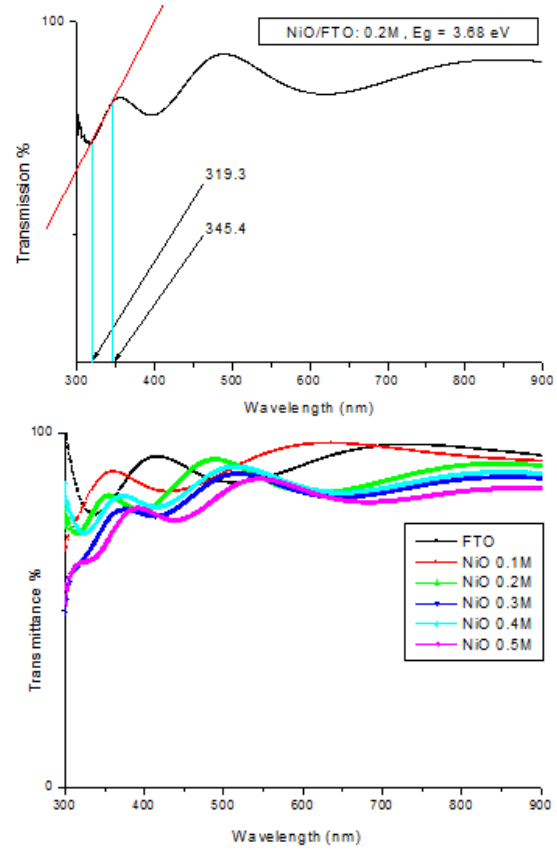
so,

$$E_g = 3.68 \ eV$$

Fig. 4. Transmittance spectra of FTO only and of NiO thin films grown on FTO substrates at various solution concentrations.

Based on the calculation of the average value ofeach energy gap value, we can find the results as follows:

$$E_{gA} = \frac{1240}{\lambda_A} = 3.59 \text{ eV}$$

and,

$$E_{gB} = \frac{1240}{\lambda_B} = 3.8835 \text{ eV}$$

$$E_{g-Mean} = E_g = \frac{E_{gA} + E_{gB}}{2}$$

or,

$$E_{g-Mean} = E_g = 620 \times \frac{(\lambda_A + \lambda_B)}{(\lambda_A \times \lambda_B)}$$

In this case, we can find the E_g value as follows:

$$E_{g-Mean} = E_g = 620 \times \frac{(319.3 + 345.4)}{(319.3 \times 345.4)}$$

so,

$$E_{g-Mean} = E_g = 3.736 \ eV$$

Table 1. Energy gap values at different NiO concentrations

NiO Concentration	0.1M	0.2M	0.3M	0.4M	0.5M	FTO
E_g for Classical Method (eV)	3.93	3.92	3.86	3.79	3.75	3.67
E_g for New Method (eV)	3.74	3.68	3.57	3.52	3.38	3.62
Error = ($E_{gMeasured}$-$E_{gClassical}$)/ $E_{gClassical}$	0.04	0.06	0.07	0.07	0.09	0.01

The comparison of the energy gap values for solution concentrations between 0.1 and 0.5M based on the classical method and on the new formula is shown in Table 1. It is seen that the results obtained are in good agreement with the results of the conventional calculation method. We can mention the difference of 5% between the estimated value and the conventional value for pure FTO. This difference varies in the range from 0.19eV to 0.37eV depending on the NiO concentration from 0.1M to 0.5M. This small variation can be justified by the position of the tangent line which is seen as a challenge to improve this analytical model. Generally, the results clearly show the ease of calculating the E_g value based on a single formula.

It is also important to note that the verification was made for other materials such as ITO, CuO, etc. and confirmed the accuracy of the proposed model.

DISCUSSION

Pankove [49] proposed a technique based on traced optical absorbance data to determine the energy gap. The work of Tauc *et al.*[48] was applied to the study of the optical and electronic properties of amorphous germanium. The Tauc diagram is a graph commonly used to determine the optical band gap of a material, usually a semiconductor. The optical band gap can be determined using the Tauc's relation [48, 49] which is given by:

$$(\alpha h\nu)^p = A\left(h\nu - E_g\right) \tag{16}$$

where, α is the absorption coefficient, *h* is the Planck's constant, *A* is a constant, *v* is the transition frequency, E_g is the band gap corresponding to a particular transition occurring in the film and *p* can take values according to:
- Direct allowed transitions: *p*=2,
- Direct forbidden transitions: *p* =2/3,
- Indirect allowed transitions: *p*= 1/2,
- Indirect forbidden transitions: *p*= 1/3.

Generally, the allowed transitions dominate based on the absorption processes, so, *p*=2 or *p*=1/2, in case when the transitions are direct or indirect, respectively.

This new approach has led us to find a well-defined formula of the E_g value. The logical steps during the demonstration confirm the accuracy of the results. In addition, the examples proposed in this study illustrate the effectiveness of this formula when we compare it with other works [40, 41, 50, 51].

In this paper, we have tried to put forward a new approach that helps to avoid the overlap in the E_g calculation.

CONCLUSIONS

In conclusion, we proposed a new analytical model based on the transmittance curve in order to calculate the E_g value. This study was based on real examples to calculate the E_g value. Examples were composed of thin film samples which contained ZnO/FTO or NiO/FTO. In addition, we carefully checked the values obtained with other results. We found the value of E_g = 3.263 eV in the ZnO/FTO example; this value is in correspondence with the literature. So, equation (11) gives a new formula developed according to well-defined steps.

Finally, it may be important to facilitate the calculation of the E_g value in subjects that use the transmittance curves.

REFERENCES

1. P. Mishra, R. S. Yadav, A. C. Pandey, *Bulg. Chem. Commun.,***42**, 560 (2010).
2. S. I. Gudkov, K. D. Baklanova, M. V. Kamenshchikov, A. V. Solnyshkin, A. N. Belov, *Phys. Solid. State*, **60**, 4 (2018).
3. Y. Takeshi, J. Kaji, K. Koda, K. Takashima, M. Nakano, H. Fukunaga, *IEEE Trans. Mag.*, **54**, 11 (2018).
4. N. G. Kostova, M. Fabian, E. Dutkova, *Bulg. Chem. Commun., ***51**, 433 (2019).
5. B. Swati, N. Lohia, D. Rehani, S. Mehra, R. Datt, G. Gupta, D. Haranath, S. Sharma, *Opt.*, 164015 (2019).
6. M. Cheng, Z. B. Chen, J. W. Xing, *IEEE Trans. Mag.*, **54**, 5 (2018).

7. D. Selloum, A. Henni, A. Karar, A. Tabchouchea, N. Harfoucheb, O. Bachaa, S. Tingryc, F. Roseid, *Solid State Sciences,* **92**, 76 (2019).

8. N. Kaneva, A. Bojinova, K. Papazova, D. Dimitrov, *Bulg. Chem. Commun.*, **51**, 406 (2019).

9. I. A. Tambasov, M. N. Volochaev, A. S. Voronin, N. P. Evsevskaya, A. N. Masyugin, A. S. Aleksandrovskii, T. E. Smolyarova, *Phys. Solid. State,* **61**, 10 (2019).

10. M. Sadullah, J. Kaur, R. Basu, A. K. Sharma, *Opt.* 163715 (2019).

11. A. Shokri, K. Mahanpoor, *Bulg. Chem. Commun.,* **50**, 27 (2018).

12. C. Sungju, J. Y. Kim, J. Rhee, H. Kang, S. Park, D. M. Kim, S. J. Choi, D. H. Kim, *IEEE Elect. Dev. Lett.*, **40**, 4 (2019).

13. A. Henni, N. Harfouche, A. Karar, D. Zerrouki, F. X. Perrin, F. Rosei, *Solid State Sciences*, **98**, 106039 (2019).

14. W. Rakhrour, D. Selloum, A. Henni, N. Cherrad, I. Chikouche, M. Benalia, S. Mouffok, M. Djedid, N. Bouzar, S. Tingry, *J. Inorg. Organomet. Polym. and Mat.*, **31**, 62 (2021).

15. B. A. Belyaev, N. A. Drokin, V. A. Poluboyarov, *Phys. Solid*. State, **60**, 2 (2018).

16. A. L. Diaz, M. R. Cabello, J. Alvarez, A. R. Bretones, S. G. García, *IEEE Trans. Mic. Theor. Tech.*, **66**, 2 (2018).

17. S. Zhang, H. D. Hadi, Y. Wang, B. Liang, V. T. Tiong, F. Ali, Y. Zhang, T. Tesfamichael, L. H. Wong, H. Wang, *IEEE Jour. Photov.*, 3 (2018).

18. M. E. Kompan, Y. P. Stepanov, *Phys. Solid. State,* **56**, 6 (2014).

19. H. Y. Liu, C. C. Hung, W. C. Hsu, *IEEE Elect. Dev. Letters,* **39**, 10 (2018).

20. F. Lisco, P. M. Kaminski, A. Abbas, K. Bass, J. W. Bowers, G. Claudio, M. Losurdo, J. M. Walls, *Thin Solid Films*, **582**, (2015).

21. Y. M. Kim, H. B. Kang, G. H. Kim, C. S. Hwang, S.-M. Yoon, *IEEE Elect. Device Letters,* **38**, 10 (2017).

22. M. Etminan, N. S. Hosseini, N. Ajamgard, A. Koohian, M. Ranjbar, *Optik,* **199**, 163517 (2019).

23. M. A. Chergui, D. Djouadi, B. Benhaoua, A. Chelouche, M. Boudissa, *Optik*, **180**, (2019).

24. M. J. Park, J. Y. Jung, S. M. Shin, J. W. Song, Y. H. Nam, D. H. Kim, J. H. Lee, *Thin Solid Films,* **599**, (2016).

25. P. R. Dilber, L. B. Chandrasekar, N. M. S. S. Bathusha, R. Chandramohan, M. Karunakaran, S. R. Srikumar, *Phys. Solid State,* **60**, 5 (2018).

26. Y.J. Jia, W.X. Su, Y.B. Hu, H.N. Chen, *Bulg. Chem. Commun.,* **49**, 190 (2017).

27. S. Krishnaswamy, V. Ragupathi, S. Raman, P. Panigrahi, G. S. Nagarajan, *Optik,* **194**, (2019).

28. S. T. Zhang, G. Vitrant, E. Pernot, C. Jiménez, D. M. Rojas, D. Bellet, *Nanomaterials,* **8**, 6 (2018).

29. M. A. Sulimov, M. V. Yakushev, I. Forbes, J. M. Prieto, A. V. Mudryi, J. Krustok, P. R. Edwards, R. W. Martin, *Phys. Solid State,* **61**, 5 (2019).

30. M. Tani, Y. Kawamura, M. Horita, Y. Ishikawa, Y. Uraoka, IEEE, Osaka, 2011, p. 84.

31. A. Zaiour, A. Benhaya, T. Bentrcia, *Optik,* **186**, (2019).

32. R. Sharma, S. L. Patel, S. Chander, M. D. Kannan, M. S. Dhaka, *Phys. Letters*, **384**(24)**,** 126557 (2020).

33. S. Tomita, S. Hayashi, Y. Tsukuda, M. Fujii, *Phys. Solid State,* **44**, 3 (2002).

34. H. Slimani, N. Bessous, S. Dagher, A. Hilal-Alnaqbi, M. El Gamal, B. Akhozheya, M. Mohammed, *Materials Research Express,* **2**, 025026 (2020).

35. N. Kamarulzaman, M. F. Kasim, R. Rusdi, *Nano Research Letters,* **10**, 1 (2015).

36. V. Srikant, D. R. Clarke, *J. Appl. Physics,* **83**, 5447 (1998).

37. A. Sáenz-Trevizo, P. Amézaga-Madrid, P. Pizá-Ruiz, P. Pizá-Ruiza, W. Antúnez-Floresa, M. Miki-Yoshida, *Materials Research,* **19**, 33 (2016).

38. Z. Jalil, M. I. Bukhari, *Journal of Physics: Conference Series. IOP Publishing,* 032020 (2018).

39. A. Arif, O. Belahssen, S. Gareh, S. Benramache, *Journal of Semiconductors,* **36**, 013001 (2015).

40. F. K. Shan, Y. S. Yu, *J. Europ. Ceramic Society,* **24**, 1869 (2004).

41. N. Guermat, W. Daranfed, K. Mirouh, *Ann. Chimie Sci. Materiaux,* **44**, 347 (2020).

42. S. Marouf, A. Beniaiche, H. Guessas, A. Azizi, *Materials Research*, **20**, 88 (2016).

43. N. Hacini, M. Ghamnia, M. A. Dahamni, A. Boukhachem, J. Pireaux, L. Houssiau, *Coatings,* **11**, 202 (2021).

44. N. Shakti, P. S. Gupta, *Appl. Physics Research,* **2**, 19 (2010).

45. K. O. Ukoba, A. C. Eloka-Eboka, F. L. Inambao, *Renewable and Sustainable Energy Reviews,* **82**, 2900 (2018).

46. F. Hajakbari, M. T. Afzali, A. Hojabri, *Acta Phys.,* **131**, 417 (2017).

47. A. Echresh, M. A. Abbasi, M. Z. Shoushtari et al. *Semicond. Science and Tech.,* **29**, 115009 (2014).

48. J. Tauc, R. Grigorovici, A. Vancu, *Phys. Status Solidi*, **15**, (1966).

49. J. I. Pankove, Optical Processes in Semiconductors, Dover Publications, Inc., New York, 1971.

50. B. D. Viezbicke, S. Patel, B. E. Davis, D. P. Birnie, *Phys. Status Solidi,* **252**(8), 1700 (2015).

Comparison of antioxidant activity and determination of epigallocatechin gallate and trace elements of green tea samples manufactured and exported by Turkey

L. Paşayeva[1], D. Yuvalı[2], E. Köngül Şafak[1], G. Şeker Karatoprak[1,3*], İ. Narin[2]

[1]Department of Pharmacognosy, Faculty of Pharmacy, Erciyes University, 38039, Kayseri, Turkey
[2]Department of Analytical Chemistry, Faculty of Pharmacy, Erciyes University, 38039, Kayseri, Turkey
[3]Ziya Eren Drug Application and Research Center, Erciyes University, Kayseri, Turkey

Green tea is one of the extensively used drinks in the world. Green tea extract contains several polyphenolic compounds and catechins. Epigallocatechin-3-gallate (EGCG) and epicatechin 3-gallate (ECG) are the most effective antioxidants. In this study, the relation between EGCG content and the antioxidant effect of samples purchased from four different manufacturers was investigated. The antioxidant effects of blended tea samples which contain additives (such as ginger, lemon) and pure green tea samples were compared *via* DPHH$^\bullet$ and ABTS$^{+\bullet}$ radical scavenging tests and β-carotene linoleic acid inhibition methods. The total ash content of green tea samples was determined according to the ISO 1575 test method. All samples were analyzed for trace elements by flame atomic absorption spectrometry (FAAS) after wet digestion. Some tea samples showed a higher (-)-EGCG content (e.g. 164.27 μg in 1 mL infusion for GT-A$_7$), nevertheless, all samples possessed good antioxidant activity. GT-A$_6$ showed the highest level of DPPH$^\bullet$ scavenging activity with 86.0 ± 0.1% inhibition. The TEAC value of GT-A$_5$ and GT-A$_7$ was determined to be 2.58 mmol/L/Trolox. The results of the total ash content (in the range of 5% to 7%) and of the trace elements contents suggest that all tea samples are of high quality.

Keywords: (-)-EGCG, green tea, trace element, antioxidant, LC-MS/MS.

INTRODUCTION

Tea is one of the most widely consumed beverages obtained from *Camellia sinensis* leaves and buds [1]. There are three types of tea like green tea, oolong tea and black tea depending on the level of oxidation. Green tea is an ancient beverage, which was consumed as a medicine and a healthful drink. This plant was used for headaches, body aches and pains, digestion, depression, detoxification in traditional Chinese medicine [2]. Numerous *in vitro* studies showed that fresh green tea leaves are very effective antioxidants. Subject to no fermentation, green tea leaves retain their green color and almost all of their original polyphenol content. Green tea phenolic compounds are mainly composed of catechins (epigallocatechin gallate ((-)-EGCG), epigallocatechin (EGC), epicatechin gallate (ECG) and epicatechin (EC), flavanols and phenolic acids [3]. Green tea also contains other compounds such as vitamins (B, C, E), volatile components and minerals but also some toxic metals such as cadmium (Cd) and lead (Pb) [4].

Green tea and black tea consumption has been increasing in Turkey in recent years, too. Turkey gives importance to tea agriculture and has an important place in the world tea export market. While the first three countries in tea exports are the Netherlands, Belgium and Germany, also Turkish tea is exported to many countries such as the USA, Georgia, Turkish Republic of Northern Cyprus, Singapore, England, Sweden and Mexico. Therefore, many different kinds of green tea assortments developed by tea companies are available in the Turkish market and are also exported abroad. It is stated that these teas sold in markets have high antioxidant activity and that the antioxidant activity of the tea samples is further enhanced by various additives like ginger, lemon, cinnamon, etc. But many factors can affect the quality of green tea during the manufacturing process (a certain grade of fermentation, heating, etc.). Also as a daily beverage, it is important to know the percentage of trace elements leaching into infusions. Therefore, in this study we aimed to: 1) determine the (-)-EGCG content because of its relationship to antioxidant activity; 2) investigate the antioxidant activities *via* radical scavenging (DPPH and ABTS) and β-carotene bleaching assays; 3) monitor the concentration of trace elements, particularly in view of allowable limits and total ash content. This is the first comparative study of antioxidant properties and trace element contents of green tea samples manufactured and exported by Turkey.

---

* To whom all correspondence should be sent:
E-mail:gskaratoprak@gmail.com;
gskaratoprak@erciyes.edu.tr

MATERIAL AND METHODS

Plant material and reagents

In this study, 14 green tea bag samples: GT-A (from Firm 1), GT-A1(soft), GT-A2 (soft with jasmine), GT-A3 (bergamot), GT-A4 (jasmine), GT-A5 (ginger and lemon), GT-A6 (vitamins), GT-A7 (mint and lemon), GT-A8 (chai), GT-A9 (ginkgo), GT-B (from Firm 2), GT-C (from Firm 3), GT-D (from Firm 4), GT-D (from Firm 5), were purchased from Turkey markets. The tea bag samples were chosen from different firms; 10 samples were from one firm and all the others from different firms (Table 1). All chemicals were obtained from the Sigma Chemical Company (St. Louis, MO). Stock solutions (1000 mg/L) of the elements (Mn, Cu, Cr, Cd, Pb, Ni, Fe, Zn) were prepared by dissolving appropriate amounts of their nitrate salts in 1.0 % (v/v) HNO_3 and further diluted daily prior to use.

Determination of total ash content

The total ash content of green tea samples was determined according to the ISO 1575:2015 test method. According to this method, the powdered green tea samples were weighed into a prepared dish and the test portion was heated at a temperature near 100°C until the moisture was expelled. The dish was transferred to a furnace and heated at 525±25 °C until the ash was visibly free from carbon particles. The cooled ash was moistened with distilled water, then dried on a steam bath and then on a hot-plate. The dish was returned to the furnace for 60 min, cooled in a desiccator and weighed. Then it was heated again in the furnace for 30 min, cooled and weighed. These operations were repeated until the difference between two successive weighings did not exceed 0.001 g. This test was done in triplicate and the mean ash content was determined.

Determination of trace elements in green tea samples

A Varian AA240 model atomic absorption spectrometer equipped with single element hollow cathode lamps and anair-acetylene burner was used for the determination of metals. The instrumental parameters were used according to the manufacturer's recommendations. The wet digestion method developed by Narin *et al.* (2004) was used for the sample preparation [5]. For the determination of trace elements, green tea samples (1.000 g) were leached with a mixture of concentrated nitric acid and hydrochloric acid (3:1 v/v). After digestion, samples were filtered and diluted to 10 mL with ultra-deionized water. Blank digestions were carried in the same way.

Quantitative determination of (-)-EGCG in green tea samples

LC-MS/MS experiments were carried out using a Shimadzu LC-MS/MS 8040 (Shimadzu, Japan). A pneumatically assisted electrospray ionization (ESI) ion source was used throughout the experiments. Multiple-reaction monitoring (MRM) conditions were established for standard. The following instrumental settings were used for MRM analysis: heat block temperature, 400 °C; DL temperature, 250 °C; nebulizing gas (N_2), 3 L/min; drying gas (N_2), 15 L/min; collision energy, 25.0, 12.0, 9; dwell time, 100 msec.

The mass spectrometric behavior of (-)-EGCG was studied using both positive-ion and negative-ion ESI. In this experiment, we observed that the negative-ion mode is more sensitive for the detection and analysis of (-)-EGCG.

A mixture of acetic acid-water (1:99, v/v) and acetic acid-methanol (1:99, v/v) was selected as the mobile phase. The mobile phase consisted of 50% acetic acid-water and 50% acetic acid-methanol solution at a flow rate of 0.4 mL/min, and 1 µL of the standard and samples was injected. 1000 µg/mL stock solution of (-)-EGCG was prepared by dissolving the reference standard in methanol and calibration standards (100, 50, 10, 5, 2.5 and 1 µg/mL) were prepared by dilution of the stock solution. For tea sample solutions, 100 µL of infusion was dissolved in 900 µL of ultra-deionized water.

Linearity of the methods was established by triplicate injections of each concentration of standard solutions. Response function of the standard calibration curve was y = 50752x + 30595. The correlation coefficient (r^2) of the calibration curve was 0.9997.

Evaluation of the antioxidant activity of the sample infusions

Each tea bag sample was infused with 250 mL of boiling water (the equivalent of one teacup) for 10 minutes and filtered. The antioxidant activity of tea infusions was evaluated using 2,2-diphenyl-1-picrylhydrazyl (DPPH$^\bullet$) and 2,2'-azino-bis (3-ethylbenzothiazoline-6-sulphonic acid) (ABTS$^{+\bullet}$) radical scavenging and inhibition of *β*-carotene/linoleic acid co-oxidation methods.

DPPH$^\bullet$ radical scavenging method. DPPH$^\bullet$ scavenging abilities of the tea samples were determined using the method of Gyamfi *et al.* [6]. Catechin, epicatechin and epigallocatechin gallate

were used as positive standards. The % inhibition was calculated using equation (1):

% inhibition $= (Abs_{control} - Abs_{sample}/ Abs_{control}) \times 100$ (1)

- *ABTS$^{+\bullet}$ radical scavenging method.* 2,2-Azinobis(3-ethylbenzothiazoline-6-sulfonate) radical (ABTS$^{+\bullet}$) test was used as an alternative for radical scavenging activity determination. Catechin, epicatechin and epigallocatechin gallate were used as positive standards at a concentration of 100 µg/mL. Absorbance was measured on a UV spectrophotometer at 734 nm [7].

- *Inhibition of β-carotene/linoleic acid co-oxidation method.* The *β*-carotene bleaching method [8] was performed to determine the antioxidant activity of tea samples. Absorbance was measured using a spectrophotometer at 470 nm. The antioxidant activity was calculated according to equation (2):

$AAC = [(Abs^{120}_{sample} - Abs^{120}_{control})/ (Abs^0_{control} - Abs^{120}_{control})] \times 100$ (2)

RESULTS AND DISCUSSION

Determination of total ash content of samples

Ash content is an important quality control parameter of tea, a measure of inorganic inclusions and is linked to the mineral content that indicates the quality of the material. In this study, the total ash content was determined by the ISO 1575 test method. According to Turkish Food Codex requirements, the total ash content must be between 4% and 8% [9]. When the total ash content results of the test samples were taken into consideration, it was determined that all samples agree with the Turkish Food Codex in the range of 5% to 7%. These values indicate that no contamination occurred during processing and purport high quality and purity of the tea samples. The results of the tea samples are given in Table 1.

Table 1. Sample codes, total ash content, DPPH$^\bullet$ and ABTS$^{\bullet+}$ radical scavenging results and amount of (-)-EGCG in samples.

Samples	Additives	Total ash content	DPPH$^\bullet$	ABTS$^{\bullet+}$	(-)-EGCG content
		(%)	%Inhibition	TEAC (mmol/L/Trolox)	(µg/mL infusion)
GT-A (Firm 1)	-	7.41 ± 1.23	79.7 ± 3.9	2.54 ± 0.07	86.88 ± 0.59
GT-B (Firm 2)	-	5.52 ± 0.11	82.2 ± 1.7	2.57 ± 0.03	54.18 ± 0.59
GT-C (Firm 3)	-	5.49 ± 1.48	82.7 ± 1.8	2.47 ± 0.00	104.45 ± 1.97
GT-D (Firm 4)	-	6.04 ± 0.72	81.2 ± 1.0	2.58 ± 0.00	104.10 ± 1.45
GT-E (Firm 5)	-	5.38 ± 0.12	79.4 ± 0.8	2.34 ± 0.20	16.98 ± 0.33
GT-A$_1$	Soft	5.38 ± 0.09	81.2 ± 2.7	2.56 ± 0.04	84.90 ± 0.77
GT-A$_2$	Soft with jasmine	6.96 ± 0.63	78.5 ± 3.7	2.57 ± 0.00	85.57 ± 0.69
GT-A$_3$	Bergamot	5.47 ± 1.21	81.3 ± 2.7	2.55 ± 0.04	52.77 ± 5.18
GT-A$_4$	Jasmine	5.12 ± 0.02	81.4 ± 0.3	2.58 ± 0.00	85.90 ± 0.26
GT-A$_5$	Ginger and lemon	6.01 ± 0.02	82.5 ± 1.5	2.58 ± 0.00	79.06 ± 0.64
GT-A$_6$	Vitamins	7.10 ± 0.08	86.0 ± 0.1	2.57 ± 0.00	122.67 ± 1.38
GT-A$_7$	Mint and lemon	5.95 ± 0.17	84.4 ± 0.9	2.58 ± 0.01	164.27 ± 2.28
GT-A$_8$	Chai	6.88 ± 0.84	82.7 ± 2.8	2.55 ± 0.00	133.40 ± 2.40
GT-A$_9$	Ginkgo	6.19 ± 1.05	84.2 ± 0.4	2.51 ± 0.01	106.96 ± 0.18

Table 2. Levels of the investigated ions in the green tea samples.

Concentration (µg/g)[a]

Sample	Mn	Cu	Cr	Cd	Pb	Ni	Fe	Zn
GT-A1	1288.6±23.7	11.4±0.5	< 2.0	1.0±0.1	6.2±0.2	9.7±0.3	333.7±39.3	24.6±1.0
GT-A2	1035.2±48.8	9.0±0.3	< 2.0	1.1±0.1	< 4.0	9.6±1.0	319.7±6.7	19.5±1.0
GT-A3	1158.5±62.5	11.0±0.2	< 2.0	< 0.1	< 4.0	10.3±0.3	352.1±19.9	25.6±03
GT-A4	1195.2±52.8	11.4±0.2	< 2.0	1.3±0.1	4.0	9.7±0.5	320.7±0.8	23.8±1.5
GT-A5	894.1±32.7	8.4±0.5	< 2.0	1.0±0.1	5.9±0.6	5.8±0.2	348.0±2.8	19.9±1,4
GT-A6	868.8±82.3	9.5±0.3	4.4± 0.3	< 0.1	< 4.0	9.4±1.0	286.4±10.9	22.8±0.0
GT-A7	1083.9±61.9	9.9±0.2	< 2.0	1.0±0.1	< 4.0	7.4±0.1	369.4±0.9	19.2±0.7
GT-A8	841.1±17.6	8.2±0.7	< 2.0	1.1±0.1	< 4.0	5.4±0.6	250.0±16.2	20.8±0.6
GT-A9	1305.7±48.4	12.6±1.0	< 2.0	1.1±0.0	< 4.0	8.6±0.4	355.9±27.7	22.3±1.0
GT-A	1083.4±20.6	9.0±0.5	< 2.0	1.1±0.1	< 4.0	5.2±0.6	253.4±2.3	18.7±1.2
GT-B	1083.1±4.2	7.6±0.3	< 2.0	1.2±0.1	< 4.0	4.0±0.3	179.0±16.6	15.1±1.4
GT-C	841.2±6.2	5.2±0.4	< 2.0	1.1±0.1	< 4.0	<3.0	240.1±3.4	13.4±0.9
GT-D	991.2±16.3	8.8±0.7	< 2.0	1.4±0.1	< 4.0	5.0±0.5	275.7±25.1	18.4±2.0
GT-E	933.4±4.5	7.8±0.4	8.1 ± 1.0	1.4±0.1	< 4.0	8.1±0.8	360.4±22.9	17.2±1.7

[a]Data are expressed as mean ± standard deviation (n=3).

Trace elements in green tea samples

The bio elements and toxic metal concentrations of tea samples are given in Table 2. Cadmium, which has a toxic effect on organs and systems such as kidneys, skeletal system and respiratory system, is classified as a human carcinogen. The Joint Expert Committee on Food Additives (JECFA) has determined the weekly tolerable cadmium level (PTWI) as 7 µg/kg body weight [10]. The levels of cadmium were in the range of 1.0-1.4 µg/g in our analyzed samples. The highest and lowest levels of cadmium were found in the GT-D and GT-A1 samples, respectively. These results suggest that the green tea consumption does not exceed the PTWI recommendation for this metal. The levels of cadmium in the tea samples were under the detection limits of the method applied, hereby, it was concluded that green tea consumption is not dangerous for human health.

Lead toxicity is a particularly insidious hazard with the potential of causing irreversible health effects. It interferes with several body functions primarily affecting the central nervous, hematopoietic, hepatic and renal systems by producing serious disorders. The highest concentration of Pb was found in the GT-A1 and GT-A5 samples (6.2 ± 0.2; 5.9 ± 0.6 µg/g, respectively). Pb concentration in the other samples was lower than 4.0 µg/g. The temporary PTWI doses of Pb from all sources tolerated by a healthy human are established as 0.025 mg/kg body weight [11]. Considering the average concentration of Pb

in the respective tea samples, it was determined that they did not threaten health.

The daily requirement for manganese has been established as 6–11 mg/day for a person aged 9-70 years [12]. The lowest manganese level was found in GT-A8 as 841.1 µg/g while the highest was 1288.6 µg/g in GT-A1. According to our results, a cup of tea provides a dietary intake of manganese in the range of 13.33 - 21.33%.

Copper is a trace element that can be found in almost every cell of a human organism. According to our analysis, the maximum concentration of Cu is in GT-A (12.6 µg/g) and the minimum concentration of Cu is in GT-C (5.2 µg/g). The daily requirement for copper has been established as 5-10 mg/day for a healthy person aged 9-70 years [12]. According to the results of our samples, one cup of tea per day provides approximately0.1-0.25%. These results suggest that green tea samples are not a rich source of Cu in the daily diet.

Chromium is an essential nutrient for the body (blood, urine, and body tissues) and is normally present in food. The FDA has determined that the chromium concentration in bottled drinking water should not exceed 0.1 mg/L. The highest concentration of chromium was found at 8.1 µg/g in GT-E and 4.4 µg/g in GT-A6. Cr^{3+} concentration in the other samples was lower than 2.0 µg/g [12, 13]. When the results were examined, even a cup of tea with the highest amount of chromium (GT-E) consumed per day is within the limits determined by the FDA.

Nickel is a nutritionally essential trace element but excessive Ni intake is harmful to humans [14]. The concentration of nickel was found lower than 3.0 µg/g in GT- and 10.3 µg/g in $GT-A_3$. The daily requirement for nickel has been established as 100-600 µg/day for an adult person [12]. When the analysis results were examined, it was clear that green tea samples are not a rich source of nickel.

Iron is a very important element for humans and animals. The daily requirement for iron is 40-45 mg/day. In the green tea samples, GT-B was found to contain the lowest concentration for iron of 179.0 µg/g and $GT-A_7$ was found to contain the highest concentration of 369.4 µg/g [12]. The results of the iron analysis in the tea samples are consistent with the literature and support the view that tea infusions are not an important source of Fe [15].

An adult person needs to intake 23-40 mg/day of zinc for daily dietary requirements. The lowest zinc concentration was found to be 13.4 µg/g in GT-C and the highest concentration was found to be 25.7 µg/g in $GT-A_3$ [16]. Zinc content in tea infusions was found to be low, and therefore cannot be regarded as a major dietary source.

Quantitative determination of (-)-EGCG in green tea samples

Fragmentation of $[M-H]^-$ ion (m/z 457) of (-)-EGCG resulted in three major ions at m/z 125, 169, and 305. The m/z 125 ion represents an unmodified A-ring, the m/z 169 ion is due to the loss of an intact gallic acid anion, while the ion at m/z 305 results from the neutral loss of gallic acid [17] (Fig.1). In our study, three of the most abundant product ions observed were m/z 125 and m/z 169 and 305. The LC-MS/MS spectrum of (-)-EGCG is presented in Fig. 1.
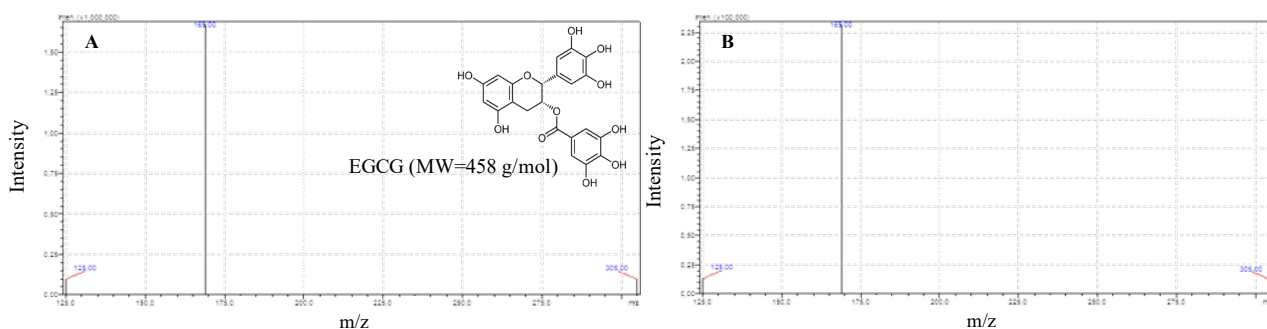
Figure 1. LC-MS/MS mass spectra of (-)-EGCG (A) and GT-A_7 (B)
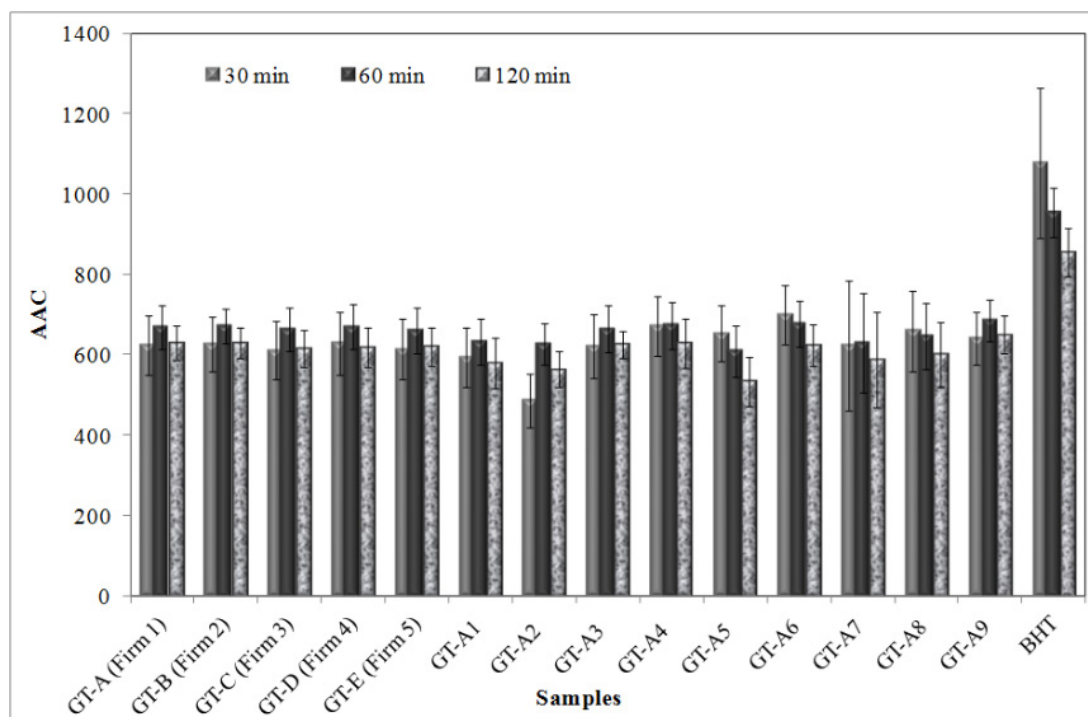
Figure 2. Effect of the samples and positive control (BHT) on *β*-carotene/linoleic acid co-oxidation. Data are expressed as mean ± standard deviation (n=3).

All samples were analyzed in triplicate. The results are shown in Table 1. It is observed that "blended" tea samples have a lower (-)-EGCG content than "pure" green tea samples. The tea sample named GT-A_7 presented the highest amount of (-)-EGCG (164.27 μg in 1 mL infusion). The LC-MS/MS spectrum of GT-A_7 is shown in Fig.2.GT-A_7 sample was found more active than catechin and epicatechin as positive controls in the ABTS test. This tea sample also showed the highest level of DPPH$^\bullet$ scavenging activity with 86.4 ± 0.9 % inhibition. So, it can be concluded that mint and lemon additives do not affect the antioxidant activity but the latter is generally affected by the amount of EGCG.

Evaluation of the antioxidant activity of the infusions

DPPH$^\bullet$ and ABTS$^{\bullet+}$ radical scavenging inhibitions of samples are given in Table 1. Although there is no significant difference among tea samples, GT-A_6 showed the highest level of DPPH$^\bullet$ scavenging activity with $86.0 \pm 0.1\%$ inhibition. In this experiment, the addition of vitamins or other plants like jasmine, chai, ginkgo, etc. into the tea bags did not increase the antioxidant activity. The lowest activity was observed for the GT-A_2 sample with $78.5 \pm 3.7\%$ inhibition. Since the jasmine additive in the GT-A_2 sample will cause a decrease in the amount of green tea, this may be reflected in the results of scavenging activity.

In the ABTS$^{\bullet+}$ radical scavenging method, green tea samples without additives were generally found more active than the other samples. The TEAC value of GT-A_4, GT-A_5 and GT-A_7 was determined to be 2.58 mmol/L/Trolox and was found to be higher than those of catechin and epicatechin which were used as positive controls.

The oxidation-inhibiting effect of the samples was determined in a time-dependent manner, and time-dependent alteration was observed. The inhibition percentages of all extracts are given in Fig. 2. All samples managed to inhibit β-carotene bleaching but were not found as active as the synthetic antioxidant butylated hydroxytoluene (BHT). Dissolving tea samples in water may cause a decrease in the amount of nonpolar antioxidant compounds. In this method, nonpolar antioxidants were concentrated at the lipid-air interface and provided high protection in emulsions against polar antioxidants that exist in the aqueous phase [18,19].

CONCLUSION

In the present study, we aimed to compare the relation between EGCG content and antioxidant activity of pure and blended tea samples and also to determine the percentage of trace elements leached into infusions. The highest EGCG content was found in pure tea samples and tea blends. As a result of this study, antioxidant activities of the blended samples were found higher than those of pure samples. These results indicated that the antioxidant activity is not only affected by the amount of EGCG but also by different additives. The results of the total ash and trace elements contents suggest that all tea samples which are manufactured and exported by Turkey have high quality and purity. This study supports that consumption of green tea per day has a significant beneficial effect on health.

Conflict of interest: *The authors declare that they have no conflict of interest.*

REFERENCES

1. S. N. Senanayake, *J. Funct. Food*, **5(4)**, 1529 (2013).
2. C. Cabrera, R. Artacho, R. Giménez, *J. Am. Coll. Nutr*., **25(2)**, 79 (2006).
3. A. Rietveld, S. Wiseman, *J. Nutr*., **133(10)**, 3285 (2003).
4. E. W. Chan, E. Y. Soh, P. P. Tie, Y. P. Law, *Pharmacognosy Res*., **3(4)**, 266 (2011).
5. I. Narin, M. Tuzen, M. Soylak, *Talant*a, **63(2)**, 411 (2004).
6. M. A. Gyamfi, M. Yonamine, Y. Aniya, *Gen. Pharmacol*., **32(6)**, 661 (1999).
7. M. A. Papandreou, C. D. Kanakis, M. G. Polissiou, S. Efthimiopoulos, P. Cordopatis, M. Margarity, F. N. Lamari, *J. Agric. Food Chem*., **54(23)**, 8762 (2006).
8. B. D. Oomah, G. Mazza, *J. Agric. Food Chem*., **44(7)**, 1746 (1996).
9. Turkish Food Codex Communiqué on Tea. Number 29389, Codex No 2015/30, 2015.
10. P. Vračko, J. Tuomisto, J. Grad, E. Kunsele, Exposure of children to chemical hazards in food. Fact Sheet 44 May Code RPG 4 Food Ex. European Environment and Health Information System. World Health Organization Regional Office for Europe, Copenhagen, Denmark, 2007.
11. J. Fiłon, J. J. Ustymowicz-Farbiszewska, J. Górski, J. Karczewski, *J. Elem*., **18(3)**, 381 (2013).
12. P. Trumbo, A. A.Yates, S. Schlicker, M. Poos, *J. Am. Diet Assoc*., **101**(3), 294 (2001).
13. http://www.atsdr.cdc.gov/toxprofiles/tp.asp

14. W. S. Zhon, T. Ren, L. J. Zhao, *J. Food Drug Anal.*, **24(1)**, 46 (2016).
15. R. Street, J. Száková, O. Drábek, L. Mládková, *Czech J. Food Sci.*, **24(2)**, 62 (2011).
16. S. G. Rosalind, C. K.Janet, L. Nicola, *Food Nutr. Bull.,* **37(4)**, 443 (2016).
17. C.-T. Ho, J.-K. Lin, F.Shahidi, Tea and tea products: chemistry and health-promoting properties, CRC press, Boca Raton, 2008.

18. G. Şeker Karatoprak, F. Göger, M. B. Yerer, M. Koşar, *Pharm. Biol.*, **55**, 1608 (2017).
19. L. Pizzale, R. Bortolomeazzi, S. Vichi, E. Überegger, L. S. Conte, *J. Sci. Food Agric.*, **82(14)**, 1645 (2002).
20. J. J. A. Wu, M. T. Chiang, Y. W. Chang, J. Y. Chen, H. T. Yang, C. K. Lii, H. T. Yao, *J. Food Drug Anal.*, **19(3)**, 289 (2011).

Intensification of CO_2 absorption using nanofluids in a structured packed column

P. P. Selvi*, R. Baskar

Department of Chemical Engineering, Kongu Engineering College, Perundurai, Erode-638060, Tamil Nadu, India

The current advances in science and technology revolve around sustainable development. A lot of efforts has been made to reduce carbon dioxide emission which accounts for climatic change. Among them, the carbon dioxide capture by chemical absorption is close to commercialization. This paper presents a comparative study of a conventional solvent, aqueous ammonia, with a next generation working fluid, graphene oxide nanofluid. Aqueous ammonia is used as the solvent which has good thermal and oxidative stabilities with lower regeneration energy. It is reported that nanofluids increase mass transport compared to base fluids. Instead of traditional random packing, structured packing is used which increases the efficiency of the absorption. Several other parameters are taken into consideration such as solvent flow rate, gas flow rate, temperature of the process, concentration of the solvent and gas, etc., for calculating the efficiency and mass transfer characteristics. The nanofluids are prepared by ultrasonic treatment and show good dispersion stability. This accounts for an increase in the absorption efficiency of the solvent by 82 %.

Keywords: Absorption, Nanoparticles, Mass Transfer, Carbon dioxide, Ammonia

INTRODUCTION

The recent changes in the climatic conditions of the Earth are due to the emission of greenhouse gases into the atmosphere. Usually, the carbon dioxide present in the atmosphere is utilized by green plants. Research has found that the increase in carbon dioxide content raises global warming [1]. At higher temperatures, there is a decrease in the absorption of carbon dioxide by the plants. Global Carbon Project has found that there is an increase in carbon dioxide emission of 2 % in 2018 and about 2.6 % in 2019. The scientists claim that there will be an increase in carbon dioxide emission by 45% than the preindustrial levels [2, 3]. A special report from the Intergovernmental Panel on Climate Change reported that carbon emission should fall to 50% by 2030 in order to keep the global temperatures within ±1.5 °C [4, 5]. An increase in coal consumption by 7.1% in India and 4.5% in China causes increased release of carbon dioxide into the atmosphere than normal. The shift in the trend line from an increase in carbon dioxide emission can be done by two methods. One is to support the emission reduction and the other is to restrict the emission growth of the nations that increase the emission of carbon dioxide. The increase in the growth of renewable and low carbon technologies accounts to strengthen emission reduction. Recent technologies developed should outpace the climatic impacts and drive the emission to zero by 2050 [6-8].

The main contributing factor in the chemical absorption is attributed to the packing materials. These materials provide a large area of contact between the solvent and the acidic gas phase. There are mainly two types of packing materials: dumped or random packing and regular or structured packing. In general, random packing is made of cheap inert materials such as clay, porcelain or a variety of plastics. Different packing materials have different surface area and void space between the packing which accounts for packing performance.

Table 1. Physical properties of the CO_2/NH_3 system.

Liquid density (kg/m^3)	0.86
Liquid viscosity (cp)	0.276
Gas density (kg/m^3)	1.977
Gas viscosity (kg/ms)	1.8×10^{-5}
Temperature (K)	303
Pressure (atm)	1

Most of the carbon dioxide emission comes from the power plants and chemical industries. Hence, advancement should be made to the present carbon dioxide capture technology to reduce the emission. One such technique is the Carbon Capture Sequestration (CCS). Among these techniques, the absorption of carbon dioxide by chemical solvents can be commercialized. Research has found that the amine solutions account for the increased absorption rate of carbon dioxide. Recent literature studies prove that ammonia is a promising solvent. The major advantage of ammonia over other amine solutions is that it does not degrade easily, has low energy input and no corrosion problem [9, 10]. The use of structured packing increases the efficiency and good mixing of carbon dioxide and ammonia solvent. The recent working fluid that is a nanofluid attracts the attention of the

* To whom all correspondence should be sent:
E-mail: selvi.chem@kongu.edu

recent researchers. It is found that the nanofluid increases the absorption of carbon dioxide into the solvent by several possible mechanisms. Among them, grazing or shuttle mechanism and Brownian mechanism account for mass transport [11]. During grazing mechanism, at the gas-liquid interface nanoparticles adsorb the carbon dioxide in the film layer and after some time desorb them in the solvent, which increases the rate of absorption. In the Brownian mechanism, the nanoparticles disturb the flow and enhance the mixing of the liquid leading to an increase in residence time and good gas-liquid contact within the absorption column [12]. This accounts for an increase in the rate of absorption. The aim of the present work is to examine the outcome of nanoparticles in carbon dioxide absorption by studying the effects of nanofluid concentration, liquid flow rate and its concentration.

MATERIALS AND METHODS

Synthesis of graphene oxide

Graphene is an allotrope of carbon and graphene oxide was prepared using modified Hummer's technique [13]. Graphite fine powder (0.5 g), 0.5 g of sodium nitrate and 23 ml of sulphuric acid were added in a conical flask surrounded by an ice bath with constant stirring. After 4 hours, 3 g of potassium permanganate was added and the reaction was continued for about 2 hours at 35 °C. Then, 46 ml of distilled water were added, and the mixture was kept at 98 °C for 2 hours without boiling and then the contents were let to cool to ambient temperature. After that 100 ml of distilled water were added and stirred constantly for 1 hour. Ten ml of hydrogen peroxide was added and stirred constantly for another hour. The resultant solution containing graphene oxide nanoparticles was washed, filtered and the sample was kept in an ultrasonicator to maintain the stability of the graphene nanofluid. Then the graphene nanofluid was dried and submitted to particle size analysis.

Nanofluid characterization

Particle size analysis. Graphene oxide nanoparticles, that were prepared using the modified Hummer's method, were analyzed for particle size using a particle size analyzer. Three different samples of the synthesized particles were produced. Their frequency and diameter of the particles were interpreted from the analyzer report. The readings of the three different samples were collected and an average of the three readings was made. A graph was plotted against the average diameter of the particles and their average

frequency as shown in Figure 1. It was inferred that the average size of the particle ranges from 100–530 nm [14].

Table 2. Experimental conditions of the structured packed column.

S. No	Parameter	Conditions
1	Absorption solvent	Aqueous ammonia solution
2	Gas flow rate (L min⁻¹)	9, 12, 14, 17, 19, 21, 23
3	CO₂ : Air ratio	4:1
4	Liquid flow rate (L h⁻¹)	10, 12, 15, 18, 20, 22
5	Ammonia concentration (% v/v)	2, 4, 6, 8, 10, 12
6	Temperature (⁰C)	28
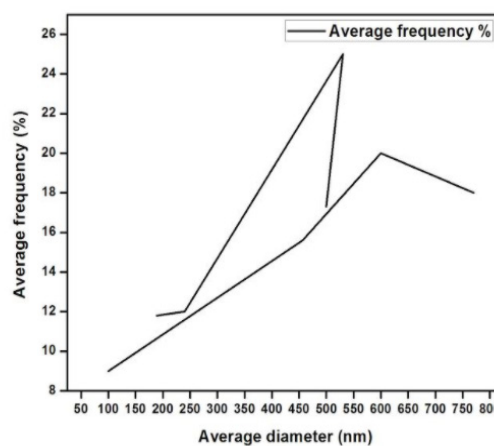
Fig. 1. Average frequency *vs* average diameter.

Experimentation for CO₂ absorption with nanofluids

The experimental setup for the packed absorption column is shown in Figure 2 and Table 1. The column was made of glass by 0.6 m height with 0.05 m ID. The absorption column was packed with laboratory BX-DX structured packing material with 0.045 m OD and 0.05 m height. Porosity of the packing material was 90 % with specific surface area of 250-750 m²/m³ (Tables 2 and 3). Both the gas and solvent flow rates were controlled by flow meters. CO₂ gas and compressed air was sent at the bottom of the column. When blend gas attained steady-state, aqueous ammonia was sent to the top of the column. After that the reacted sample was collected in the reservoir. The collected reacted sample was titrated against 0.1N HCl because, during the reaction of the gas mixture with aqueous ammonia, ammonium carbonate was formed which is a weak base and should be titrated against strong acid. The nanoparticles were taken at concentrations of 0.0001, 0.001 and 0.0015 %

413

(w/v). For stability of nanoparticles in the base liquid, it was kept in the ultrasonicator for 3 hours. The prepared nanoparticles were immediately sent to the container and used in the CO_2 capture to prevent the deposition of the nanoparticles [15].

Experimentation for enhancement of CO_2 absorption by inducing magnetic field

To generate a homogeneous magnetic field, a coil of 1.1 mm thick copper wire with windings was wrapped around the external surface of the absorption column. The coil of 0.5 m height was placed in the middle part of the column and a maximum electrical current of 2 A was applied.
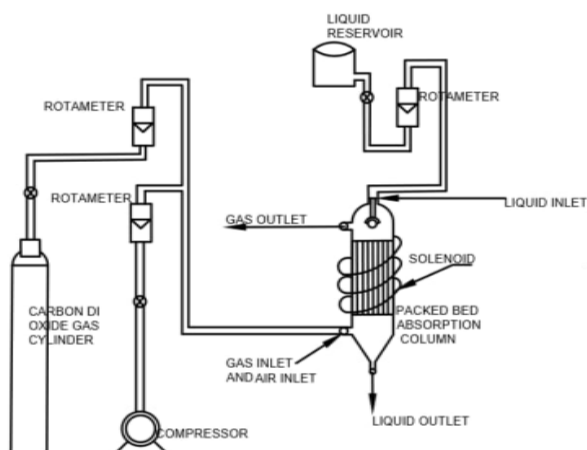
Fig. 2. Schematic diagram of the experimental setup.

Table 3. Equipment used in the study.

S.No	Component	Specification
1	Gas flow rate	1-25 lpm
2	Solvent flow rate	1-25 lph
3	CO_2 cylinder	100 % pure
4	Compressor	ELGI air compressor (0-8 kg/cm²)
5	Pump	¼ HP fractional pump (Tullu water pump)
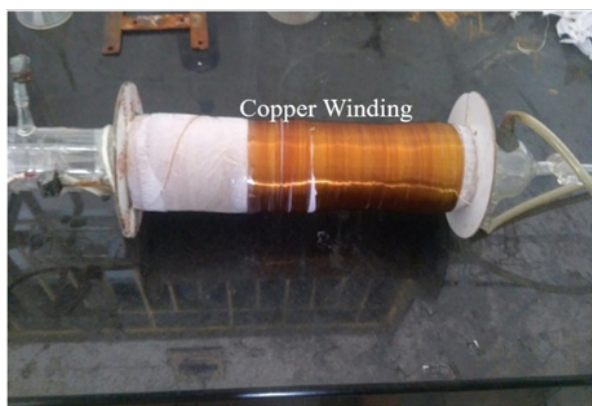
Fig. 3. Packed absorption column with external magnetic field.

RESULTS AND DISCUSSION

CO_2 absorption with structured packing employing graphene oxide nanofluid with solvent

Graphene oxide nanoparticles were dissolved in the 12 % (v/v) ammonia solvent at various concentrations ranging from 0.0001 to 0.0015 % (w/v). An enhancement of mass transfer coefficient, removal efficiency and absorption rate with the introduction of graphene oxide nanofluid was found. This enhancement was due to both Brownian motion and grazing effect. The nanoparticles increased the interfacial area, which simultaneously increased the rate of absorption. This is because nanoparticles break the gas bubbles into smaller ones and thereby the liquid ammonia molecules stick around these nanoparticles, which enhances the CO_2 absorption. Figures 4–6 & 8 infer that the % CO_2 removal, NTU, rate of absorption, and mass transfer coefficient increase with solvent flow rate and concentration. In Figure 7, HTU decreases with an enhancement of liquid flow rate along with concentration. Similar results have been reported in [17] for absorption studies of CO_2 with different nanofluids in packed and wetted-wall columns.

Effect of liquid flow rate on % CO_2 removal

The effect of liquid flow rate on % CO_2 removal for structured packing material with 12 % (v/v) solvent concentration for different graphene oxide nanofluid concentrations (varying from 0.0001 to 0.0015 % (w/v) is shown in Figure 4.
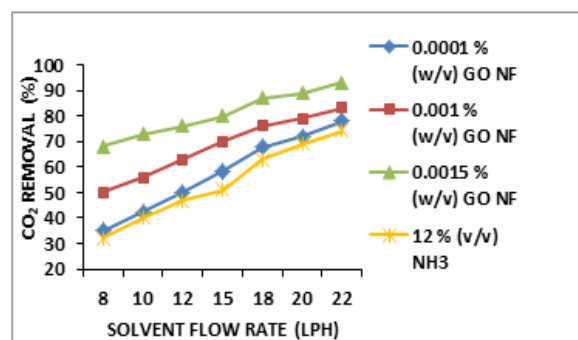
Fig. 4. Effect of solvent flow rate on % CO_2 removal by employing graphene oxide nanofluid.

It is seen that the % CO_2 removal increases with the increase in the concentration of graphene oxide. This is due to the increase in surface area of the nanoparticles which results in the enhancement of Brownian movement and the grazing effect of the nanofluid leading to a higher percentage of CO_2 removal. The gas-liquid flow rates showed a

positive effect on mass transfer. Here the liquid phase of the gas-liquid system was dominant. CO_2 absorption increased at higher solvent flow rates due to the turbulence effect. For graphene nanofluid of 0.0001 % (w/v), the % CO_2 removal efficiency was 78 %; for 0.001 % (w/v) it was 83 % and for 0.0015 % (w/v) - 93 %. Without a nanofluid, the % CO_2 removal was 74 %. Similar results have been reported in a previous study in a packed column with nanofluid [16].

Effect of solvent flow rate on rate of absorption

The effect of solvent flow rate on mass transfer rate per unit volume for a structured packing material with 12 % (v/v) solvent concentration for the different graphene oxide nanofluid concentrations (varying from 0.0001 to 0.0015 % (w/v) is shown in Figure 5.
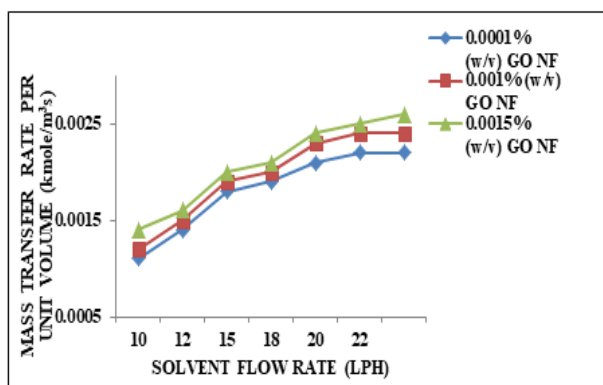
Fig. 5. Effect of solvent flow rate on the rate of absorption by employing graphene oxide nanofluid.

It is seen from this graph that the mass transfer rate increases with an increase in the concentration of nanoparticles and the maximum enhancement in the mass transfer rate was obtained at 0.0015 % (w/v) graphene oxide nanofluid. Besides, on increasing the mass fraction of nanoparticles from 0.0001 % (w/v) to 0.0015 % (w/v), the higher amount of nanoparticles supplies more energy to the solvent and thereby decreases the gas bubble size. With the Brownian movement and grazing effect, gas molecules adsorbed on the nanoparticles and moved to the liquid phase where desorption took place. The rate of absorption for 0.0001 % (w/v) graphene oxide nanofluid was 0.0022 kmol/m³s, for 0.001 % (w/v) graphene oxide nanofluid it was 0.0024 kmol/m³s and for 0.0015 % (w/v) graphene oxide nanofluid - 0.0026 kmol/m³s. As the concentration of the nanofluid increased from 0.0001 to 0.0015 % (w/v), the greater surface area of the particles led to a higher absorption rate of CO_2. Similar results have been reported in a

previous study [18] in a packed column with nanofluid.

Effect of liquid flow rate on the number of transfer units

The effect of solvent flow rate on the number of transfer units (NTU) for a structured packing material with 12 % (v/v) solvent concentration for the different graphene oxide nanofluid concentrations (varying from 0.0001 to 0.0015 % (w/v) is shown in Figure 6. The NTU is given by:

$$NTU = \ln\left(\frac{y_1}{y_2}\right)$$
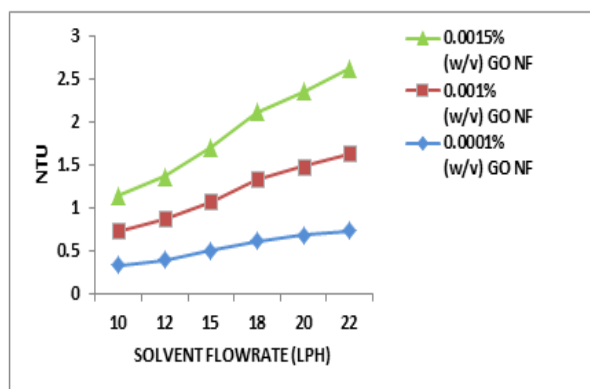
Fig. 6. Effect of solvent flow rate on NTU by employing graphene oxide nanofluid.

It is seen that the NTU value is 2.5 for 0.0015 % (w/v) graphene oxide nanofluid. For 0.001% (w/v) graphene oxide nanofluid the NTU value is 1 and for 0.0001 % (w/v) graphene oxide nanofluid the NTU is 0.5. The higher the number of transfer units, the higher will be the purity of the separation of the CO_2 gas. Hence, the NTU increased for a structured packing material with 12 % (v/v) ammonia concentration. This may be due to an increase in the number of smaller gas bubbles in the graphene oxide nanofluid. Similar results have been reported in a previous study [19] in a packed column with nanofluid.

Effect of solvent flow rate on the height of transfer unit (HTU)

The effect of solvent flow rate on HTU for a structured packing material with 12 % (v/v) solvent concentration for the different graphene oxide nanofluid concentrations (varying from 0.0001 to 0.0015 % (w/v) is shown in Figure 7. The graph illustrates the effect of HTU on the liquid flow rate for the different nanofluid concentrations. Bubble coalescence of two gas bubbles was achieved by both grazing and hydrodynamic effects when the

graphene oxide nanoparticles were present in the solvent and hence reduced the HTU value.
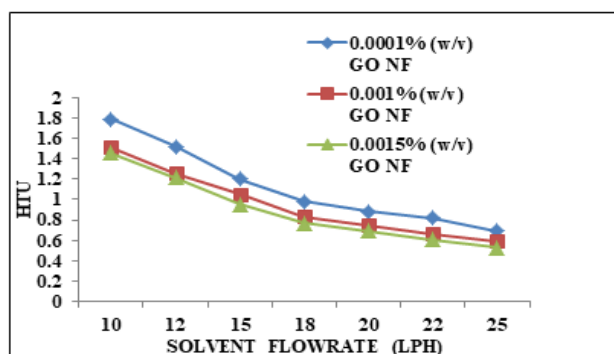
Fig. 7. Effect of solvent flow rate on HTU by employing graphene oxide nanofluid.

The HTU value is 1.8 for 0.0001 % (w/v) graphene oxide nanofluid. For both the 0.001 % (w/v) and 0.0015 % (w/v) graphene oxide nanofluids the HTU value is almost 1.5. Hence, the lower the HTU value, the higher is the separation purity of the gas thereby increasing the mass transfer coefficient. Similar results have been reported in a previous study [20] in a packed column with nanofluid.

Effect of solvent flow rate on the volumetric mass transfer coefficient

The effect of solvent flow rate on the mass transfer coefficient for a structured packing material with 12 % (v/v) solvent concentration for the different graphene oxide nanofluid concentrations (varying from 0.0001 to 0.0015 % (w/v) is shown in Figure 8. The overall mass transfer coefficient $K_G a$ in $kmol/hm^3$ is determined by:

$$K_G a = \frac{N_A}{Z\, A_C\, P_T\, \Delta y}$$

where a is the interfacial area in m^2/m^3, A_c is the area of the column in m^2, P_T is the total pressure in atm and Δy is the difference in the mole fraction.

The overall absorption rate can be described as:

$$\emptyset = K_G\, a_V\, P_{CO2}$$

Due to the hydrodynamic effect, the nanoparticles surrounding the gas molecules break the gas-liquid interfacial boundary layer into a thin layer and the gas diffusion into the liquid phase increases with the presence of graphene oxide nanoparticles near the interfacial layer which creates turbulence and increases the volumetric mass transfer coefficient. It is seen from the graph that $K_G a$ is 8 $kmol/hrm^3$ for 0.0001 % (w/v)

grapheme nanofluid. For 0.001 % (w/v) and 0.0015 % (w/v) the mass transfer coefficient is 13 and 14 $kmol/hrm^3$, respectively. This is mainly due to the introduction of a nanofluid along with the absorbent. Similar results have been reported in a previous study [17] in a packed column with nanofluid.
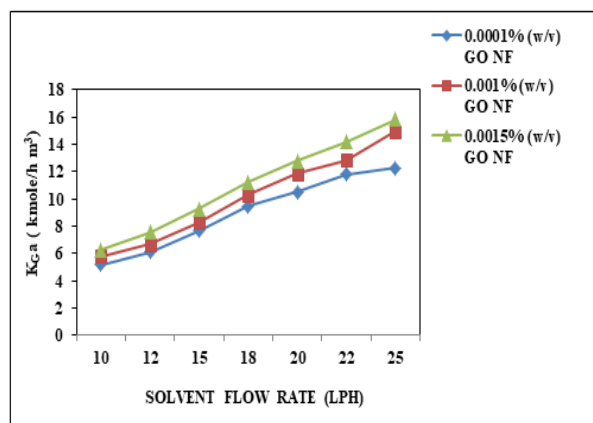
Fig. 8. Effect of solvent flow rate on the volumetric overall mass transfer coefficient by employing graphene oxide nanofluid.

CONCLUSIONS

From this study, the following conclusions are made for the absorption of CO_2 in a structured packed column using aqueous ammonia solvent, and graphene oxide nanoparticles with external magnetic field:

i. The mass transfer coefficient increased with the addition of graphene oxide nanoparticles.

ii. The increase in solvent flow rate and the increase in solvent concentration up to 12% increased the removal efficiency.

iii. Nanoparticles in the magnetic field yielded the best results compared to those without the addition of nanoparticles in a normal column.

iv. The removal efficiency in the presence of a magnetic field is 82% which is higher than former results. The 0.0015% concentration of graphene nanoparticles showed better results.

REFERENCES

1. A. H. Abdulsattar, S. Shridar, L. A. Bromley, *AIChE J*, **23,** 62 (1977).
2. A. G. Bhave, D. K. Vyas, J. B. Patel, *Renew. Ener.,* **33,** 1716 (2008).
3. S. E. Abechi, C. E. Gimba, A. Uzairu, Y. A. Dallatu, *Res. J. Chem. Sci.*, **3,** 754 (2013).
4. P. P. Selvi, R. Baskar, *J. Chem. Soc. Pak.*, **41,** 820 (2019).
5. A. Constantinou, A. Gavriilidis, *Ind. Eng. Chem. Res.*, **49,** 1041 (2010).
6. A. Bello, R. O. Idem, *Ind. Eng. Chem. Res.*, **44,** 945 (2005)

7. A. Aroonwilas, *Ind. Eng. Chem. Res.*, **43,** 2228 (2004).
8. A. Aroonwilas, P. Tontiwachwuthikul, *Chem. Eng. Sci.,* **55,** 3651 (2000).
9. A. Aroonwilas, P. Tontiwachwuthikul, *Ind. Eng. Chem. Res.*, **37,** 569 (1998).
10. A. Rahbar-Kelishamia, H. Bahmanyar, *Chem. Eng. Res. Des.*, **90,** 615 (2012).
11. A. Aboudheir, N. Ramachandran, R. Idem, P. Tontiwachwuthikul, *Ind. Eng. Chem. Res.*, **45,** 2608 (2006).
12. A. Cantu-Perez, S. Barrass, A. Gavriilidis, *Chem. Eng. J.*, **160,** 834 (2010).
13. H. A. Al-Hosney, V. H. Grassian, *Phys. Chem.*, **71,** 266 (2005).
14. A. Mohebbi, M. Taheri, H. Hashemipour, A. M. Rashidi, *J. Nat. Gas Sci. Eng.*, **28,** 410 (2016).
15. S. H. Ali, M. A. Fahim, S. Q. Merchant, *Sep. & Purif. Tech.*, **27,** 121 (2002).
16. S. S. Ashrafmansouri, M. N. Esfahany, *Intern. J. Ther. Sci.*, **82,** 84 (2014).
17. Q. Zeng, Z. Niu, Y. Guo, W. Lin, *Ind. & Eng. Chem. Res.*, **51,** 5309 (2012)
18. R. Lal, *Energy & Environ. Sci.*, **1,** 86 (2008).
19. H. Monnier, L. Falk, *Chem. Eng. Sci.,* **66,** 2475 (2011).
20. J. T. Cullinane, T. G. Rochelle, *Ind. & Eng. Chem. Res.,* **45,** 2531 (2006).

Modelling and multicriteria analysis for selection of growth rate models for batch cultivation of *Kluyveromyces marxianus var. lactis* MC 5 yeast. Part I: Modelling with different types of growth rate models

M. M. Petrov

Institute of Biophysics and Biomedical Engineering, Bulgarian Academy of Sciences,
105 Acad. George Bonchev Str., Sofia 1113, Bulgaria

To explain the kinetics of cell growth, this work examined ten unstructured models for growth rate – *Monod*, *Mink*, *Tessier*, *Moser*, *Aiba*, *Andrews*, *Haldane*, *Luong*, *Edward* and *Han-Levenspiel* in batch cultivation of *Kluyveromyces marxianus var. lactis* MC 5 yeast. For the first time, the process of modelling was done using two separate models for growth kinetics separately for the two main substrates – lactose and oxygen. The following criteria were used to validate the models: sum of squared weighted residuals, statistics λ, relative error, Fisher's experimental function, and experimental correlation coefficient. Each of the criteria was used separately for biomass / lactose or biomass / oxygen. At the end of the study, the criteria of the growth rate models were compared depending on lactose-only or oxygen-only. The model with the most criteria that meet the minimum and maximum requirements for lactose is the *Han-Levenspiel* model. In terms of oxygen, the *Moser* model has the best results.

Keywords: Modelling, Growth rate models, *Kluyveromyces marxianus var. lactis* MC 5 yeast, statistical criteria

INTRODUCTION

Strains belonging to the yeast species *Kluyveromyces marxianus* have been isolated from a wide variety of habitats. For this reason, this strain has been used for various biotechnological applications: production of enzymes, unicellular protein, aromatic compounds and ethanol, reduction of lactose content in food products, production of bioelements from cheese-whey, etc. [1].

There is currently no general mathematical model of yeast *Kluyveromyces marxianus var. lactis* MC 5 due to the extreme complexity and the great variety of vital activities of yeast and the great variety of strains. Although, there are different models of the biotechnological process and of different parts of whey fermentation [2].

The aim of this work is to model the *Kluyveromyces marxianus var. lactis* MC 5 yeast in batch cultivation with ten different models for growth rate, separately for the two main substrates – lactose and oxygen and to choose the most suitable models.

MATERIALS AND METHODS

Experimental investigation

The *Kluyveromyces marxianus var. lactis* MC 5 yeast was cultivated under the following conditions [3]:

1. Nutrient medium with basic component – whey ultrafiltrate with lactose concentration 44 g/L. The ultrafiltrate was derived from whey separated in production of white cheese and deproteinisation by ultrafiltration on LAB 38 DDS with membrane of the type GR 61 PP under the following conditions:

    −   Temperature, t 40 – 43 °C;
    −   Input pressure, P_{in} 0.65 MPa;
    −   Output pressure, P_{out} 0.60 MPa.

    The ultrafiltrate was used in native condition with lactose concentration of 44 g/L. Nutrient medium consisted of:

    − $(NH)_4HPO$ 0.6%;
    −   Yeast autolisate   5%;
    −   Yeast extract   1%;
    −   pH   5.0 – 5.2.

    The gas flow rate was Q_G = 60 L/L/h up to the 4th hour and Q_G = 120 L/L/h up to the end of the process under continuous mixing with n = 800 min⁻¹. The temperature was 29°C.

2. The changes of the microbiological process (lactose conversion in yeast's cells to protein) were studied during the strain growth:

    −   lactose concentration in the fermentation medium in oxidation and assimilation of lactose by *Kluyveromyces Marxianus var. lactis* MC 5 was determined by enzyme methods and UV tests (Boehringer Mannheim, Germany, 1983);

To whom all correspondence should be sent:
E-mail: mpetrov@biomed.bas.bg

– concentrations of cell mass and protein contents were determined on the basis of the nitrogen content (Kjeltek system 1028);

– concentration of dissolved oxygen in the fermentation medium in the process of oxidation and assimilation of lactose was determined by an oxygen sensor. The oxygen sensor produced by LKB firm was used for the measurement of the oxygen concentration in the fermentation medium.

3. Duration of the cultivation was $t_f = 12$ hours. Six fermentations were carried out in aerobic batch cultivation of *Kluyveromyces Marxianus var. lactis* MC 5. The experimental investigations were carried out on a computer controlled laboratory bioreactor 2L-M with magnetic coupling.

In modelling the process, we used the mean values of the kinetic variables from the six fermentations.

Kinetic models

The model includes cell concentration in the dependence between concentrations of the basic energetic substrates – lactose and oxygen. In all our previous works [4-7] for modelling, optimisation and optimal control for the specific growth rate we have always used *Mink* model for lactose and *Haldane* model for oxygen:

$$\mu(S,C) = \frac{\mu_m S^2}{K_S + S^2} \frac{C}{K_C + C + C^2 / K_{CI}}$$

where: S – lactose concentration, g/L; C – oxygen concentration, g/L; μ_m – maximal growth rate, h^{-1}; K_S, K_C and K_{CI} – kinetic parameters, g/g.

In contrast to the previously used approaches for process modelling, in this work, the kinetic models were developed separately for the two main substrates:

– *Biomass production from lactose-only*

$$\frac{dX}{dt} = \mu(S) X$$

$$\frac{dS}{dt} = -\frac{1}{Y_{X/S}} \frac{dX}{dt}$$

(1)

where: t – process time, h; X – biomass concentration, g/L; $\mu(S)$ – growth rate of biomass from lactose, h^{-1}; $Y_{X/S}$ – yield coefficients of formation of the biomass from lactose, g/g.

– *Biomass production from oxygen-only*

$$\frac{dX}{dt} = \mu(C) X$$

$$\frac{dC}{dt} = -\frac{1}{Y_{X/C}} \frac{dX}{dt} + k_l a(C^* - C)$$

(2)

where: $\mu(C)$ – growth rate of biomass from oxygen, h^{-1}; $Y_{X/C}$ – yield coefficients of formation of the biomass from oxygen, g/g; $k_l a$ – mass transfer coefficient, h^{-1}; C^* – maximal oxygen concentration in liquid phase, g/L.

The initial conditions of both models (Eqns. 1 and 2) were:

$X(0) = 0.2$ g/L, $S(0) = 44$ g/L; $C(0) = 6.65 \cdot 10^{-3}$ g/L, and $C^* = C(0)$.

System constraints of both models

Nearly all engineering processes have physical constraints. The lactose and oxygen concentrations must be positive all the time for the processes, otherwise, an unrealistic solution in the identification problem will be obtained [8]:

$$g_1(t,\mathbf{x}) = -S(t) \le 0$$

(3)

$$g_3(t,\mathbf{x}) = -C(t) \le 0$$

(4)

In addition, here are the following constraints for stochiometry by the processes:

$$g_2(t,\mathbf{x}) = \frac{S(0) - S(t)}{X(t) - X(0)} - \frac{1}{Y_{X/S}} \le 0$$

(5)

$$g_4(t,\mathbf{x}) = \frac{k_l a(C^* - C)}{X(t) - X(0)} - \frac{1}{Y_{X/C}} \le 0$$

(6)

where: x – vector of the kinetic parameters, $\mathbf{x} = \mathbf{x}[\mu_m^S, ..., Y_{X/S}]^T$ for model (Eqns. 1), and $\mathbf{x} = \mathbf{x}[\mu_m^C, ..., Y_{X/C}, k_l a]^T$ for model (Eqns. 2).

Specific growth rate models

The paper compares ten unstructured models [9-13]: M_1 – *Monod*, M_2 – *Mink*, M_3 – *Tessier*, M_4 – *Moser*, M_5 – *Aiba*, M_6 – *Andrews*, M_7 – *Haldane*, M_8 – *Luong*, M_9 – *Edward*, and M_{10} – *Han-Levenspiel* to explain the kinetics of cell growth (Table 1).

In Table 1: $\mathbf{Z} = [S, C]^T$ – vector with basic energetic substrates lactose and oxygen, respectively; $\mu_m^{\mathbf{Z}}$ – maximum growth rate for lactose and oxygen, respectively, h^{-1}; $K_{\mathbf{Z}}$ – *Monod* saturation constants for cell growth on lactose and oxygen, g/L; α_M – *Moser* constant; $K_{\mathbf{Z}I}$ – inhibition constants for cell growth on lactose and oxygen, g/L; K – constant in *Edward* model, g/L; $\mathbf{Z}_m$ – critical inhibitor concentrations, above which the reaction stops, g/L; m, n – constants in the *Luong* and the *Han-Levenspiel* models.

Table 1. Tested growth rate models dependent on lactose or oxygen

Model	$\mu(\mathbf{Z})$
$M_1(\mathbf{Z})$	$\mu(\mathbf{Z}) = \dfrac{\mu_m^{\mathbf{Z}} \mathbf{Z}}{K_{\mathbf{Z}} + \mathbf{Z}}$
$M_2(\mathbf{Z})$	$\mu(\mathbf{Z}) = \dfrac{\mu_m^{\mathbf{Z}} \mathbf{Z}^2}{K_{\mathbf{Z}} + \mathbf{Z}^2}$
$M_3(\mathbf{Z})$	$\mu(\mathbf{Z}) = \mu_m^{\mathbf{Z}} \left(1 - \exp(-\mathbf{Z}/K_{\mathbf{Z}I})\right)$
$M_4(\mathbf{Z})$	$\mu(\mathbf{Z}) = \dfrac{\mu_m^{\mathbf{Z}} \mathbf{Z}^{\alpha_M}}{K_{\mathbf{Z}} + \mathbf{Z}^{\alpha_M}}, \; \alpha_M > 0$
$M_5(\mathbf{Z})$	$\mu(\mathbf{Z}) = \dfrac{\mu_m^{\mathbf{Z}} \mathbf{Z}}{K_{\mathbf{Z}} + \mathbf{Z}} \exp(-\mathbf{Z}/K_{\mathbf{Z}I})$
$M_6(\mathbf{Z})$	$\mu(\mathbf{Z}) = \dfrac{\mu_m^{\mathbf{Z}} \mathbf{Z}}{(K_{\mathbf{Z}} + \mathbf{Z})(1 + \mathbf{Z}/K_{\mathbf{Z}I})}$
$M_7(\mathbf{Z})$	$\mu(\mathbf{Z}) = \dfrac{\mu_m^{\mathbf{Z}} \mathbf{Z}}{K_{\mathbf{Z}} + \mathbf{Z} + \mathbf{Z}^2/K_{\mathbf{Z}I}}$
$M_8(\mathbf{Z})$	$\mu(\mathbf{Z}) = \dfrac{\mu_m^{\mathbf{Z}} \mathbf{Z}}{K_{\mathbf{Z}} + \mathbf{Z}} \left(1 - \mathbf{Z}/\mathbf{Z}_m\right)^n$
$M_9(\mathbf{Z})$	$\mu(\mathbf{Z}) = \dfrac{\mu_m^{\mathbf{Z}} \mathbf{Z}}{K_{\mathbf{Z}} + \mathbf{Z} + \left(1 + \mathbf{Z}/K\right)\left(S^2/K_{\mathbf{Z}I}\right)}$
$M_{10}(\mathbf{Z})$	$\mu(\mathbf{Z}) = \dfrac{\mu_m^{\mathbf{Z}} \mathbf{Z}}{\mathbf{Z} + K_{\mathbf{Z}}} \dfrac{\left(1 - \mathbf{Z}/\mathbf{Z}_m\right)^n}{\left(1 - \mathbf{Z}/\mathbf{Z}_m\right)^m}$

Criteria for evaluation of the model parameters

The least-squares error is commonly employed as a criterion to inspect how close the computed profiles of the state variables come to the experimental observations [14]:

$$\mathbf{Q} = \frac{1}{N} \sum_{i=1}^{N} \left(\frac{(X_e(t_i) - X_m(t_i))^2}{X_{e\max}^2} + \frac{(\mathbf{Z}_e(t_i) - \mathbf{Z}_m(t_i))^2}{\mathbf{Z}_{e\max}^2} \right) \quad (7)$$

where: $\mathbf{Q} = [Q_1, Q_2]^T$, Q_1 and Q_2 – sums of the squares of weighted residuals lactose-only or oxygen-only; N – number of the experiments; t_i – time partitions; $X_e(t_i), X_m(t_i)$ – experimental and simulated values of biomass concentration, g/L; $X_{e\max}^2$ – maximal experimental value of biomass concentration in the end of the process, g/L; $\mathbf{Z}_e(t_i) = [S_e(t_i), C_e(t_i)]^T$, $\mathbf{Z}_m(t_i) = [S_m(t_i), C_m(t_i)]^T$ – experimental and simulated values of lactose and oxygen, respectively, g/L.

The constraints were included in the parameter estimation problem (Eqn. 7), in order to avoid unrealistic predicted values:

$$\min_{\mathbf{x}} \mathbf{J} = \mathbf{Q} + \sum_{i=1}^{4} w_i \int_{t=0}^{t_f} g_i(t, \mathbf{x}) dt \quad (8)$$

where $\mathbf{x}$ is a vector of the estimated parameters; $\mathbf{J} = [J_1, J_2]^T$, J_1 and J_2 – criteria of minimization for lactose-only and for oxygen-only; t_f – final time, h; $g_i(t, \mathbf{x})$ – system constraints, $i = 1,\ldots,4$; w_i – weight of each constraint, $w_i = 10^2$. Such a large weight of each constraint was chosen to make it easier to identify models. If the constraints are satisfied, then $g_i(t, \mathbf{x}) = 0$.

Criteria for model validation

The best values are defined by the criteria:
  – $C_1(S) \equiv J_1 \times 10^{-3}$ or $C_1(C) \equiv J_2 \times 10^{-3}$ – criteria for evaluation of parameters (Eqn. 8);
  – $C_2(S)$ or $C_2(C)$ – statistic λ. The criteria C_2 was compared to the tabular Fisher coefficient $F_T^{\lambda}(\nu_1, \nu_2)$, where ν_1 – degree of freedom of model, and ν_2 – degree of freedom of experimental data, $\nu_2 = N - 2$;
  – [$C_3(X)$ and $C_4(S)$] or [$C_3(X)$ and $C_4(C)$] – relative error (S_L) for the kinetic variables (X, S) or (X, C);
  – [$C_5(X)$ and $C_6(S)$] or [$C_5(X)$ and $C_6(C)$] – experimental Fisher coefficient for the kinetic variables (X, S) or (X, C). The obtained values of criteria C_5 and C_6 were compared to the tabular values for Fisher coefficient (F_T) for degrees of freedom $F_T(\nu_2, \nu_1)$;
  – [$C_7(X)$ and $C_8(S)$] or [$C_7(X)$ and $C_8(C)$] – experimental correlation coefficient R^2 for the kinetic variables (X, S) or (X, C). The obtained values of criteria C_7 and C_8 were compared to the tabular values of correlation coefficient $(R_T^2(\nu_2))$ with a degree of freedom ν_2. $\qquad$ (7)

Statistic λ, relative error S_L, Fisher coefficient (F) and correlation coefficient (R^2) are fully presented in [15].

RESULTS AND DISCUSSION

Modelling of the process from lactose-only or oxygen-only

In the first part of this work, the aim was to model the process separately (of course, the separation is artificial) for lactose and oxygen with 10 different growth rate models (Table 1). Here we were interested only in the results obtained for the criteria $(C_1 - C_8)$ by which the studied models were evaluated.

An algorithm and a program of COMPAQ Visual FORTRAN 90 [16] were developed in order to identify the parameters in models (Eqns. 1 – 8). All computations were performed using HexaCore

AMD Phenom II X6 1075T, 3 GHz, 8 GB RAM, Windows XP operating system (32 bit).

Tables 2 and 3 show the results for the criteria by which the models ($M_1 - M_{10}$) were validated lactose-only (Eqns. 1), and oxygen-only (Eqns. 2).

Here it is time to specify that for criteria $C_1 - C_6$ we are looking for a minimum value, and for criteria C_7 and C_8 – for a maximum one. The best values of all criteria are marked in green. The maximum values for criteria $C_1 - C_6$, and the minimum values for criteria C_7 and C_8 are marked in red.

The minimal ($C_{i\min}$) and maximal ($C_{i\max}$) values of every criterion for lactose-only and oxygen-only are shown in Table 4.

From the presented results (Table 4) it can be seen that we have better values of the criteria in the modelling of the process depending on oxygen-only. Criterion C_1 for oxygen-only has better minimum and maximum values than that for lactose-only. The difference in the minimum values for criterion C_2 is minimal (only 3% in favour of criterion C_2 for lactose-only). Only for criterion C_4(S) in lactose-only we have a better result. This should show us that the growth kinetics of biomass depend more on oxygen-only than on lactose-only.

The criteria C_2, and $C_5 - C_8$, are statistical. The theoretical values of C_2 and $C_5 - C_8$ are given in statistical tables [17]. Fisher coefficient for C_2 (Statistic λ) is $F_T^\lambda(2,11) = 4.04$. Fisher coefficients (C_5 and C_6) are $F_T(11,2) = 19.40$, and for correlation coefficients (C_7 and C_8) the tabular value is $R_T^2(11) = 0.684$ for level of significance $\alpha = 0.01$.

Table 2. Criteria for models validation for lactose-only

Models	$C_1(S)$	$C_2(S)$	$C_3^{'}(X)$	$C_4(S)$	$C_5^{'}(X)$	$C_6(S)$	$C_7^{'}(X)$	$C_8(S)$
$M_1(S)$	13.8827	151.8377	0.2262	0.5030	1.0125	1.1676	0.9864	0.9754
$M_2(S)$	9.6736	**204.1643**	0.2058	**0.6288**	1.0598	**1.0253**	**0.9744**	0.9920
$M_3(S)$	10.6736	**151.3657**	0.1982	0.3879	1.0220	1.1364	**0.9869**	0.9819
$M_4(S)$	9.2521	175.7246	0.1960	0.3883	1.0471	1.0591	0.9790	0.9894
$M_5(S)$	14.0315	151.7896	0.2274	0.5067	1.0124	1.1690	0.9863	0.9752
$M_6(S)$	13.9697	151.9010	0.2270	0.5051	1.0129	1.1684	0.9863	0.9753
$M_7(S)$	13.9765	152.1378	0.2272	0.5045	1.0130	1.1681	0.9864	0.9752
$M_8(S)$	13.8925	151.7663	0.2262	0.5036	1.0128	1.1679	0.9864	0.9754
$M_9(S)$	**14.1648**	151.9544	**0.2289**	0.5087	**1.0118**	**1.1698**	0.9863	**0.9749**
$M_{10}(S)$	**6.0574**	184.7091	**0.1641**	**0.1845**	**1.0694**	1.0313	0.9853	**0.9944**

Table 3. Criteria for model validation for oxygen-only

Models	$C_1(C)$	$C_2(C)$	$C_3^{''}(X)$	$C_4(C)$	$C_5^{''}(X)$	$C_6(C)$	$C_7^{''}(X)$	$C_8(C)$
$M_1(C)$	0.6734	**154.5335**	0.1612	0.5992	1.0127	1.0174	**0.9992**	0.9986
$M_2(C)$	1.5593	163.0421	0.1864	**0.9618**	1.0187	1.0155	**0.9988**	**0.9963**
$M_3(C)$	1.0059	161.9099	0.1748	0.8047	1.0141	1.0203	0.9991	0.9978
$M_4(C)$	**0.6727**	156.9493	**0.1596**	0.6473	**1.0115**	1.0223	**0.9992**	**0.9988**
$M_5(C)$	1.1461	160.2555	0.1818	0.2635	1.0174	1.0178	0.9989	0.9975
$M_6(C)$	1.4423	**172.3611**	**0.2021**	0.2539	1.0223	1.0235	0.9989	0.9969
$M_7(C)$	**1.6108**	169.1571	0.1941	0.2713	1.0195	**1.0286**	0.9989	0.9965
$M_8(C)$	1.1806	165.3167	0.1869	**0.2492**	1.0218	1.0164	0.9989	0.9975
$M_9(C)$	1.1256	159.8748	0.1812	0.2646	1.0176	1.0169	0.9989	0.9975
$M_{10}(C)$	1.0604	163.3446	0.1855	0.2611	**1.0226**	**1.0111**	0.9990	0.9978

Table 4. Intervals of variation of lactose-only and oxygen-only criteria

Lactose-only			Oxygen-only		
Criteria	$C_{i\min}$	$C_{i\max}$	Criteria	$C_{i\min}$	$C_{i\max}$
$C_1(S)$	6.0574	14.1648	$C_1(C)$	**0.6727**	1.6108
$C_2(S)$	**151.3657**	204.1643	$C_2(C)$	154.5335	172.3611
$C_3^{'}(X)$	0.1641	0.2289	$C_3^{''}(X)$	**0.1596**	0.2021
$C_4(S)$	**0.1845**	0.6288	$C_4(C)$	0.2492	0.9618
$C_5^{'}(X)$	1.0118	1.0694	$C_5^{''}(X)$	**1.0115**	1.0226
$C_6(S)$	1.0253	1.1698	$C_6(C)$	**1.0111**	1.0286
$C_7^{'}(X)$	0.9744	0.9869	$C_7^{''}(X)$	**0.9988**	0.9992
$C_8(S)$	0.9749	0.9944	$C_8(C)$	**0.9963**	0.9988

The criterion $C_2 > F_T^\lambda(2,11) = 4.04$, the experimental Fisher coefficients, criteria (C_5 and C_6) $< F_T(11, 2) = 19.40$, and the experimental correlation coefficients criteria (C_7 and C_8) $> R_T^2(11) = 0.684$.

From the presented results (Tables 2, 3, and 4) it can be seen that with regard to the validation criteria (C_2, $C_5 - C_8$) all growth rate models, depending only on lactose or oxygen, are adequate and each of them can be used for modelling.

The kinetic parameters (due to artificial separation) of the individual growth rate models are not shown in this part of the work. They differ significantly from each other. For example, in the study on lactose-only, the maximum growth rate is $\mu_m \approx 1.0$, and on oxygen only: $0.60 \le \mu_m \le 0.74$. For this reason, no significant conclusions can be drawn from their values.

Fig. 1 shows the results for the biomass formation depending on lactose-only or oxygen-only.

(a)

(b)
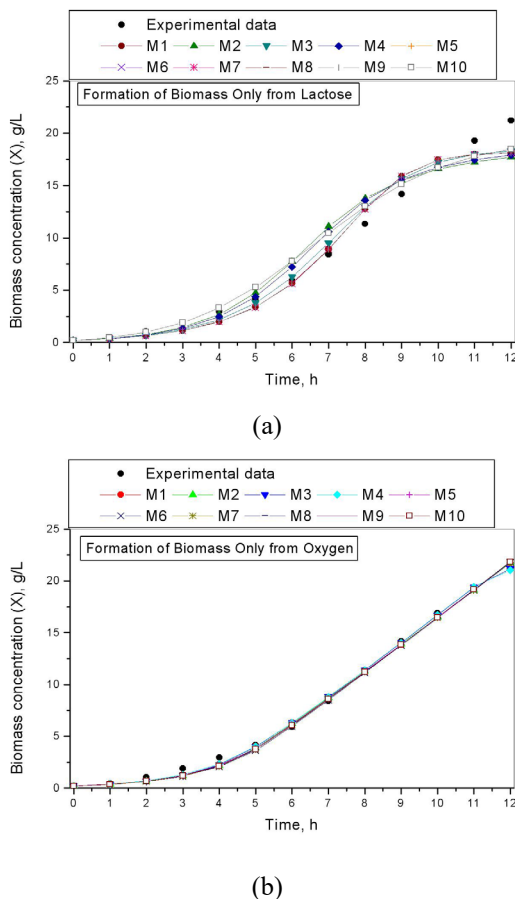
Fig. 1. Formation of biomass: a) Formation of biomass from lactose-only, b) Formation of biomass from oxygen-only.

Fig. 1a shows that the biomass concentration depends only on lactose present and there is a discrepancy between the experimental and

simulated data for the kinetic variable. Fig. 1b shows that the biomass concentration depends only on oxygen present where is a different situation. All investigated growth rate models describe very well the experimental values of the kinetic variables of the process.

Fig. 2 shows the results of lactose or oxygen concentration for models (Eqns. 1) and (Eqns. 2).

(a)

(b)
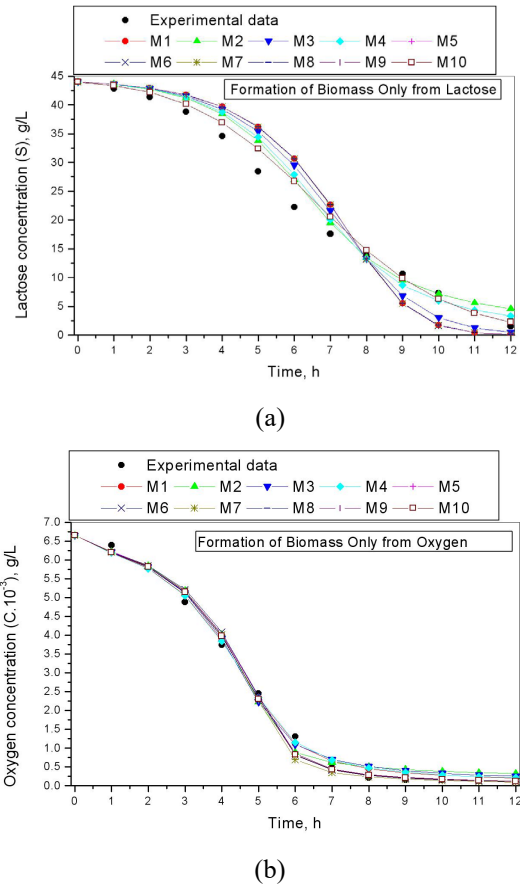
Fig. 2. Lactose and oxygen concentration models: (a) Lactose concentration, (b) Oxygen concentration.

Figs. 2a and 2b show a situation similar to the reasoning made for Figs. 1a and 1b. The modelling of the lactose concentration model (Eqns. 1) shows a relatively lower correspondence between the experimental and simulated results compared to the results obtained by model (Eqns. 2), shown in Fig. 2b.

Finally, if we look formally at choosing a lactose-only growth rate model, we will notice (Table 2) that the model with the best results (criteria $C_1(S)$, $C_3'(X)$, and $C_4(S) \to$ min, and $C_8(S) \to$ max) is that of $M_{10}(S)$. Therefore, we choose the *Han-Levenspiel* model as the most suitable for modelling growth rate only from lactose.

Regarding the formal choice of growth rate model only from oxygen (Table 3), the best results by most criteria has the model $M_4(C)$. For this

model we have: $C_1(C)$, $C_3''(X)$ and $C_5''(X)$ → min, and criteria $C_7''(X)$ and $C_8(C)$ → max. Therefore, a logical choice for the oxygen-only growth rate is the *Moser* model.

CONCLUSIONS

In this work, ten unstructured models in batch cultivation of *Kluyveromyces marxianus var. lactis* MC 5 yeast were studied. For the first time in modelling this process two kinetic models were used, separately for lactose and oxygen. The comparison of the obtained results with the statistical criteria: statistics λ, Fisher's function and the correlation coefficient, showed that all the ten models are adequate and can be used to model the process depending on lactose-only or oxygen-only.

The formal choice of growth rate model showed that this is the *Han-Levenspiel* model for lactose-only, and the Moser model for oxygen-only.

In the next part of the work, the PROMETHEE II method will be applied to finally determine the best models for lactose and oxygen. These models will be modelled and studied.

REFERENCES

1. B. Llorente, A. Malpertuy, G. Blandin, F. Artiguenave, P. Wincker, B. Dujon, *FEBS Lett.*, **487**, 71 (2000).
2. M. Petrov, T. Ilkova, *Ecology – Scientific Articles*, **2**, 256 (2007).
3. P. Angelov, M. Petrov, St. Tzonkov, Proc. Int. Workshop and Young Scientist School Bioprocess Engineering, Sofia, 1995, p. 114.
4. M. Petrov, T. Ilkova, in: Automatic and Informatics (Proc. Int. Conference Automatic and Informatics, 2008, Sofia), 2008, p. II.13.
5. M. Petrov, *Int. J. Bioautomation*, **5**, 39 (2006).
6. M. Petrov, in: BioPS (Proc. 19th Int. Symposium Bioprocess Systems, Sofia, 2006), 2006, p. I.31.
7. M. Petrov, T. Ilkova, J. Vanags, *Int. J. Bioautomation*, **19**, S81 (2015).
8. K. Dutta, V. Dasuc, B. Mahanty, A. Prabhua, *Biochem. Eng. Q.*, **29**, 437 (2015).
9. N. Gera, R. V. S. Uppaluri, S. Sen, V. Dasuc, *Chem. Biochem. Eng. Q.*, **22**, 315 (2008).
10. R. Giridhar, A. Srivastava, *Chem. Biochem. Eng. Q.*, **14**, 133 (2000).
11. D.-J. Kim, J.-W. Choi, N.-C. Choi, B. Mahendran, C.-E. Lee, *Appl. Microbiol. Biotechnol.*, **69**, 456 (2005).
12. P. Saravanan, K. Pakshirajan, P. Saha, *Bulg. Chem. Commun.*, **43**, 502 (2011).
13. D. Sudipta, S. Mukherjee, *Int. J. Water Resour. Environ. Eng.*, **2**, 40 (2010).
14. Y. Chen, F.-S. Wang, *Industrial and Eng. Chem. Res.*, **42**, 6843 (2003).
15. M. Petrov, T. Ilkova, *J. Int. Sci. Publ. Mater. Methods Technol.*, **10**, 468 (2016).
16. COMPAQ Visual FORTRAN Programmer's Guide, v. 6.6, Compaq Computer Corporation, Houston, Texas, 2001.
17. I. Vuchkov, St. Stoyanov, Mathematical Modelling and Optimization of Technological Objects, Technique, Sofia, 1986, p. 47, (in Bulgarian).

Study of wear intensity of solid nanocoatings deposited on steel 1.2080 (X12)

V. Rupetsov[1*], Iv.Uzunov[2], A. Mishev[3], Iv. Panov[4], E. Velev[1]

[1] *Plovdiv University "Paisii Hilendarski", 24 Tzar Assen Str. 4000 Plovdiv, Bulgaria,*
[2] *Central Laboratory of Applied Physics, Bulgarian Academy of Sciences, 61 Sankt Petersburg Blvd., 4000 Plovdiv, Bulgaria*
[3] *University Stuttgart, Germany*
[4] *Technical University - Sofia, Plovdiv Branch, 25 Tsanko Diustabanov Str., 4000 Plovdiv, Bulgaria*

The wear resistance of hard nanocoatings - TiN, TiCN and nc-TiAlN/a-Si$_3$N$_4$ - deposited on tool steel 1.2080 (X12) was studied. One-factor experimental tests on specific wear intensity resulting from the load were performed. The research methodology is based on the volume of the removed material. Correlation dependences of the specific wear intensity on the load were found. A comparative assessment of the individual coatings was made and practical guidelines for their application were proposed.

Keywords: multilayer coating, wear intensity, PVD method

INTRODUCTION

Tool steel 1.2080 (X12) is widely used for the manufacture of cutting and forming tools for plastic deformation. The increase of the service life of these tools is achieved primarily by increasing the wear resistance of the cutting and forming elements [1, 2]. The chemical-thermal methods for coating [3-5] do not always meet the tribological requirements toward the forming tools made of X12 tool steel. Under certain operating conditions (high process temperatures) these tools are not sufficiently effective from a tribological point of view, which limits their wide application. This type of coating is further developed by adding different amounts of other elements during the process of laying in order to improve the physical, mechanical and tribological properties of the coating. For example, by adding carbon, TiCN is obtained which combines both the high hardness and the low friction coefficient of TiC with the high strength of TiN [6-8]. Adding aluminum and boron produces TiAlN, TiBN or TiB$_2$, respectively [9-14]. These additives improve the tribological characteristics of the friction surfaces [15-19], which leads to improvement of the dynamic behavior of the technological processes [9, 20, 21].

An important requirement is to apply coatings with small thickness (about 1-3 μm), which is achieved by the nanotechnologies of the vacuum deposition methods (PVD, CVD). These methods provide high purity, very good adhesion to the substrate, good uniformity and density of the layers, small residual stresses and microdefects in the structure, possibility for deposition of ultra-thin layers, very good possibilities for controlling the thickness, structure, mechanical stresses and other parameters of the layers, all listed leading to high quality of the obtained coatings [9, 22].

The results from numerous studies of various types of coatings deposited on a particular material reveal their tribological characteristics. However, no studies have been performed of the different hard-alloy coatings on the same material and no comparative analysis of them has been made. Such an analysis is important for the practical application of the coatings.

EXPERIMENTAL

This work aims at studying the specific wear intensity of TiN and TiCN hard coatings and of the nanocomposite coating nc-TiAlN/a-Si$_3$N$_4$ deposited on tool steel 1.2080 (X12), as well as at making a comparative analysis of these coatings and giving recommendations for their practical application.

- Samples of tool steel were made, with the following characteristics (Table 1):

Table 1.

Notation	EN	DIN	Böhler	DS
	1.2080	*X210Cr12*	*K100*	*X12*
Composition	C 2%; Si 0.1-0.4%; Mn 0.15-0.45%; Ni ≤0.4%; S ≤0.03%; P≤0.03%;Cr 11.5-13%			

*To whom all correspondence should be sent:
E-mail: velko_r@abv.bg

- The samples were subjected to heat treatment in the sequence: annealing, hardening and tempering with the following characteristics of the modes:
- Annealing - heating to a temperature of 800 - 850 °C, holding for 1 (one) hour and cooling with the furnace. Hardness after annealing - 230-250 HB;
- Hardening - heating in a vacuum furnace to a temperature of 1000-1050°C, holding for 35 minutes and cooling in a stream of nitrogen under pressure. Hardness after hardening - 64-65 HRC;
- Low-temperature tempering - heating to a temperature of 180-200°C for a minimum of 2 (two) hours after reaching the pre-set temperature and cooling in calm air. Hardness after tempering - 59-60 HRC.
- The samples were divided into three groups:
  - group A: unhardened, ground to roughness Ra = 0.11 μm;
  - group B: hardened to hardness HRC=59-60 and ground to roughness Ra = 0.11 μm;
  - group C: hardened to hardness HRC=59-60 and polished to roughness Ra = 0.02 μm;
- Both the TiN and TiCN hard coatings and the nanocomposite coating nc-TiAlN/a-Si$_3$N$_4$ were applied by the electric arc PVD method in a vacuum chamber: coating thickness - 2 μm; temperature of coating - 300 ºC; hardness - (30-31) GP.
- Measurement of the parameters of the wear trace was performed with TESA microscope, magnification 100×.
- The specific wear intensity I_w was determined by the volume method, using the dependence [23, 24]:

$$I_w = \frac{V}{F.L}, \text{mm}^3/\text{N.m,} \tag{1}$$

where V is the volume of the amount of removed material (the trace), mm^3;

F is the normal load, N; L is the distance or the run of the sample relative to the counter-body, m.

- For more convenient, fast and acurate calculation of the parameters from the formula above, a program was generated in MS Excel [2].

RESULTS AND DISCUSSION

The experimental studies were conducted by the method "Ball on Flat Sliding Wear Test" with horizontal orientation of the tested surface (Fig. 1)

on a SIIP-1 stand (Fig. 2) [23].
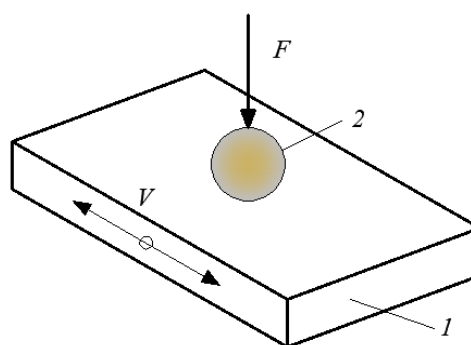
Fig. 1. Friction scheme according to the Ball on Flat Sliding Wear Test

Fig. 2. General view of a SIIP stand for testing wear resistance

The variable factor here is the load F (N), varying from 1 to 5 N. Three experiments were conducted for each value of the load. The constant factors are: the speed V=20 mm/s and the length of the distance L=75 m. The width of the trace is measured in five points and then the average value taken.

Table 2 presents the results for the specific wear intensity of the TiN hard coating, Table 3 gives the results for the specific wear intensity of the TiCN hard coating, and Table 4 shows the results for the specific wear intensity of the nc-TiAlN/a-Si$_3$N$_4$ nanocomposite.

Table 2.

Load F, N	X12_A	X12_B	X12_C
TiN Specific wear intensity as a function of the load I_w=f (N), V=20mm/s = const, L=75m = const			
1	4.175	13.547	12.266
2	2.312	14.492	10.161
3	6.121	15.018	13.942
4	19.547	14.561	12.914
5	19.368	13.977	12.657

Table 3.

Load F, N	X12_A	X12_B	X12_C
TiCN Specific wear intensity as a function of the load I_w=f (N), V=20mm/s = const, L=75m = const			
1	11.521	7.068	5.171
2	10.982	7.523	3.315
3	7.643	6.675	2.967
4	8.109	7.419	2.454
5	15.24	7.311	2.255

Table 4.

Load F, N	X12_A	X12_B	X12_C
nc-TiAlN/a-Si$_3$N$_4$ Specific wear intensity as a function of the load Iw=f (N), V=20mm/s = const, L=75m = const			
1	88.893	79.084	75.547
2	73.956	82.279	80.098
3	71.327	60.414	86.778
4	70.603	62.255	83.009
5	199.839	84.985	121.515

The graphics and the correlation dependences of the wear intensity on the load for the different coatings are given in Figures 3, 4 and 5.
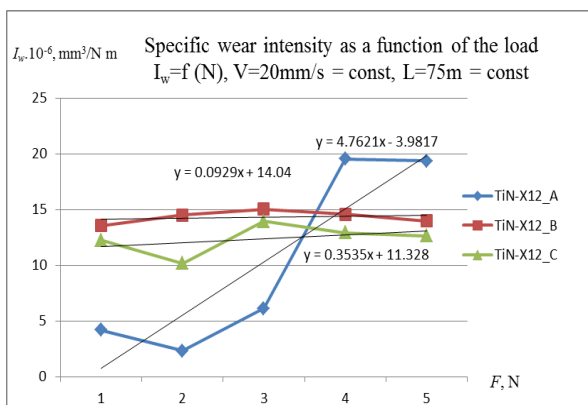
Fig. 3. Specific wear intensity for TiN, depending on the load
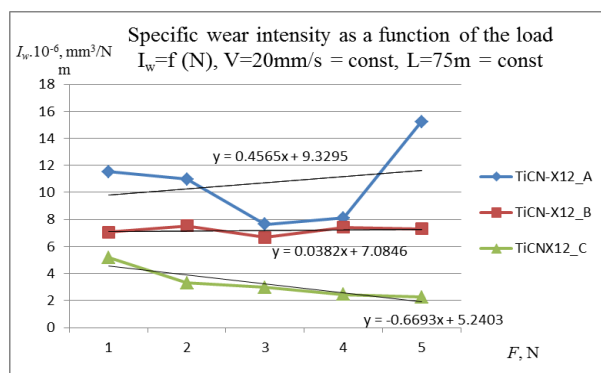
Fig. 4. Specific wear intensity for TiCN, depending on the load
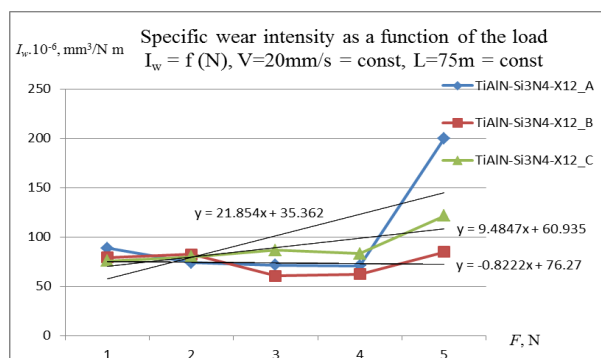
Fig. 5. Specific wear intensity for nc-TiAlN/a- Si$_3$N$_4$, depending on the load

A comparative assessment of the uncoated samples and the three types of coatings for the following surfaces was made: unhardened and ground (Table 5); hardened and ground (Table 6) hardened and polished (Table 7).

Table 5.

Load N	E_X12_A	TiN-X12_A	TiCN-X12_A	TiAlN/Si$_3$N$_4$-X12_A
Specific wear intensity as a function of the load I_w = f (N), V=20mm/s = const, L=75m = const				
1	78.189	4.175	11.521	88.893
2	77.602	2.312	10.982	73.956
3	166.609	6.121	7.643	71.327
4	179.268	19.547	8.109	70.603
5	424.063	19.368	15.24	199.839

Table 6.

Load N	E_X12_B	TiN-X12_B	TiCN-X12_B	TiAN/SI3N4-X12_B
Specific wear intensity as a function of the load I_w = f (N), V=20mm/s = const, L=75m = const				
1	5.2809	13.547	7.068	79.084
2	49.874	14.492	7.523	82.279
3	43.828	15.018	6.675	60.414
4	91.679	14.561	7.419	62.255
5	128.543	13.977	7.311	84.985

Table 7.

Load N	E_X12_C	TiN-X12_C	TiCN-X12_C	TiAlN/Si3N4-X12_C
	Specific wear intensity as a function of the load $I_w = f(N)$, V=20mm/s = const, L=75m = const			
1	62.075	12.266	5.171	75.547
2	87.334	10.161	3.315	80.098
3	90.493	13.942	2.967	86.778
4	146.221	12.914	2.454	83.009
5	287.34	12.657	2.255	121.515

The graphics and the correlation dependences of the wear intensity on the load for the uncoated samples and the three types of coatings, deposited on the different technological surfaces, are given in Figs. 6, 7 and 8.
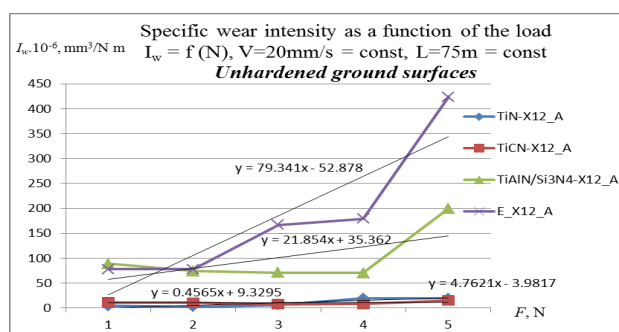
Fig. 6. Specific wear intensity as a function of the load for unhardened ground surfaces
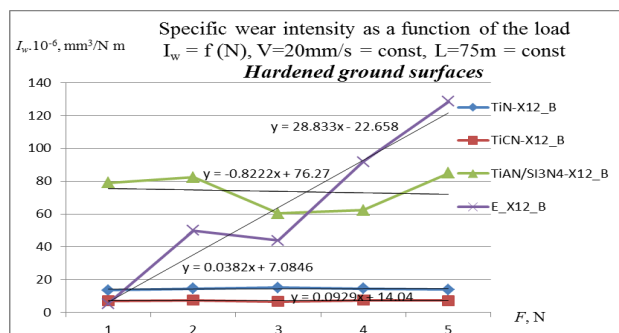
Fig. 7. Specific wear intensity as a function of the load for hardened ground surfaces
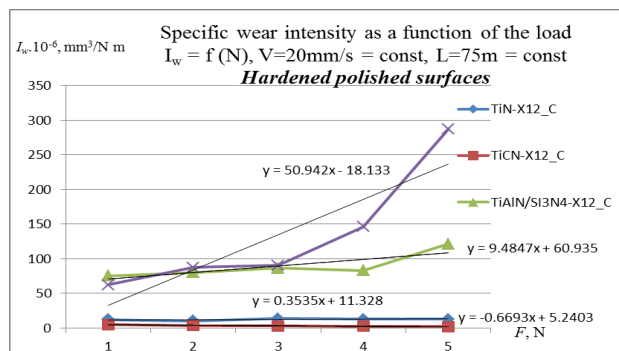
Fig. 8. Specific wear intensity as a function of the load for hardened polished surfaces

CONCLUSIONS

The following conclusions can be drawn from the analysis of the obtained experimental results:

1. TiN and TiCN hard coatings, applied by the PVD method on tool steel 1.2080 (X12), reduce the volume of the trace and the intensity of wear compared to uncoated surfaces.

2. The nc-TiAlN/a-Si$_3$N$_4$ nanocomposite, deposited on tool steel 1.2080 (X12), shows only slight improvement in the wear intensity, and with hardened ground surfaces even worsening is observed (Fig. 7), which may be due to the high brittleness of the coating, which cracks under load and forms abrasive micro-particles. This leads to increased abrasive wear. Similar results for this type of coating have been obtained in other studies [25].

3. It is recommended for equipment, made of tool steel 1.2080 (X12), with unhardened ground surfaces, subjected to intensive wear, to be coated with the hard coatings TiN and TiCN, showing the same wear resistance (Fig. 6).

4. It is recommended for equipment, made of tool steel 1.2080 (X12), with hardened ground and hardened polished surfaces, if subjected to intensive wear, to be coated with the TiCN hard coating, showing the best wear resistance (Figs. 7 and 8).

REFERENCES

1. G. Mishev, U. Heisel, *Journal of the Technical University at Plovdiv*, **13** (6), 23 (2006), ISSN 1310-8271.
2. V. Rupetsov, ZEA-PRINT, 2018, ISBN 978-619-196-073-6.
3. V. Toshkov, A. Ziumbilev, G. Mishev, N. Tonchev, Proceedings of the 1st International Conference "The Coatings in Manufacturing Engineering", Thessaloniki/Greece , 1999, p. 433.
4. G. Mishev, A. Zyumbilev, Y. Simeonova, N. Proyiyschev, Proceedings of the 4th International Conference on Tribology, Kayseri/Turkey, 2002, vol. I, p. 205.
5. G. Mishev, S. Dishliev, J. Simionova, E. Assenova, Proceedings of the 16th International Colloquium Tribology, Ostfildern, Germany, 2008, ISBN 3-924813-73-6.
6. N. Petkov, E. Kashkarov, A. Obrosov, T. Bakalova, P. Kejzlar, Hr. Bahchedzhiev, *Journal of Materials Engineering and Performance*, **28** (1), 343 (2019), ISSN: 1059-9495.
7. N. Petkov, T. Bakalova, Hr. Bahchedzhiev, P. Louda, P. Kejzlar, P. Capkova, M. Kormunda, P. Rysanek, *Journal of Nano Research*, **51**, 78 (2018), ISSN: 1661-9897.
8. N. Petkov, T. Bakalova, Hr. Bahchedzhiev, P. Kejzlar, P. Louda, *Journal of Nano Research*, **49**, 98 (2017).

9. G. Mishev, Reibung in geradlinig bewegten Maschinensystemen, Fast print Books, 2020, ISBN: 978-619-236-163-1

10. Z. Zhou, W. M. Rainforth, Q. Luo, P. Eh. Hovsepian, J. J. Ojeda, M. E. Romero-Gonzalez, *Acta Materialia* **58,** 2912 (2010).

11. W. Grzesik, Z. Zalisz, S. Krol, P. Nieslony, *Wear*, **261,** 1191 (2006).

12. R. D. Torres, P. C. Soares Jr., C. Schmitz, C. J. M. Siqueira, *Surface & Coatings Technology,* **205,** 1381 (2010).

13. S.-Y. Yoon, K. O Lee, S. S. Kang, K. H. Kim, *Journal of Materials Processing Technology* **130–131,** 260 (2002).

14. J. L. Mo, M. H. Zhu, B. Lei, Y. X. Leng, N. Huang, *Wear*, **263,** 1423 (2007).

15. G. Mishev, *Journal of the Balkan Tribological Association,* **3** (1), 38 (1997), ISSN 1310-4772.

16. G. Mishev, Proceedings of the 2nd World Tribology Congress, Wien/Austria, 2001, ISBN 3-901657-07-X.

17. T. Bakalova, N. Petkov, T. Blažek, P. Kejzlar, P. Louda, L. Voleský, *Defect and Diffusion Forum,* **368**, 59 (2016), ISSN: 1662-9507.

18. T. Bakalova, N. Petkov, Hr. Bahchedzhiev, P. Louda, *Manufacturing Technology*, **16** (5), 859 (2016), ISSN 1213-2489.

19. T. Bakalova, N. Petkov, Hr. Bahchedzhiev, P. Kejzlar, P. Louda, M. Durak, *Manufacturing Technology*, **17** (5), 652 (2017), ISSN 1213-2489.

20. G. Mischev, Reibung in den geradlinig bewegten Maschinensystemen, Proceedings of the 15th International Colloquium Tribology, Stuttgart/ Ostfildern, Germany, 2006, ISBN 3-924813-62-0.

21. G. Mischev, Proceedings of the 13th International Colloquium Tribology, Stuttgart/Ostfildern, Germany, 2002, vol. II, p. 867, ISBN 3-924813-48-5.

22. G. Mishev, K. Atanassova, Proceedings of "ICMEN", Greece, 2002, p. 577, ISBN 960-431-811-X.

23. V. Rupetsov, *Journal of Food and Packaging Science, Technique and Technologies*, **1** (4), 60 (2014), ISSN 1314-7773.

24. S. Dishliev, *Fundamental sciences and application,* **14** (2) 2009, Proceedings of the International Conference Engineering, Technologies and Systems TECHSYS' 2009, ISSN 1310-271.

25. G. Mishev, S. Dishliev, V. Rupetsov, *Tribological Journal BULTRIB,* **4**, 147 (2014), ISSN 1313-9878.

Experimental investigation of thermal & electrical performance of PV module using wick biomaterials

V. K. Sohpal[1*], S. Kumar[2]

[1]Chemical Engineering, SBS State University, Gurdaspur, Punjab
[2]Mechanical Engineering, SBS State University, Gurdaspur, Punjab

A photovoltaic module (PV) absorbs a considerable amount of solar irradiance that is converted into electricity, and the major part of solar energy produces heat, and consequently, causes thermal degradation of the PV. Therefore, cooling of the PV module is an essential integral part of a system to decrease the effect of high temperature to obtain the PV panel's high electrical performance. Hence, passive cooling was investigated with cotton and jute wick biomaterial with different water streams in the present work. It was observed that the thermal performance of the PV system with jute and husk for two streams of water (0.02 Kg/s and 0.05 Kg/s) increases by 15-18%. The increase in short circuit current with jute wick material is higher than with husk wick material. Average output power rises by 8-10% with both biomaterials and correspondingly, the electrical efficiency also increases by 9.0-9.8%. We experimentally found that a water stream of 0.05 Kg/s controlled thermal performance and improved proficiency.

Keywords: Jute, husk, thermal, electrical, photovoltaic module.

INTRODUCTION

With an increase in population and living standard power requirement also increases, and the geographical place restricts the supply of conventional sources. The problem in the north India border region is that it is necessary to produce the energy locally. The PV system is the most suitable alternative system for water pumps in agriculture fields, street lighting, and residential area. Installation and operational module of the PV system are quite simple, but its electrical efficiency drops in the months May-June due to high temperature in the Northern region of India. Published literature reveals that the PV module's temperature can be minimized by a cooling system arrangement with the PV module. He *et al.* [1] designed an experimental study on PV modules under natural water circulation and observed that the PV module's energy-saving efficiency was much higher than that of the individual PV plate and the conventional solar collector. Chandrasekar *et al.* [2] investigated the PV module's thermal and electrical performance with a cooling system using cotton wick with water, Al_2O_3/water nanofluid, and CuO/water nanofluid. Teo *et al.* [3] designed, fabricated, and experimentally investigated a hybrid photovoltaic/ thermal (PV/T) solar system. The experimental results showed that the temperature dropped significantly and boosted solar cells' efficiency by 12 % - 14 %. Rahman *et al.* [4] observed the effects of various operational constraints (irradiation intensity, cooling fluid mass flow rate, humidity and dust) on PV module performance. They observed that the module temperature dropped to 22.4 °C, improved the output power by 8.04 W and increased the electrical efficiency by 1.23% using water cooling on the PV module. Hasanuzzaman *et al.* [5] reviewed the literature works rendered to attain enhanced efficiency through cooling systems. The passive cooling arrangement is found to accomplish a reduction in PV module temperature by 6–20 °C with a step up in electrical efficiency up to 15.5% maximum. Elnozahy *et al.* [6] investigated the performance of the PV module after cooling and surface cleaning and observed that cooled and surface-cleaned module has an efficiency of 11.7% against 9% for the module without cooling and cleaning. Rostami *et al.* [7] investigated the use of high-frequency ultrasound for improved cooling of a PV module. Results showed that cooling by atomized nanofluid was more efficient than cooling by atomized pure water. Idoko *et al.* [8] applied the water-cooling technique on the PV module's surface with an aluminum heat sink. The experiment recorded an increase in power by 20.96 watts, and an increase in efficiency by around 3%. Elminshawy *et al.* [9] experimentally investigated passing pre-cooled ambient air over the back panel surface and observed an upgrading in the PV module output power and electrical efficiency to around 18.90 % and 22.98 %, respectively. Winston *et al.* [10] studied the uplift in performance, efficiency, and developed an economical cooling system using air-conditioners. The results showed that the PV module, being cooled, showed 7.2 % higher electrical efficiency.

Bashir *et al.* [11] analyzed a water-cooled photovoltaic/thermal system to enhance efficiency by absorbing the heat. They concluded that temperature drop, and electrical efficiency of c-Si, p-Si were higher by 13 % and 6.2 %, respectively. Li *et al.* [12] focussed on the conversion efficiency techniques of heat transfer in PV modules and proposed passive cooling methods, and integrated energy-saving efficiency gains the power generation and the shading performance. Abdollahi *et al.* [13] introduced a PV module with a hybrid cooling system and used nano-based composed oil to achieve higher efficiency. Rosa-Clot *et al.* [14] suggested a cooling system to improve the PV module's efficiency and observed that the impact of cooling on the lifetime of the PV gives positive results due to the reduction of the thermal shocks. Elbreki *et al.* [15] combined the planar reflector and back-plate extended surface with a module to optimize its efficiency. A parametric study concluded that the lapping fins have a superior performance in reducing PV module temperature. Younas *et al.* [16] used a simple cooling system and achieved a 1.61 % increase in the PV module's overall efficiency. The performance ratio increased as high as 12.85 %. Tiwari *et al.* [17] designed, fabricated, and investigated the cooling system experimentally and observed improved electrical performance.

Literature review reveals that a lot of research progress has been made in advance of a cooling system for the PV module. The research literature deals with the cooling of the PV module using different cooling systems, namely natural, hybrid, air conditioning, nanomaterial, and composite cooling systems. Hence, the present work's objective is to develop a simple passive cooling system with biomaterials that are available even in a remote area of India. The cooling of the PV system with husk and jute wick structures in the presence of a different stream of water is presented.

EXPERIMENTAL

Methodology and setup

The photographic view of the experimental PV module is shown in Fig. 1. This experimental setup was operated from 9:00 am to 4:30 pm in May 2019 on the roof of the Mechanical Engineering Department of Beant College of Engineering & Technology, Gurdaspur, located on 32.0613°N 75.4411°E position. The PV module's performance was observed on the first day for the PV module with jute wick structure and the subsequent days with husk wick structures on 30 min intervals against the reference PV module. The average of the ambient temperatures measured during these days was

considered as the ambient temperature for comparing the results. The experimental setup consists of two solar panels of 100 watts each, a digital multimeter for measuring the open-circuit voltage (V_{OC}) and short-circuit current (I_{SC}) of the solar panel. A six-channel temperature indicator is placed in each solar panel at the appropriate location to measure the temperature accurately. Power meter is used to measure the intensity of solar irradiance falling on the solar panel in experimental observation. A tray made up of a galvanized iron sheet of dimensions 800 mm×450 mm×40 mm supports the different wicked materials behind one of the solar systems. A constant head device (CHD) was placed below the water tank to maintain the stream of water (0.02 and 0.05 Kg/s).

Fig. 1. Photograph of the experimental PV module

Reduction of data

The output power (P) of the PV module is a product of voltage (V) and current (I) data and electrical efficiency and fill factor are given by the following equations:

$$\eta_E = \frac{V * I_{sc} * f(f)}{I * A_c} \tag{i}$$

$$f(f) = \frac{P}{V * I_{sc}} \tag{ii}$$

Electrical efficiency (η_E) and fill factor (*f*) are functions of current (I), voltage (V), area of solar cell (A_C), and incident solar irradiance (I_{SC}). Thermal proficiency (η_T) of the PV module is dependent upon mass flow rate (m), specific heat (C_p), inlet and outlet temperature (T_i & T_o), global solar irradiance (G_{SC}), and area of the thermal accumulator.

$$\eta_T = \frac{m * c_p * (T_o - T_i)}{G_{sc} * A} \tag{iii}$$

The calculations indicated that the mathematical errors involved in the estimations of η_E and η_T are at a minimum level (±0.20%).

RESULTS AND DISCUSSION

Calibration of thermocouple

Accurate measurement of temperature throughout the experiment is an utmost requirement. With this objective, five thermocouples were placed on the backside of both PV modules. It was observed that the variation of temperature between thermometer and thermocouple at different points is less than 0.42 % during morning and afternoon time of measurement in the month of May. The five average temperatures of thermocouple and thermometer measured on the back surfaces of the PV module are plotted in Fig. 2. Thus, it was confirmed that the average temperatures of the thermometer and thermocouple are approximately the same, hence, the K type thermocouple tested in this experiment was used in the present work.
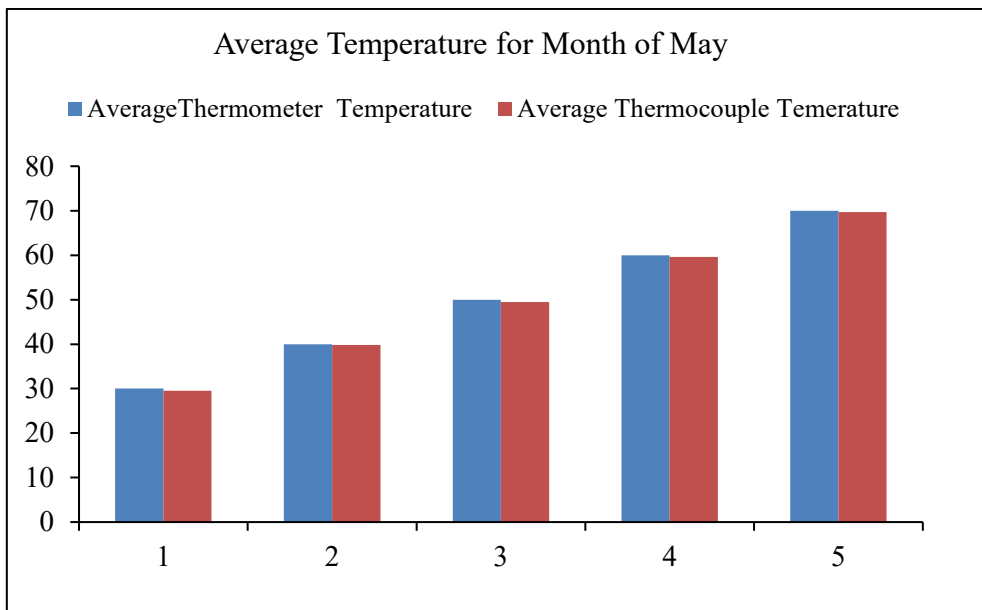
Fig. 2. Calibration of average temperature of thermocouple with reference to thermometer
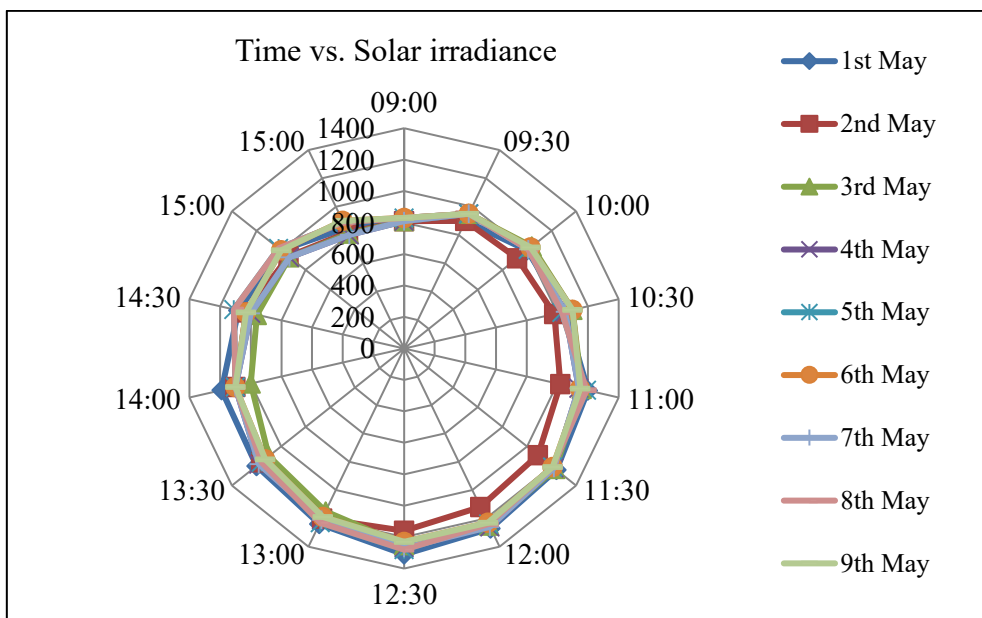
Fig. 3. Solar radiation measurement with respect to time using a solar power meter at equatorial location 32.0613°N 75.4411°E
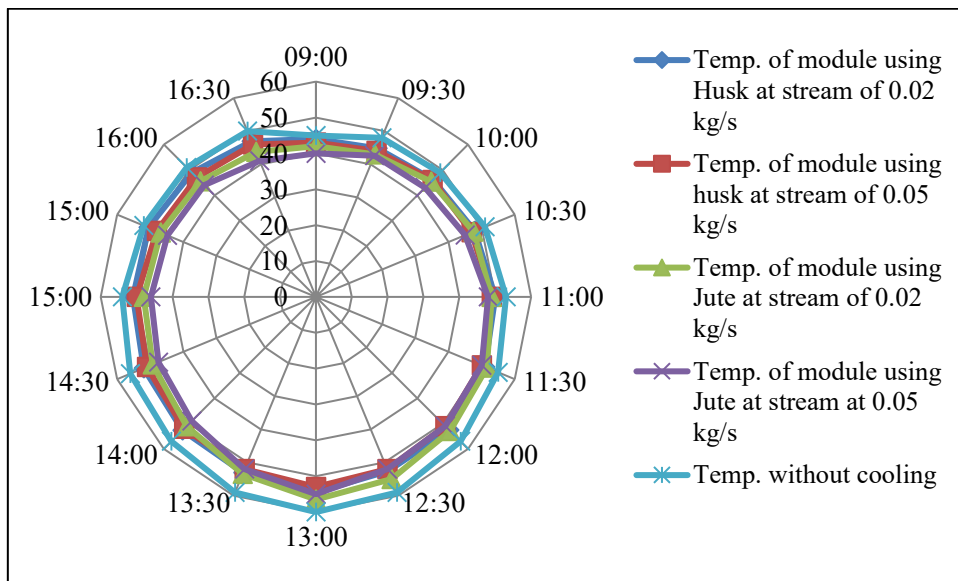
Fig. 4. Variation of temperature in PV module with time and under different operating conditions

The hourly solar radiation data measured using an ambient weather solar power meter/ pyranometer for nine consecutive days of experimentation from May 1st to 9th 2019, are presented in Fig. 3. It is observed that the rising and falling solar irradiation values during the day are due to a change in sun location with time. Fig. 3 reveals that the radiation intensity on the experimentation setup was parallel. It is observed that due to the location of the experimental setup, maximum solar power (1310, 1240 W/m²) prevailed at around 12.30-1.30 pm, and minimum solar irradiance (810, 850 W/m²) was detected at 9.00 am and 3.00 pm, respectively. May 1st - 9th solar intensity data were used for the present analysis for the PV module's electrical and thermal performance employing jute/water and husk/water biomaterial.

Thermal characteristics

Thermal performance assessment was executed through the hourly temperature data of the PV module under different operating conditions, as shown in Fig. 4. The hourly variation of temperature under the five operating conditions is continuous. The maximum temperature of the PV reference modules is around 59-60 °C from 12.30 to 1.30 pm. The temperature profiles of the PV module are approximately equal for different cases of experiments, i.e., different biomaterial, stream of water, and without cooling. The reliability of the PV module under different operating conditions was authenticated. It is observed that the temperature of the reference PV module is top during the day with a maximum of 60 °C, and the temperature of the module is reduced to 52.6 °C, 52 °C, 55 °C, 52 °C at the same time when cooling with husk and jute wick

is provided in combination with two different water streams (0.02 and 0.05 Kg/s), respectively. Combination of jute and husk biomaterial with a water stream of 0.02 Kg/s reduces the temperature by 8.33 % and 12.33 %, respectively, toward the reference module. On the other hand, when the water stream increased from 0.02 to 0.05 Kg/s, jute and husk wick material corresponded to a reduction of about 13 % and 16 % in module temperature compared to the module temperature obtained without cooling. On comparing the cooling performance of the wick biomaterial, it is clear that the highest level of cooling performance is achieved in husk wick structures with both streams of water. A higher water stream favours the thermal cooling with both wick biomaterials. Overall, the moist condition of the biomaterial with water at the backside of the module was maintained with CHD to decline the module temperature. Fig. 4 shows that the radar curve representing the variation of module temperature throughout the day using biomaterial wick in combination with two water streams is a cyclic structure.

Electrical characteristics

Fig. 5 depicts the variation of output power (W) of the module with time under different working conditions. Experimental investigation shows that the cooling system offers the maximum output power. The maximum output power of 80, 80.5 W was obtained using husk and jute material without water at time 12.30 pm. Minimum output power without cooling with both biomaterials observed was 48 and 45 W for husk and jute, respectively, around 4.30 pm, at the same time of observation for the module of husk wick structures with a water stream

of 0.02 and 0.05 Kg/s increased output power by 8.2 % and 9.5 % corresponding to the case without cooling. The output power for jute wick material was higher than that of the husk supported module with both streams of water.

Current-voltage characteristic curve (Fig. 6) demonstrates the PV module with different arrangements of cooling and without cooling. Simpson numerical integration technique was used to calculate the area under the curve to evaluate the cooling performance. It was found that the area

under the curve for the module without cooling with biomaterial is smaller than the maximum area under the curve observed with biomaterial with a water stream of 0.05 Kg/s. Both biomaterials with a water stream of 0.05 Kg/s cover an area under the curve higher by 5-8 % compared to the stream of 0.02 Kg/s. Fig. 6 also indicates that maximum cooling is achieved with wick biomaterials in combination with water.
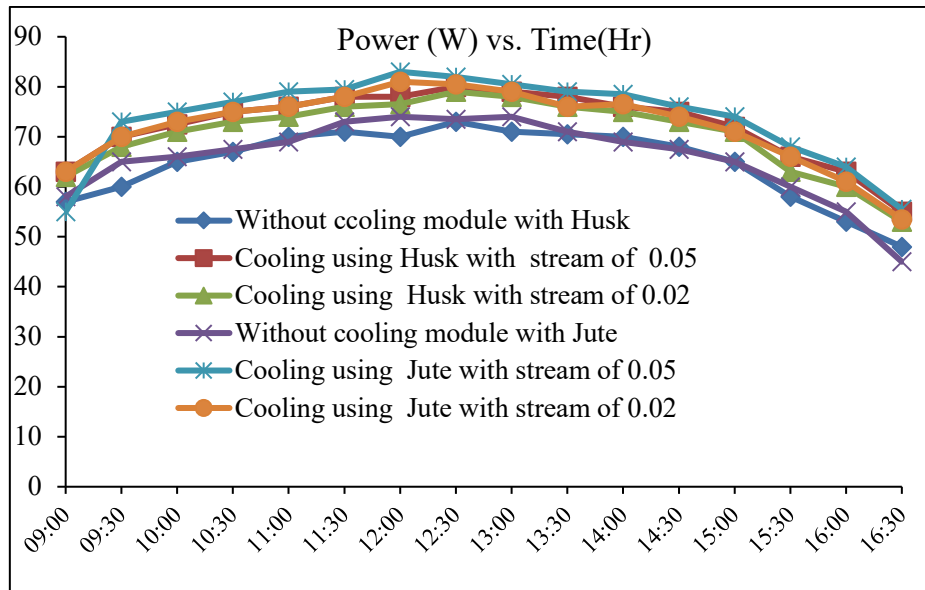
Fig. 5. Variation of output power in PV module with time under different operating conditions of cooling
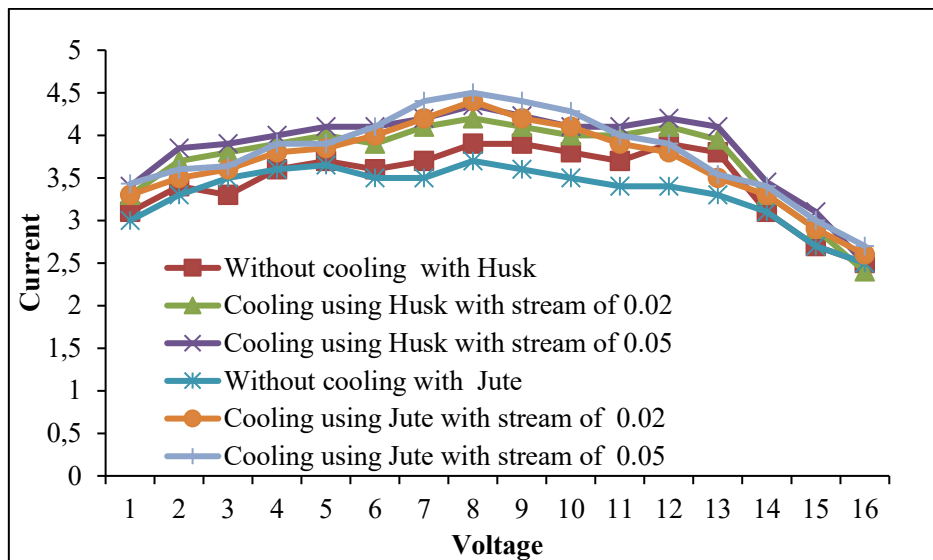
Fig. 6. Current-voltage characteristic curve of the PV module under different operating conditions
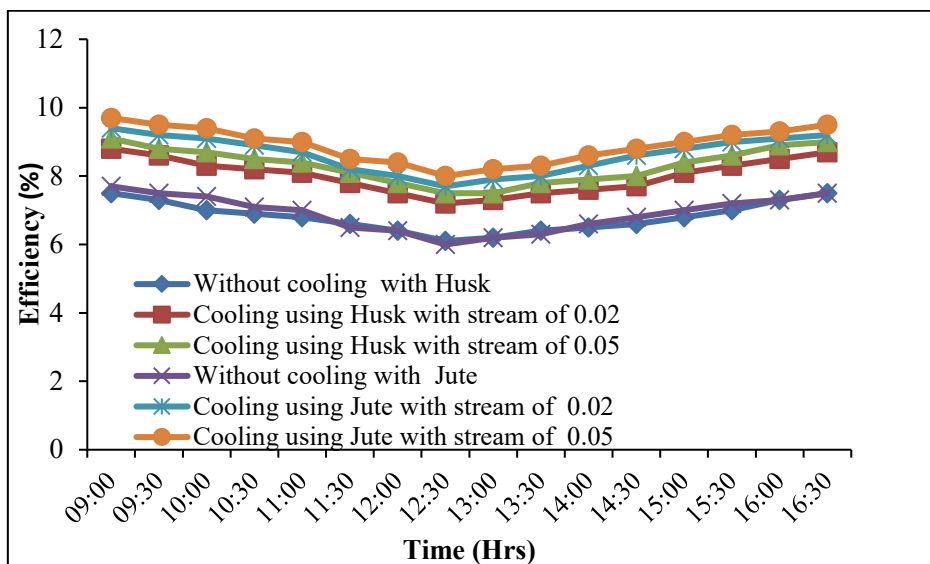
Fig. 7. Electrical efficiency of the PV module with respect to time under different operating conditions

Results supported that maximum output power is achieved when the PV module is cooled with wick biomaterial in combination with the different water streams. From equation (iii), the fill factor was evaluated using open-circuit voltage (V_{oc}), incident solar irradiance (I_{SC}) corresponding to maximum Pm. The maximum fill factor value obtained was 0.82 in jute biomaterial with a cooling stream of 0.05 Kg/s. As regards the fill factor, it was observed that jute biomaterial with cooling of 0.02 Kg/s has the same value (around 0.78) as husk with a stream of 0.05 Kg/s.

Fig. 7 depicts the variation of electrical efficiency of the PV module with time under different operating conditions. From the previous output of results, it is clear that the higher electrical efficiency of the PV module is a result of the cooling arrangement. Maximum efficiency of 9.4% to 9.7 % was obtained using jute wick biomaterial in combination with a water stream of 0.02 or 0.05 Kg/s. The PV module efficiency was about 8.1 % and 9.1 % when using husk biomaterial, with a water stream of 0.02 and 0.05 Kg/s respectively. Without cooling with the biomaterial, electrical efficiency remained 7.5 % (husk) and 7.7 % (jute). As the temperature of the PV module increases, uniform movement of electrons takes place, and the electrical impedance reduces the efficiency of the module. Hence, the experimental results point out that the PV module temperature has a substantial effect on the PV system's output power and efficiency. PV module temperature and efficiency are correlated parameters, as deduced from Figs. 5 and 7. The module without cooling arrangement has high temperature and low efficiency between 6-7.3 %. The efficiency ranges from 9.1 % to 7.5 % with husk

and water stream of 0.05 Kg/s in the temperature range of 45–60 °C. Wicked jute biomaterial with a water stream of 0.05 Kg/s has a higher efficiency of 9.5 to 8.0 % at the same temperature, but the temperature coefficient ranges from -0.3 to 0.27 °C^{-1}. The present investigation's temperature coefficient value shows a better result with cooling and an overall improvement compared to the conventional system.

CONCLUSIONS

Passive cooling was performed in a PV experimental setup with wicked biomaterial under constant water stream. Based on work conducted, it was observed that the temperature of the PV module without cooling reached to 60 °C, while with cooling, the corresponding temperature was reduced by 20 % with jute biomaterial. Jute biomaterial with a water stream of 0.05 Kg/s displayed better performance as compared to husk biomaterial. Maximum output power was achieved for both biomaterials around 80 W with the higher stream of water. The electrical efficiency improved by 7.0 to 9.0 %, for husk and jute wicked biomaterial, respectively. It was also found that the thermal degradation of PV modules is reduced with a cooling system suitable for optimizing output power and life cycle.

REFERENCES

1. W. He, Y. Zhang, J. Ji, *Applied Thermal Engineering*, **31**(16), 3369 (2011).
2. M. Chandrasekar, S. Suresh, T. Senthilkumar, *Energy Conversion and Management*, **71**, 43 (2013).
3. H. G. Teo, P. S. Lee, M. N. A. Hawlader, *Applied Energy*, **90**(1), 309 (2012).

4. M. M. Rahman, M. Hasanuzzaman, N. A. Rahim, *Energy Conversion and Management*, **103**, 348 (2015).

5. M. Hasanuzzaman, A. B. M. A. Malek, M. M. Islam, A. K. Pandey, N. A. Rahim, *Solar Energy*, **137**, 25 (2016).

6. A. Elnozahy, A. K. A. Rahman, A. H. H. Ali, M. Abdel-Salam, S. Ookawara, *Energy and Buildings*, **88**, 100 (2015).

7. Z. Rostami, M., Rahimi, N. Azimi, *Energy Conversion and Management*, **160**, 141 (2018).

8. L. Idoko, O. Anaya-Lara, A. McDonald, *Energy Reports*, **4**, 357 (2018).

9. N. A. Elminshawy, A. M. I. Mohamed, K. Morad, Y. Elhenawy, A. A. Alrobaian, *Applied Thermal Engineering*, **148**, 1 (2019).

10. D. P. Winston, P. Pounraj, A. M. Manokar, R. Sathyamurthy, A. E. Kabeel, *Desalination*, **435**, 140 (2018).

11. M. A. Bashir, H. M. Ali, K. P. Amber, M. W. Bashir, H. Ali, S. Imran, M. S. Kamran, *Thermal Science*, **22**(6) Part A, 2401 (2018).

12. H. Li, J. Zhao, M. Li, S. Deng, Q. An, F. Wang, *Solar Energy*, **181**, 70 (2019).

13. N. Abdollahi, M. Rahimi, *Renewable Energy*, **147**, 302 (2020).

14. M. Rosa-Clot, G. M. Tina, in: Floating PV Plants, Academic Press, 2020, p. 67.

15. A. M. Elbreki, K. Sopian, A., Fazlizan, A. Ibrahim, *Case Studies in Thermal Engineering*, 100607 (2020).

16. M. F. Younas, M. Abubaker, H. M. Ali, M. A. Nawaz, M. Hassan, M. J. Awan, K. A. Sultan, *VW Applied Sciences*, **2**(1), 52 (2020).

17. A. K. Tiwari, R. Kumar, R. R. Pande, S. K. Sharma, V. R. Kalamkar, in: Advances in Energy Research, Vol. 1, Springer, Singapore, 2020, p. 159.

Modelling and multicriteria analysis for selection of growth rate models for batch cultivation of *Kluyveromyces marxianus var. lactis* MC 5 yeast.
Part II: Multi-criteria decision analysis for selecting of growth rate model

M. M. Petrov

Institute of Biophysics and Biomedical Engineering; Bulgarian Academy of Sciences, 105 Acad. George Bonchev Str., Sofia 1113, Bulgaria

In the second part of the work we apply the PROMETHEE II method for multi-criteria decision analysis to determine the most appropriate models of the ten unstructured models studied in the first part – *Monod, Mink, Tessier, Moser, Aiba, Andrews, Haldane, Luong, Edward* and *Han-Levenspiel* for the growth rate as a function of *lactose-only* or *oxygen-only* in the batch cultivation of the yeast *Kluyweromyces marxianus var. lactis* MC 5. The results obtained after application of PROMETHEE II method showed that the most suitable pair of models is the *Tessier* model for *lactose-only* and the *Monod* model for *oxygen-only*.

Keywords: Multi-criteria decision analysis, yeast *Kluyveromyces marxianus var. lactis* MC 5, PROMETHEE II method, growth rate models

INTRODUCTION

Multi-criteria decision analysis (MCDA) is a branch of operation research models and a well-known field of decision-making. The main objective of MCDA is to select the alternative that has the highest score according to the set of evaluation criteria [1].

There are several different methods, of which the most important are analytic hierarchy processes [2], elimination and choice expressing reality [3], multi-attribute utility theory [4], preference ranking organization methods (PROMETHEE) [5, 6], etc.

A study of various mathematical models of the specific growth rate of a batch process of yeast *Saccharomyces cerevisiae* for ethanol production was performed. The selection of the most suitable model was made using the PROMETHEE II method performed by Petrov [7].

Modelling and simulation of the process for ten unstructured models in batch cultivation of yeast *Kluyveromyces marxianus var lactis* MC 5 were performed. For the first time in modelling and simulation of this process two independent kinetic models were used, separately for *lactose* and *oxygen*, performed by Petrov [8].

In this study, the PROMETHEE II method was used to evaluate and select growth rate models for batch process of yeast *Kluyveromyces marxianus var. lactis* MC 5. After selecting the most appropriate models, the process will be simulated with the selected specific growth rate.

MATERIALS AND METHODS

Kinetic models

The kinetic models are proposed independently in [8]:

- *Biomass formation from lactose-only*

$$\frac{dX}{dt} = \mu(S)\, X$$

$$\frac{dS}{dt} = -\frac{1}{Y_{X/S}}\frac{dX}{dt} \tag{1}$$

- *Biomass formation from oxygen-only*

$$\frac{dX}{dt} = \mu(C)\, X$$

$$\frac{dC}{dt} = -\frac{1}{Y_{X/C}}\frac{dX}{dt} + k_l a (C^* - C) \tag{2}$$

where: t – process time, h; X – *biomass* concentration, g/L; S – *lactose* concentration, g/L; $\mu(S)$ – growth rate of biomass from *lactose-only*, h^{-1}; $Y_{X/S}$ – yield coefficients of formation of the *biomass* from *lactose*, g/g; C – *oxygen* concentration, g/L; $\mu(C)$ – growth rate of biomass from *oxygen-only*, h^{-1}; $Y_{X/C}$ – yield coefficients of formation of the *biomass* from *oxygen*, g/g; $k_l a$ – mass transfer coefficient, h^{-1}; C^* – maximal *oxygen* concentration in liquid phase, g/L.

The initial conditions of both models (Eqns. 1, 2) are: $X(0) = 0.2$ g/L, $S(0) = 44$ g/L; $C(0) = 6.65 \times 10^{-3}$ g/L, and $C^* = C(0)$.

To whom all correspondence should be sent:
E-mail: mpetrov@biomed.bas.bg

Specific growth rate models

In the first part [8] of this work, modelling and simulation of ten unstructured models was performed (Table 1): M_1 – *Monod*, M_2 – *Mink*, M_3 – *Tessier*, M_4 – *Moser*, M_5 – *Aiba*, M_6 – *Andrews*, M_7 – *Haldane*, M_8 – *Luong*, M_9 – *Edward* and M_{10} – *Han-Levenspil* to explain the cell growth kinetics.

Table 1. Tested growth rate models dependent on *lactose* or *oxygen*

Model	$\mu(\mathbf{Z})$
$M_1(\mathbf{Z})$	$\mu(\mathbf{Z}) = \dfrac{\mu_m^{\mathbf{Z}} \mathbf{Z}}{K_{\mathbf{Z}} + \mathbf{Z}}$
$M_2(\mathbf{Z})$	$\mu(\mathbf{Z}) = \dfrac{\mu_m^{\mathbf{Z}} \mathbf{Z}^2}{K_{\mathbf{Z}} + \mathbf{Z}^2}$
$M_3(\mathbf{Z})$	$\mu(\mathbf{Z}) = \mu_m^{\mathbf{Z}} \left(1 - \exp\left(-\mathbf{Z}/K_{\mathbf{Z}I}\right)\right)$
$M_4(\mathbf{Z})$	$\mu(\mathbf{Z}) = \dfrac{\mu_m^{\mathbf{Z}} \mathbf{Z}^{\alpha_M}}{K_{\mathbf{Z}} + \mathbf{Z}^{\alpha_M}}, \alpha_M > 0$
$M_5(\mathbf{Z})$	$\mu(\mathbf{Z}) = \dfrac{\mu_m^{\mathbf{Z}} \mathbf{Z}}{K_{\mathbf{Z}} + \mathbf{Z}} \exp\left(-\mathbf{Z}/K_{\mathbf{Z}I}\right)$
$M_6(\mathbf{Z})$	$\mu(\mathbf{Z}) = \dfrac{\mu_m^{\mathbf{Z}} \mathbf{Z}}{(K_{\mathbf{Z}} + \mathbf{Z})(1 + \mathbf{Z}/K_{\mathbf{Z}I})}$
$M_7(\mathbf{Z})$	$\mu(\mathbf{Z}) = \dfrac{\mu_m^{\mathbf{Z}} \mathbf{Z}}{K_{\mathbf{Z}} + \mathbf{Z} + \mathbf{Z}^2/K_{\mathbf{Z}I}}$
$M_8(\mathbf{Z})$	$\mu(\mathbf{Z}) = \dfrac{\mu_m^{\mathbf{Z}} \mathbf{Z}}{K_{\mathbf{Z}} + \mathbf{Z}}\left(1 - \mathbf{Z}/\mathbf{Z}_m\right)^n$
$M_9(\mathbf{Z})$	$\mu(\mathbf{Z}) = \dfrac{\mu_m^{\mathbf{Z}} \mathbf{Z}}{K_{\mathbf{Z}} + \mathbf{Z} + \left(1 + \mathbf{Z}/K\right)\left(S^2/K_{\mathbf{Z}I}\right)}$
$M_{10}(\mathbf{Z})$	$\mu(\mathbf{Z}) = \dfrac{\mu_m^{\mathbf{Z}} \mathbf{Z}}{\mathbf{Z} + K_{\mathbf{Z}}} \dfrac{\left(1 - \mathbf{Z}/\mathbf{Z}_m\right)^n}{\left(1 - \mathbf{Z}/\mathbf{Z}_m\right)^m}$

In Table 1: $\mathbf{Z} = [S, C]^{\mathrm{T}}$ – vector with basic energetic substrates *lactose* and *oxygen*, respectively; $\mu_m^{\mathbf{Z}}$ – maximum growth rate for *lactose* and *oxygen*, respectively, h^{-1}; $K_{\mathbf{Z}}$ – *Monod* saturation constants for cell growth on *lactose* and *oxygen*, g/L; α_M – *Moser* constant; $K_{\mathbf{Z}I}$ – inhibition constants for cell growth on *lactose* and *oxygen*, g/L; K – constant in *Edward* model, g/L; $\mathbf{Z}_m$ – critical inhibitor concentrations, above which the reactions stops, g/L; m, n – constants in the *Luong* and the *Han-Levenspiel* models.

Criteria using PROMETHEE II method

The criteria used in the PROMETHEE II method are the same as those used in [8]: $C_1(S)$ / $C_1(C)$ – criteria for evaluation of kinetic parameters; $C_2(S)$ / $C_2(C)$ – statistic λ; [$C_3'(X)$ and $C_4(S)$] or [$C_3''(X)$ and $C_4(C)$] – relative error (S_L) for the kinetics variables (X, S) or (X, C); [$C_5'(X)$ and $C_6(S)$] or [$C_5''(X)$ and $C_6(C)$] – experimental Fisher coefficient for the kinetic variables (X, S) or (X, C); [$C_7'(X)$ and $C_8(S)$] or [$C_7''(X)$ and $C_8(C)$] – experimental correlation coefficient R^2 for kinetic variables (X, S) or (X, C).

Background of PROMETHEE II method

The basic principle of PROMETHEE II is based on a pair-wise comparison of alternatives along each recognized criterion. Alternatives were evaluated according to different criteria, which had to be maximized or minimized. The implementation of the PROMETHEE II required two additional types of information [5, 6]:

- *Selection of the Weight*

Determination of the weight is an important step in most of the multi-criteria methods. PROMETHEE II assumes that the decision-maker is able to weigh the criteria appropriately, at least when the number of criteria is not too large.

- *Selection of the Preference Function*

For each criterion, the preference function translates the difference between the evaluations obtained by two alternatives into a preference degree, ranging from zero to one. In order to facilitate the selection of a specific preference function, Brans and Vincke [5] propose six basic types: Type I – Usual criterion; Type II – U-shape criterion; Type III – V-shape criterion; Type IV – Level criterion; Type V – linear with an indifference criterion; and Type VI – Gaussian criterion. The decision-making process using the PROMETHEE method consists of five steps, which are described in detail in [5, 6].

- *The Software Packages*

In our work, we used the new PROMETHEE-GAIA Academic Edition software to solve the multi criteria decision making problem, called Visual PROMETHEE by PROMETHEE-GAIA.net [9], and developed under the guidance of B. Mareschal.

RESULTS AND DISCUSSION

The modelling and simulation results for *lactose-only*, and *oxygen-only* are described in detail in [8].

Tables 2 and 3 show the results for the criteria by which the models ($M_1 - M_{10}$) are validated.

Table 2. Criteria for models validation from *lactose-only*

Models	$C_1(S)$	$C_2(S)$	$C_3'(X)$	$C_4(S)$	$C_5'(X)$	$C_6(S)$	$C_7'(X)$	$C_8(S)$
$M_1(S)$	13.8827	151.8377	0.2262	0.5030	1.0125	1.1676	0.9864	0.9754
$M_2(S)$	9.6736	**204.1643**	0.2058	**0.6288**	1.0598	**1.0253**	**0.9744**	0.9920
$M_3(S)$	10.6736	**151.3657**	0.1982	0.3879	1.0220	1.1364	**0.9869**	0.9819
$M_4(S)$	9.2521	175.7246	0.1960	0.3883	1.0471	1.0591	0.9790	0.9894
$M_5(S)$	14.0315	151.7896	0.2274	0.5067	1.0124	1.1690	0.9863	0.9752
$M_6(S)$	13.9697	151.9010	0.2270	0.5051	1.0129	1.1684	0.9863	0.9753
$M_7(S)$	13.9765	152.1378	0.2272	0.5045	1.0130	1.1681	0.9864	0.9752
$M_8(S)$	13.8925	151.7663	0.2262	0.5036	1.0128	1.1679	0.9864	0.9754
$M_9(S)$	**14.1648**	151.9544	**0.2289**	0.5087	**1.0118**	1.1698	0.9863	**0.9749**
$M_{10}(S)$	**6.0574**	184.7091	**0.1641**	**0.1845**	**1.0694**	1.0313	0.9853	**0.9944**

Table 3. Criteria for model validation from *oxygen-only*

Models	$C_1(C)$	$C_2(C)$	$C_3''(X)$	$C_4(C)$	$C_5''(X)$	$C_6(C)$	$C_7''(X)$	$C_8(C)$
$M_1(C)$	0.6734	**154.5335**	0.1612	0.5992	1.0127	1.0174	**0.9992**	0.9986
$M_2(C)$	1.5593	163.0421	0.1864	**0.9618**	1.0187	1.0155	**0.9988**	**0.9963**
$M_3(C)$	1.0059	161.9099	0.1748	0.8047	1.0141	1.0203	0.9991	0.9978
$M_4(C)$	**0.6727**	156.9493	**0.1596**	0.6473	**1.0115**	1.0223	**0.9992**	**0.9988**
$M_5(C)$	1.1461	160.2555	0.1818	0.2635	1.0174	1.0178	0.9989	0.9975
$M_6(C)$	1.4423	**172.3611**	**0.2021**	0.2539	1.0223	1.0235	0.9989	0.9969
$M_7(C)$	**1.6108**	169.1571	0.1941	0.2713	1.0195	**1.0286**	0.9989	0.9965
$M_8(C)$	1.1806	165.3167	0.1869	**0.2492**	1.0218	1.0164	0.9989	0.9975
$M_9(C)$	1.1256	159.8748	0.1812	0.2646	1.0176	1.0169	0.9989	0.9975
$M_{10}(C)$	1.0604	163.3446	0.1855	0.2611	**1.0226**	**1.0111**	0.9990	0.9978

Here it is time to specify that for criteria $C_1 - C_6$ we are looking for min., and for criteria C_7 and C_8 – for max. The best values of all criteria are marked in green. The maximum values for criteria $C_1 - C_6$ and the minimum values for criteria C_7 and C_8 are marked in red.

Application of PROMETHEE II method

Selection of the weight

Criteria $C_1 - C_4$ are the most important. That is why for them we choose double weight (in %): $w_j = 17\%, j = 1, ..., 4$ in comparison with criteria $C_5 - C_8$: $w_j = 8\%, j = 5, ..., 8$. The sum of all weights fulfils the condition: $\Sigma w_j = 100\%, j = 1, …, 8$.

Selection of the Preference Function

Choosing a preference function is a very important task. In this work, we have chosen to have a strict preference for the alternative with the highest value. For this reason, Type I – usual criterion has been chosen for all criteria. Its function is preferably shown in Fig. 1.

$$p(x) = \begin{cases} 0 & x \leq 0 \\ 1 & x > 0 \end{cases}$$
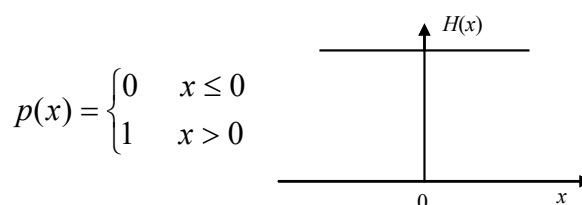
Fig. 1. Type I – Usual criterion

We used PROMETHEE Academic Edition software [9] to solve the multi-criteria decision making problem. The results for different growth rate models when a PROMETHEE II method was applied are shown in Table 4.

The models with the highest Rank (Table 4) for growth rate are: model M_3 (*Tessier*) for *lactose-only* and model M_1 (*Monod*) for *oxygen-only*:

$$\mu(S,C) = \mu_{\max}(1 - \text{EXP}(-S/K_S)) \frac{C}{(K_C + C)} \quad (3)$$

Table 4. Results after application of the PROMETHEE II method

Lactose-only				
Rank	Action	ϕ	ϕ^+	ϕ^-
1	**$M_3(S)$**	**0.5556**	**0.7778**	**0.2222**
2	$M_{10}(S)$	0.3889	0.6944	0.3056
3	$M_4(S)$	0.2407	0.6204	0.3796
4	$M_1(S)$	0.2315	0.5926	0.3611
5	$M_8(S)$	0.1944	0.5741	0.3796
6	$M_2(S)$	-0.1852	0.4074	0.5926
7	$M_6(S)$	-0.2222	0.3796	0.6019
8	$M_7(S)$	-0.3056	0.3333	0.6389
9	$M_5(S)$	-0.3241	0.3241	0.6481
10	$M_9(S)$	-0.5741	0.2037	0.7778
Oxygen-only				
Rank	Action	ϕ	ϕ^+	ϕ^-
1	**$M_1(C)$**	**0.5833**	**0.7870**	**0.2037**
2	$M_4(C)$	0.5648	0.7778	0.2130
3	$M_3(C)$	0.1852	0.5648	0.3796
4	$M_9(C)$	0.1759	0.5833	0.4074
5	$M_5(C)$	0.1389	0.5648	0.4259
6	$M_{10}(C)$	0.0926	0.5185	0.4259
7	$M_8(C)$	-0.1111	0.4167	0.5278
8	$M_6(C)$	-0.4815	0.2593	0.7407
9	$M_7(C)$	-0.5000	0.2315	0.7315
10	$M_2(C)$	-0.6481	0.1574	0.8056

The kinetic model of the process has the form:

$$\frac{dX}{dt} = \mu(S,C)\,X$$
$$\frac{dS}{dt} = -\frac{1}{Y_{X/S}}\frac{dX}{dt} \qquad , \qquad (4)$$
$$\frac{dC}{dt} = -\frac{1}{Y_{X/C}}\frac{dX}{dt} + k_l a(C^* - C)$$

The criteria for the model (Eqn. 4) differ from the criteria used in modelling and simulation of the process independently of *lactose* and *oxygen*. In this case, instead of eight criteria we have eleven. This is because we already have three kinetic variables of the process (X, S and C):

- C_1 – criteria for evaluation of kinetic parameters in model;
- C_2 – *statistic λ*;
- $C_3(X)$, $C_4(S)$, $C_5(C)$ – relative error (S_L) for the kinetic variables of the model;
- $C_6(X)$, $C_7(S)$, $C_8(C)$ – experimental Fisher coefficients for the kinetic variables of the model;
- $C_9(X)$, $C_{10}(S)$, $C_{11}(C)$ – experimental correlation coefficients R^2 for kinetic variables of the model.

Criteria (C_1) for evaluation of kinetic parameters in the model (Eqns. 4) are determined by the following dependence:

$$C_1 = \frac{1}{N}\sum_{i=1}^{N}\left(\frac{(X_e(t_i) - X_m(t_i))^2}{X_{e\max}^2} + \frac{(S_e(t_i) - S_m(t_i))^2}{S_{e\max}^2} + \frac{(C_e(t_i) - C_m(t_i))^2}{C_{e\max}^2}\right)$$
$$(5)$$

where: C_1 – sums of the squares of weighted residuals; N – number of the experiments; t_i – time partitions, h; $X_e(t_i), S_e(t_i), C_e(t_i)$ – measurement values of kinetic variables, g/L; $X_m(t_i), S_m(t_i), C_m(t_i)$ – simulated values with models of kinetics variables, g/L; $X_{e\max}^2, S_{e\max}^2, C_{e\max}^2$ – maximal measurement values of kinetic variables, g/L.

In the next part of the work a simulation of the model will be performed.

Simulation

An algorithm and program of COMPAQ Visual FORTRAN 90 [10] were developed in order to identify the parameters in the model (Eqn. 4) for batch cultivation process of yeast *Kluyweromyces marxianus var. lactis* MC 5. For solving the nonlinear problem for computing criteria C_1, we used a direct search method, a subroutine BCPOL with double precision from IMSL Math/Library [11]. All computations were performed using HexaCore AMD Phenom II X6 1075T, 3 GHz, 8 GB RAM, Windows XP operating system (32 bit).

The calculated values of the kinetic parameters in the model are shown in Table 5.

Table 5. Calculated values of kinetic parameters

Parameter	Search bound	Value
$\mu_{\max}$	[0.1, 1.0]	0.7405
K_S	[0.01, 5.0]	0.0101
K_C	[0.1, 7.0]×10⁻³	0.4654×10⁻³
$Y_{X/S}$	[0.1, 1.5]	0.4334
$Y_{X/C}$	[0.1, 5.0]	3.9101
$k_l a$	[80.0, 180]	164.0484

The calculated values of the model validation criteria ($C_1 - C_{11}$) are as follows: $C_1 = 6.83 \times 10^{-3}$; $C_2 = 149.84$; $C_3 = 0.188$; $C_4 = 0.340$; $C_5 = 0.428$; $C_6 = 1.05$; $C_7 = 1.06$; $C_8 = 1.01$; $C_9 = 0.987$; $C_{10} = 0.994$; $C_{11} = 0.997$.

The criteria C_2, and $C_6 - C_{11}$, are statistical. The theoretical values of C_2 and $C_6 - C_{11}$ are given from statistical tables [12]. Fisher coefficient for C_2 (*Statistic λ*) is $F_T^{\lambda}(2,11) = 4.04$. Fisher coefficients for criteria $C_6 - C_8$ are $F_T(11,2) = 19.40$, and correlation coefficient for criteria $C_9 - C_{11}$ is $R_T^2(11) = 0.684$ for level of significance $\alpha = 0.01$. The experimental Fisher coefficients criteria are $C_2 > F_T^{\lambda}(2,11) = 4.04$ and $(C_6 - C_8) < F_T(11, 2) =$

19.40. The experimental correlation coefficients criteria are$(C_9 - C_{11}) > R_T^2(11) = 0.684$.

From the comparison of the criteria $(C_2, C_6 - C_{11})$ for validation of the model with their tabular values,

it can be seen that it is adequate and can be used for modelling.

The following figures show the experimental and simulated results for the concentration of biomass, lactose and oxygen.
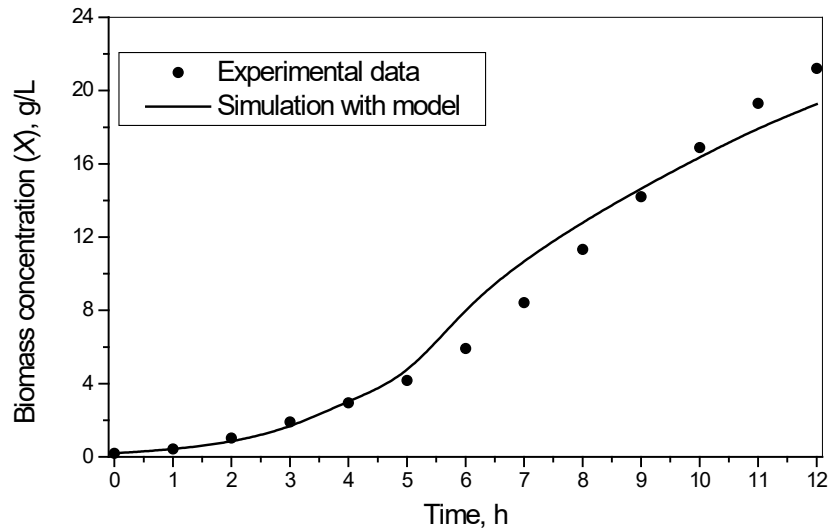
Fig. 2. Experimental and simulated results for biomass concentration
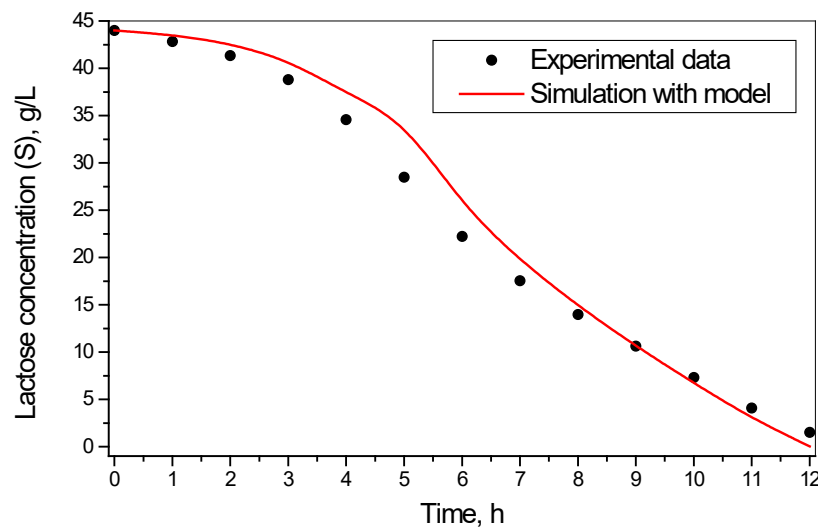
Fig. 3. Experimental and simulated results for *lactose* concentration
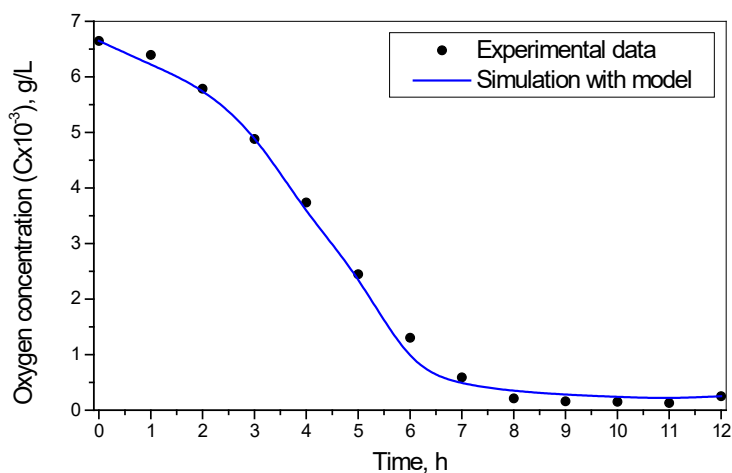
Fig. 4. Experimental and simulated results for *oxygen* concentration

From the results obtained in the process simulation (Figs. 2 - 4), it can be seen that the selected model of the specific growth rate well describes the experimental and model results.

CONCLUSIONS

The application of the PROMETHEE II method has shown that the most suitable pair of models is the *Tessier* model for *lactose-only* and the Monod model for *oxygen-only*. The *Tessier-Monod* specific process growth model is adequate and can be used for modelling.

In our future work, a multi-objective parameter estimation for the six fermentations and sensitivity analysis in batch cultivation of yeast *Kluyveromyces marxianus var. lactis* MC 5 will be performed. In this way the optimal values of the kinetic parameters will be determined for the model used for modelling, optimisation and optimal processes control.

REFERENCES

1. R. A. Taha, A. T. Daim, in: Research and Technology Management in the Electricity Industry, T. Daim, T. Oliver, J. Kim (eds.), Springer, London, UK, 2013, p. 17.
2. R. W. Saaty, *Mathematical Model*, **9**(3-5), 161 (1987).
3. J. Figueira, V. Mousseau, B. Roy, in: International Series in Operations Research and Management Science, S. Greco (ed.), vol. **78**, Springer, New York, 2005, p. 133.
4. J. Dyer, in: International Series in Operations Research and Management Science, S. Greco (ed.), vol. **78**, Springer, London, UK, 2005, p. 265.
5. J.-P. Brans, P. Vinke, *Manag. Sci.*, **31**, 647 (1985).
6. J.-P. Brans, B. Mareschal, *Decis. Support Syst.* **12**, 297 (1994).
7. M. Petrov, *Fermentation*, **5**(3), art. no. 61 (2019).
8. M. Petrov, *Bulg. Chem. Commun.*, **53** (4) (2021), in press.
9. http://www.promethee-gaia.net/software.html
10. COMPAQ Visual FORTRAN Programmer's Guide, v. 6.6, Compaq Computer Corporation, Houston, Texas, 2001.
11. IMSL Math/Library User's Manual, IMSL, Inc., Houston, Texas, 1991.
12. I. Vuchkov, St. Stoyanov, Mathematical Modelling and Optimisation of Technological Objects, Technique, Sofia, 1986, p. 47, (in Bulgarian).

Parameter optimization of a semi-batch water decontamination slurry photocatalytic reactor using Taguchi-Grey technique

G. Munteanu[1], P. Karakashkova[2], A. Eliyas[2*]

[1] *Ilie Murgulescu Institute of Physical Chemistry, Romanian Academy, 202 Splaiul Independentei St., 060021Bucharest, Romania*

[2] *Institute of Catalysis, Bulgarian Academy of Sciences, Acad. G. Bonchev St., Bl.11, 1113 Sofia, Bulgaria*

The aim of the present research work was to optimize the input parameters and the efficiency of operation of a slurry semi-batch water purification photocatalytic reactor, aiming at maximum efficiency. The response function upon varying the input parameters was the conversion degree of the model water contaminant Acid Black 194 azo dye (AB194). The optimization procedure is based on the application of combined methodology – experimental plan, which is based on Taguchi L9 Orthogonal Array (OA 3^4) and Grey Relational Analysis (GRA). The highest conversion degree (degree of decolorization – response function) was achieved at the lowest AB194 azo dye initial concentration, under UV-C illumination intensity of 0.07 W/cm^2, and 400 rpm magnetic stirrer operation rate, while increasing the O_2 flow rate above 10 L/h did not give any substantial increase in the decolorization degree.

Keywords: photocatalytic reactor, water purification, Taguchi-Grey methodology

INTRODUCTION

Chromium Acidic Black Diazo Dye (Colour Index Acid Black 194) is used for colouring textiles and anodized aluminium articles [1]. Discharging it into the waterways is strictly forbidden by the present day safety regulations, because it represents a health hazard. It is manufactured by the Bulgarian factory BULCOLOR in the town of Kostenetz and it is known that this dye is especially stable to UV-light irradiation, which is of great advantage in view of its practical application [1]. This fact makes it also suitable to be a model waste water contaminant in view of its stability (see Fig. 1).
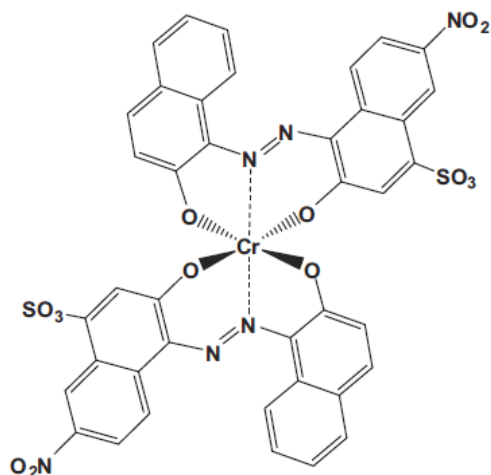
Figure 1. Chromium Acidic Black Diazo Dye AB194 – structural formula

Different configurations of slurry photocatalytic reactors have already been proposed and studied aiming at simpler mathematical models for designing the reactors and improving their efficiency [2]. The present study was carried out using a semi-batch photocatalytic slurry reactor, reported by us previously [3]. The batch consisted of a fixed volume of model contaminant waste water and fixed amount of suspended TiO_2 Degussa P25 photocatalytic material. The construction of the reactor enables feeding a continuous flow of oxygen – for this reason the reactor belongs to the group of semi-batch reactors, i.e. one of the reactants (the pollutant) is in a fixed amount and the other reactant (the oxygen) is in continuous flow – photocatalytic oxidation reaction. A horizontal quartz tube is mounted in the reactor enabling insertion of different types of cylindrical illumination lamps – UV-A, UV-C and visible light lamps. The lamp in the quartz tube is situated perpendicularly to the shaft of the Pyrex glass reactor (see Fig. 2).

One possible approach in the optimization of the operational input parameters is based on the Design of Experiments (DoE) ranging from complete factorial design to Taguchi's method [4-6] which is time saving and lowering the expenses for the experimental runs. The latter statistical method [4] observes the values of the response function upon varying many input factors. In our case of photocatalytic reactor for waste water decontamina-

---

tion using azo dye model contaminant (AB194) the response function is the degree of decolorization of the dye solution in the course of illumination followed spectrophotometrically or we can take the time interval needed for achieving complete decolorization (i.e. 99.9% photo-oxidative conversion degree). Taguchi's method is based on using orthogonal arrays (OAs) of different kinds – in our previous study on photocatalytic air purification [7] we made use of L32 OA for the case of 5 input parameters on 5 levels (5^5). The present study applies a much simpler case of statistical analysis for the specific case of a water decontamination photocatalytic reactor. This is the L9 OA which involves 4 parameters on 3 levels (3^4) making only 9 experiments, while the complete factorial design 3^4 means carrying out 81 experiments.

The aim of the study was to improve the efficiency of a semi-batch slurry photocatalytic reactor for oxidative degradation of azo dye model waste water contaminant over commercial TiO$_2$ semiconductor material Degussa P25, upon varying the photo-oxidation process input parameters. The parameters were as follows: initial concentration of the dye: 1 mmol\L to 5 mmol\L (P1), different types of illumination - UV-C, UV-A and visible light at intensities 0.07 W/cm^2 to 8.9 W/cm^2 (P2) measured by Cole-Parmer radiometer VLX-3W, different speed of the magnetic stirrer in the slurry 400-600 rpm (P3) and different oxygen flow rates 8L/h up to 12 L/h (P4). Then Grey Relational Analysis (GRA) [8, 9] was applied to find out which ones of the input parameters are significant and what is the percentage of their contribution to the conversion degree and what is the optimal set of the operational conditions to achieve a maximum of the conversion degree based on ANOVA Analysis of Variance statistical tool.

EXPERIMENTAL

In order to develop a statistical model to analyze the effect of input parameters P1-P4 a first order linear mathematical model and ANOVA technique were used to verify the model competency. The investigation was focused on the direct effect of the input process parameters on the single response function – degree of decolorization of the azo dye Acid Black 194 (conversion degree). The investigated input parameters were the initial azo dye concentration, the type of illumination source, the magnetic stirrer speed of operation and the oxygen feed flow rate into the reactor. The Taguchi L9 orthogonal array was used for the design of the experiments and to optimize the parameters.

Regression coefficients were calculated using 4 factors on a three levels central composite design with 95% of confidence level. The central composite first order design is the most efficient tool in response with a minimal number of experimental runs without great loss of accuracy. The ANOVA comprises the sum of squares and degrees of freedom. The sum of squares is transformed into contributions from regression model as well as residual error. A first-order linear model was developed to predict the resultant response function F – decolorization degree: F = f(C^0_{ad}, I_{uv}, R_{st}, O_{2fl}) – the regression coefficients were calculated using a four factor – three level central composite design. If the calculated confidence value – deviation of predicted conversions from the experimentally measured conversions, i.e. the model deviation is less than 0.05 % – is greater than the standard tabulated value of 95 % for confidence level, then the model is considered to be adequate within the confidence limits. This validates the significance of the model – the testing was done using the ANOVA. The value of deviation was less than 0.05 %, which proves the significance of the model. The determination coefficient of the square quadratic error R^2 exhibits the goodness of fit of the model.

In the experimental runs a semi-batch semi-continuous flow slurry photocatalytic reactor for water purification (Fig. 2) was applied and the degree of decolorization of a solution of Acid Black 194 azo dye was evaluated using CAMSPEC spectrophotometer Model M501 (UK) monitoring the wave length of maximum extinction (absorbance) at 570 nm for this specific azo dye. Different types of lamps were used – UV-A (polychromatic BLB i.e. Black Light Blue lamp with maximum at 365 nm), UV-C (monochromatic 254 nm TUV lamp) – both giving intensity of illumination of 0.07 W per cm^2 and visible light of 8.9 W per cm^2.

RESULTS AND DISCUSSION

The commercially available photocatalyst Degussa P25 TiO$_2$ (75% anatase and 25% rutile) was used as standard material. The single-point BET method (30% N$_2$ + 70% He mixture at inlet flow rate of 15 ml/min – adsorption of N$_2$ as a monolayer at the boiling temperature of liquid nitrogen 77 K) showed that the Degussa P25 TiO$_2$ specific surface area was 50 m^2/g.

The anatase (A) is generally accepted to be the better photocatalyst under UV-illumination than rutile (R), whose crystals are more compact and therefore the specific surface area is smaller.

However, there exists a synergistic effect [3] between anatase and rutile – their band gaps are different (3.0 eV for rutile corresponding to adsorption edge λ_{max} = 413 nm and 3.2 eV for anatase corresponding to adsorption edge λ_{max} = 388 nm). The positions of the conduction and the valence bands of these two semiconductors allow charge carrier separation as the valence bands merge – therefore the holes are migrating freely. However, the conduction bands (A/R) are separated and the photoexcited electrons remain localized. The company Degussa has made use of this synergistic effect and it produces the best commercially available photocatalyst (having ratio A:R = 3:1). If this charge separation model is correct, then the best ratio A:R would be 1:1, however in this specific case the surface area would be too low because of the high content of rutile [3]. So obviously Degussa Co. has found out an optimal combination between synergism and specific surface area at 3:1.

The measure of the photocatalytic activity was taken to be the azo dye degree of decolorization (single response function) as a result of varying the four input parameters on three levels (Table 1). The O_2 feed flow rate created a large oxygen excess with respect to the stoichiometrically required amount for oxidation reaction.

Table 1. Four input parameters of the photoreactor on three levels

Symbol	Input Parameter	Level 1 -1	Level 2 0	Level 3 1
P1	AB194 initial concentration	1 mmol/L	3 mmol/L	5 mmol/L
P2	Type of illumination	UV-C 0.07 W/cm^2	UV-A 0.07 W/cm^2	Visible 8.9 W/cm^2
P3	Magnetic stirrer speed	400 rpm	500 rpm	600 rpm
P4	Oxygen flow rate	8 L per hour	10 L per hour	12 L per hour

The first variable input parameter was the azo dye Acid Black194 initial concentration from 1 mmol/L to 5 mmol/L (P1), while the type of illumination UV-C (TUV), UV-A (BLB) 0.07 W/cm^2 and visible light 8.9 W/cm^2 was the second input parameter (P2), the speed of the magnetic stirrer in the slurry from 400 to 600 rpm was the third input parameter (P3) and the oxygen flow rate from 8 to 12 L/h was the fourth input parameter (P4). In all the experimental runs the oxygen concentration was in large excess with respect to the stoichiometrically required oxygen amount to achieve 99.9% conversion (Table 2).

The main task of the study was the development of a mathematical function (statistical model), based on four input parameters on three levels to predict the values of the single response function, which have already been measured experimentally (Table 2) with the possibly smallest model deviation. The model should describe the relationship between the input process parameters and the response function. This would enable the determination of the optimal levels of process variable parameters that could produce a desirable output (the highest conversion degree).

Table 2. Experimental design – central composite design matrix

Trial No	P1	P2	P3	P4	Response conversion %
1	-1	-1	-1	-1	83.70
2	-1	0	0	0	72.40
3	-1	+1	+1	+1	50.10
4	0	-1	0	+1	80.00
5	0	0	+1	-1	61.50
6	0	+1	-1	0	39.50
7	+1	-1	+1	0	70.10
8	+1	0	-1	+1	52.90
9	+1	+1	0	-1	30.80

Therefore, in the current investigation a first-order linear model was developed to predict the resultant conversion degree. The response function can be expressed as follows:

$$F = f(C^0_{ad}, I_{uv}, R_{st}, O_{2fl}) \tag{1}$$

where C^0_{ad} is the inlet concentration of azo dye AB194, I_{uv} is the type of illumination and its intensity, R_{st} is the rate of stirring and O_{2fl} is the oxygen flow rate. The regression coefficients were calculated using a four factor - three level central composite design in MINITAB 15 BASICS

statistical software with 95% confidence level. The mathematical model developed using the evaluated regression coefficients for calculating the resultant conversion degree F is given by the following expression (2):

$$F = A + B\ C^0_{ad} + C\ I_{uv} + D\ R_{st} + E\ O_{2fl} = A + B\ P1 + C\ P2 + D\ P3 + E\ P4 \qquad (2)$$

Validating the adequacy of the model. Analysis of variance (ANOVA) was used to assess the relationship between the response variable and one or more predictor variables. We obtained the following values for the coefficients:

$$F = 60.1 - 8.7\ P1 - 18.9\ P2 + 0.93\ P3 + 1.16\ P4 \qquad (3)$$

This model predicts the following values of the conversion (response function), which are compared with the experimentally observed values in Table 3.

As we can see, the percentages of the errors are varying between 0.2% (exp. 4) up to 4.9% in only one case (exp. 2) – these errors are acceptable. The coefficients of parameters P3 and P4 are very small, compared to the coefficients for P1 and P3 as it can be seen in equation (3). This suggests that we are probably in a situation of superparametrization. Let us check this point - so we can make one more iteration – let us first eliminate P3 (influence of stirrer speed) and vary the other three parameters P1, P2, P4 – now we obtain the following equation:

$$F = 60.1 - 8.7\ P1 - 18.9\ P2 + 0.93\ P3 + 1.7\ P4 \qquad (4)$$

Table 4 lists the experimental conversions and the simulated values, as well as the errors.

Table 3. Comparison of the observed values and the predicted values of AB194 degree of decolorization (response function) with all four parameters P1, P2, P3, P4 and the resulting percentage of error.

Trial No	P1 P2 P3 P4	Observed conversion	Predicted conversion	% Error
1	-1 -1 -1 -1	83.70	85.6	2.3
2	-1 0 0 0	72.40	68.8	4.9
3	-1 1 1 1	50.10	52.0	3.7
4	0 -1 0 1	80.00	80.2	0.2
5	0 0 1 -1	61.50	59.9	2.6
6	0 1 -1 0	39.50	40.3	1.9
7	1 -1 1 0	70.10	71.2	1.6
8	1 0 -1 1	52.90	51.6	2.4
9	1 1 0 -1	30.80	31.3	1.6

Table 4. Comparison of the observed values and the predicted values of AB194 degree of decolorization (response function) with three parameters P1, P2, P4 and the resulting percentage of error

Trial No	P1 P2 P4	Observed conversion	Predicted conversion	% Error
1	-1 -1 -1	83.70	86.6	3.3
2	-1 0 0	72.40	68.8	4.9
3	-1 1 1	50.10	51.1	2.0
4	0 -1 1	80.00	80.2	0.2
5	0 0 -1	61.50	58.9	4.2
6	0 1 0	39.50	41.2	4.2
7	1 -1 0	70.10	70.3	0.3
8	1 0 1	52.90	52.5	0.7
9	1 1 -1	30.80	31.3	1.6

Now let us make one last iteration eliminating both P3 and P4 and leaving only P1 and P2 as significant input parameters for the semi-batch photoreactor – these data are listed in Table 5. Eliminating two of the parameters of the square average deviation it becomes double (these values are not listed in Table 5). The final conclusion is that the input parameters P3 and P4 must also be taken into account, although their contributions are not so significant as the contributions of input parameters P1 and P2.

Table 5. Comparison of the observed values and the predicted values of AB194 degree of decolorization (response function) with two main parameters P1, P2 and the resulting percentage of error.

Trial No	P1	P2	Observed conversion	Predicted conversion	% Error
1	-1	-1	83.70	87.7	4.6
2	-1	0	72.40	68.8	4.9
3	-1	1	50.10	49.9	0.3
4	0	-1	80.00	79.0	1.2
5	0	0	61.50	60.1	2.3
6	0	1	39.50	41.2	4.2
7	1	-1	70.10	70.3	0.3
8	1	0	52.90	51.4	2.9
9	1	1	30.80	32.5	5.2

CONCLUSIONS

The highest degree of decolorization in a semi-batch slurry photoreactor for waste water decontamination was achieved at the lowest concentration of the azo dye model waste water pollutant of 1 mmol/L AB194, UV-C illumination, 400 rpm magnetic stirrer rate, while increasing the O_2 flow rate above 10 L/h did not give any substantial increase in the decolorization degree. All four input parameters must be taken into account in spite of the fact that the contributions of P1 and P2 (dye concentration and illumination) are much more significant but nevertheless, the other two input parameters (rate of stirring the suspension P3 and oxygen feed flow rate P4) cannot be entirely disregarded.

IN MEMORIAM: *Let us honour the memory of our colleague and friend Prof. Gabriel Munteanu, Ilie Murgulescu Institute of Physical Chemistry, Romanian Academy, who was the driving force of our research cooperation, of which this is the last one of our common research articles.*

REFERENCES

1. E. Stoyanova, S. Takeva, Z. Kostov, D. Stoychev, *Transactions of the Institute of Metal Finishing,* **82,** 157 (2004).
2. G. Li Puma, *Environmental Science and Technology*, **37**(24), 5783(2003).
3. L. Petrov, V. Iliev. A. Eliyas, D. Tomova, G. Li Puma, *Journal of Environmental Protection and Ecology* (B.EN.A) **8** (4), 881 (2007).
4. R. K. Roy, Design of Experiments Using the Taguchi Approach: 16 Steps to Process Improvement, Wiley Intersc. Publ., New York, 2001.
5. D. S. Sivia, Data Analysis. A Bayesian Tutorial for Scientists and Engineers, Oxford Sci. Publ., Clarendon Press, Oxford, 1996.
6. A. L. Horvath, Calculations in Industrial Chemistry. A Series of Solved Problems, Wiley & Sons, 1996.
7. A. Eliyas, G. Munteanu, P. Karakashkova, M. Fabian, *Bulg. Chem. Commun.*, **52** (2), 305 (2020).
8. T. N. Obee, S. O. Hay, *Environ. Sci. Technol.*, **31**, 2034 (1997).
9. K.-L. Chang, K. Sekiguchi, Q. Wang, F. Zhao, *Aerosol Air Qual. Res*., **13**, 618 (2013).

Influence of the binder on the mechanical stability and electrochemical properties of Zn electrode for rechargeable zinc-air batteries

B. Abrashev*, D. Uzun, V. Terziev, G. Raikova, K. Petrov

Acad. E. Budevski Institute of Electrochemistry and Energy Systems, Bulgarian Academy of Sciences, Acad. G. Bonchev Str., Bl. 10, 1113 Sofia, Bulgaria

The development of electrically rechargeable zinc-air batteries is a challenge to the efforts of many scientists for decades. The optimization of a zinc electrode as a function of its reversibility and mechanical stability is a key factor for battery efficiency improving and approaching to the Zn-air system commercialization. The present investigation is focused on the improvement of the zinc electrode with regard to its wettability and with aim to reduce the volume change caused by the density difference between the charged zinc and discharged ZnO electrode, respectively. Originally, the Zn-paste is made of a mixture of Zn powder, ZnO, additives and binding agents (usually carboxymethyl cellulose, CMC). However, the use of CMC as a gelling agent is not appropriate as it tends to swell in aqueous solution and reduce the capacity of cells over long-term reversibility tests. Our results showed that the replacement of CMC with polymer-type gelling agents such as polytetrafluoroethylene (PTFE) or teflonized Vulcan XC-72 carbon blacks with 35 wt% PTFE (TV35) binders significantly improved the electrochemical performance of the electrode resulting in higher specific discharge capacity and also in good durability and stability. Different contents of PTFE and TV35 on a zinc electrode in 6 M KOH were examined. Maximum initial discharge capacity of 498 mAh.g^{-1} was registered by the addition of 13 wt% TV35 to the pasted zinc electrode.

Keywords: Zn electrode, PTFE, Teflonized carbon blacks, Discharge capacity

INTRODUCTION

Nowadays, there is an urgent need to develop efficient, safe and affordable energy storage devices for both electric vehicles and stationary grid storage. Rechargeable metal-air batteries have the potential to store and release high amounts of energy in a short time when required. From the group of metals used Mg, Zn, Al, Fe, Ca, Li, zinc is the most active one in aqueous electrolytes. Zn electrode is cheaper and non-toxic. It operates well in humid environment and has low self-discharge, and can also be recharged *via* ZnO. Due to the oxygen supply from the atmosphere, Zn-air batteries have drastically higher theoretical energy density than traditional Ni-MH and lithium-ion batteries, which have had practical applications for a long time. Although the rechargeable Zn-air batteries are in a very mature state, there are many barriers towards their commercialization, the main is the lifetime (number of charge/discharge cycles) which is related to the degradation of the electrodes during cycling and leads to a rapid decrease of their capacity. Despite the numerous studies that problem is still not solved.

The problems associated with the zinc electrode can be structured in three main groups: (1) corrosion (release of hydrogen as a parasitic reaction) and dissolution, (2) dendritic formation at charge, combined with electrode change due to no uniform dissolution of zinc; (3) passivation of zinc electrode with ZnO layer formation due to zinc ions saturation [1-12]. The increase of the specific electrode surface [13-15] (standard battery optimization approach) by regulating the morphology of the starting material and the process conditions that provide a porous structure with good contact between the grain boundaries activates also the corrosion and passivation processes. The classical zinc reversible electrodes operate with a Zn/ZnO mixture [16-18]. For inhibition of the degradation processes several approaches, based on introduction of additives which modify the electrode, reduce self-corrosion, prevent passivation, dendritic formation and change in electrode shape, such as zinc alloys formation (Pb, Bi, Sn, In) [13, 19-21] oxide additives (Al$_2$O$_3$, Bi$_2$O$_3$, In$_2$O$_3$, TiO$_2$, [13, 20, 22-25] or gelling agents or binders such as carboxymethyl cellulose [16, 17, 26, 27] are used. The current work is focused on the investigation of the influence of different binders on the mechanical stability and electrical properties of the Zn electrode for rechargeable zinc-air batteries. The replacement of carboxymethyl cellulose (CMC) with polytetrafluoroethylene (PTFE) and teflonized Vulcan XC-72 carbon blacks (TV35) of different contents in Zn/ZnO paste electrodes were examined by charge/discharge tests using a KOH-based electrolyte in half-cell configuration. The discharge capacity of the first cycle was chosen as the criterion to define the optimum amount of binder.

* To whom all correspondence should be sent:
E-mail: babrashev@iees.bas.bg

EXPERIMENTAL

Electrode preparation

The zinc electrode was prepared as a mixture of zinc and zinc oxide (UMICORE). The initial powders were in the micrometric range (particle size of 100–300 μm) and metallic traces (*viz.* In, Bi, Al) were present. The active Zn paste was deposited on 9 cm^2 of stainless steel mesh (counter electrode) and pressed for 3 min with 300 kg.cm^{-2} at 300ºC. The quantity of gelling agent was varied in the range of 40 mg to 150 mg keeping the amount of Zn/ZnO constant: *Binder 1* - PTFE (Sigma Aldrich, emulsion); *Binder 2* - teflonized (35 wt%) carbon blacks (Vulcan XC-72, Cabot corp.).

Experimental conditions

The charge/discharge tests were conducted using six-channels Galvanostat 54 (PMC) testing system with custom software developed at IEES-BAS [28-30]. The cell discharge was controlled by limiting time or voltage. The charge was defined by time with the voltage limit reaching up to +2.5 V. The testing was done in a half cell configuration in 6M KOH-based electrolyte using HydroFlex hydrogen reference electrode (Gaskatel) and stainless steel counter electrode (CE) in a specially designed three-electrode cell (Fig. 1). The electrodes were loaded with 5 mA.cm^{-2} (440 min charge and 400 min discharge).

Fig. 1. General view of the experimental set up.

RESULTS AND DISCUSSION

The preliminary investigation of pasted Zn electrode prepared as most commonly used for secondary alkaline zinc-air battery was conducted. The performed charge/discharge test presented in Fig. 2 shows that the fabricated zinc electrode (with 1.4 wt% CMC) withstands up to 20 cycles. Better results with respect to the discharge capacity (240 mAh.g^{-1}) were obtained while utilizing lower current densities (5 mA.cm^{-2}). However, the obtained Zn electrode has low mechanical and

electrochemical stability and needs further improvements.
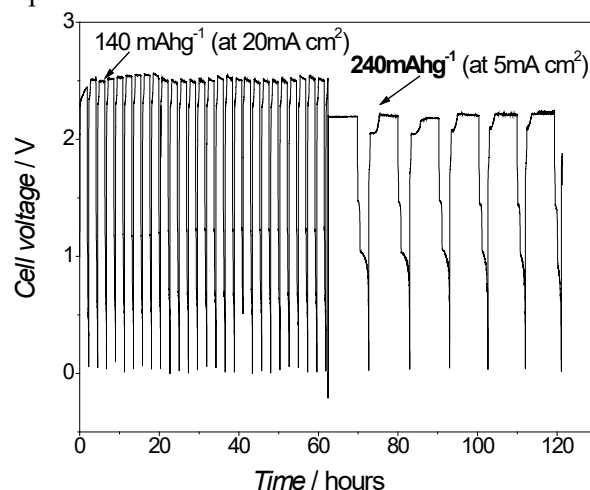
Fig. 2. Initial exploratory charge/discharge battery cycling test. The electrode is loaded with 20mA.cm^2 (110min charge/100 min discharge) and then with 5 mA.cm^{-2} (440 min charge /400 min discharge). The cell voltage is measured *versus* RHE. The Zn electrode contains 1.4 wt.% carboxymethyl cellulose (CMC).

The replacement of CMC with PTFE during the preparation of the Zn electrode brings an increase of the initial nominal discharge capacity (Fig. 3).
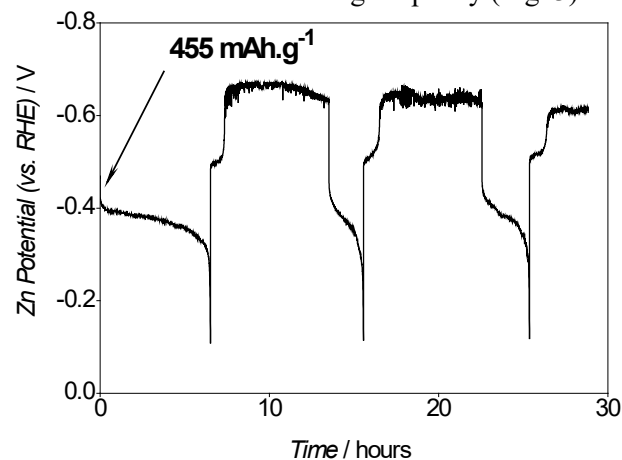
Fig. 3. Charge/discharge performance of the Zn electrode with 150 mg PTFE.

The best results were obtained after the addition of 150 mg PTFE (Fig. 3). To reach this capacity, the amount of PTEF was changed in the range of 40 mg to 200 mg keeping Zn/ZnO constant. The results presented on Figure 4 show that the optimal ratio PTFE:Zn-paste is 1:5.

In order to achieve comparatively high nominal capacity, the pure PTFE binder was replaced with TV35. Keeping the proportion of active Zn/ZnO paste constant, the TV35 amount was varied in the same proportions as PTFE binder - from 40 mg up to 200 mg (Fig. 5). The optimum ratio of TV35 to Zn/ZnO was found to be 1:7 (Fig. 6).
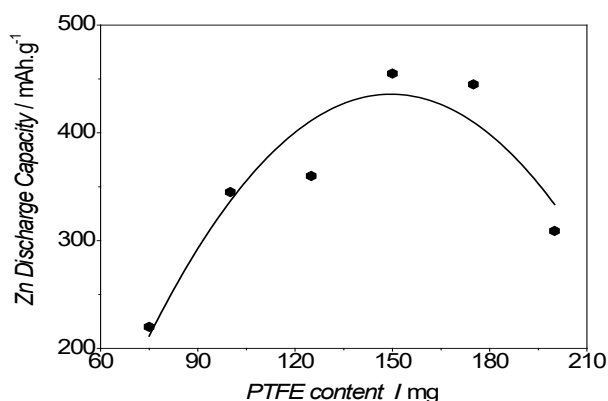
Fig. 4. Dependence of the Zn electrode capacity on the PTFE content.

The maximum initial discharge capacity reaches *ca.* 500 mAh.g^{-1}, i.e. it is 100% for the active zinc electrode (nominal *vs.* calculated mAh.g$^{-1}_{Zn}$). However, this capacity gradually decreased to 80 mAh.g^{-1} during the cycling test. The high specific surface area of the added TV35 decreases the density of the Zn electrode and it even shows a capacity improvement.
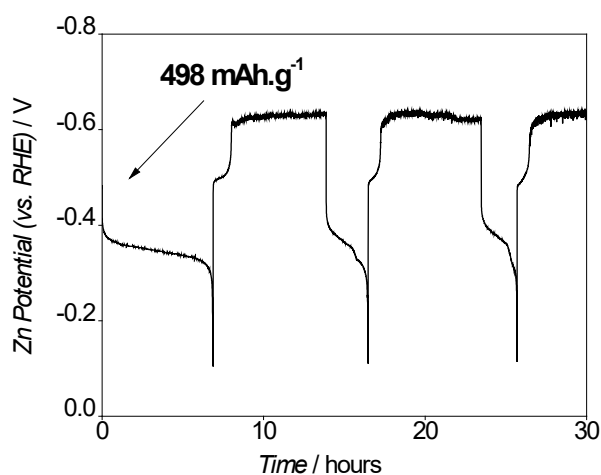
Fig. 5. Charge/discharge performance of the Zn electrode with 100 mg TV35.

In respect to the discharge capacity, the cycle life of the as prepared zinc electrode drastically decreases with the increase of TV35 amount (Fig. 7). The maximum numbers of charge/discharge cycles were obtained for a sample containing 50 mg TV35, but only 430 mAh.g^{-1} capacity was reached. The high specific surface area of the added Vulcan carbon blacks decreased the density of the Zn electrode and it even showed a capacity improvement at the beginning; the further increment of carbon content decreasing the electric conductivity of Zn electrode.
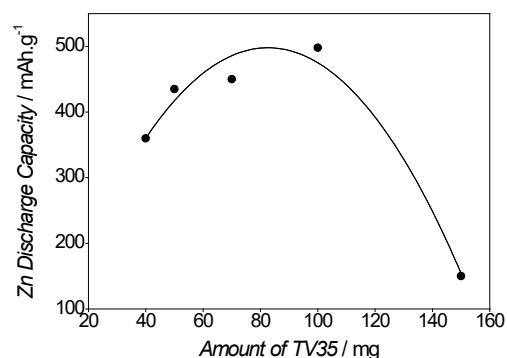
Fig. 6. Dependence of the Zn electrode capacity on the TV35 content.

Finding the right dependence binder amount vs. durability *vs.* high discharge rate capability is a very complex gathering, as the cell performance is mostly dependent from the Zn electrode degradation.
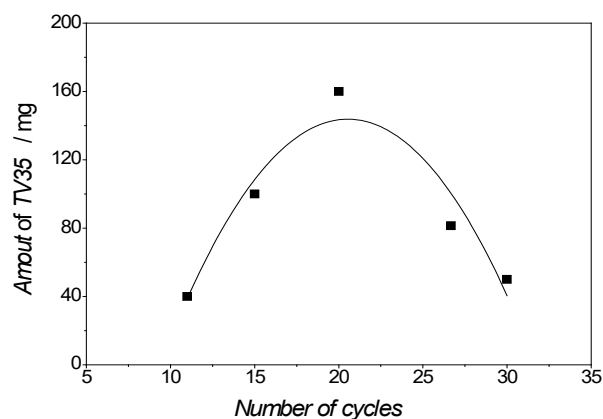
Fig. 7. Dependence of the Zn electrode life cycles on the TV35 content

CONCLUSIONS

In order to improve the discharge performance of the Zn anode, different binders were applied to the initial Zn-paste composition. The impact of using PTFE or teflonized carbon blacks (TV35) instead of carboxymethyl cellulose was examined by electrochemical charge/discharge tests. The obtained results showed that the porous zinc electrode is sufficiently prevented from the side of passivation during the operation of the cell in both, PTFE and TV35, but in search of high initial capacity, TV35 gives better results. A solution to improve the stability of electrode could be found through the combination of the three binders, achieving good balance of their capacity, charge–discharge cycling life and rate capability.

REFERENCES

1. A. Sumboja, J. Chen, Y. Zong, P. S. Lee, Z Liu, *Nanoscale*, **9**, 774 (2017).
2. P. Gu, M. Zheng, Q. Zhao, X. Xiao, H. Xue, H. Pang, *J. Mater. Chem., A*, **5**, 7651 (2017).
3. S. Clark, A. Latz, B. Horstmann, *Batteries* (mdpi) **4, 5** (2018).
4. A. R. Mainara, E. Iruina, L. C. Colmenaresa, A. Kvashaa, I. de Meatzaa, M. Bengoecheaa, O.Leoneta, I. Boyanoa, Zh.Zhangc, J. Blazqueza, *J. Energy Storage,* **15**, 304 (2018).
5. P. Pei, K. Wang, Z. Ma, *Appl. Energy*., **128**, 315 (2014).
6. Al. Rojas-Herndndez, M. Teresa Ramlrez, *J. Electrochem. Soc.,* **138**, 365 (1991).
7. H. Kim, G. Jeong, Y. U. Kim, J. H. Kim, C. M. Park, H. J. Sohn, *Chem. Soc. Rev.,* **42**, 9011 (2013).
8. G. X. Zhang, *ECS Transactions,* **16**, 47 (2009).
9. L. M. Baugh, A. Higginson, *Electrochimica Acta,* **30**(9), 1163 (1985).
10. L. Binder, K. Kordesch, *J. Electroanal Chem.,* **180**, 495 (1984).
11. T. C. Adler, F. R. McLarnon, E. J. Cairns, *J. Electrochern. Soc.,* **140**, 2 (1993).
12. D. Schröder, N. Nitin, S. Borker, M. König, U. Krewer, *J. Appl. Electrochem.,* **45**, 427 (2015).
13. Q. C. Horn, Sh. Y.Horn, *J. Electrochem. Soc.,* **150**, A652 (2003).
14. Rh. Mohamed, X. Cheng, E. Fabbri, P. Levecque, R. Kotz, O. Conrad, Th. J. Schmidt, *J. Electrochem. Soc.,* **162**, 6, F579 (2015).
15. A. R. Mainar, L. C. Colmenares, J. Alberto Blázquez, I. Urdampilleta, *International Journal of Energy Research,* 1-16, (2017), https://doi.org/10.1002/er.3822.
16. J. Phillips, S. Mohanta, C. Maske, D. C. Bose, J. J. Wu, B.L. McKinney, Patent 2010; US 291, 439 A1, 2010.
17. C. W. Lee, S. W. Eom, K. Sathiyanarayann, M. S. Yun, *Electrochim. Acta*, **52**, 1588 (2016).
18. R. C. Kainthla, J. M. David, US Patent App. 10/006,793, 2003.
19. F. Drillet, M. Adam, S. Barg, A. Herter, D. Koch, V. M. Schmidt, M. Wilhelm, *ECS Trans.,* **28**, 13 (2010).
20. C. Zhang, J. M. Wang, L. Zhang, J. Q. Zhang, C. N. Cao, *Journal of Applied Electrochemistry,* **31**, 1049 (2001).
21. L. Hongxia, W. Zhilin, *Advanced Materials Research,* **721**, 95 (2013).
22. J.-S. Lee, S. T. Kim, R. Cao, N.-S. Choi, M.n Liu, K. T. Lee, J. Cho, *Adv. Energy Mater.,* **1**, 34 (2011).
23. S.-M. Lee, Y.-J. Kim, S.-W. Eom, N.-S. Choi, K.-W. Kim, S. Baek, *J. Power Sources,* **227**, 177 (2013).
24. R. Raicheff, M. Mladenov, L. Stoyanov, N. Boshkov, V. Bachvarov, *Bulg. Chem. Commun.,* **48** (1), 61 (2016).
25. C.-C. Yang, W.-C. Chien, P.-W. Chen, C.-Y. Wu, *J. Appl. Electrochem.,* **39**, (2009).
26. T. Yager, Patent 2012; WO 2012/044319 A1, (2012).
27. J. Zhang, Q. Zhou, Y. Tang, L. Zhang, Y. Li, *Chem. Sci.,* **10**, 8924 (2019)
28. J. Blazquez, D. Vladikova, Z. Stoynov, B. Abrashev, M. Slavova, B. Burdin, E. Mihaylova-Dimitrova, L. Colmenares, A. R. Mainar, *Bulg. Chem. Commun.* **50**, 189 (2018).
29. E. Mihaylova-Dimitrova, B. Burdin, E. Mladenova, B. Abrashev, M. Slavova, D. Vladikova, *Nanosciences & Nanotechnology*, **19**, 2 (2019).
30. Zinc-Air Secondary innovative nanotech based batteries for efficient energy storage (ZAS, Horizon 2020, GA 646186), https://www.sintef.no/projectweb/zas/

Selected papers from

7th International Conference on New Trends in Chemistry,
September 25-26, 2021, Online https://icntcconference.com/.

Selected papers from

7th International Conference on New Trends in Chemistry,
September 25-26, 2021, Online https://icntcconference.com/.

Investigation of photocatalytic degradation of methylene blue by titanium dioxide composites

E. Akyol*, G. Tonbul

Department of Chemical Engineering, Yıldız Technical University, 34210 Istanbul, Turkey

In this study, titanium dioxide (TiO_2) nanoparticles were prepared from titanium powder by a simple flame transfer method. Hydroxyapatite (HAp) and barium sulfate ($BaSO_4$) were used to prepare titanium dioxide nanocomposites and their characterization was performed by using X-ray diffraction, Fourier transform infrared resonance (FT-IR) and BET surface area analysis techniques. The effect of HAp/TiO_2 and $BaSO_4/TiO_2$ nanocomposites on the degradation of methylene blue was investigated. It was observed that the photocatalytic properties of nanocomposites with hydroxyapatite and barium sulfate were slightly better when compared to pure titanium dioxide.

Keywords: Titanium dioxide, Nanocomposites, Photocatalytic, Hydroxyapatite, Barium sulfate.

INTRODUCTION

Nanocomposite materials are widely used in many fields due to their superior performance [1, 2]. Various nanoparticle materials with a diameter of less than about 100 nanometers are used in industrial applications such as electronics, optics, cosmetics, pharmaceuticals, etc. [3-5]. As the particle size gets smaller, the solid particles tend to show different properties from the bulk material. Even physical properties such as melting point and dielectric constant can change when the particle reaches a size of a few nanometers [6]. The optical property of the nanoparticle varies greatly depending on whether the nanoparticle is an insulator, semiconductor or metal. [7]. Titanium dioxide is considered a more promising catalyst compared to all other semiconductor photocatalytic materials due to its good inertness, eco-friendliness, low cost, non-toxicity, high photocatalytic activity, strong oxidizing power and long-term stability against photo and chemical corrosion [8-12]. TiO_2 is a wide-bandgap metal oxide semiconductor widely recognized with photocatalytic properties for pollution removal from polluted water and gases. Most photocatalysts are metal oxide pure semiconductors and their doped forms. Among various photocatalytic-based metal oxides such as ZnO, Nb_2O_3, SnO_2, Al_2O_3, nano TiO_2 stands out with its superior photocatalytic properties [13].

In this study, synthesis of titanium dioxide nanocomposites with hydroxyapatite and barium sulfate and investigation of their photocatalytic properties were aimed.

EXPERIMENTAL

Preparation and Characterization of Nanocomposites

Titanium powder (-325 mesh, 99.5 %) was provided by Alfa Aesar. Barium chloride ($BaCl_2$) was purchased from J. T. Baker. Sodium sulfate (Na_2SO_4) and hydroxyapatite (HAp) were from Sigma-Aldrich. TiO_2 synthesis procedure was reported previously in detail [14]. Synthesis of $BaSO_4$ nanocrystals was carried out by a previously described chemical precipitation method [15, 16]. Briefly, crystal growth of barium sulfate was achieved by slow mixing of equal volumes (0.1 M) of barium chloride and sodium sulfate solutions in presence of additives.

Particle size of the produced TiO_2 was investigated using laser diffraction (Micromeritics Saturn DigiSizer 5200 VI.10.). TiO_2 particles had a size between 200 and 400 nm. Characterization of functional groups present in the composites was performed by FT-IR spectroscopy (PerkinElmer Spectrum 100). The XRD patterns of the pure TiO_2 and composites of TiO_2 were recorded on a diffractometer (Panalytical X'Pert Pro PW 3040/60) with nickel filtered CuK (λ = 1.54 Å) as a radiation source and at a 2θ scan speed of 1°/min at 30 kV and 20 mA.

The surface areas of the TiO_2 composites were analyzed by the Brunauer-Emmett-Teller (BET) method. Nitrogen sorption isotherms according to the multiple-point BET (Brunauer, Emmett and Teller- COSTECH Kelvin Sorptometer 1042) method were used to determine the specific surface area of the samples.

---

* To whom all correspondence should be sent:
E-mail: eakyol@yildiz.edu.tr

To evaluate the degradation rate of methylene blue, samples were collected at different times and analyzed by UV–Visible spectroscopy (Perkin Elmer), considering the main peak of this dye located at 665 nm.

RESULTS AND DISCUSSION

Characterization

Figure 1 shows the FT-IR spectra of neat TiO_2 and of the prepared nanocomposites. The presence of $BaSO_4$ and HAp was confirmed by FT-IR analysis. X-ray diffraction patterns of bulk TiO_2 (a), HAp/TiO_2 nanocomposites (b) and $BaSO_4/TiO_2$ nanocomposites (c) are seen in Figure 2, respectively. A rutile structure is seen with the 2θ peak at 27.6°. The pattern reveals the successful formation of HAp and conforms to the HAp standard (Joint Committee on Powder Diffraction Standards) JCPDS pattern 01-072-1243) shown in Figure 2 (b). All the diffraction peaks in Fig. 2 (c) matched with the reference of the barite structure (JCPDS No:01-080-0512).

BET surface area and total pore volume of the samples are given in Table 1. The BET surface area of the prepared TiO_2 particles was 0.1754 m^2/g, the BET surface area of HAp/TiO_2 composite was 1.1162 m^2/g and the BET surface area of $BaSO_4/TiO_2$ was 1.9913 m^2/g. BET analysis showed that the addition of $BaSO_4$ and HAp increased both surface area and pore ratio. The surface area increased more than 10 times in the presence of barium sulfate.
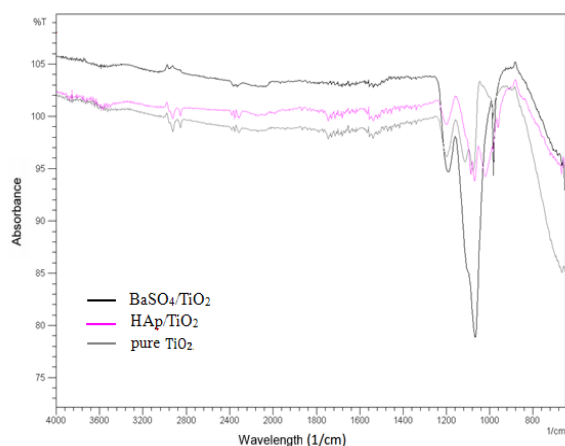
Figure 1. FT-IR analysis of titanium dioxide composites
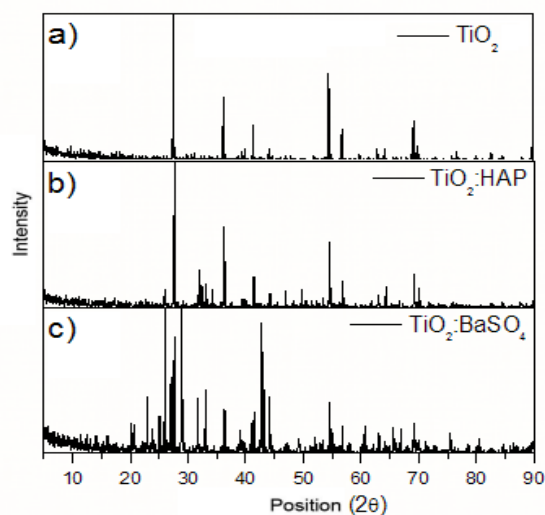
Figure 2. X-ray diffraction patterns of TiO_2 composites

Table 1. BET surface area of TiO_2 composites

Samples	BET Surface Area (m^2/g)	Total Pure Volume (cm^3/g)
Pure TiO_2	0.1754	0.0403
HAp/TiO_2	1.1162	0.2564
$BaSO_4/TiO_2$	1.9913	0.4574

Photocatalytic Decomposition of Methylene Blue

Photocatalytic decomposition graphs of methylene blue are shown in Figure 3. Experiments were carried out for 8 hours. It was observed that the variation of the concentration values with time is not linear. Figure 3 (a) shows the concentration-time plot of the degradation of methylene blue with neat TiO_2.

It can be seen from this graph that the concentration decreased from 0.0173 mmol/L to 0.0157 mmol/L over 8 hours. Figure 3 (b) shows the degradation of methylene blue with a sample of $BaSO_4/TiO_2$. The concentration decreased from 0.0165 mmol/L to 0.0158 mmol/L over time. In this graph, the concentration values are relatively linear after the sixth hour. Decomposition test data of methylene blue with HAp/TiO_2 sample is shown in Figure 3 (c). It was observed that the concentration decreased from 0.0173 mmol/L to 0.0155 mmol/L within 8 hours. In the present work, it was observed that the addition of HAp and $BaSO_4$ does not significantly modify the physicochemical properties of sulfated TiO_2, as can be seen in Fig. 3. Thus, as expected, the photocatalytic degradation efficiency of methylene blue in the presence of all the samples is very similar to each other within 8 hours of reaction time. No deactivation of the photocatalysts was observed even after 18 hours of reaction time.

CONCLUSIONS

In the present study, HAp/TiO$_2$ and BaSO$_4$/TiO$_2$ nanocomposites were successfully synthesized and their effects on photocatalytic degradation of methylene blue were examined. In the degradation experiments of methylene blue with all three samples, it was observed that the degradation values obtained after 8 hours were very close to each other. When compared according to the amount of absorption in studies with methylene blue, it was observed that HAp/TiO$_2$ > BaSO$_4$/TiO$_2$ >pure TiO$_2$.
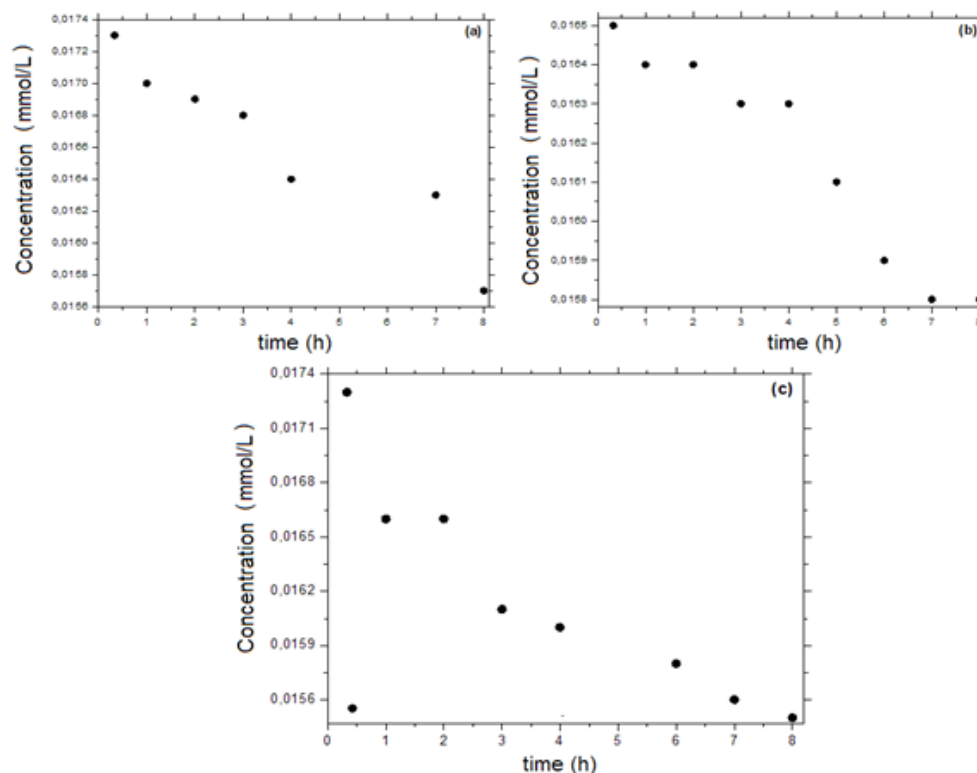
Figure 3. Methylene blue degradation over 8 h using a) TiO$_2$, b) BaSO$_4$/TiO$_2$, c) HAp/TiO$_2$

REFERENCES

1. P. H. C. Camargo, K. G. Satyanarayana, F. Wypych, *Materials Research*, **12**, 1 (2009).
2. A.T. Erciyes, Y. Bayram, E. Akyol, *Journal of the Indian Chemical Society*, **96,** 1181 (2019).
3. S. Chawla, Nanoparticles and Fluorescence, in: M. Aliofkhazraei (ed.) Handbook of Nanoparticles. Springer, Cham., 2016.
4. M. Bundschuh, J. Filser, S. Lüderwald, M. S. McKee, G. Metreveli, G. E. Schaumann, R. Schulz, S. Wagner, *Environmental Sciences, Europe*, 30, 6 (2018).
5. M. A. Subhan, K. P. Choudhury, N. Neogi, *Nanomanufacturing,* **1,** 75 (2021).
6. S. Mourdikoudis, M. P. R. M. Pallares, N. T. K. Thanh, *Nanoscale*, **10**, 12871 (2018).
7. A. M. Abu-Dief, *Journal of Nanotechnology and Nanomaterials*, **1,** 5 (2020).
8. C.H.A. Tsang, K. Li, Y. Zeng, W. Zhao, T. Zhang, Y. Zhan, R. Xie, D.Y.C. Leung, H. Huang, *Environment International,* **125,** 200 (2019).
9. Y. Wang, Y. Huang, W. Ho, L. Zhang, Z. Zou, S. Lee, *Journal of Hazardous Materials*, **169,**77 (2009).
10. C. Xu, G. P. Rangaiah, X. S. Zhao, *Industrial & Engineering Chemistry Research*, **53**, 14641 (2014).
11. C. H. Kwon, H. Shin, J. H. Kim, W. S. Choi, K. H. Yoon, *Materials Chemistry and Physics,* **86,** 78 (2004).
12. A. M. Ali, M. A. Sayed, H. Algarni, V. Ganes, M. Aslam, A. A. Ismail, H. M. El-Bery, *Catalysts*, **11**, 1062 (2021),
13. P. Benjwal, B. De, K. K. Kar, *Applied Surface Science*, **427**, 262 (2018).
14. S. Senol, E. Akyol, *Materials Science-Poland*, **38**(3), 443 (2020).
15. E. Akyol, M. A. Cedimagar, *Crystal Research and Technology*, **51**, 393 (2016).
16. E. Akyol, O. Ara, M. Oner, *Desalination and Water Treatment*, **52**, 5965 (2014).

Theoretical and experimental photodegradation of Phosmet *via* oxidation techniques in the presence of aqueous TiO₂ suspension

B. Eren[1], Y. Y. Gurkan[2*]

[1]Tekirdag Namık Kemal University, Faculty of Agriculture, Tekirdag, Turkey
[2]Tekirdag Namık Kemal University, Department of Chemistry, Tekirdag, Turkey

This study is conducted with the aim to analyze the reaction kinetics of Phosmet with the OH radical, and to determine its mechanism. Due to the lack of experimental evidence of radical intermediate products occurring during the reactions, the theoretical stage has been quite informative. In this study, in order to theoretically determine all probable reaction paths, geometric optimization of the reactants and transition state complexes was conducted using DFT/B3LYP/6-31G(d) basic set of Quantum Mechanical Density Functional Theory (DFT). As a result of the calculations, the energy values at ground state, and rate constant and activation energies (E_a) at transition state (TS) of the probable reaction paths were determined. And finally, the primary intermediate products were found out by the determination of the atom where the OH radicals attach, and the hydrogen atoms they had removed. The reaction mechanism was clarified through the determination of the intermediate products. Since the reactions of pesticides with OH radical are important both in terms of water purification and atmospheric chemistry, the calculations were carried out in gaseous phase and also at aqueous phase by modelling the solvent impact. In the experimental stage, the degradation reactions under UV-light impact of the pesticide, chosen as pollutant, in aqueous TiO₂ suspensions, were analyzed. At the end of this research, the optimum photocatalyst amount and TiO₂ concentration were determined. The degradation rates were determined, the impact of the initial concentration was analyzed, and the reaction products were identified.

Keywords: Phosmet, DFT, Heterogeneous catalysis, Aqueous TiO₂, TS.

INTRODUCTION

There is increasing need for pesticides due to the increasing population in the world. Due to the considerable toxicity of these substances, they require their amount to be traced in nature. Pesticides cause acute and chronic poisoning, also lead to cancer, allergic reactions, damage of the nervous system, learning disability and memory loss, and additionally, cause disorder in enzyme balance as well as damage and mutation in intracellular DNA molecules [1, 2].

Organophosphorus compounds are widely used as pesticides, and these substances react with the OH radical, which is one of the atmospheric radicals, by reaching the atmosphere. The durability of organophosphorus pesticides (OPs) in the nature is short due to their fast decomposition. These pesticides degrade fast; therefore, they do not cause long-term damage. However, they are considerably poisonous. In addition to killing non-targeted insects, these pesticides harm both human and nature. In addition, since they do not have a stable structure, they are applied over and over, and therefore, they are considered as costly [3-10].

Phosmet is an organic compound, and it is known that organic pollutants are present in water at low concentrations. Biomolecules, which are hydroxyl scavengers at different rates, are specific detectors for hydroxyl radicals due to their hydroxylation capability. Any hydroxyl radical attacking an aromatic compound leads to a formation of a hydroxylated new product, and these new products may be more harmful that the original product at the beginning of this process. Therefore, it is essential that these products be observed [11].

Recently, the removal of organic residues using advanced oxidation processes has been observed for water purification technologies. Basically, photocatalytic processes, using semiconductors, which can produce reactive hydroxyl radicals when exposed to UV-radiation, were analyzed in detail [12-14]. Photocatalytic oxidation is one of the advanced technologies in the removal of pollutants due to its effectiveness in the mineralization of organic pollutants [15]. TiO₂ is the most commonly used photocatalysts among others, because it is obtainable, cheap, non-toxic, and has a relatively high chemical stability [16]. TiO₂ is used successfully for the degradation of pesticides [17-19].

Phosmet, which is used as OP1 abbreviation in the study, is an organophosphate insecticide used on plants and animals. While it is used mainly for the control of larvae of codling moth on apple trees, it is also used on various fruit plants, ornamental plants, and grapes for the control of suckers, acari, and aphids [20, 21], while it is also used in veterinary fields in the control of pigswill [22]. OP1, which is used as an insecticide and acaricide, is an offensive smelling, off-white crystalline solid [23]. Its melting point is 72-72.7 $^\circ$C, and decomposes below its boiling point. Its water solubility at 25 $^\circ$C is 25 mg/L [24] while it is stable at normal storage conditions [25], it is relatively stable at acidic conditions, and decomposes rapidly above 100° C [26]. When heated, it releases extremely toxic fumes such as nitrogen oxide, phosphorous oxide, sulfur oxide [27]. It also has an abrasive effect on metals [28].

METHODOLOGY

In order to theoretically determine all the possible reaction paths of OP1, geometric optimizations were done using the DFT/B3LYP/6-31G(d) basic set of Quantum Mechanical Density Functional Theory (DFT). Energy values were calculated and geometric optimizations were done at all molecular orbital calculations using Gauss View 5.0.8 molecular visualization program and Gaussian 09 program [29]. The energy of decomposition reactions of all organic compounds is affected by the water molecules in aqueous environments. In addition, geometric flexion in solutions is induced by H_2O. In other words, the presence of a dielectric environment such as H_2O leads to a relaxation in geometry, and this situation has an energy reducing, and stabilizing effect [11]. Therefore, in order to explain the solvent effect of H_2O on OP1+ ·OH reaction energy, CPSM set of COSMO (conductor-like screening solvation model) within the Gaussian 09 packaged software was used. The rate constants and activation energies of the analysed reactions were found out using Transition State Theory (TS) [29]. TS is based on the principle that an equilibrium exists between the reactants in a reaction and the transition state complex. The following equations are used in order to calculate the transition state complexes: E_a activation energies and k constant of OP1 for h = 6.62607×10^{-34} J × s, R = 1.987 cal × mol^{-1} × K^{-1}, T = 298 K and $k_B = 1.38.10^{-23}$ J × K^{-1}; Ea = E_{TS} - ($E_{initial\ molecule}$ + $E_{·OH}$) × 627.509 kcal/mol

$$k = \frac{k_B \cdot T}{h} \cdot \frac{Q_{TS}}{Q_{initial\ molecule} \times Q_{OH}} \cdot e^{\frac{-E_a}{R.T}}$$
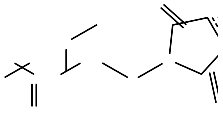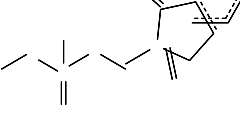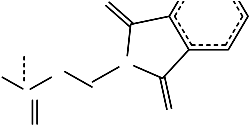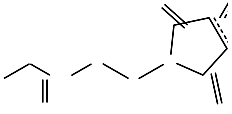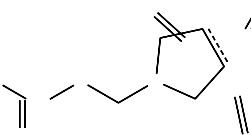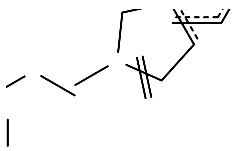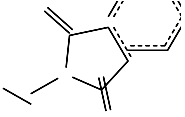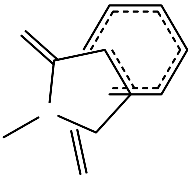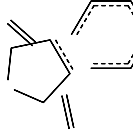
As an experimental method, a stock solution of 10^{-2} M of Phosmet was prepared. In the experimental stage, white-coloured, solid, Sigma Aldrich branded Phosmet product number 36195 with a melting point of 73 $^\circ$C was used. In order to prepare the reaction solution, the determined amount of TiO_2 was weighed and put in the reaction vessel, and the suspension was prepared by adding distilled water. In the experiments, Sigma-Aldrich brand, number 13463-67-7 CAS, odourless, white, TiO_2 powder insoluble in water at 25 $^\circ$C was used. In order to prepare a good suspension, the reaction vessel was shaken for 15 min in an ultrasonic bath. The organic pollutant concentration was adjusted to be 10^{-4} M by adding the stock solution onto this suspension, and the suspension volume was completed to 600 mL. Samples of 10 mL were taken from the prepared suspensions with a pipette, and the rest was placed into a photoreactor in order to be illuminated. A special cylindrical Keriman UV18/8 branded reactor was used in the experiments. As a light source, there were 18 8W UV fluorescent lamps at equal intervals within the cylinder. All experiments were carried out in a Pyrex beaker. The homogenous distribution of TiO_2 particles was provided by shaking the beaker used as a reaction vessel. Since the normal filtration process was not sufficient, samples were filtered in vacuum using 0.2 µm filter-paper in order to remove the TiO_2 particles from the environment. The filtrates were taken into test tubes, and their absorbance was measured on a UV-visible spectrophotometer (Perkin Elmer) at a previously found λ_{max} = 318 nm.

RESULTS AND DISCUSSION

Theoretical Findings for the Ground State

Organophosphorus insecticides are esters of phosphoric acid (H_3PO_4) as a chemical structure. Phosphorus (P) atom is mostly attached to methoxy (OCH_3) or ethoxy (OC_2H_5) as two ester groups. Two methoxy ester groups in the OP1 molecule are seen in Figure 1. The third ester group can be an aliphatic, homocyclic or heterocyclic structure and is attached to the phosphorus atom by ester (P-O-R) or thioester (P-S-R) bonds. This weak bond increases the electrophilicity of the phosphorus atom and gives it electron withdrawing property. In the OP1 molecule, there is a P=S bond instead of P=0, and since two oxygen and two sulfur atoms are attached, the molecule is called dithiophosphate.

Figure 1. The optimized geometric structure of OP1 *via* DFT method. (Grey, C; white , H; blue, N; red, O; yellow, S; orange, P)

When the mulliken loads of the OP1 molecule in Table 1 are analysed, the electronegative atoms are N_{13}, O_{23}, O_{22}, O_{15}, O_{14}, S_{21}, respectively. As it can be seen in Figure 1, O_{14} and O_{15} of these atoms form a double bond with C_7 and C_8 atoms. Since these bonds are stable, the bonds are not expected to break. O_{23}, O_{22} atoms are the second and third electronegative atoms.

Bond lengths of O_{22}-C_{24} and O_{23}-C_{28} in Table 2 are 1.44291 Å; 1.44322 Å, respectively, and the bond angle of $P_{20}O_{22}C_{24}$ is 119.67251^0, while the bond angle of $P_{20}O_{23}C_{28}$ is the third widest bond angle with 121.09768^0. Based on this information, it is expected that the methyl groups of C_{24} and C_{28} atoms will break. So it is understood that this is the first stage of degradation mechanism N_{13} is the most electronegative atom. Looking at the area surrounded by this atom; in Table 2, N_{13}-C_{16} with a bond length of 1.43704 Å, although the N atom is the most electronegative atom, since there are bonds longer than this bond length, it is predicted that if there is a bond break here, it will happen after the other bonds. Even the fact that the bond angles $C_8N_{13}C_{16}$ and $C_7N_{13}C_{16}$ in Table 2 have the widest bond angles with 124.831020; 123.050860 respectively, this will not change the situation.

Table 1. Energy values of OP1 in gaseous and aqueous phases, and their mulliken loads in gaseous phase.

(OP1)Phosmet ($C_{11}H_{12}NO_4PS_2$)	Gaseous Phase (kcal × mol^{-1})	Aqueous Phase (kcal × mol^{-1})	Mulliken Loads	
			C_3	-0.009525
			C_6	-0.006066
	ΔE= -1919.615320	-1919.629150	**N_{13}**	**-0.511680**
	ΔH= -1919.614376	-1919.628206	**O_{14}**	**-0.466116**
	ΔG= -1919.685580	-1919.701667	**O_{15}**	**-0.476781**
			S_{19}	0.001346
			P_{20}	0.752968
			S_{21}	**-0.357536**
			O_{22}	**-0.497179**
			O_{23}	**-0.504260**

Table 2. Bond lengths and bond angles of atoms of the OP1 molecule.

	Bond Length	(Å)	Bond Angle	(°)
OP1	O_{22}-C_{24}	1.44291	$C_{24}O_{22}P_{20}$	**119.67251**
	O_{23}-C_{29}	1.44322	$O_{22}P_{20}S_{19}$	95.84725
	P_{20}-O_{23}	1.62316	$O_{23}P_{20}S_{21}$	115.24231
	P_{20}-S_{21}	**1.94862**	$S_{19}P_{20}S_{21}$	**117.55240**
	P_{20}-S_{19}	**2.12454**	$O_{23}P_{20}S_{19}$	107.49501
	C_{16}-S_{19}	**1.86489**	$P_{20}S_{19}C_{16}$	102.77144
	C_{16}-N_{13}	1.43704	$P_{20}C_{16}N_{13}$	112.40431

Table 3. Energy values in gaseous phase of fragments of OP1 molecule at ground state.

Fragments	Gaseous Phase (kcal/mol)	Fragments	Gaseous Phase (kcal/mol)
OP1	$\Delta E = -1,204,575.890$ $\Delta H = -1,204,575.297$ $\Delta G = -1,204,619.979$	OP11	-1,179,928.733 -1,179,928.141 -1,179,971.732
OP12	-1,155,290.148 -1,155,289.556 -1,155,328.230	OP13	-1,132,713.373 -1,132,712.780 -1,132,753.264
OP14	-1,108,069.620 -1,108,069.028 -1,108,106.729	OP15	-1,060,850.034 -1,060,849.441 -1,060,886.944
OP16	-596,407.784 -596,407.191 -596,438.267	OP17	-346,545.368 -346,544.775 -346,572.369
OP18	-321,892.733 -321,892.140 -321,918.274		
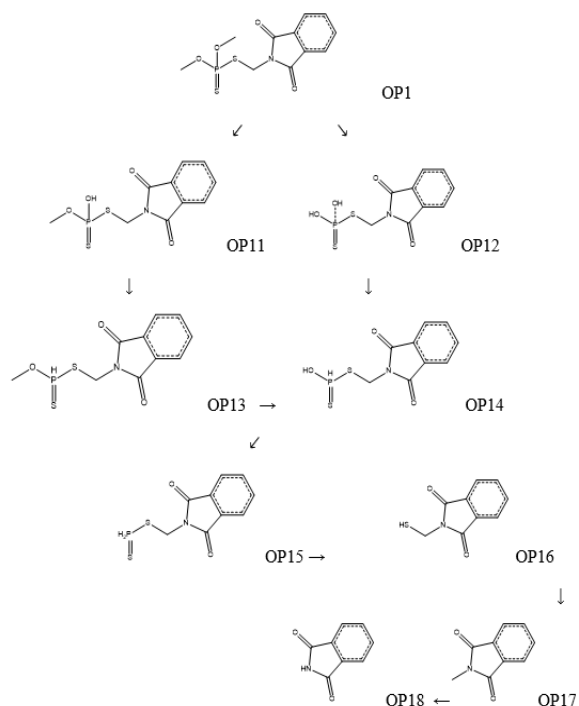
Figure 2. The degradation mechanism of OP1 molecule at ground state.

For the fragments in Table 3, the energy values in the gaseous phase were examined. The lowest energy level, in other words the degradation path starting from the most stable fragment for OP1 in Figure 2, was determined both in the light of the above mentioned predictions, and by the analysis of the energy values of each fragment in Table 3.

Theoretical Findings for the Transition State Complexes

Reactants were used in this study in order to find out the transition state complexes. An appropriate initial geometry estimation was made according to the reaction paths by using the optimum geometric parameters. Transition position complexes were modelled for the reactions that occur with OH addition and H removal. While modeling, C-O bond was chosen as the reaction coordinate. During the calculations, the length of this bond was varied between 1,400-3,000 Å.

As the reaction path; the distance of the forming H_2O molecule, and the length of the bond of OH were chosen, and the dihedral angles and bond lengths related to this group were changed during calculations in order to determine the place of the OH radical according to the molecule. $OP1_{TS1}$ and $OP1_{TS2}$ transition state complexes are obtained *via* OH radical approach with TS to C_3 and C_4 atoms in the benzene ring, and OH bonding to C_3 and C_4 atoms in OP1 molecule. $OP1_{TS3}$ transition position complex is obtained by removing the H atom with

TS from the C_{16} atom in the OP1 molecule and forming the H_2O molecule. When the OH radical approaches to the C_{24} and C_{28} atoms in the OP1 molecule, the $OP1_{TS4}$ transition position complex is obtained by removing the H from the methyl group of the C_{28} atom and separating a H_2O molecule. All of these transition positions are shown in Figure 3.

The H atom is broken off from the methyl groups at the ends of the molecule and the H_2O molecule is separated, thus, radical formations are realized. This takes place faster than the removal of H atoms from the methyl groups attached to the closed ring or the removal of H atoms from the methyl groups in the intermediate region of the molecule. Attachment of the OH radical to the closed ring takes place at the last step. To clarify this order of velocity, C-OH and $C...H_2O$ bond lengths are given in Table 4. It is seen that the molecule with the longest bond length reacts faster.
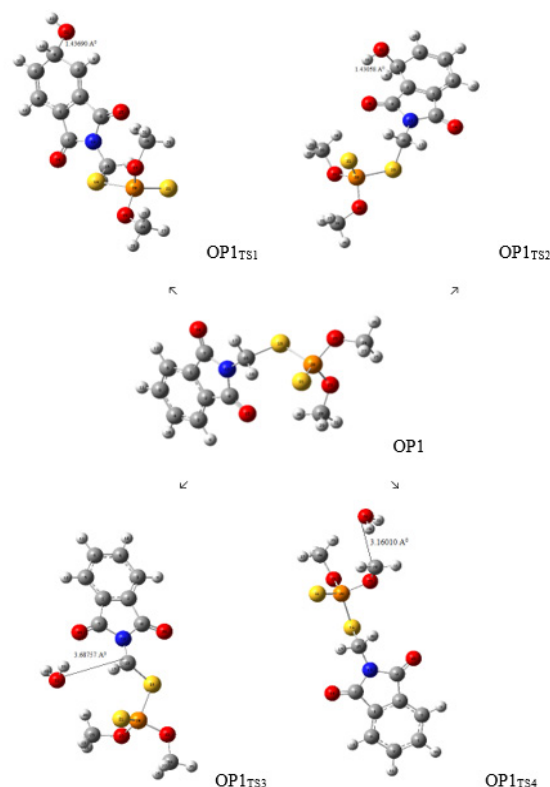
Figure 3. Optimized geometric structures of four possible TS approximations of the OP1 molecule. (Grey, C; white , H; blue, N; red, O; yellow, S; orange, P)

Experimental Findings

Impact of Photocatalyst Concentration. In order to determine the impact of photocatalyst concentration, the TiO_2 concentration was changed as (0.1- 0.5) g/100 mL in suspensions with an initial concentration of $1.0×10^{-4}$ mol L^{-1} at the natural pH of all substances. The obtained results are given in Figure 4; degradation % for 30, 60, and 90 min,

respectively, at the y axis; and TiO_2 values of (0.1-0.5) g/100 mL at the x axis.
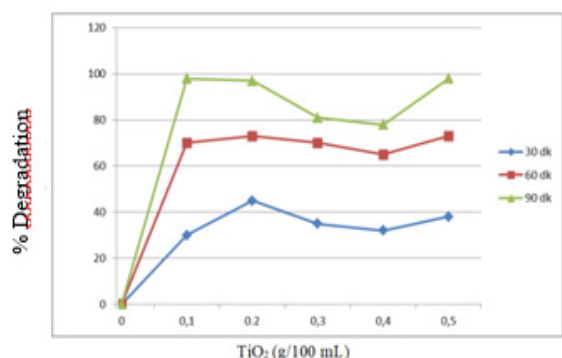
Figure 4. Optimum photocatalytic degradation.

As the TiO_2 concentration increased, the photocatalytic degradation rate increased up to a specific limit of concentration, and then showed a slow decrease. Maximum degradation was obtained at 0.2 g/100 mL of TiO_2 concentration, and this concentration was taken as optimum photocatalyst concentration in all experiments. After the 0.2 g/100 mL optimum value in Figure 4, it was found out that there were other factors getting involved in the degradation rate. As TiO_2 concentration increases, the interparticle distance decreases. Particles form groups by coming together, and this leads to the reduction of the interphase surface. Since organic matters are oxidized on TiO_2 surface by their .OH, the reduction of the interphase surface reduces the possibility of the oxidation of substances; in other words, it reduces the possibility of fragmentation into smaller substances. Moreover, TiO_2 particles prevent the system from absorbing light, and even lead to light scattering.

Impact of Light and Photocatalyst

In order to conduct the degradation of organic matters in heterogeneous photocatalytic degradation systems, the three factors, namely light-semiconductor-O_2, have to be altogether present in the system. Pretestings were conducted in order to determine the impact of light alone on the degradation of substances, and the absorption on TiO_2 particle surface for the substance. These experiments were conducted in the presence of light only, in TiO_2 presence only, and in the presence of TiO_2+light as three repetitions. The results of these experiments are given in Figure 5. The figure shows the change of C/C_o against time (t). C_o is taken as the initial concentration of the substance, whereas C shows the concentration of the substance in t time.
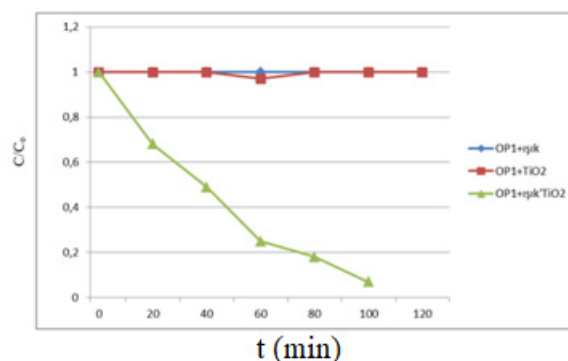
Figure 5. Effect of light and TiO_2 on the photocatalytic degradation of OP1.

As seen in Figure 5, when the change of C/C_o against time is analyzed, it can be seen that there was no concentration change when OP1 was illuminated (exposed to light) alone. However, when OP1 was kept in the dark together with TiO_2, a slight change in the concentration was observed due to absorption. When OP1 was present in an environment together with both light and TiO_2, it was found out that OP1 was degraded to a great extent. The concentration change at the end of 100 min was found out to be 93%.

Impact of the Initial Concentration

It was analyzed whether the initial concentration had an impact on the photocatalytic degradation rate by changing the initial concentration as $(6.0-14.0) \times 10^{-5}$ mol L^{-1}. The k rate constants, and r regression values are given in Table 5. The reaction rate constant decreases as the initial concentration increases. However, this decrease declines at lower concentrations.

Table 4. Q values, E_a activation energies, and k rate constants of the studied molecules

Molecule	E_a (kcal × mol^{-1})	k	C-OH (Å)	C...H$_2$O (Å)
OP1$_{TS1}$	18.578	6.017×10^{-8}	1.43690 (benzene)	
OP1$_{TS2}$	19.920	9.199×10^{-9}	1.43058 (benzene)	
OP1$_{TS3}$	23.528	3.818×10^{-10}		3.68757(intermediate region)
OP1$_{TS4}$	**13.466**	**0.049**		**3.16010 (at the end)**

Table 5. Impact of the initial concentration.

OP1	6.0×10^{-5}	8.0×10^{-5}	10.0×10^{-5}	12.0×10^{-5}	14.0×10^{-5}
k /10^{-18} min^{-1}	2.45±0.002	2.13±0.003	1.76±0.001	1.58±0,004	0.99±0.005
r	0.9885	0.9748	0.9526	0.996	0.9874

The results of the experiments are given in Figure 6. The Figure shows the e-base logarithm, and the change of ln C according to time for different initial concentrations of organic matter concentrations. The reaction rate constant decreases as the initial concentration increases. However, this decrease declines at low concentrations. Due to the reaction rate constant k being dependent on the initial concentration, it can be said that the degradation reaction is apparently a first-order reaction.

The system consists of two phases. OH radicals result from the OH$^-$ ions absorbed at the TiO$_2$ surface. Since the organic substance also wants to be absorbed at the TiO$_2$ surface, it slows down the formation of OH radicals by impeding the transition of OH$^-$ ions into the catalytic space at the surface.

♦ 6×10^{-5} mol L^{-1}
■ 8×10^{-5} mol L^{-1}
▲ 10×10^{-5} mol L^{-1}
X 12×10^{-5} mol L^{-1}
✳ 14×10^{-5} mol L^{-1}
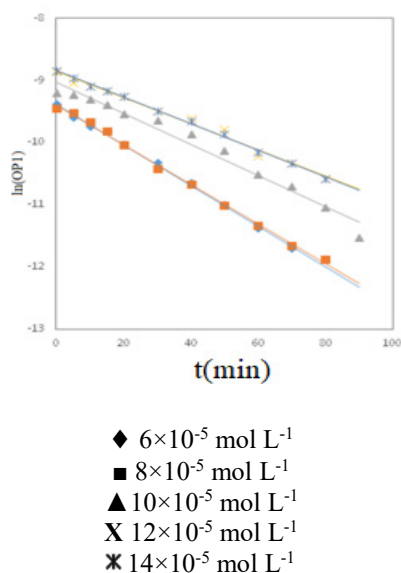
Figure 6. The impact of the initial concentration of OP1 on the photocatalytic degradation rate.

CONCLUSIONS

This research was conducted both theoretically and experimentally by the use of Phosmet (OP1), which was part of a study carried out with seven pesticides comprising four organophosphorus, and three carbamate pesticides. The photocatalytic degradation of OP1 was investigated in aqueous TiO$_2$ suspensions with UV light. The best degradation rate was obtained at 10×10^{-5} mol L^{-1} initial concentration with UV/ TiO$_2$. Experimental results indicated that the maximum degradation of OP1 occurred at 0.2 g/100 mL TiO$_2$ concentration. Based on the results of DFT calculations, weakly

bonded pre-reactive complexes were important for the degradation reactions because they were reducing the energy barrier.

Radical formation through the H atom being broken off from the methyl groups at the ends of the molecule and the H$_2$O molecule being separated takes place faster than the removal of H atoms from the methyl groups attached to the closed ring or the removal of H atoms from the methyl groups in the intermediate region of the molecule. In conclusion, the degradation pathway at ground state of Phosmet molecule, as given in Figure 2, and all the transition positions, as given in Figure 3, clarify the degradation mechanism of Phosmet molecule in the nature in terms of atmospheric and aqueous chemistry.

REFERENCES

1. G. Dolapsakis, I. G. Vlachonikolis, C. Varveris, A. M. Tsatsakis, *European Journal of Cancer,* **37**, 1531 (2001).
2. L. Sarabia, I. Maurer, E. Bustos Obregon, *Ecotoxicology and Environmental Safety*, **72**, 938 (2009).
3. R. Atkinson, S. M. Aschmann, M. A. Goodman, A. M. Winer, *Int. J. Chem. Kinet.,* **20**, 273 (1988).
4. M. A. Goodman, S. M. Aschmann, R. Atkinson, A. M. Winer, *Arch. Environ. Contam. Toxicol*., **17**, 281 (1988).
5. M. A. Goodman, S. M. Aschmann, R. Atkinson, A. M. Winer, *Environ. Sci. Technol.,* **22**, 578 (1988).
6. R. Atkinson, J. Arey, *Chem. Rev*., **103**, 4605 (2003).
7. S. M. Aschmann, E. C. Tuazon, R. Atkinson, *J. Phys. Chem. A*, **109**, 11828 (2005).
8. S. M. Aschmann, E. C. Tuazon, R. Atkinson, *J. Phys. Chem. A*, **109**, 2282 (2005).
9. S. M. Aschmann, R. Atkinson, *J. Phys. Chem. A,* **110**, 13029 (2006).
10. S. M. Aschmann, E. C. Tuazon, W. D. Long, R. Atkinson, *J. Phys. Chem. A*, **114**, 3523 (2010).
11. B. Eren, Y. Yalçın Gürkan, *JSCS*., **82** (3), 277 (2017).
12. I. Losito, A. Amorisco, F. Palmisano, *Journal of Chromatography A,* **1187** (1-2), 145 (2008).
13. M. A. Oturan, J. J. Aaron, *Crit. Rev. Environ. Sci. Technol*., **44**, 2577 (2014).
14. Y. S. Wu, C. C. Chen, Y. C. Huang, W. Y. Lin, Y. T. Yen, C. S. Lu, *Sep. Sci. Technol*, **51**, 2284 (2016).
15. Y. Wang, H. Zhao, J. Gao, G. Zhao, Y. Zhang, . *Phys. Chem*. C, **116**, 7457 (2012).
16. X. Chen, S. S. Mao, *Chem. Rev*., **107**, 2891 (2007).
17. M. Sturini, E. Fasani, C. Prandi, A. Casaschi, A. Albini, *J. Photochem, Photobiol. A: Chem.,* **101**, 251 (1996).

18. H. F. Lai, C. C. Chen, R. J. Wu, C. S. Lu, *J. Chin. Chem. Soc.,* **59**, 87 (2012).
19. Y. Yalçın Gürkan, E. Kasapbaşı, Z. Çınar, *Chemical Engineering Journal*, **214**, 34 (2013).
20. http://www.drugbank.ca/drugs/DB11.448.
21. http://extoxnet.orst.edu/pips/phosmet.htm.
22. https://www.ncbi.nlm.nih.gov/mesh/68.010.706.
23. M. J. O'Neil, The Merck Index - An Encyclopedia of Chemicals, Drugs, and Biologicals. (13th ed.), Whitehouse Station, NJ: Merck and Co. Inc., 2001, p.1315.
24. C. D. S. Tomlin, Phosmet (732-11-6), in: The e-Pesticide Manual. (13th ed.), UK, British Crop Protection Council, 2004-05.
25. G. D. Clayton, F. E. Clayton, Patty's Industrial Hygiene and Toxicology (3rd ed.), New York, John Wiley & Sons, 2A, 2B, 2C, 1981, p. 4822.
26. D. Hartley, H. Kidd, The Agrochemicals Handbook. (2nd ed.), Lechworth, Herts, England, The Royal Society of Chemistry A., 1987, p. 325.
27. R. J. Lewis, Sax's Dangerous Properties of Industrial Materials (9th ed.), NY, Van Nostrand Reinhold, 1-3, 1996b, p. 2698.D. Hartley, H. Kidd, The Agrochemicals Handbook, (2nd ed.), Lechworth, Herts, England, The Royal Society of Chemistry A. 1987, p. 325.
28. Gaussian 09, Revision B.04, Gaussian Inc., Pittsburgh, PA, 2009

Surface modification of zeolite and kaolin with 3-(aminopropyl) triethoxysilane and 3-(trimethoxysilyl) propyl methacrylate

C. Özel[1], C. Akat[1], R. Alosmanov [2], M. U. Kahveci[3], C. Emir[1], S. Yücel[1*]

[1]Yildiz Technical University, Faculty of Chemical and Metallurgical Engineering, Department of Bioengineering, Istanbul, Turkey
[2] Bakü State University Faculty of Chemistry, Department of High-Molecular Compounds Chemistry, Bakü, Azarbeijan
[3]İstanbul Technical University, Chemistry Department, İstanbul, Turkey

Zeolites are crystalline, hydrated aluminosilicates of alkaline earth cations composed of 3-dimensional frameworks, which have been widely used for adsorbents, catalysts, ion exchangers, molecular sieves for separation, and sorting the molecules according to their crystalline size dimensions. Kaolin is an industrial clay, consisting of hydrated aluminum silicate mineral, named kaolinite. Kaolin is used for various purposes in paper coating and filling, ceramics, cracking catalysts, and many other uses. Kaolin functions as pharmaceutical excipient in commercial products, such as granulating agent, film-coating additive, anti-caking agent and also accelerates blood clotting. Surface modification of kaolin allows it to be used in different industries and for different purposes. Surface modification of inorganic materials can be carried out by means of silanol agents. (3-Aminopropyl) triethoxysilane (APTES), 3-(trimethoxysilyl) propyl methacrylate (MPTMS), (3-aminopropyl) trimethoxysilane (APTMS) are known important silanization agents used for surface modification. The aim of this study is the surface modification of a zeolite and kaolin with APTES and MPTMS at different ratios and in different solvent media (ethanol, toluene, DMSO). The structures of the samples were investigated using zeta potential, Fourier transform infrared analysis (FTIR) and scanning electron microscopy (SEM). It was determined that the optimum APTES modification ratio for zeolite was 1:10 in toluene, while the optimum MPTMS modification ratio of kaolin was 1:3. It was revealed that the layered structure of kaolin is interleaved with DMSO solvent.

Keywords: Zeolite, Kaolin, APTES, MPTMS, Silanization.

INTRODUCTION

Zeolite structures consist of SiO_4 and AlO_4 primary units. About 100 different architectures are known which are based on vertex-sharing SiO_4 and AlO_4 tetrahedra and these units are into a truncated octahedron. Zeolites are used in several areas such as laundry detergents, oil refining and petrochemical industries, adsorbents, gas separations, agriculture and major application areas as adsorbents, catalysts, and ion exchange material. Although not as good as silica gel and aluminum oxide, zeolites also have high water adsorption capacity [1–3]. However, the adsorption capacity decreases depending on the temperature increase. Zeolite is used in biomedical applications due to its antibacterial and biocompatibility properties. Surface modified zeolites provide advantageous and beneficial usage in various specific biomedical application areas such as drug delivery, soft and hard tissue applications, hemostatic agents. For example, products containing zeolite applied directly to the wound are used by the United States (US) military to stop bleeding and create hemostasis. Rapid and on-site blood loss can be intervened by using zeolite and zeolite-containing products in frequently occurring traffic accidents, domestic injuries, and war wounds. It functions as a practical and easy-to-use absorbent material that dehydrates the blood and adheres to the injured tissue and provides hemostasis to prevent deaths due to blood loss [4–6]. Zeolite can be used as an absorbent material that can dehydrate blood, adhere to injured tissue, and induce hemostasis [7].

Kaolin occurs in a layered structure and is composed of sheets of Si tetrahedral and Al octahedral with common oxygen, with the formation of a 1:1 layer [8]. It has two different basal cleavage faces [9]. One basal face consists of a tetrahedral siloxane surface with very inert Si-O-Si links. The other basal surface consists of an octahedral, gibbsite $(Al(OH)_3)$ sheet [10]. Kaolin is an important mineral in the world market. Kaolin can be used as an additive that can improve the properties of materials by modifying the surface. These materials are used in paper coating and filler, ceramics, paint, plastic, rubber, fiberglass, cracking catalysts and many other uses. Functions as a pharmaceutical excipient in commercial products; It is a granulating agent, film coating additive, diluent, pelletizing agent, suspending and anti-caking agent, it also

---

accelerates blood coagulation [11]. Kaolin has also been observed to accelerate the cessation of bleeding by activating the hemostatic factors Factor XII, Factor X, Factor V, and platelets. More importantly, kaolin has good biocompatibility.

In order to improve the good mechanical property and biocompatibility to the biomedical implants consisting of surface modification of substrates has been widely studied in the past years. Surface modification by APTES containing a high density of primary amino groups was reported to be a reliable way to bind a protective film with good biocompatibility [12]. Owing to the protonation of amino groups, bioactive matters, or drug carrier systems could be immobilized on the surface through zwitterionic pairs. Two different surface modifications of kaolin and zeolite can occur. The physical modification takes place by affecting the chemical composition and by the use of high temperatures. Chemical modification occurs by changing the structure, surface functional groups and surface area by organic compounds, acids or bases [13]. (3-Aminopropyl) triethoxysilane (APTES), 3-(trimethoxysilyl) propyl methacrylate (MPTMS), (3-aminopropyl) trimethoxysilane (APTMS) are known important silanization (silane-coupling) agents used for surface modification of materials. Silanization is a low-cost and very effective covalent coating method for modifying the surface of materials containing large numbers of hydroxyl groups. Bonding of silicon-based molecules on zeolite or kaolin occurs when hydroxyl groups on surfaces can bind to silicon atoms. There are many types of commercially available silanization agents. They are easy to react with a hydroxylated surface and introduce active groups (e.g., amino group and carboxyl group) to the surface of the material [14]. The aim of this study is to perform surface modifications of zeolite and kaolin using different ratios of APTES and MPTMS, as well as in different solvents (ethanol, toluene, DMSO). The characterization of the samples was peerformed by zeta potential analysis, FTIR and SEM analysis.

EXPERIMENTAL

Inorganic substrates used in this study, zeolite and kaolin, surface modification agents APTES and MPTMS, silanization agents, solvents ethanol (EtOH), toluene (T) and dimethyl sulfoxide (DMSO) were commercially obtained from Merck (KGaA, Darmstadt, Germany).

Surface modification studies of the zeolite were carried out by using different ratios (1:4, 1:5, 1:10, 1:40, 1:80 (w/v) in toluene, 1:4 in ethanol) of the silanization agent APTES. All samples are presented in Table 1. In order to obtain a zeolite-APTES 1:5 (w/v) ratio, initial 0.05 g amount of zeolite was weighed and dried in a moisture analyzer RADWAG MA 50.R (Bracka, Poland) at 105 °C. Then the zeolite was dispersed in 5 mL of toluene for 15 min in an ultrasonic water bath. Then, 250 µl of APTES was added dropwise to the mixture at 100 °C for 24 hours. To eliminate unbound silanization agents, it was centrifuged at 9000 rpm for 10 min, and washed 3 times. The amine-modified zeolite obtained after washing was dried using a vacuum oven at 50 °C. Other zeolite-APTES ratios were prepared by applying the same method.

The kaolin substrate surfaces were treated with different ratios of MPTMS silanization agent (1:3, 1:5, 1:10 (w/v) with/without DMSO). 1 g of kaolin was weighed and dried in a moisture analyzer at 105 °C. Kaolin was dispersed in 9 mL of DMSO and 1 mL of water at 60 °C for 10 days. DMSO expands the layers of kaolin (intercalation effect) and activates the more active -SH groups instead of -OH groups [15]. Then, this solution was brought to room temperature, the mixture was centrifuged at 9000 rpm for 10 min, and the washing process with toluene was repeated 5 times. It was dried in a vacuum oven at 50 °C. Dried kaolin (1 g) was treated with 5 mL of MPTMS at 150 °C for 2 days, in order to obtain a kaolin-MPTMS ratio of 1:5. Then, this solution was brought to room temperature, the mixture was centrifuged at 9000 rpm for 10 min, and the washing process with toluene was repeated 5 times. It was dried in a vacuum oven at 50 °C. To see the effect of DMSO, the same procedures were done without using DMSO. Other kaolin-MPTMS ratios were prepared by applying the same method.

Table 1. Ratios and abbreviations used in zeolite and kaolin surface modification

Component	Ratio	Abbreviation
Zeolite:APTES: EtOH	1:4	ZAE-4
Zeolite:APTES:T	1:4	ZAT-4
Zeolite:APTES:T	1:5	ZAT-5
Zeolite:APTES:T	1:10	ZAT-10
Zeolite:APTES:T	1:40	ZAT-40
Zeolite:APTES:T	1:80	ZAT-80
Kaolin:DMSO		KD
Kaolin:MPTMS: EtOH	1:5	KME-5
Kaolin:MPTMS:T	1:5	KMT-5
Kaolin:DMSO: MPTMS	1:3	KDM-3
Kaolin:DMSO: MPTMS	1:5	KDM-5
Kaolin:DMSO: MPTMS	1:10	KDM-10
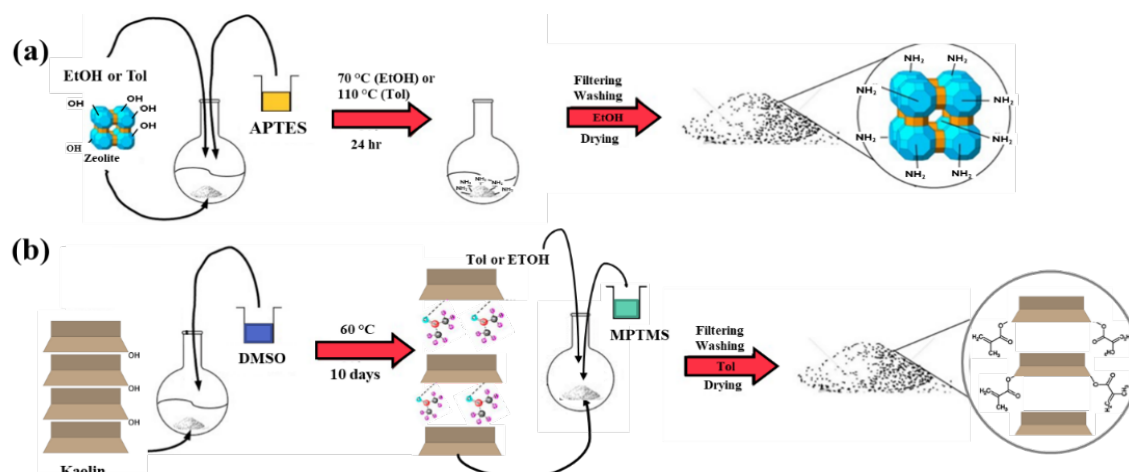
Figure 1. Scheme of modification of (a) zeolite with APTES and (b) kaolin with MTMS. The zeta potential measurement after the surface modification with MPTMS after DMSO intercalation showed that it increased up to -4.39 mV, but it did not increase in direct proportion to the MPTMS ratio.

Characterization

Zeta Potential Analysis

The zeta potentials (ζ potential) distribution for zeolite and kaolin by Zetasizer Nano ZS (Malvern Instruments, Worcestershire, UK) instrument with 4.0-mV He–Ne laser (633 nm) at 25 °C and scattering angle of 90° were measured. Samples suspensions were homogenized using an ultrasonic probe. Zeta potential distribution was determined with the help of the laser Doppler electrophoresis method. The analysis was repeated three times. The electrophoretic mobility of the particles is automatically calculated and converted into the zeta potential. The zeta potential measurements were performed in phosphate buffer solution (PBS).

Fourier Transform Infrared Spectrometric (FTIR) Analysis

FTIR spectroscopy was used to understand the effect of physicochemical methods on the surface chemistry of modified zeolite and kaolin. FTIR spectra were collected and recorded in the region of 650-4000 cm^{-1} on a FTIR spectrophotometer (IR Prestige-21, Shimadzu, Japan). Prior to analysis, modified zeolite and kaolin samples were placed in a vacuum oven at 50 °C for 24 hours and kept in a desiccator to avoid contact with air humidity.

Scanning Electron Microscopy (SEM)

SEM analysis will examine the surface morphologies and distribution of surface-attached polymer chains in composites. Au coating was applied for all samples before scanning.

Statistical Analysis

The results are presented as mean ± SD and the degree of statistical significance was calculated by t-test, considering a significance level at $p<0.05$.

RESULTS AND DISCUSSION

In the present study, zeolite and kaolin were modified with two different silanization agents, APTES and MPTMS, respectively, in different ratios and different solvent media for determining the optimum silanization agent ratio for further biomedicine applications. Different ratios used in surface modification were investigated successfully for surface modification of zeolite and kaolin. APTES modified zeolite and MPTMS modified kaolin were prepared following the procedure shown in Figure 1. For zeolite modifications, different ratios of APTES were prepared in toluene or ethanol and dried. On the other hand, kaolin was modified with MPTMS with or without DMSO to investigate the intercalation effect. The prepared materials were characterized by zeta potential, FTIR, and SEM analysis.

Zeta Potential Analysis

The value of the zeta potential is a sign of the surface charge and stability of a material that importantly affects the modification of the material. Besides, large values of zeta potential (above 30 mV positive values or below -30 mV negative values) indicate great electrostatic repulsive interplays between materials, meaning less agglomeration [16]. Zeta potential of APTES modified zeolites is shown in Figure 2(a). The zeta potential result of zeolite was -24.4 ± 1.22 mV. This is due to the hydroxyl (OH) groups on the surface of zeolites [17]. As a result of the modification of zeolites with APTES in ethanol and toluene, it was observed that the zeta potentials approached positive

-14.87 ± 0.47 and -7.23 ± 0.87 mV, respectively. It showed that the zeta potential results in the APTES modification with toluene had less negative value and thus more of the NH$_2$ group with a positive charge, which is consistent with the literature data. Therefore, it was decided to use toluene solvent for further modification. It was observed that the zeta potential of APTES modified zeolites is positive with the increase in the ratio of APTES (from -7.23 to +5.62 mV). Besides, it was observed that treatment of zeolites only in solvents without using APTES had little effect on their zeta potentials. Zeta potential value of zeolite in ethanol is -18.33 ± 0.87 and in toluene -17.53 ± 0.93 mV (data not shown).

The results of the zeta potentials of kaolin were examined, it was observed that kaolin has also a negative zeta potential due to the OH groups on the surface, such as zeolite. The zeta potential of KD appeared to be -27.2 ± 0.98 mV, which was due to the negative charges of the -SH groups of DMSO. The kaolin modifications without DMSO treatment were examined, it was observed that the zeta potentials of these samples increased negatively in the MPTMS modification in toluene and ethanol. Similarly to the zeolite sample, toluene was a more effective solvent for kaolin. The zeta potential measurement after the surface modification with MPTMS after DMSO intercalation showed that it increased up to -4.39 mV, but it was observed that it did not increase in direct proportion to the MPTMS ratio.

FTIR Analysis

Figure 3 shows the FTIR spectra of the zeolite and APTES-modified zeolites. The peaks at wavenumbers 673 and 960 cm^{-1} represent the symmetric stretching of Si–Al–O and symmetrical stretching Si-O groups present in the structure of the zeolite. The peak observed at 1655 cm^{-1} wavenumber
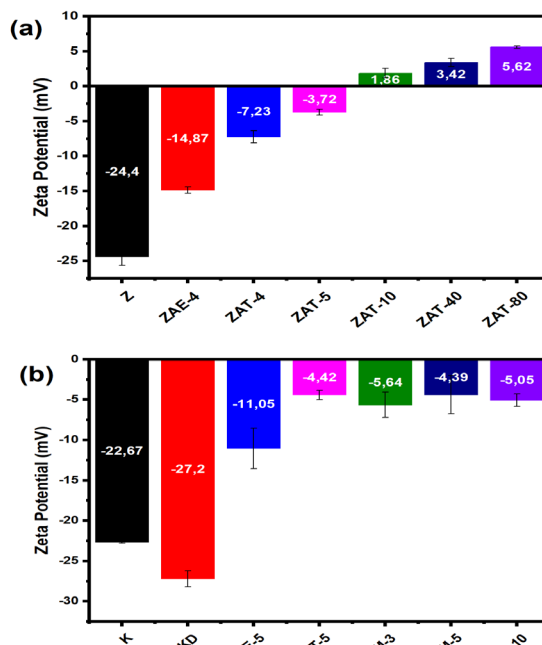
Figure 2. Zeta potential of (a) zeolite and (b) kaolin particles.

represents the –OH groups, bending vibration of physically adsorbed water molecules on zeolite surface. The wide peak at 3690-3200 cm^{-1} shows the -OH stretching vibration of the zeolite [19, 20]. Figure 3(a) represents the zeolite (Z), ZAE-4 and ZAT-4 FTIR spectra. One of the APTES, which was observed around 1644 cm^{-1}, is the peak belonging to the NH$_2$ group. This peak refers to "the N–H bending vibration of primary amine" in the aminopropyl group in the structure of APTES [21]. The peaks of aliphatic –CH, –CH$_2$, –CH$_3$ stretching vibrations appeared in the ZAT-5 sample at a wavenumber of 2930 cm^{-1}. The increased intensity of absorption peaks in the range of 1500–1300 cm^{-1}, representing the Si–CH$_2$ and Si–CH$_3$ stretching vibrations of silane groups, was successfully demonstrated in the
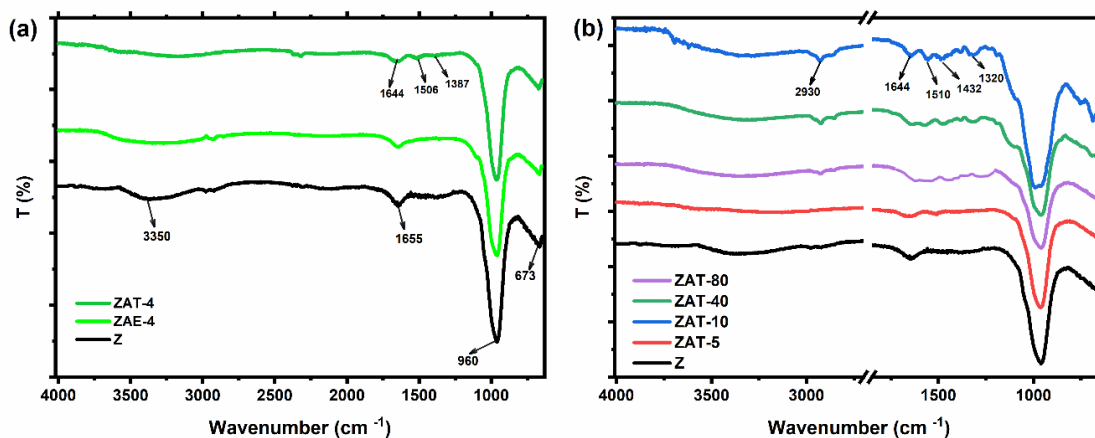
Figure 3. FTIR spectra of (a) zeolite modification in toluene and ethanol and (b) zeolite modifications at different APTES ratio.

ZAT-5 sample. This clearly shows that APTES on the surface of the zeolite binds successfully on ZAT-5 sample [22]. Therefore, it was determined to use toluene as an efficient solvent for further APTES modifications. Figure 3(b) shows the FTIR spectra of APTES zeolite samples at different ratios. It was observed that the characteristic peaks of APTES increased proportionally as the APTES ratio increased. The ZAT-10 sample is the first sample with a positive zeta potential and was chosen as the optimum ratio for APTES modification because it was the first sample to show that it was adequately modified with APTES in the FTIR spectra.

FTIR spectra of kaolin (K) and MPTMS modified kaolin are shown in Figure 4. Kaolin has Si tetrahedral and Al octahedral layers [8]. While the peaks observed at 3697, 3669 and 3653 cm^{-1} in the FTIR spectrum of kaolin indicate interlamellar hydroxyl (–OH) groups in the Al octahedral layers, the peak at 3618 cm^{-1} indicates hydroxyl groups in the intralamellar structure [15, 23]. Peaks observed at 1114, 1001, and 786 cm^{-1} wavenumbers indicate regular Si-O and Al-O bending vibrations in the kaolin structures and the poorly discrete peaks established to the Si-O stretching vibrations [24]. By intercalation of DMSO to kaolin, hydroxyl group peaks at 3697 and 3618 cm^{-1} were maintained, but the peak intensity at 3697 cm^{-1} decreased. Besides,

in Figure 4(b) new peaks were emerging in the FTIR spectrum of KD sample. Peaks at 3018 and 2936 cm^{-1} showed the stretching vibration absorption of –CH_3 groups and the peaks at 1433, 1401, 1394 and 1318 cm^{-1} were attributed to bending vibration in DMSO in the kaolin layers. All these results suggested hydrogen bond formation between the outer Al–OH of the kaolin layer and the S=O groups of DMSO molecules [23].

On the FTIR spectrum of KDM-5 sample, peaks for inter- and intralamellar hydroxyls groups were detected at 3699 cm^{-1}, and 3618 cm^{-1} while intralamellar hydroxyls peaks are not shown. The peak observed at 1720 cm^{-1} was attributed to C=O. Peaks at 2945 and 1470 cm^{-1} represent symmetric and asymmetric stretching of the CH_3 and CH_2 groups, respectively [15, 25]. All KDM samples were observed to be successfully modified with MPTMS silanization agent. However, the aforementioned peaks could not be observed in the samples modified without DMSO treatment like KTM-5 and KEM-5 (see Figure 4(a)). Similar to the zeta potential results, Figure 4(c) shows that the KDM-3, KDM-5 and KDM-10 samples have the same characteristic peak intensities. Therefore, KDM-3 was found with the optimum ratio for MPTMS modification of kaolin.
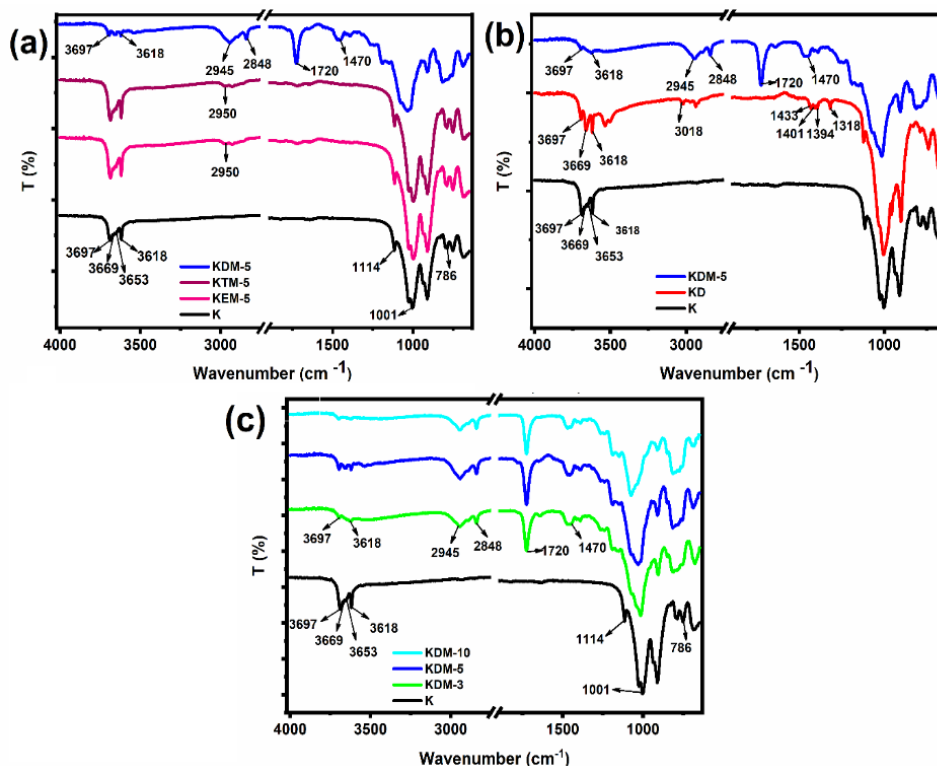
Figure 4. FTIR spectra of kaolin modification (a) in toluene, ethanol and only MPTMS (b) DMSO and MPTMS and (c) at different MPTMS ratios.

SEM Analysis

Figure 5 shows the SEM image of zeolite and ZAT-10 samples. The morphology of the zeolite was found to be irregular three-dimensional cubic structure with a diagonal length of about 4 μm. The morphology of the ZAT-10 particles was found irregular and asymmetric spherical-like shape rather than cubic shape. The zeolite surfaces were quite rough and discontinuous [26]. Aggregation was observed in both zeolite and ZAT-10. ZAT-10 tends to form larger aggregates due to new adhesive forces between the amine functional groups, compared to zeolites [27].
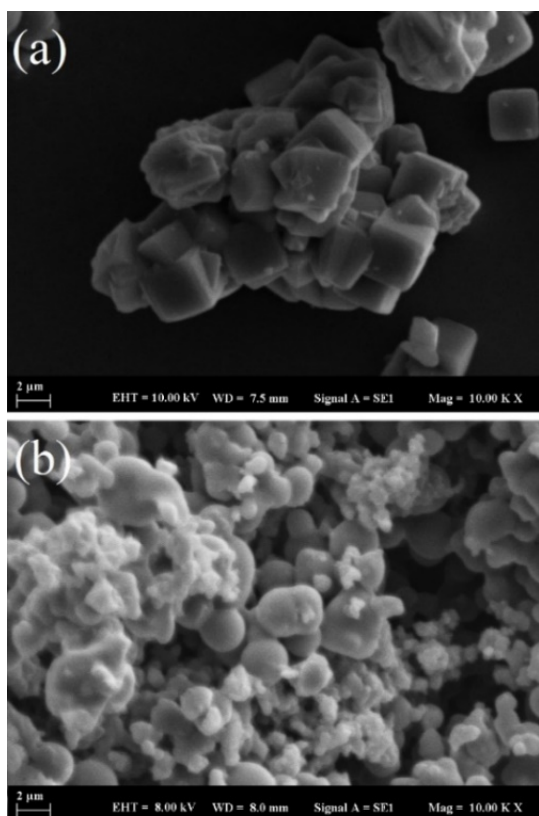
Figure 5. SEM images of (a) K and (b) KDM-5 samples

The morphology of the kaolin and KDM-5 particles was observed with SEM as illustrated in Figure 6. The structure of raw kaolin was proven to have platy, layered structure, and its morphology to be book-like in SEM images [28, 29]. After intercalation with DMSO and modification with MPTMS, adjacent layers were delaminated and distances between layers were expanded. In Figure 6(b), it is seen that the book-like kaolin is separated into layers and these particles are disordered and randomly dispersed [28]. Low zeta potential value of KDM-5 sample has allowed to adhere to particles themselves and caused aggregation.
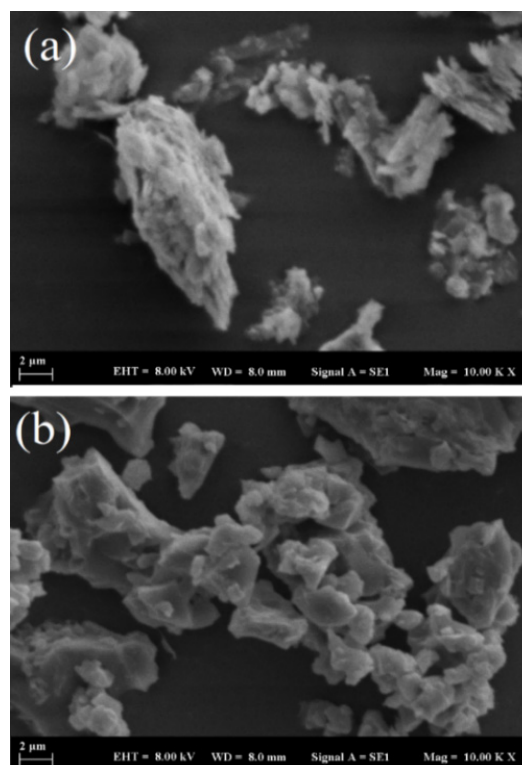
Figure 6. SEM images of (a) zeolite and (b) ZAT-10 samples

CONCLUSION

In summary, we introduced zeolite and kaolin modification with silanization agents, APTES and MPTMS, respectively. Samples were characterized using FTIR, SEM, and zeta potential analysis. In conclusion, the surfaces of zeolite and kaolin were successfully modified with silanization agents in toluene solution. Increasing concentration of APTES caused increased peak intensity, while by increasing concentration of MPTMS, intensity of peaks remained constant. The kaolin layered structures were delaminated by DMSO. The optimum ratio for modification of zeolite with APTES was found to be 1:10 (w/v), while for kaolin with MPTMS it was 1:3 (w/v).

REFERENCES

1. P. A. Jacobs, E. M. Flanigen, J. C. Jansen, H. van Bekkum, Introduction to Zeolite Science and Practice, Elsevier, Amsterdam, The Netherlands, 2001.
2. P. Terzioğlu, S. Yücel, M. Öztürk, *Water Sci. Technol.,* **75**, 358 (2017).
3. P. Terzioğlu, S. Yucel, *BioResources* **7**, 5435 (2012).

4. L. M. Jurkić, I. Cepanec, S. K. Pavelić, K. Pavelić, *Nutr. Metab. (Lond).,* **10**, 1 (2013).

5. H. B. Alam, Z. Chen, A. Jaskille, R. I. L. C. Querol, E. Koustova, R. Inocencio, R. Conran, A. Seufert, N. Ariaban, K. Toruno, P. Rhee, *J. Trauma - Inj. Infect. Crit. Care,* **56**, 974 (2004).

6. M. C. Neuffer, J. McDivitt, D. Rose, K. King, C. C. Cloonan, J. S. Vayer, *Mil. Med.,* **169**, 716 (2004).

7. J. K. Wright, J. Kalns, E. A. Wolf, F. Traweek, S. Schwarz, C. A. K. Loeffler, W. Snyder, L. D. Yantis, J. Eggers, *J. Trauma - Inj. Infect. Crit. Care,* **57**, 224 (2004).

8. M. Massaro, C. G. Colletti, G. Lazzara, S. Riela, *J. Funct. Biomater.,* **9**, 58 (2018).

9. C. S. J. Hurlbut, Dana's Manual of Mineralogy, 18th ed., John Wiley & Sons Ltd, New York, NY, USA, 1971.

10. D. J. A. Williams, K. P. Williams, *J. Colloid Interface Sci.,* **65**, 79 (1978).

11. M. E. Awad, A. López-Galindo, M. Setti, M. M. El-Rahmany, C. V. Iborra, *Int. J. Pharm.,* **533**, 34 (2017).

12. C. Wang, G. Zhang, Z. Li, Y. Xu, X. Zeng, S. Zhao, J. Deng, H. Hu, Y. Zhang, T. Ren, *Tribol. Int.,* **137**, 46 (2019).

13. D. Panda, S. K. Singh, E. Anil Kumar, in: Advances in Energy Research, Springer, Singapore, 2020, p. 541.

14. M. Aliofkhazraei, in: Handbook of Nanoparticles, Springer International Publishing, Switzerland, 2016.

15. B. F. Ferreira, K. J. Ciuffi, E. J. Nassar, M. A. Vicente, R. Trujillano, V. Rives, E. H. de Faria, *Appl. Clay Sci.,* **146**, 526 (2017).

16. I. S. Grover, S. Singh, B. Pal, *Appl. Surf. Sci.,* **280**, 366 (2013).

17. T. Kuzniatsova, Y. Kim, K. Shqau, P. K. Dutta, H. Verweij, *Microporous Mesoporous Mater.,* **1**–**3**, 102 (2007).

18. E. Tiryaki, Y. Başaran Elalmış, B. Karakuzu İkizler, S. Yücel, *J. Drug Deliv. Sci. Technol.,* **56**, 101517 (2020).

19. F. Jamshaid, M. R. Dilshad, A. Islam, R. U. Khan, A. Ahmad, M. Adrees, B. Haider, *Microporous Mesoporous Mater.,* **309**, 110579 (2020).

20. W. H. Flank, in: Molecular Sieves—II, ACS publications, 1977, p. 43.

21. I. A. Rahman, M. Jafarzadeh, C. S. Sipaut, *Ceram. Int.,* **35**, 1883 (2009).

22. L. D. Anbealagan, T. Y. S. Ng, T. L. Chew, Y. F. Yeong, S. C. Low, Y. T. Ong, C.-D. Ho, Z. A. Jawad, *Membr.,* **11**, 630 (2021).

23. H. Qu, S. He, H. Su, *Sci. Reports,* **9**, 1 (2019).

24. L. Domka, N. Stachowiak, A. Malicka, *Polish J. Chem. Technol.,* **10**, 5 (2008).

25. I. M. F. Lopes, K. Abersfelder, P. W. Oliveira, S. H. Mousavi, R. M. R. Junqueira, *J. Mater. Sci.,* **53**, 11367 (2018).

26. H. Li, J. Xu, J. Wang, J. Yang, K. Bai, J. Lu, Y. Zhang, D. Yin, *J. Membr. Sci.,* **471**, 84 (2014).

27. H. Sanaeepur, A. Kargari, B. Nasernejad, *RSC Adv.,* **4**, 63966 (2014).

28. H. Cheng, Q. Liu, J. Zhang, J. Yang, R. L. Frost, *J. Colloid Interface Sci,.* **348**, 355 (2010).

29. H. Wang, C. Li, Z. Peng, S. Zhang, *J. Therm. Anal. Calorim.,* **105**, 157 (2011).

Investigation of stability and activity of poly(ethylene-alt-maleic anhydride) copolymer at different pHs and in simulated body fluids

D. Ş. Daşdan

Yildiz Technical University, Department of Chemistry, İstanbul, Turkey

Poly(ethylene-alt-maleic anhydride) copolymers are used in various applications as emulsion stabilizers, detergent compositions, viscosity modifiers and drug delivery systems. This work aimed at determining the stability and activity of poly(ethylene-alt-maleic anhydride) copolymer (PEAMA) as drug carrier candidate at different pHs and in various artificial body fluid media such as 5% dextrose solution, PBS solution and 0.9% isotonic NaCl solution. To determine the stability of PEAMA, the polydispersity, particle size, mobility and zeta potential of PEAMA were measured at different pH values and in various artificial body fluid media *via* zetasizer. The activity of PEAMA was investigated at different pH values and in various artificial body fluid media based on the time effect by UV/VIS measurements. According to the obtained results, the optimum conditions of stability and activity of PEAMA copolymer were determined.

INTRODUCTION

Maleic anhydride (MA) copolymers have often been used as reactive macromolecules displaying various biological activities, such as direct antitumor effectors. The antitumor activity of these copolymers has been demonstrated to be dependent upon the amount of hydrogen bonding between carboxyl groups and the nature of their distribution on side chains. MA-containing copolymers, also known as polyanhydrides, the highly reactive anhydride ring on the MA portion can be bound by the ring-opening reaction to amino or hydroxyl groups of nucleophilic reagents resulting in either ester/carboxylic acid or amide/carboxylic acid structures. When the drug conjugate is being released, the carrier copolymer might display its own biological activity, in an increasing fashion, via the carbonyl groups that are freed [1-5]. The important copolymer of MA is poly(ethylene-alt-maleic anhydride) copolymer. Poly (ethylene-alt-maleic anhydride) (Scheme 1) is a nontoxic polyanhydride. It is a synthetic copolymer of maleic anhydride and is used as viscosity modifier for solution, suspension or emulsion, dispersing aid for insoluble solids and a wide variety of purposes in biotechnological applications. It is soluable in DMSO+water mixture [6]. Physicochemical properties such as particle size, surface charge and zeta potential of polymer-drug delivery systems are important parameters by the means of their interactions with plasma proteins [7-10].
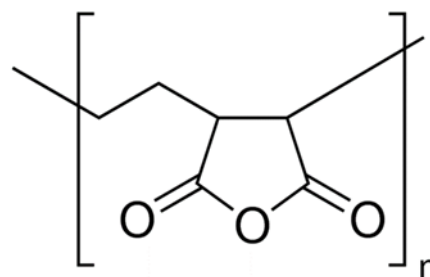
Scheme 1. Chemical structure of poly(ethylene-alt-maleic anhydride)

In the present work, zetasizer and UV/VIS measrements were used to determine the activity and stability of poly(ethylene-alt-maleic anhydride) at different pHs and in simulated body fluids.

EXPERIMENTAL

Poly(ethylene-alt-maleic anhydride, M_w =100,000-500,000 g/mol; T_g=235 °C), DMSO and phosphate buffer saline tablets (PBS) were purchased from Sigma-Aldrich. Dextrose 5 % and NaCl 0.9 % solutions were biological grade. The particle size and zeta potential of poly(ethylene-alt-maleic anhydride) at different pHs and in simulated body fluids such as % 5 dextrose, 0.9 % isotonic NaCl and PBS solutions were measured *via* Brookhaven 90 Plus/BI-MAS (Multi Angle Particle Sizing) and Brookhaven Zeta Potential Analyzer. The controlling activity of poly(ethylene-alt-maleic anhydride) at different pHs and in simulated body fluids such as 5 % dextrose, 0.9 % isotonic NaCl and PBS solutions were checked by Shimadzu UV mini-

* To whom all correspondence should be sent:
E-mail: dolunaykar@yahoo.com

1240 spectrometer. PEAMA forms a gel in water. Because of this, to prepare homogenous solutions, PEAMA solutions were prepared by dissolving in 5 % DMSO (v/v) and diluting with water.

RESULTS AND DISCUSSION

The stability and activity of PEAMA solutions, prepared at different pH values, were measured with a Zetasizer and a UV/Vis spectrophotometer, respectively.

Zetasizer measurements of polydispersity, particle size, mobility and zeta potential of PEAMA give the stability information in aqueous solution and were done *via* Zetasizer at different pHs. The zetasizer measurements results of PEAMA at different pHs are given in Table 1.

Table 1. Zetasizer measurements of PEAMA at different pHs

pH	PDI	Particle size (nm)	Mobility	Zeta Potential (mV)
2	0.333	350	-2.99	-38.24
3	0.361	465	-3.03	-38.79
4	0.372	900	-2.99	-38.30
5	0.467	880	-2.98	-38.11
6	0.377	1220	-3.00	-38.38
7	0.385	1370	-2.95	-37.78
8	0.395	1110	-2.97	-38.06
9	0.320	1425	-2.99	-38.22
10	0.354	1300	-3.03	-38.76
11	0.422	1170	-3.02	-38.60
12	0.385	1100	-3.02	-38.62

The particle size distribution of PEAMA at different pHs was found to be between 0.3 and 0.4. It means that PEAMA particles at different pHs are monodisperse and show homogenous dispersion. The particle size of PEAMA varies between 300 and 1400 nm with increasing pH. The PEAMA particles at different pHs were negatively charged and preserved their stability because of higher zeta potential values as about 39 mV. No aggregation or coagulation of PEAMA particles in solutions of different pH was seen.

The activity and stability of PEAMA at different pHs were checked by UV/VIS spectrometry and the spectrum is given in Fig. 1.

The activity and stability of PEAMA particles at the studied pHs were controlled at 230 nm. The activity and stability of PEAMA particles did not change and they continued their activity and stability at all pHs.
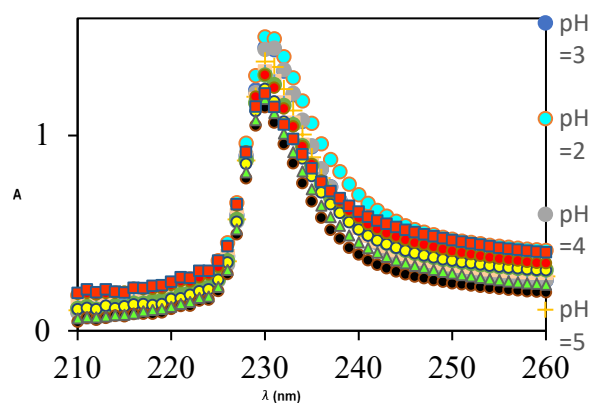
Fig. 1. UV/VIS spectrum of PEAMA at different pHs

The zetasizer measurement results of PEAMA in 5 % dextrose solution as a function of time are given in Table 2.

Table 2. Zetasizer measurements of PEAMA in 5 % dextrose solution as a function of time

Time	PDI	Particle size (nm)	Mobility	Zeta Potential (mV)
0	0.190	595	-3.03	-38.79
15 min	0.314	465	-2.99	-38.24
30 min	0.268	500	-2.99	-38.31
1 h	0.311	480	-2.98	-38.11
2 h	0.277	520	-3.00	-38.38
3 h	0.290	465	-2.95	-37.78
1 d	0.179	630	-3.03	-38.79
2 d	0.154	610	-2.95	-37.78
1.w	0.226	615	-3.03	-38.79
2.w	0.207	570	-3.03	-38.79
3.w	0.265	585	-3.03	-38.79
4.w	0.246	575	-3.03	-38.79

PEAMA particles in 5 % dextrose solution were highly monodisperse because of PDI values between 0.1 and 0.2. The particle size of PEAMA changed between 400 and 600 nm with time. The PEAMA particles in 5 % dextrose solution were negatively charged and preserved their stability because of higher zeta potential values as about 39 mV. No aggregation or coagulation of PEAMA particles in %5 dextrose solution as a function of time was seen.

The activity and stability of PEAMA in 5 % dextrose solution were monitored by UV/VIS and the spect The activity and stability of PEAMA particles in 5 % dextrose solution were checked by consideration of the 230 nm peak. The activity and stability of PEAMA particles did not change and they continued their activity and stability in 5 % dextrose solution up to 4 weeks.

The activity and stability of PEAMA in 5 % dextrose solution were monitored by UV/VIS and the spectrum is given in Fig. 2.
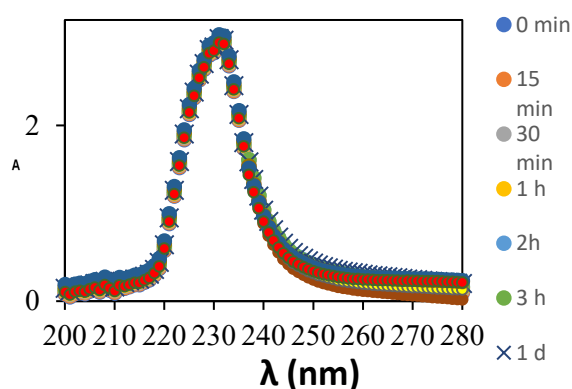
Fig. 2. UV/VIS spectrum of PEAMA in 5 % dextrose solution as a function of time

The zetasizer measurement results of PEAMA in PBS solution as a function of time are given in Table 3.

Table 3. Zetasizer measurements of PEAMA in PBS solution as a function of time

Time	PDI	Particle size (nm)	Mobility	Zeta Potential (mV)
0	0.409	740	-3.03	-38.79
15 min	0.419	1100	-2.99	-38.24
30 min	0.400	1080	-2.99	-38.31
1 h	0.392	1045	-2.99	-38.11
2 h	0.434	1035	-2.95	-38.78
3 h	0.404	925	-2.98	-37.10
1 d	0.391	825	-3.03	-38.79
2 d	0.398	470	-3.03	-37.79
1.w	0.377	440	-3.03	-38.79
2.w	0.414	580	-2.98	-38.19
3.w	0.404	645	-2.95	-38.79
4.w	0.375	665	-3.03	-38.79

PEAMA particles in PBS solution as a function of time were monodisperse because of PDI changing between 0.3 and 0.4. The particle size of PEAMA changed and bigger particles started to form after 15 min. After 2 h, the size of the PEAMA particles started to decrease from 3 h to 4 w. The PEAMA particles in PBS solution were negatively charged and preserved their stability because of higher zeta potential values as about 39 mV. No aggregation or coagulation of PEAMA particles in PBS solution was seen as a function of time.

The activity and stability of PEAMA in PBS solution were monitored by UV/VIS and the spectrum iss given in Fig. 3.
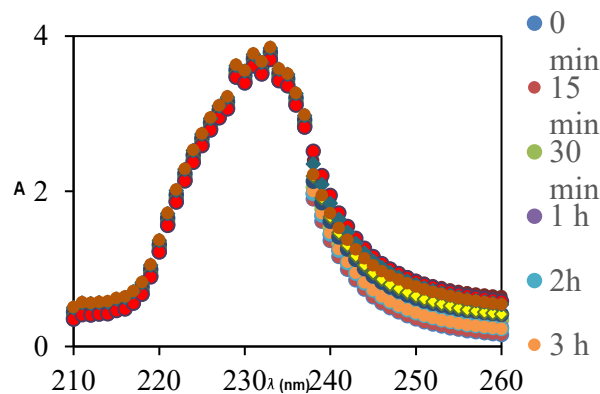
Fig. 3. UV/VIS spectrum of PEAMA in PBS solution as a function of time

The activity and stability of PEAMA particles in PBS solution were checked by consideration of the 230 nm peak. The activity and stability of PEAMA particles did not change and they continued their activity and stability in PBS solution up to 4 weeks.

The zetasizer measurement results of PEAMA in isotonic NaCl solution (0.9 %) as a function of time are given in Table 4.

Table 4. Zetasizer measurements of PEAMA in isotonic NaCl solution as a function of time

Time	PDI	Particle size (nm)	Mobility	Zeta Potential (mV)
0	0.342	185	-3.00	-38.42
15 min	0.344	200	-2.99	-38.30
30 min	0.311	175	-3.03	-38.79
1 h	0.346	240	-2.99	-38.24
2 h	0.361	250	-2.98	-38.13
3 h	0.366	250	-2.97	-37.98
1 d	0.343	200	-3.03	-38.79
2 d	0.363	240	-2.98	-38.11
1.w	0.339	250	-2.99	-38.25
2.w	0.362	255	-2.99	-38.24
3.w	0.359	245	-2.98	-38.11
4.w	0.354	250	-3.03	-38.79

PEAMA particles in isotonic NaCl solution as a function of time were monodisperse. The particle size of PEAMA in isotonic NaCl solution was about 200 nm. The PEAMA particles in isotonic NaCl solution were negatively charged and preserved their stability because of higher zeta potential values as about 39 mV. No aggregation or coagulation of PEAMA particles in isotonic NaCl solution as a function of time was seen.

The activity and stability of PEAMA in isotonic NaCl solution were monitored by UV/VIS and the spectrum is given in Fig. 4.
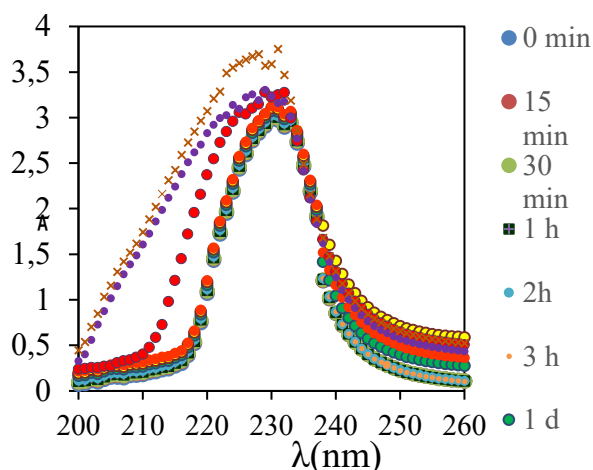
Fig. 4. UV/VIS spectrum of PEAMA in isotonic NaCl solution as a function of time

The activity and stability of PEAMA particles in isotonic NaCl solution was checked by consideration of the 230 nm peak. The activity and stability of PEAMA particles did not change and they continued their activity and stability in isotonic NaCl solution up to 4 weeks.

CONCLUSIONS

The stability and activity of PEAMA particles at different pHs and in simulated body fluids were determined *via* zetasizer and UV/VIS measurements. It was determined that PEAMA particles at different pHs and in simulated body fluids were negatively charged, monodisperse and preserved their activity and stability up to 4 weeks without any aggeragation and coagulation. According to the obtained results, it was concluded that PEAMA copolymer was a suitable candidate for drug delivery systems in all pH ranges and simulated body fluids.

REFERENCES

1. I. Popescu, D. M. Suflet, I. M. Pelin, G. C. Chitanu, *Rev. Roum. Chim.*, **56**, 173 (2011).
2. Z. M. Rzaev, *Journal of Polymer Science Part A: Polymer Chemistry*, **37**, 1095 (1999).
3. A. Boztuğ, S. Basan, *Journal of Materials Science*, **39**, 6843 (2004).
4. H. K. Can, Ö. A. Gürpinar, M. A. Onur, Z .M. Rzaev, A. Güner, *Journal of Applied Polymer Science*, **115**, 1366 (2010).
5. R. B. Seymour, F. F. Harris, I. Branum, *Industrial & Engineering Chemistry*, **41**, 1509 (1949).
6. D.-L. Fang, Y. Chen, B. Xu, K. Ren, Z.-Y. He, L-L. He, Y. Lei, C.-M. Fan, X.-R. Song, *Int. J. Mol. Sci.*, **15**, 3373 (2014).
7. S. Honary, F. Zahir, *Tropical Journal of Pharmaceutical Research*, **12** (2), 265 (2013).
8. D. S. Dasdan, A. Dizdar, G. Karakus, *Bulg. Chem. Commun.*, **49**, Special Issue 1, 43 (2017).
9. J. A. C. Barbosa, M. S. E. Abdelsadig, B. R. Conway, H. A. Merchant, *International Journal of Pharmaceutics,* **X**(1), 1, 100024 (2019).
10. D. Putnam, C. A. Gentry, W. P. Daniel, R. Langer, *Proceedings of National Academy of Sciences of the United States of America*, **98**(3), 2001.
11. D. S. Dasdan, G. Tosun, Y. Karahan, *Bulg. Chem. Commun.*, **50**, Special Issue 1, 5 (2018).

Thermal analysis and isoconversional kinetic study of thermal decomposition of polycyclohexene oxide polystyrene (PCHO-PST) comb-shaped polymer

H. Dolas[1*], N. Genli[2]

[1]Harran University, Hilvan Vocational School, Program of Occupational Health and Safety, Sanliurfa 63900, Turkey
[2]Dicle University, Diyarbakir Vocational School of Technical Sciences, Chemical and Chemical Processing Technologies, Diyarbakır, 21280, Turkey

In this study we aimed to investigate the thermal and the kinetic parameters of the thermal decomposition reaction of poly cyclohexene oxide polystyrene (PCHO-PSt) comb-shaped polymer. The polymer of epoxy end-functionalized polystyrene was synthesized by atom transfer radical polymerization (ATRP) and the glass transition of polystyrene present as a unit in the polymer was determined. The thermal characteristics of the polymer were evaluated through thermal analysis, differential thermal analysis (DTA), thermogravimetric analysis-derivative thermogravimetry (TG-DTG) under nitrogen atmosphere at 3, 5, 7 and 10 ºC min^{-1} from 30 ºC to 600 ºC. The obtained results were supported by differential scanning calorimetry (DSC). The glass transition of the PCHO-PSt was seen at 79 ºC. The crystallization and melting temperatures of the PCHO-PSt were determined as 142 and 240 ºC, respectively. The polymer decomposition was seen in the range of 320-350 ºC depending on the heating rate. Based on the isoconversional method, the activation energy was calculated by the free model approach of the Ozawa-Flynn-Wall method (OFW). The highest activation energy was found as 160.82 kJmol^{-1} at 30% conversion. It was found that the activation energy decreased as conversion increased.

Keywords: Comb-shaped polymer, TGA-DTA, DSC, Pyrolysis, Activation energy

INTRODUCTION

The polymers bearing an end-functional group are important because of their use as forerunners of block and graft polymers. Atom transfer radical polymerization (ATRP) method was preferred to synthesize these polymers because of its easy experimental setup, use of inexpensive catalyst, without the formation of side products. Also, the polymers synthesized using ATRP have been used for coating and adhesives, in medical and environmental fields.

The reaction kinetics gives information about the durability and decomposition temperature of a polymer under various thermal conditions [1]. To determine the kinetic data of polymer decomposition, thermal analysis methods are generally used. Thermogravimetric-differential thermal analysis (TG-DTA), as well as differential scanning calorimetry (DSC) are counted in among these methods. Mostly, in the evaluation of data these methods are performed together as they complete each other. Measurements are based on the weighing of the polymer mass with time in TG analysis (TGA). The temperature is different between a reference material and the worked material. In DTA this difference is quantified as a function of temperature or time and is given in related plots as heat flow. In this way, we can get information about the heat absorbed or emitted by a chemical system by determining DTA data.

DSC data are utilized for determination of the crystallization temperature (T_c), the melting point (T_m), the heat of fusion (ΔH_f), the heat of crystallization (ΔH_c), and glass transition (Tg) of polymers. Also, DSC may be performed to determine the unique features of particular polymers, polymer additives that show thermal transitions and polymer alloys. Some materials do not show a net transition case as they are heated. In this case they are present in glassy state. This state is seen in amorphous materials, named as glass transition [2].

Kinetics

The decomposition mechanism of a polymer or a composite can be impossible to understand and it can't be solved in this situation. Isoconversional methods are suggested to study the kinetics of a non-isothermal process [3]. In isoconversional method, it is assumed that the basic kinetic equation for solid state decomposition reaction is a function of temperature and conversions [4]. This case can be expressed by:

$$\frac{d\alpha}{dt} = k(T)f(\alpha) \qquad (1)$$

---

* To whom all correspondence should be sent:
E-mail: hacerdolas@hotmail.com,
        hacerdolas@harran.edu.tr

In here f(α) is the conversion function, α is the degree of conversion. A temperature dependence of the rate constant is expressed by k(T). The Arrhenius equation means this dependence as follows:

$$k(T) = A exp\left(-\frac{E_a}{RT}\right) \qquad (2)$$

As known, the R, T, A and E terms in the equation mean universal gas constant, temperature, pre-exponential factor and energy of activation, respectively. Then Eqn. 1 can be rewritten as:

$$\frac{d\alpha}{dt} = A exp\left(-\frac{E_a}{RT}\right) f(\alpha) \qquad (3)$$

As Eqn. 3 can be difficult to measure accurately, the temperature dependence in Eqn. 3 can be rewritten as:

$$\beta\frac{d\alpha}{dT} = A exp\left(-\frac{E_a}{RT}\right) f(\alpha) \qquad (4)$$

where $\beta = \frac{T-T_0}{t} = \frac{dT}{dt} = constant$ is the linear heating rate in C°/min.

In the literature, many researchers have investigated the thermal decomposition processes of polymers and ligands [5, 6]. Kinetic parameters such as A and E were determined by kinetic methods such as Kissinger and Crane and Ozawa–Flynn–Wall. These methods are isoconversional. During applying the methods, conversion was constant, temperature was not. Sahin *et al.* [7] investigated the thermal decomposition of derivatives of boron using Coats-Redfern thermal analysis. Recently, researchers prepared nanocomposites from polymer-nanoparticles couples such as polystyrene (PS)-ZnO [8] and polyethylene-graphene [9] and the thermal stability of these nanocomposites was investigated and the influence of nanoparticles was reported. TG-DTA data were used to evaluate the results during the investigation of these properties of nanocomposites.

In this study, the thermal decomposition of the PCHO-PSt comb-shaped polymer bearing epoxy end-functionalized polystyrene and the change in Tg of PSt when it was used as a unit of the polymer were investigated.

EXPERIMENTAL

Material and methods

Calcium hydride (CaH$_2$) was used to distill cyclohexene oxide (CHO) and styrene (St) and they were held at +4 °C in an atmosphere of nitrogen before the process. Also, in the process compounds

such as pyridine, CuBr, 3-chloroperoxybenzoic acid, 2-bromopropanoyl bromide, sodium bicarbonate (NaHCO$_3$) and 3-cyclohexene-1-methanol were used. The polymerization was carried out *via* ATRP. Dichloromethane (CH$_2$Cl$_2$) was used as a solvent. In this stage chemicals such as diphenyliodonium hexafluorophosphate (Ph$_2$I$^+$PF$_6^-$), and 2,2–bipyridine were used in the radical polymerization and the selected photoinitiator was 2,2-dimethoxy-2-phenyl acetophenone (DMPA) (Irgacure 651). All chemicals were used as received without further purification.

Synthesis

The cyclohexene oxide end-functional macro monomer of polystyrene (CHO-PSt) and its polymer, (PCHO-PSt comb-shaped polymer) were synthesized by atom transfer radical polymerization according to our previous study [10]. Synthesis route is given in Scheme 1.
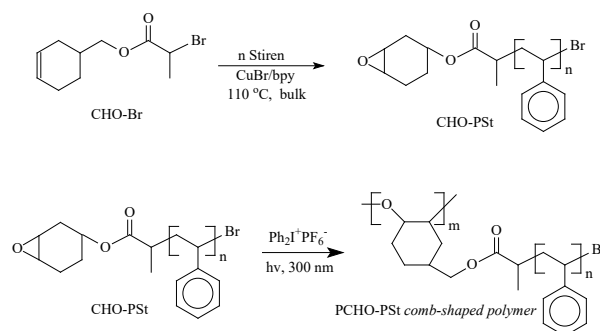
Scheme 1. Synthesis route of the PCHO-PSt comb-shaped polymer

Based on this, firstly the condensation of 3-cyclohexene-1-methanol with 2-bromopropanoyl bromide was carried out for the synthesis of the 3-cyclohexenylmethyl-2-bromopropanoate. Subsequently, to obtain the epoxy end-functional initiator as used in ATRP, epoxidation of the obtained 3-cyclohexenylmethyl-2-bromopropanoate was performed using 3-chloroperoxybenzoic acid. The macro monomer of polystyrene with an epoxy end group was obtained by means of this initiator in conjunction with the cuprous complex Cu(I)Br/bipyridine with styrene (St) in bulk at 110 °C. The obtained CHO end-functional macro monomers were used as precursors in the photoinitiated cationic polymerization.

TG-DTA experiments

The thermal characteristics of PCHO-PSt comb-shaped polymer decomposition were recorded on a DTG-60H Simultaneous DTA-TG apparatus (SHIMADZU Scientific Instruments Incorporated,

Kyoto, Japan). The sample was weighed in the range of 4-5 mg in a platinum pan including alumina (α-alumina (α-Al$_2$O$_3$) powder for DTA Standard Material). TGA experiments were performed in the range of 30 °C-600 °C at the heating rates of 3, 5, 7 and 10 °C min^{-1}, atmosphere conditions were a flow rate of 20 mL min^{-1} of the nitrogen gas. In DSC tests a method consisting of heating or cooling the polymer was applied in inert gas media at a certain flow rate and at a certain heating/cooling rate based on ASTM D:3417-99 and ASTM D:3418-03. In the DSC test the amount of used compound was 10-11 mg, heating program was from 20 °C to 280 °C for 1st heating and holding at 280 °C for 5 min, cooling from 280 °C to -100 °C and holding at -100 °C for 5 min, then from -100 °C to 280 °C for 2nd heating. Heating rate was 10 °C min^{-1} at a flow rate of 50 mL min^{-1} of nitrogen gas.

RESULTS AND DISCUSSION

In the TGA stage, 3, 5, 7, and 10 °C min^{-1} as heating rates were selected and TG curves were obtained in the range of 30-650 °C. Derivative thermogravimetric (DTG) curves were formed by taking the derivation of TG curves. The TGA and DTG curves of PCHO-PSt comb-shaped polymer decomposition are shown in Fig. 1.

As is seen, the initial mass loss temperature was shifted from 316.07 °C at 3 °C min^{-1} to 343.71 °C at 10 °C min^{-1} (Fig. 1a). It was thought that the mass loss ended up at 409.11 °C and 452.92 °C for 3 °C

min^{-1} and 10 °C min^{-1}, respectively. During the decomposition, the uniform peak observed in Fig. 1 b, illustrated the DTG curve. The maximum mass loss rate was shifted to higher temperature. So, the temperature was 398.45 °C for 10 °C min^{-1}, while it was 370.74 °C for 3 °C min^{-1}. The thermal decomposition of the PCHO-PSt comb-shaped polymer started at a higher temperature, as heating rate was increased. This phenomenon can be attributed to the distribution of the heat in the polymer, which may decrease by the higher heating rate.

To see the phase transitions of PCHO-PSt comb-shaped polymer, DTA was performed at different heating rates within the range of 30-650 °C. Fig. 2a illustrates the obtained DTA curves at related heating rates.

According to graphs an endothermic peak was observed at 88 °C, which belonged to the glassy transition. This transition was clearly confirmed from the DSC graph (Fig. 2b). On the DTA graph in the range of 161 °C - 243 °C a change in endothermic energy was observed. This thermal change may be described as the melting transition due to no considerable mass loss in this temperature range of the TGA curve (Fig. 1a), referring to the reported melting point (T$_m$) range of polystyrene (PSt) [11]. The Tg and Tm values were shifted to lower values due to the epoxy group presence in the polymer chain and the comb shape of the polymer.
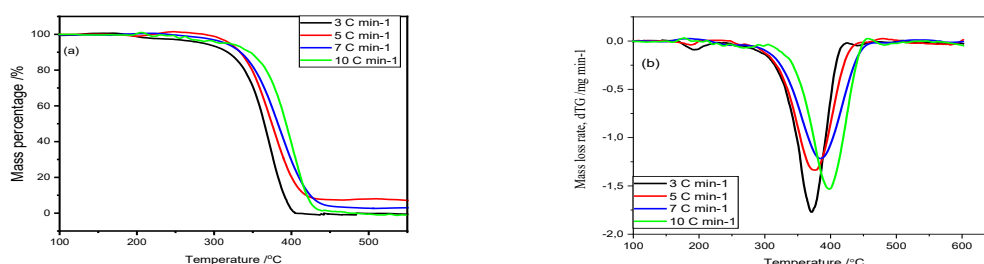
Fig. 1. TGA (a) and DTG (b) curves of the PCHO-PSt comb-shaped polymer at 3, 5, 7, and 10 C min^{-1}
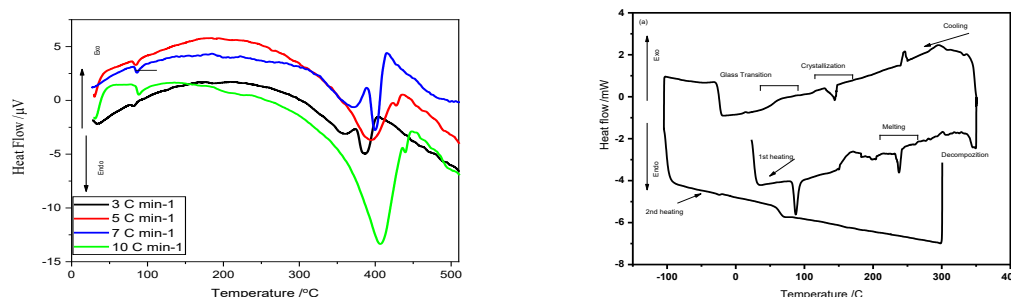
Fig. 2. Graphs of (a) DTA curves, **(b)** DSC curves of the PCHO-PSt comb-shaped polymer (amount: 10 mg; temperature: 350/-100 °C; gas flow rate: 50 mL min^{-1} and heating/cooling rate: 10 °C min^{-1})

In the DTA curves observed exothermic and endothermic physical transitions took place due to the thermal history of the polymer, which are attributed to crystallization and melting, respectively. For the determination of the net values of these transitions it is necessary to evaluate the DSC cooling curve because the polymer was present at steady and pure situation after the 1st heating.

Fig. 2b illustrates the DSC curves of the polymer during 1st heating, cooling, and 2nd heating processes. The 1st heating was important as showing the thermal history of the polymer. So, glassy transition (Tg) region was seen at the range of 78-90 °C. The region was seen at lower temperature, compared with literature [2]. This may be caused by the effect of other units in the polymer chain on the PSt unit as a plasticizer.

From the graph an exothermic change is observed from 173.62 °C to at 199.73 °C. From the TG curve this change was identified as crystallization because of lack of mass loss in the temperature range. so, the area under this range, that is crystallization enthalpy, was calculated as 9.7 J g^{-1} and a DSC peak was read as 184.95 °C. This value conformed with the literature for thermal crystallization [12]

The melting started at 217 °C and ended at 250.62 °C. The area under this range, that is fusion enthalpy, was calculated as 16.29 J g^{-1} by the DSC software. And the polymer was decomposed at 321.65 °C. During this phenomenon the absorbed heat from the medium was calculated as 532.86 J g^{-1}.

The glass transition peak can be observed in both TG and DSC curve. Crystallization and melting peaks were monitored in TG and DTA and DSC. In adition to glass transition, crystallization and melting, starting of decomposition can be seen from the graph as about 320-350 °C from the curves.

Kinetic parameters calculation of PCHO-PSt comb-shaped polymer decomposition.

To use the kinetic equation, the solution of Eqn. 5 integration is primarily necessary [13]:

$$\int_0^\alpha \frac{d\alpha}{f(\alpha)} = g(\alpha) = A\beta^{-1} \int_0^T exp\left(-\frac{E}{RT}\right) dT \qquad (5)$$

The Doyle [14] approximation was one of the used approaches for the solution of the integration. The Ozawa-Flynn-Wall (OFW) [15, 16] method was derived by applying Doyle approaches for the temperature integral in Eqn. 5, respectively. For the OFW method:

$$g(\alpha) = \left(\frac{A}{\beta}\right) 0.00484 exp\left(-1.052\frac{E}{RT}\right) \qquad (6)$$

Eqn. (7) is obtained by rearranging the natural logarithmic Eqn. (6):

$$ln(\beta) = ln\left(\frac{AE}{Rg(\alpha)}\right) - 5.331 - 1.052\frac{E}{RT} \qquad (7)$$

To obtain the activation energy (E) by using this method, firstly, the graphs including regression lines of ln (β) *versus* T^{-1} were formed at different heating rates and different conversions, separately. Then, the energy values were calculated from the slope of each regression line. In our study, to determine the kinetic parameters of PCHO-PSt comb-shaped polymer decomposition, Ozawa-Flynn-Wall methods (OFW) was selected as isoconversional method. To draw the related graphs eight conversions from 20% to 90% with an increment of 10 were used for kinetic calculation. Related temperature for each conversion was read from the TGA curve. Thus, the formed regression lines according to this information are presented in Fig. 3a. According to the graph the parallel lines were attributed to a single decomposition mechanism or a combination of many reactions.

The correlation coefficient (R) referring to the accuracy of data and the activating energy (E$_A$) were calculated from the slope of the related regression line for each conversion. The graph of the calculated activation energy values and the slope of the lines *versus* conversion is given in Fig. 3b, R is listed with other values in Table 1.

As seen from the figure, the highest activating energy is at 30% conversion as 160.82 kJmol^{-1}. Then, the change in activation energy with conversion was trending a decrease as conversion was increasing. The cause of this might be the decreasing at molecule count to react. This result conformed with literature [5].

Table 1. Slope, R and E values calculated by the OFW method

α (%)	Slope	R	E (kJ mol^{-1})
20	18.972	0.9985	149.14
30	20.349	0.9841	160.82
40	18.538	0.9854	146.50
50	18.547	0.9921	146.79
60	17.401	0.9991	137.52
70	17.662	0.9995	139.58
80	15.451	0.9974	122.11
90	15.694	0.9611	124.03
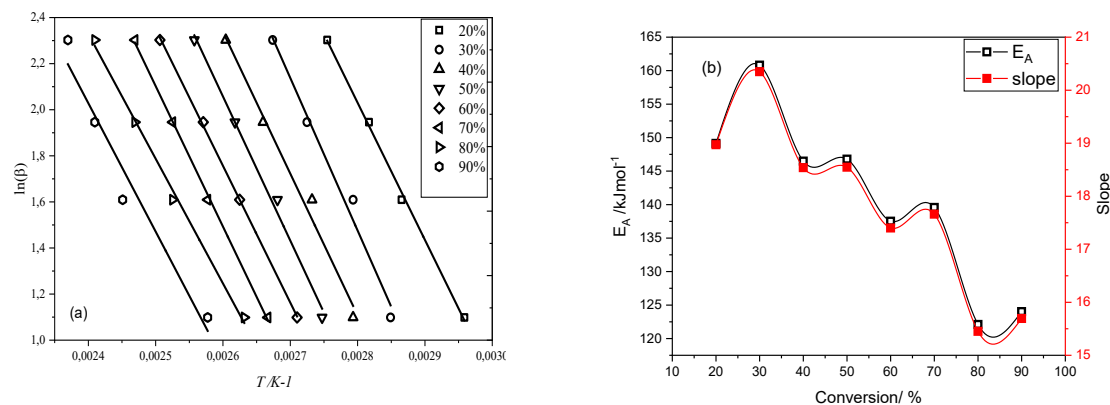
Fig. 3. (a) Regression lines to the decomposition of PCHO-PSt comb-shaped polymer based on OFW method at 3, 5, 7 and 10 C min^{-1} and (b) Activation energy changing with conversion calculated by the OFW method.

CONCLUSIONS

In this study, the thermal characteristics and activation energy calculation of PCHO-PSt comb-shaped polymer decomposition were evaluated through TGA. The initial mass loss temperatures were observed in the higher temperature region as the the heating rate, as well as the maximum value of the mass loss rate increased. In the DTA curves the temperature range of the glass transition, crystallization and melting of the polymer were determined. So, the polymer started freezing at 245 $^{\circ}$C (melting region during heating) and crystallized at 149-132 $^{\circ}$C. The glass transition was shifted to 67-70 $^{\circ}$C due to cooling. These results conformed with TG.

From the graph an exothermic change was observed from 173.62 $^{\circ}$C to 199.73 $^{\circ}$C. From the TG curve this change was identified as crystallization because of lack of mass loss in the temperature range. The melting started at 217 $^{\circ}$C and ended at 250.62 $^{\circ}$C. The area under this range, that is fusion enthalpy, was calculated to be 16.29 J g^{-1} by DSC software. The polymer was decomposed at 321.65 $^{\circ}$C. During this phenomenon the absorbed heat from the medium was calculated as 532.86 J g^{-1}. To calculate the activation energy, the OFW method was selected and the value of the average activation energy deducted from the method was 140.81 kJ mol^{-1}. The maximum activation energy achieved was 160.82 kJ mol^{-1} at 30% conversion.

REFERENCES

1. S. A. El–Sayed, M. E. Mostafa, *Energy Convers. Manage.*, **8,** 165 (2004).
2. C. J. Dyre, *Reviews of Modern Physics*, **78(3),** 953 (2006).
3. R. Ebrahimi-Kahrizsangi, M. H. Abbasi, *Trans. Nonferrous Met. Soc. China*, **18,** 217 (2008).
4. M. E. Brown, D. Dollimore, A. K. Galwey, Comprehensive chemical kinetics, Elsevier, Amsterdam, vol. **22,** 1980.
5. O. Sahin, E. Tas, H. Dolas, *Journal of Thermal Analysis and Calorimetry,* **89,** 123 (2007).
6. L. Na, Z. Xingke, Y. Junrong, W. Yan, Z. Jing, H. Zuming, *Journal of Thermal Analysis and Calorimetry,* **140**, 283 (2010).
7. O. Sahin, E. S. Cennetkusu, H. Dolas, M. Ozdemir, *Thermochimica Acta*, **440,** 7 (2006).
8. H. F. Ashraf, F. A. N. Abdullah, A. M. Shehab, *Polymers*, **12,** 1935 (2020).
9. J. Iman, S. Mohamadreza, K. Fatemeh, R. Seeram, A. Ehsan, S. T. Ying, K. Mohammadreza, A. Majid, S. A. Ahmad Ramazani, M. Omid, R. G. Erfan, *Molecules*, **26**, 1597 (2021).
10. D. Mustafa, I. Oner, A. Aslisah, G. Nasrettin, *Reactive & Functional Polymers*, **70**, 28 (2010).
11. J. R. Wunsch, Polystyrene-Synthesis, Production and Applications. Simithers Rapra Publishing, p. 15. ISBN 978-1-85957-191-0. 2000; Retrieved 25 July 2012.
12. E. Petrillo, R. Russo, C. D'aniello, V. Vittoria, *J. Macromolecule Sci.-Phys.* B37, **1**, 15 (1998).
13. P. Šimon, P. S. Thomas, J. Okuliar, A. Ray, *J. Therm. Anal. Cal.,* **72,** 867 (2002).
14. C. D. Doyle, *J. Appl. Polym. Sci.,* **6,** 639 (1967).
15. J. H. Flynn, L. A. Wall, *Polym. Lett.,* **4,** 323 (1966).
16. T. Ozawa, *Bull. Chem. Soc. Jpn.*, **38**, 1881 (1965).

Preliminary investigation into the synthesis and characterisation of single nucleotide polymorphs of human glutathione-*S*-transferase class PI

S. Mathura

University of the Witwatersrand, Johannesburg, South Africa

This preliminary work probes the structure-function relationship of single nucleotide polymorphs (SNP) of human glutathione-s-transferase class pi (hGSTP1-1). To this end, two SNPs were synthesised by site-directed mutagenesis: P124A and Y80C, both in the all-helical C-terminal domain of hGSTP1-1. The mutant proteins were then expressed using standard overexpression methods; both mutants expressed fewer colonies and produced less protein relative to wildtype. Proteins were structurally characterised by spectroscopy relative to wildtype. Preliminary circular dichroism findings revealed minor alterations of the Y80C structure whilst P124A remained unchanged, relative to wildtype. Similarly, fluorescence spectroscopy findings for Y80C remained unchanged for P124A, relative to wildtype. Interestingly, thermal denaturation studies revealed destabilisation in the mutant enzymes compared to wildtype (TmWT = 55 ± 3 °C; TmP124A = 51 ± 3 °C; TmY80C = 47 ± 3 °C).

Keywords: hGSTP1-1; SNP; polymorphism; structure-function relationship; detoxification proteins.
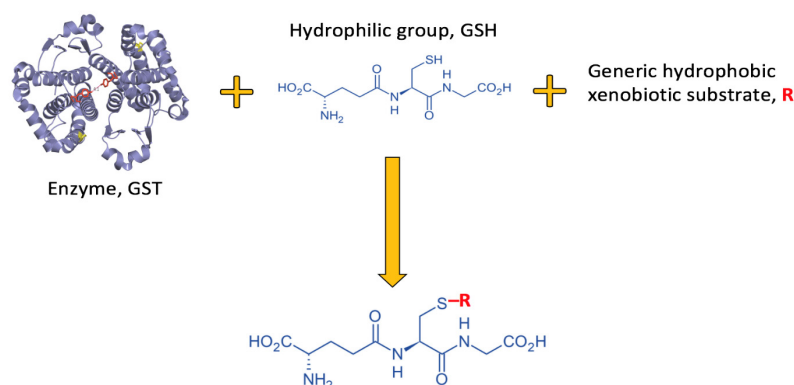
Scheme 1. Demonstrating the generic pathway for the conjugation of the phase II detoxification enzyme GST [6] to the hydrophilic group reduced glutathione (GSH) and to the xenobiotic substrate (R). Adapted from [5].

INTRODUCTION

Cytosolic glutathione-S-transferases (GSTs, E.C. 2.5.1.18, formerly called '*ligandin*') are a superfamily of multifunctional proteins. GST protein functions include both catalytic and non-catalytic roles such as redox reactions, intracellular binding of ligands, ligand transport. Of particular interest is its role as classical phase II detoxification enzyme [1-3].

As classical phase II detoxification enzymes, GSTs play a critical role in protecting the cell against oxidative stress and in the detoxification of xenobiotics [3, 4]. Cellular detoxification of xenobiotics is achieved by catalysing the covalent binding of reduced glutathione (GSH) onto nonpolar xenobiotic molecules through a nucleophilic attack mechanism. GST binds GSH and initiates the deprotonation of the sulfhydryl group. The reduced glutathione-GST complex then binds to the xenobiotic substrate (Scheme 1). The metabolised xenobiotics are then expelled through the mercapturate pathway [3-5].

Structurally, there are three main GST families: cytosolic, mitochondrial and microsomal (or MAPEG proteins). Each family comprises a number of classes (Table 1). Human GST enzymes comprise 11 classes [2, 7, 8]. This work focuses on the structure and function of canonical cytosolic human GST class Pi (hGSTP1-1). Mutations in hGSTP1-1 structure, specifically single nucleotide polymorphisms (SNP), have been linked to several human diseases and ailments [7-12]. Probing the structural integrity of hGSTP1-1 and related SNP mutations is therefore of interest as it would lend insight into the complex structure-function relationship of these enzymes.

---

* To whom all correspondence should be sent:
E-mail: sadhna.mathura@wits.ac.za

Table 1. GST superfamilies and classes. Human classes are underlined. Soluble mammalian classes are italicised. Human GST enzyme of interest (pi) is in bold [2, 7, 8].

GST Superfamily	Number of Classes	Class Names
Cytosolic	13	*alpha*, beta, delta, epsilon, *zeta*, *theta*, *mu*, nu, ***pi***, *sigma*, tau, phi, *omega*
Mitochondrial	1	*kappa*
Microsomal (MAPEG)	4	I, II, III, IV
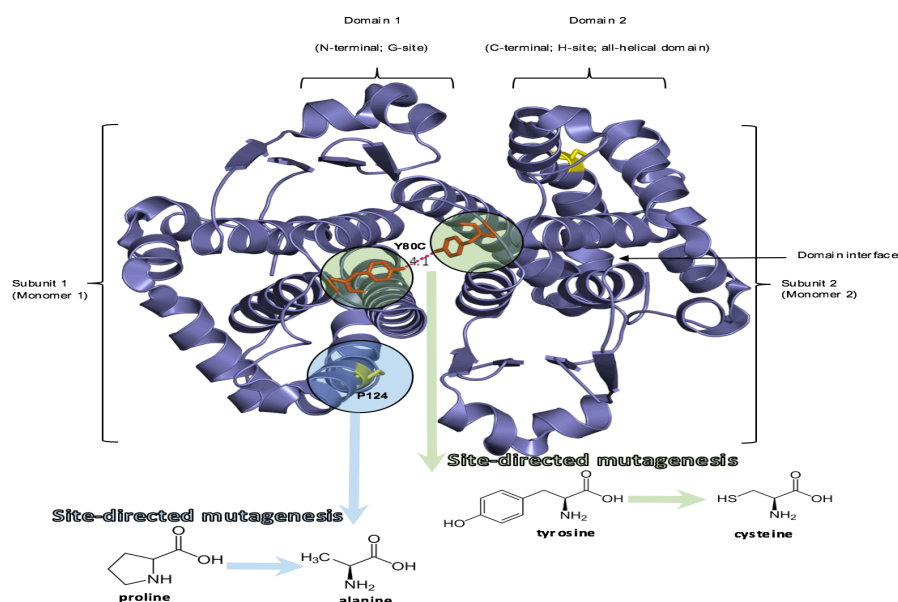
Figure 1. Quaternary structure of homodimeric hGSTP1-1 [5], indicating subunits, domains and interfaces. The highlighted regions show the SNP residues of interest in this work: P124A (blue) and Y80C (green).

Structurally, hGSTP1-1 is a homodimeric protein consisting of about 200 amino acids (Figure 1). The protein has a canonical fold comprising two distinct domains: a thioredoxin-like N-domain, and an all-helical C-domain [2, 3].

The structural GST fold is considered to have evolved from a thioredoxin/glutaredoxin common ancestor to which the all-helical C-domain was added [4]. There are two active sites: a GSH-specific G-site within the smaller N-terminal thioredoxin-like domain; and a non-specific hydrophobic substrate-binding H-site (target for xenobiotics) contained within the larger all-helical C-terminal domain.

Probing hGSTP1-1 structure-function relationship by examining SNPs has been well-characterised in the N-domain, and has provided considerable insight into the active sites, particularly the G-site [12-14]. In this work however, we will examine selected SNPs in the all-helical C-domain. Our strategy is to compare the structure of each SNP to that of wild type (WT) to elucidate how the identity of the residue at those respective positions influences the structural, catalytic and stability properties at the binding sites. This information should provide some structural evidence for the correlated diseases.

In this preliminary report, we have synthesised and structurally characterised two interesting C-domain SNPs (Figure 1):

(1) P124A which is of interest given its proximity to the subunit interface and,

(2) Y80C which is of interest given its proximity to both subunit and domain interfaces, and is highly conserved, suggesting structural significance.

EXPERIMENTAL

Mutagenesis, transformation and sequencing of mutants P124A and Y80C

hGSTP1-1 mutants, P124A and Y80C, were synthesised by site-directed mutagenesis (Stratagene QuickChange™ II, CA, United States), using recombinant plasmids that code for wildtype hGSTP1-1. Oligonucleotide primers for the mutagenesis were designed using Primer-X software [16]. Plasmid DNA was verified by sequencing analysis (Inqaba Biotechnical Industries (Pty) Ltd, Pretoria, South Africa) and aligned using BLAST [17] and 4Peaks software [18]. Plasmids were then transformed into *E. coli* T7 cells for overexpression of the mutant enzymes using standard methods [19].

Overexpression and purification mutants P124A and Y80C using standard methods

Mutant enzyme overexpression was induced using an IPTG (0.2 mM; 30°C; 8 h). The cultured cells were harvested by centrifugation, re-suspended (50 mM Tris-HCl buffer, pH 8.0; -20 °C). Purification was achieved using cobalt HisTrap™ column with binding buffer [50 mM Tris-HCl pH 8.0, 0.5 M NaCl, 50 mM imidazole (eluted with 300 mM), 0.02 % sodium azide], and analysed using SDS-PAGE [16-19].

Structural characterisation of mutants P124A and Y80C using standard methods [16]

Both far-UV circular dichroism (CD) and fluorescence emission spectra measurements were conducted with 1 μM of both wildtype and mutant enzymes in phosphate buffer (pH 7.4, 20 mM, 20 °C). Buffer also included 1mM DDT and 0.02% (w/v) NaN3. Data were recorded on a Jasco J-810 and represent an average of 10 accumulations. Fluorescence measurements were an average of three accumulations and were conducted on a Perkin-Elmer LS50B. Spectra were corrected for buffer.

RESULTS AND DISCUSSION

Synthesis data: primer design, sequencing and alignment, overexpression (SDS-PAGE)

The hGSTP1-1 mutants P124A and Y80C were synthesised to investigate the structure-function relationship of the wildtype hGSTP1-1. The first step in this process is accurate primer design in order to code for the correct single nucleotide mutation. Both the forward and reverse primers were successfully designed using Primer-X [16] for the tyrosine to cysteine, and the proline to alanine point mutations, respectively (Table 2). The underlined bases represent the coding for the mutations of interest.

The second step in the process of generating the hGSTP1-1 mutants was DNA sequencing and sequence alignment analysis to confirm that each of the selected mutations had to be achieved, as well as to confirm the absence of any other mutation (Figures 2 and 3 for mutants Y80C and P124A,

respectively). Sequencing data indicate that mutant codon for tyrosine was replaced by cysteine (Figure 2) for the Y80C mutation and the proline was replaced by alanine (Figure 3). The truncated sequence alignment for mutant Y80C indicates a 99% alignment with known hGSTP1-1 wildtype protein. The same was noted for P124A. This indicates that there were no other mutations.

Following the sequencing and alignment, both mutant proteins and wildtype were overexpressed and purified using standard methods [16, 19]. Once purified, the protein was analysed by mass using SDS-PAGE analysis (Figure 4). Proteins for both wildtype and mutants were successfully expressed and purified to a single band at the anticipated mass (25 kDa). Mass for mutants was consistent with standard calibration data (Figure 4). SDS-PAGE analysis of wildtype (blue triangle) and mutants Y80C (red circle) and P124A (orange square) was plotted on the standard curve which was fitted to a straight line (R = 0.970). Equation of the fitted line is y = -0.020x + 2.203.

Characterization data: structural analysis

hGSTP1-1 and mutants were structurally characterised using both far-UV CD and fluorescence emission spectra spectroscopy to probe their secondary structure and unfolding pathways. Far-UV CD spectra show similar spectral profiles for both mutants and wildtype with peaks at 190 nm, 208 nm and 222 nm (Figure 5). There is however diminished intensity for the Y80C mutant suggesting that the chromophore is likely being shielded in some way, relative to wildtype. This observation may indicate an opening up of the structure around the chromophore.

The fluorescence emission spectra for wildtype and mutants are reported below (Figure 6). What is interesting is that we would expect the Y80C mutant to have a diminished intensity relative to wildtype given that the tyrosine has been replaced by a cysteine. However, this is not the case, suggesting that there is a possible opening up of the secondary structure to expose other fluorescent moieties on the protein. Solid state analysis would add more information here.

Table 2. Forward and reverse primers used for site directed mutagenesis of P124A and Y80C mutants of hGSTP1-1. Primers designed using Primer-X [16]

Primer	Sequence
Y80C-forward	5'-ttcaagctgggcctggact**gt**cccctgccctacttg-3'
Y80C-reverse	5'-caagtagggcagggg**ac**agtccaggcccagcttgaa-3
P124A-forward	5'-cttcagttgcccgg**cc**agtgccttcacat-3'
P124A-reverse	5'-atgtgaaggcactgg**cc**gggcaactgaag-3'
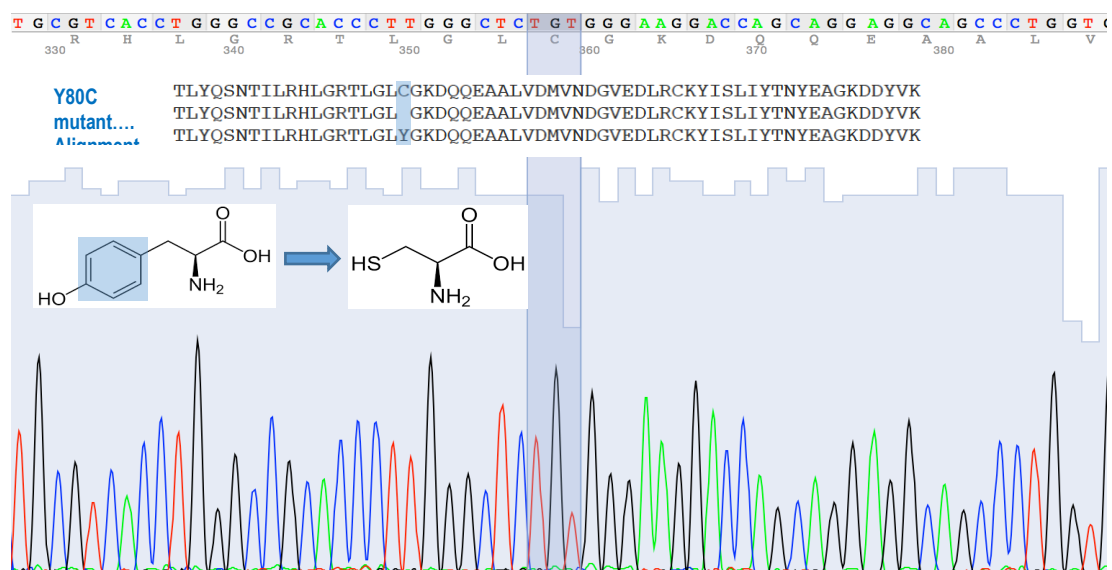
Figure 2. Sequencing data indicating mutant codon for tyrosine to cysteine replacement (highlighted in yellow) and subsequent alignment of mutant Y80C sequence against wildtype (highlighted in blue).
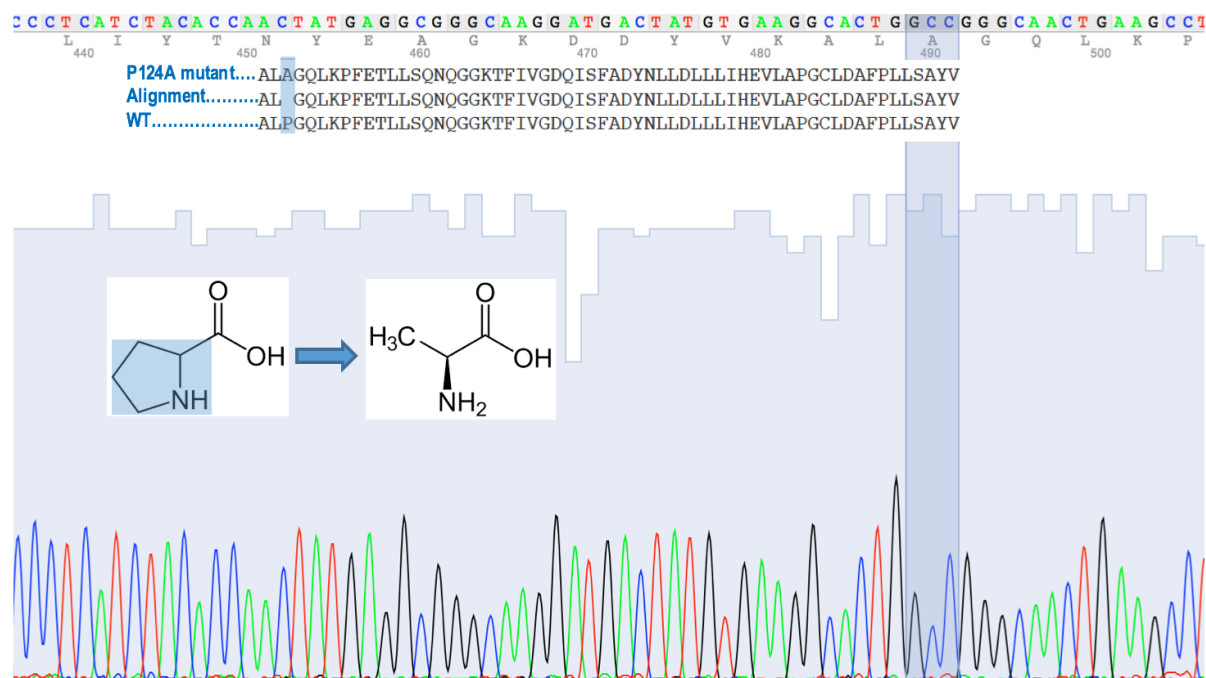
Figure 3. Sequencing data indicating the mutant codon for the proline to alanine replacement (highlighted in yellow) and the subsequent alignment of mutant P124A sequence against wildtype (highlighted in blue).
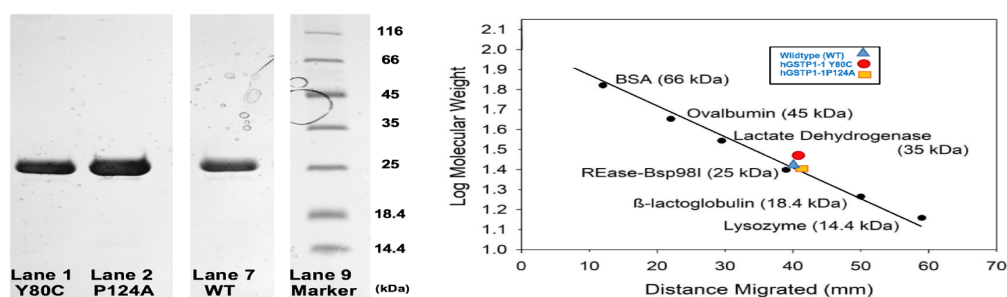
Figure 4. SDS-PAGE analysis of WT (Lane 7) and mutants Y80C (Lane 1) and P124A (Lane 2). Gel specs: 16% acrylamide; glycine; 120 V; 5 µL sample load; ~5 µg.

483
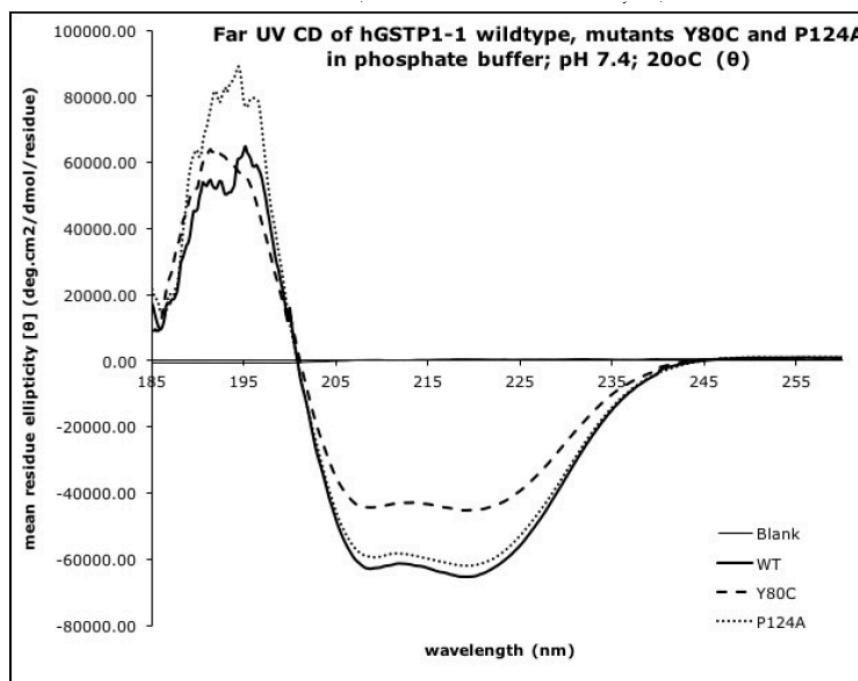
Figure 5. The resultant far-UV CD spectra for the WT dimer (5 μM) (——); mutant Y80C (5 μM) (- - -) and P124A (5 μM) (....) in 20 mM sodium phosphate buffer pH 7.4, containing 1 mM EDTA and 0.02% (w/v) NaN are shown.
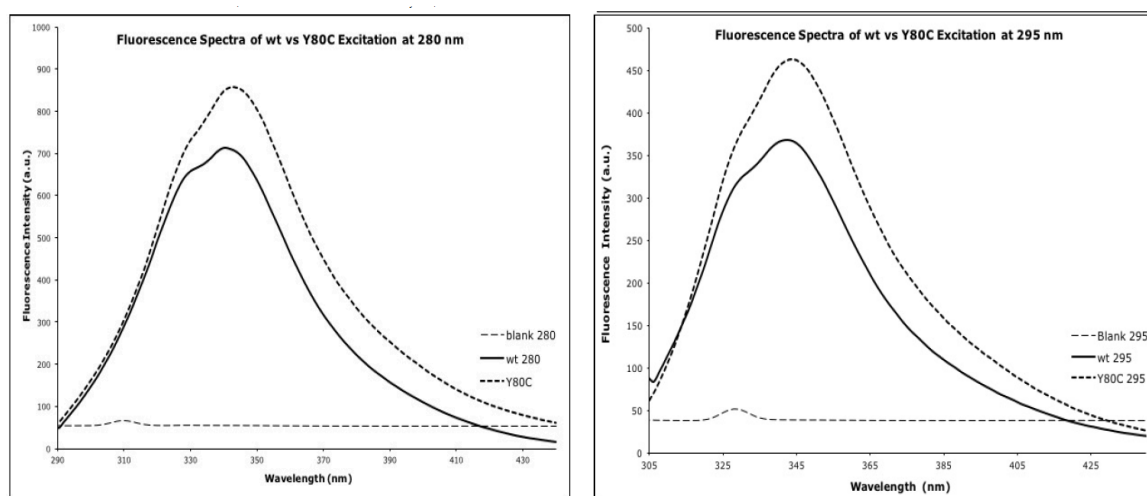
Figure 6. The resultant fluorescence spectra for the WT dimer (2 μM) (——) and mutant Y80C (2 μM) (- - -) in 20 mM sodium phosphate buffer pH 7.4, containing 1 mM EDTA and 0.02% (w/v) NaN are shown.

This observation is further supported by the thermal unfolding observations (Figure 7). We see that the mutants start to denature at a lower temperature (51 ± 3 °C and 47 ± 3 °C for P124A and Y80C, respectively) as compared to wildtype (55 ± 3 °C). This suggests that the hGSTP1-1 native protein is destabilised by changing the tyrosine-80 residue to cysteine.

CONCLUSIONS AND FUTURE WORK

Mutants P124A and Y80C were synthesised and structurally characterised for the hGSTP1-1 protein. The Y80C mutation has more effect on structural stability than the P124A mutation. As this is preliminary work, more data is required to understand the extent of this unfolding. Future work would include functional analysis (enzymatic activity) and solid state analysis by crystal structure.
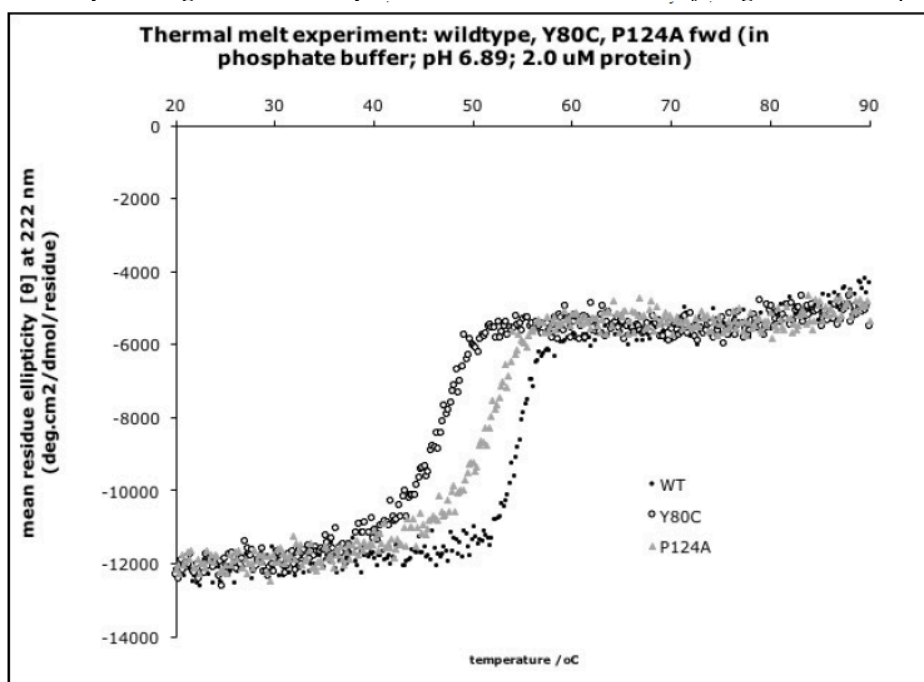
Figure 7. Far-UV CD spectra for the WT dimer (2 μM) (•); mutant Y80C (2 μM) (o) and P124A (2 μM) (Δ) as a function of temperature at a single wavelength. The CD spectra were measured at 222 nm with temperatures varying from 20 to 80° C. Experiments performed in 20 mM sodium phosphate buffer pH 7.4, containing 1 mM EDTA and 0.02% (w/v) NaN3 are shown

REFERENCES

1. A. J. Oakley, *Curr. Opin. Struct. Biol.,* **15**, 716 (2005).
2. D. Sheehan, G. Meade, V. M. Foley, C. A. Dowd, *Biochem. J*, **360** (1), 1 (2001).
3. O. Vasieva, Curr. Mol. Med., **11**, 129 (2011).
4. R. N. Armstrong, *Chem. Res. Toxicol.,* **10**, 2 (1997).
5. D. M. Townsend, K. D., Tew, *Oncogene*, **22**, 7369 (2003).
6. hGSTP1-1 structure PDB ID: 2a2r: http://www.rcsb.org/pdb/
7. T. M. Buetler, D. J. Eaton, *Environ. Carcinogen. Ecotoxicol. Rev.*, **C10**, 181 (1992).
8. K. D. Tew, Y. Manevich, C. Grek, Y. Xiong, J. Uys, D. M. Townsend, *Free Rad. Biol. Med.*, **51**(2), 299 (2011).
9. J. D. Hayes, R. C. Strange, *Pharmacology*, **61**, 154 (2000).
10. C. C. McIlwain, D. M. Townsend, K. D. Tew, *Oncogene*, **25**, 1639 (2006).
11. P.G. Board, Functional Genomics of the Human Glutathione Transferases, in: Encyclopedia of Drug Metabolism and Interactions, Wiley Online Library, 2012.
12. SNP database project: https://www.ncbi.nlm.nih.gov/snp/
13. U. M. Hezagyt, B. Mannervick, G. Stenberg, *J. Biol. Chem.*, **279**, 9586 (2003).
14. M. Widersten, R. H. Kolm, R. Björnestedt, B. Mannervik, *Biochem. J.*, **285,** 377 (1992).
15. PrimerX software: http://bioinformatics.org/primerx
16. Z. Molaudzi, Structural and functional analysis of peroxiredoxin 6 and glutathione transferase P1-1, University of the Witwatersrand, Johannesburg, South Africa, dissertation, 2017.
17. BLAST software: https://blast.ncbi.nlm.nih.gov/Blast.cgi
18. 4Peaks software: https://nucleobytes.com
19. M. Chang, J. L. Bolton, S. Y. Blond, *Protein Expr. Purif.*, **17**, 443 (1999).

Ceramics based on powder mixtures of β-tricalcium phosphate and potassium hydrogen sulfate prepared under mechanical activation in acetone medium

T. V. Safronova[1*], M. M. Akhmedov[2], T. B. Shatalova[1], S. A. Tikhonova[1], G. K. Kazakova[1], M. R. Kaimonov[1], A. V. Knotko[1]

[1] Lomonosov Moscow State University, Leninskie Gory, 1, 119991, Russia, Moscow

[2]A. N. Kosygin State University of Russia (Technology. Design. Art), Sadovnicheskaya str., 33, p. 1, 117997 Moscow, Russia

Powder mixtures of β-tricalcium phosphate β-$Ca_3(PO_4)_2$ and potassium hydrogen sulfate $KHSO_4$ homogenized under mechanical activation in acetone medium in a planetary mill were used for producing ceramics in the K_2O-CaO-SO_3-P_2O_5 system. Powder mixtures were made at molar ratios of $Ca_3(PO_4)_2/KHSO_4$ established as 7/2, 4/2 and 1/2. According to XRD analysis data β-tricalcium phosphate β-$Ca_3(PO_4)_2$ was the main phase in all homogenized powder mixtures. After firing at 700-900 ºC the phase composition of ceramic samples made from powder mixtures with molar ratios of $Ca_3(PO_4)_2/KHSO_4$ =7/2, 4/2 contained β-tricalcium phosphate β-$Ca_3(PO_4)_2$, calciolangbeinite $K_2Ca_2(SO_4)_3$ and potassium calcium phosphate $Ca_{10}K(PO_4)_7$. Phase composition of ceramic samples from powder mixtures with a molar ratio of $Ca_3(PO_4)_2/KHSO_4$ established as 1/2 contained calciolangbeinite $K_2Ca_2(SO_4)_3$, β-calcium pyrophosphate β-$Ca_2P_2O_7$ and potassium sulfate K_2SO_4. Ceramic materials containing the biocompatible phases mentioned above can be recommended for bone implants creation.

Keywords: tricalcium phosphate, potassium hydrogen sulfate, calciolangbeinite, potassium calcium phosphate, potassium sulfate, calcium pyrophosphate

INTRODUCTION

There is nowadays demand to create new biocompatible and bioresorbable materials for development of regenerative medicine methods of bone defect treating [1]. It is impossible to create man-made analogues of natural bone. But it is possible to create close to perfect inorganic ceramic materials for compensation of bone defects of critical size for the period of its regeneration [2]. The mineral and chemical composition of the inorganic part of the bone can be a hint for implant material creation [3]. There is the list of phases of ceramics which can slowly dissolve and, therefore, can be gradually resorbed by the body, while releasing biocompatible ions and stimulate bone regeneration [4]. Some of these ions can be used as building materials for bone restoration and other can become a part of body fluids. It is worth mentioning the following biocompatible and bioresorbable ceramic phases: β-tricalcium phosphate β-$Ca_3(PO_4)_2$, pyrophosphate $Ca_2P_2O_7$, potassium-substituted tricalcium phosphate $KCa_{10}(PO_4)_7$, potassium rhenanite $KCaPO_4$, calcium sulfate anhydrite $CaSO_4$ and calciolangbeinite $K_2Ca_2(SO_4)_3$.

The simple way to manage the rate of resorbability of ceramic composite material consists in an intentional combination in the microstructure of different phases with different rates of solubility. The phase of calcium sulfate anhydrite in ceramic materials is introduced in order to control the limit and rate of resorption of the material intended for the treatment or temporary compensation of a bone defect during its restoration. The use of calcium sulfate anhydrite as a phase of a ceramic material for bone implants is of interest both by itself and in combination with other ceramic phases capable to be resorbed [5].

Different oxide systems were used for bioceramics creation up to nowadays. The most popular of them are CaO-P_2O_5, CaO-MgO-P_2O_5, Na_2O-CaO-P_2O_5, K_2O-CaO-P_2O_5. Probably one attempt was made to create a ceramic composite in the K_2O–CaO–SO_3–P_2O_5 oxide system [6] Ceramics containing tricalcium phosphate β-$Ca_3(PO_4)_2$, potassium-substituted tricalcium phosphate $Ca_{10}K(PO_4)_7$ and calciolangbeinite $K_2Ca_2(SO_4)_3$ were created based on powder mixtures prepared from calcium hydroxyapatite $Ca_{10}(PO_4)_6(OH)_2$ and potassium hydrogen sulfate $KHSO_4$ [6].

The aim of the present study consisted in creation of ceramic composites with biocompatible and bioresorbable phases in the K_2O–CaO–SO_3–P_2O_5 system based on powder mixtures of β-tricalcium phosphate β-$Ca_3(PO_4)_2$ and potassium hydrogen sulfate $KHSO_4$.
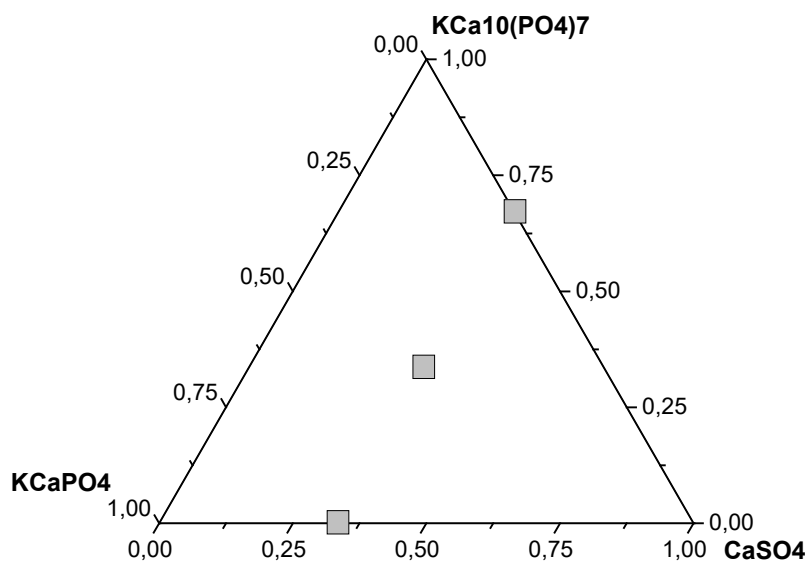
Fig. 1. Planned phase compositions of ceramic materials

EXPERIMENTAL

Planned phase compositions of ceramic samples are pointed in the diagram presented in Fig. 1. The following reactions (1-3) were used for calculation of the quantity of starting components (i.e. β-tricalcium phosphate β-$Ca_3(PO_4)_2$ and potassium hydrogen sulfate $KHSO_4$) of powder mixtures for preparation of ceramic samples with phase compositions pointed on the diagram (Fig. 1).

$$7Ca_3(PO_4)_2 + 2KHSO_4 \rightarrow CaSO_4 + \mathbf{2KCa_{10}(PO_4)_7} + SO_3 + H_2O \tag{1}$$

$$4Ca_3(PO_4)_2 + 2KHSO_4 \rightarrow CaSO_4 + \mathbf{KCa_{10}(PO_4)_7} + \mathbf{KCaPO_4} + SO_3 + H_2O \tag{2}$$

$$Ca_3(PO_4)_2 + 2KHSO_4 \rightarrow CaSO_4 + \mathbf{2KCaPO_4} + SO_3 + H_2O \tag{3}$$
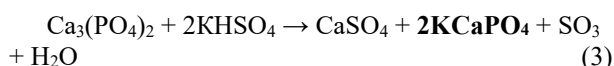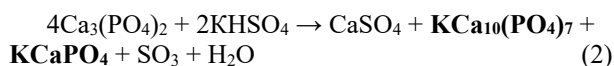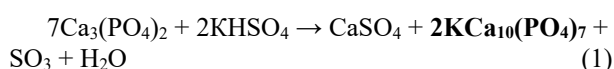
β-Tricalcium phosphate β-$Ca_3(PO_4)_2$ (Sigma Aldrich, CAS # 7758-87-4, purum p.a., ≥96.0%) and potassium hydrogen sulfate $KHSO_4$ (Russian Federation State Standard GOST 4223-75, CAS# 7646-93-7) were used for powder mixtures preparation. Powders of β-tricalcium phosphate β-$Ca_3(PO_4)_2$ and potassium hydrogen sulfate $KHSO_4$, grinding media made of zirconium dioxide ZrO_2, and acetone (Russian Federation State Standard GOST 2603-79) were placed in containers made of agate. Then, the containers with powders, ZrO_2-grinding media, and acetone were fixed in a planetary mill. The planetary mill treatment of powder mixtures was conducted for 15 min at a rotation speed of 500 rpm and at ratio powder: grinding media = 1:5. Then, for acetone evaporation

the powder mixtures were dried in air at ambient temperature for 2 h. After drying, the powder mixtures were passed through a sieve with mesh size of 200 μm. Compact powder pre-ceramic samples in the form of disks of 12 mm in diameter and 2–3 mm thick were made from the prepared powder mixtures using a Carver laboratory press model C hand press at specific pressure of 100 MPa without any technological binder. The powder pre-ceramic samples were fired at 700, 800, 900 °C with a heating rate of 5°C/min and holding time of 2 hours at the specified temperature.

Linear shrinkage and geometrical density of ceramic samples were determined by measuring their weight and size (with accuracy of ±0.05 mm) before and after firing. X-ray powder diffraction (XRD) analysis of powder mixtures after treatment in the planetary mill and samples after firing was conducted on a Rigaku D/Max-2500 diffractometer with rotating anode (Japan) using CuKα radiation. Phase analysis was performed using ICDD PDF2 database [1]. Synchronous thermal analysis was performed on a Netzsch STA 409 PC Luxx (Germany) thermal analyzer at a heating rate of 10°C/min. Sample weight was at least 10 mg. The study of the composition of the gas phase resulting from sample decomposition was conducted with a Netzsch QMS 403C Aëolos (Germany) quadrupole mass spectrometer coupled with a Netzsch STA 409 PC Luxx thermal analyzer. Mass spectra were recorded for molecular weights 18 (H_2O) and 64 (SO_2). Microstructure of samples was studied by scanning electron microscopy using a Carl Zeiss

LEO SUPRA 50VP (Germany, auto emission source) at accelerating voltage of 3–20 kV in secondary electrons (SE2 detector). Samples were coated by chromium layer (up to 10 nm).

RESULTS AND DISCUSSION

XRD data of powder mixtures of β-$Ca_3(PO_4)_2$ and $KHSO_4$ after mechanical activation in acetone medium are presented in Fig. 1. As we can see the phase composition of the powder mixtures did not change remarkably during homogenization. According to XRD analysis data β-tricalcium phosphate β-$Ca_3(PO_4)_2$ was the main phase in all powder mixtures after treatment in a planetary mill in acetone medium during 15 min. Only the powder mixture prepared at molar ratio of $Ca_3(PO_4)_2$ / $KHSO_4$ = 1/2 with the biggest quantity of potassium hydrogen sulfate had small quantities of additional phases. Potassium hydrogen sulfate phosphates $K_4H_5(SO_4)_3PO_4$ and $K_8H_9(SO_4)_7PO_4$ were found additionally to β-tricalcium phosphate β-$Ca_3(PO_4)_2$ in the powder mixture with molar ratio of $Ca_3(PO_4)_2$ / $KHSO_4$ = 1/2. Presumably the following sequence of reactions could take place in case of local excess of potassium hydrogen sulfate $KHSO_4$ in acetone medium:

$$Ca_3(PO_4)_2 + 2KHSO_4 \rightarrow K_2Ca(SO_4)_2 \cdot H_2O + 2CaHPO_4 \tag{4}$$

$$K_2Ca(SO_4)_2 \cdot H_2O \rightarrow K_2Ca(SO_4)_2 + H_2O \tag{5}$$

$$CaHPO_4 + 4KHSO_4 + xH_2O \rightarrow K_4H_5(SO_4)_3PO_4 + CaSO_4 \cdot xH_2O \tag{6}$$

$$CaHPO_4 + 8KHSO_4 + xH_2O \rightarrow K_8H_9(SO_4)_7PO_4 + CaSO_4 \cdot xH_2O \tag{7}$$
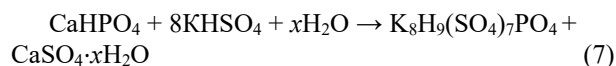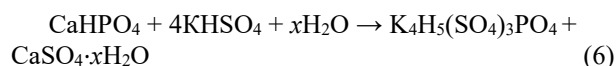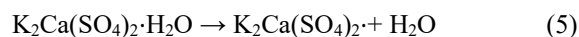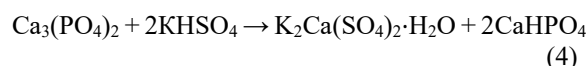
Reflexes of phases of hydrated gypsum $CaSO_4 \cdot xH_2O$ or syngenite $K_2Ca(SO_4)_2 \cdot H_2O$ were not found according to XRD data in the powder mixtures with a molar ratio of $Ca_3(PO_4)_2$ / $KHSO_4$ = 1/2 after their treatment in a planetary mill in acetone medium presumably because of small quantities or due to their presence in quasi-amorphous form.

To keep in mind molar ratios of starting components in powder mixtures we can rewrite reaction (4) for the molar ratio of $Ca_3(PO_4)_2$ / $KHSO_4$ = 4/2 (reaction 8) and for the molar ratio of $Ca_3(PO_4)_2$ / $KHSO_4$ = 7/2 (reaction 9) as follows:

$$4Ca_3(PO_4)_2 + 2KHSO_4 + H_2O \rightarrow K_2Ca(SO_4)_2 \cdot H_2O + 2CaHPO_4 + 3Ca_3(PO_4)_2 \tag{8}$$

$$7Ca_3(PO_4)_2 + 2KHSO_4 + H_2O \rightarrow K_2Ca(SO_4)_2 \cdot H_2O + 2CaHPO_4 + 6Ca_3(PO_4)_2 \tag{9}$$
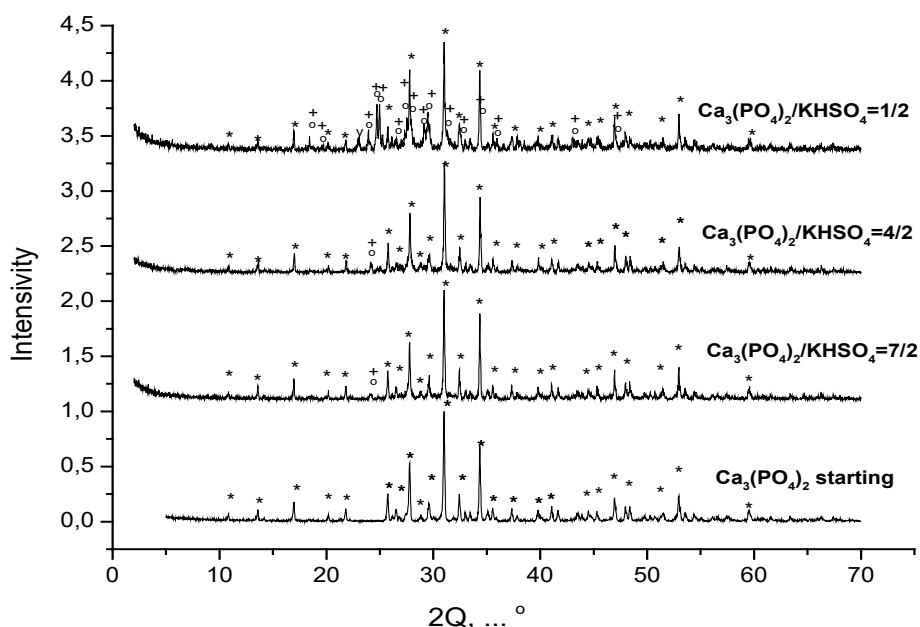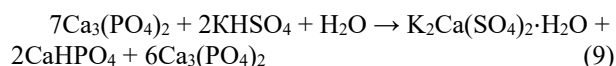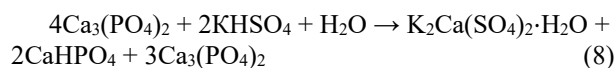
Fig. 2. XRD data of powder mixtures of β-$Ca_3(PO_4)_2$ and $KHSO_4$ after mechanical activation in acetone medium.
* - β-$Ca_3(PO_4)_2$, PDF-Card 9-169; o – $K_8H_9(SO_4)_7PO_4$, PDF-Card 48-709; + – $K_4H_5(SO_4)_3PO_4$, PDF-Card 48-710; v - $KHSO_4$, PDF-Card 11-649

This formal presentation of possible processes can help to understand the dominant presence of β-$Ca_3(PO_4)_2$ and absence of reflexes of acidic potassium hydrogen sulfate phosphates at XRD graphs for powder mixtures with molar ratios of $Ca_3(PO_4)_2$ / $KHSO_4$ = 4/2 and $Ca_3(PO_4)_2$ / $KHSO_4$ =

7/2 because potassium hydrogen sulfate was taken in quantities that were lower than it was necessary for development of reaction (4).

Comparison of the microstructures of the prepared powder mixtures (Fig. 3) allows us to make a conclusion about a slight difference of particle dimensions of different powder mixtures. The higher the content of potassium hydrosulfate powder the lower is the particle dimension.

Thermal analysis data indicate a decrease in the mass of the powder mixtures during heating (Fig. 4 a). The higher the content of calcium hydrosulfate in the initial mixtures, the greater is the change of the mass of the powders. DSC data are presented in Fig. 4 b.

One can see two endothermal peaks at 210 °C and at 868 °C on the DSC curve for powder mixture prepared at molar ratio of $Ca_3(PO_4)_2/KHSO_4$ established as 1/2. The first peak can be attributed to a process of salts decomposition and water release (Fig. 5 a).

The second peak can be attributed to eutectic melting point (867 °C [8]) present in the system $K_2SO_4 - CaSO_4$. Formation of potassium sulfate K_2SO_4 can take place due to formation of calciolangbeinite (potassium calcium double sulfate) $K_2Ca_2(SO_4)_3$ from syngenite $K_2Ca(SO_4)_2 \cdot H_2O$ (reaction 10) [9]:
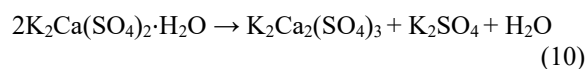
$$2K_2Ca(SO_4)_2 \cdot H_2O \rightarrow K_2Ca_2(SO_4)_3 + K_2SO_4 + H_2O \tag{10}$$

The higher the content of calcium hydrosulfate in the initial mixtures, the greater is the change of the mass of the powders. The mass spectrometry data for m/Z=18 (Fig. 5 a) reflect the release of water from the studied powder mixtures. The change of the powder mixture masses takes place due to the release of physically bound water at a temperature about 100 °C. The change of the powder mixture masses takes place due to decomposition of different hydrated salts in the range about 200-500 °C for all powder mixtures. The change of the powder mixture masses due to water release takes place in the range of 500 - 800 °C for powder mixtures with molar ratio $Ca_3(PO_4)_2/KHSO_4 = 7/2$ and 4/2; and in the range of 550-600°C for the mixture with molar ratio $Ca_3(PO_4)_2/KHSO_4 = 1/2$.

(a) β-$Ca_3(PO_4)_2$

(b) $Ca_3(PO_4)_2/KHSO_4 = 7/2$

(b) $Ca_3(PO_4)_2/KHSO_4 = 4/2$
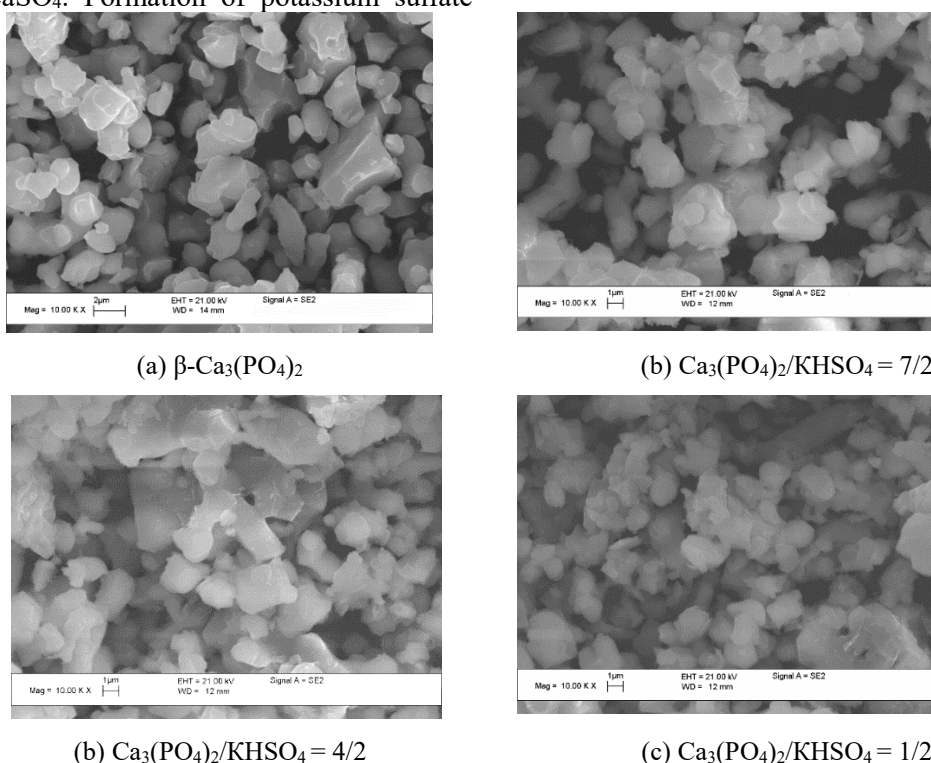
(c) $Ca_3(PO_4)_2/KHSO_4 = 1/2$

Fig. 3. Microstructure of starting powder of β-tricalcium phosphate β-$Ca_3(PO_4)_2$ (a) and powder mixtures after mechanical activation in acetone medium prepared at molar ratio of $Ca_3(PO_4)_2/KHSO_4$ established as 7/2 (b), 4/2 (c) and 1/2 (d).

(a) TG

(b) DSC
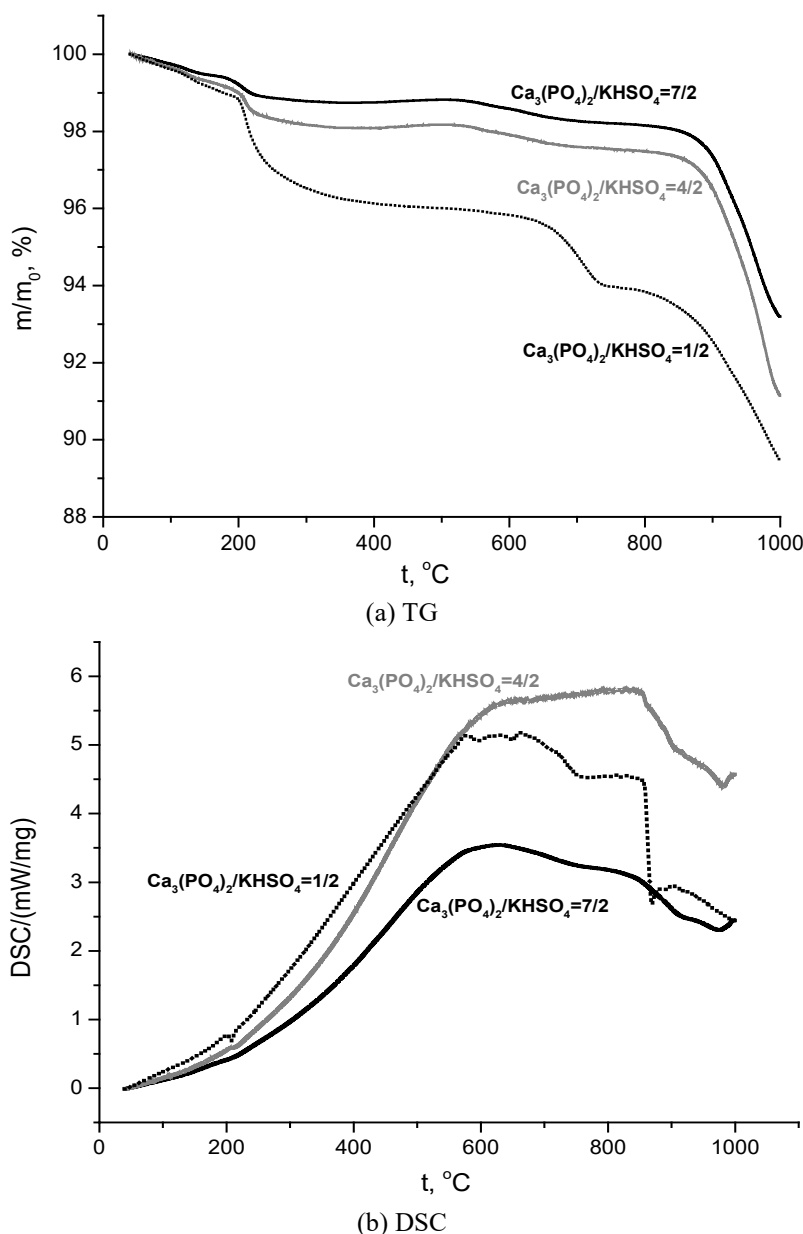
Fig. 4. Thermal analysis data for powder mixtures prepared from β-$Ca_3(PO_4)_2$ and $KHSO_4$ using mechanical activation treatment: TG (a); DSC (b).

The mass spectrometry data for m/Z= 64 reflect the release of sulfur oxide SO_2 from the studied powder mixtures. Sulfur oxide SO_2 evolution from powder mixture prepared at molar ratio of $Ca_3(PO_4)_2/KHSO_4$ established as 1/2 started at 670 °C; from powder mixture prepared at molar ratio of $Ca_3(PO_4)_2/KHSO_4$ established as 4/2 started at 850 °C and from powder mixture prepared at molar ratio of $Ca_3(PO_4)_2/KHSO_4$ established as 7/2 started at 880 °C. At 1000 °C SO_2 evolution process for powder mixtures with molar ratios $Ca_3(PO_4)_2/KHSO_4 = 7/2$ and 4/2 had the tendency to finish. For powder mixture with molar ratio $Ca_3(PO_4)_2/KHSO_4 = 1/2$ the change in the mass of the samples due to the release

of sulfur oxide took place without any tendency to finish up to 1000 °C. The higher the content of potassium hydrogen sulfate in the initial mixture, the more noticeable is the contribution of this process to the change in the mass of powder mixtures. We assume that SO_2 evolution can be due to formation of potassium substituted tricalcium phosphate from potassium sulfate and calcium phosphates. For powder mixture with molar ratio $Ca_3(PO_4)_2/KHSO_4 = 1/2$ with reference to reaction 4 the following reactions during heating can be suggested:

$$K_2Ca(SO_4)_2 \cdot H_2O + 2CaHPO_4 \rightarrow 1/2K_2Ca_2(SO_4)_3 + 1/2K_2SO_4 + Ca_2P_2O_7 + 2H_2O \qquad (11)$$
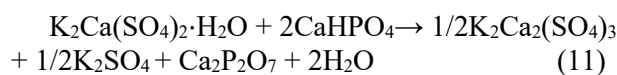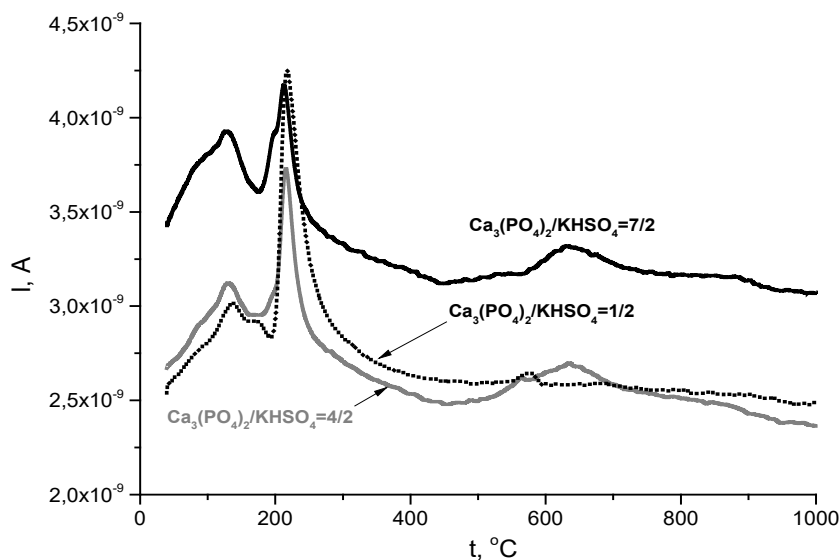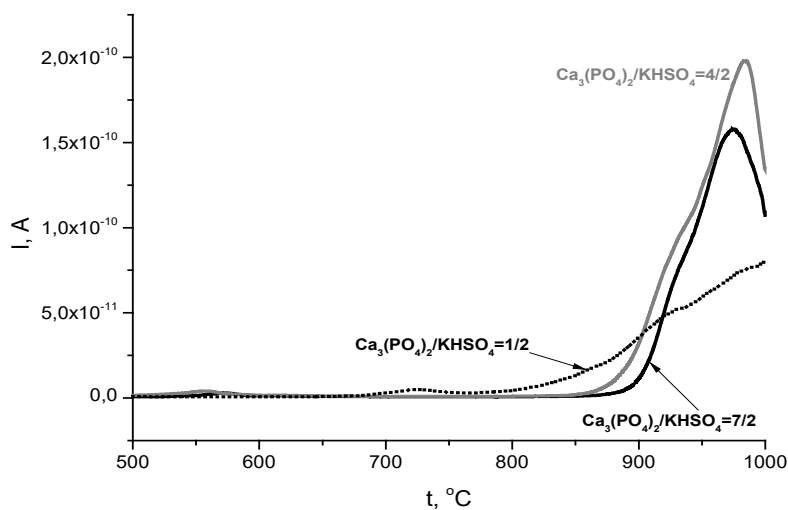
(a) MS_18_H$_2$O

(b) MS_64_SO$_2$

Fig. 5. Thermal analysis data for powder mixtures prepared from β-Ca$_3$(PO$_4$)$_2$ and KHSO$_4$ using mechanical activation treatment: MS_18_H$_2$O (a); MS_64_ SO$_2$ (b).

For a powder mixture with molar ratio Ca$_3$(PO$_4$)$_2$/KHSO$_4$ = 4/2 with reference to reaction 8 the following reaction during heating can be suggested:

K$_2$Ca(SO$_4$)$_2$·H$_2$O + 2CaHPO$_4$ + 3Ca$_3$(PO$_4$)$_2$ →

→1/2 K$_2$Ca$_2$(SO$_4$)$_3$ + Ca$_2$P$_2$O$_7$ + 1/2 K$_2$SO$_4$ + 3Ca$_3$(PO$_4$)$_2$ +2H$_2$O   (12)
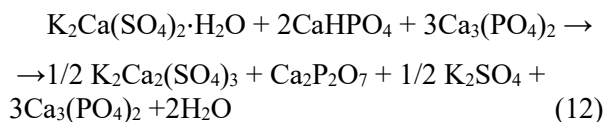
For powder mixture with molar ratio Ca$_3$(PO$_4$)$_2$/KHSO$_4$ = 7/2 with reference to the reaction 9 the following reaction during heating can be suggested:

K$_2$Ca(SO$_4$)$_2$·H$_2$O + 2CaHPO$_4$ + 6Ca$_3$(PO$_4$)$_2$ →

→ 1/2K$_2$Ca$_2$(SO$_4$)$_3$ + Ca$_2$P$_2$O$_7$ +1/2K$_2$SO$_4$ +

6Ca$_3$(PO$_4$)$_2$ + 2H$_2$O   (13)
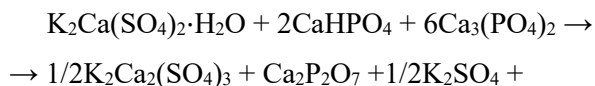
Formation of potassium substituted tricalcium phosphate can be described by reaction (14).

3Ca$_3$(PO$_4$)$_2$ + 1/2Ca$_2$P$_2$O$_7$ + 1/2K$_2$SO$_4$ → Ca$_{10}$K(PO$_4$)$_7$ + 1/2SO$_3$ (14)
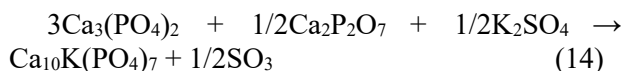
Reactions 11-14, written taking into account the data of XRD of powder mixtures after treatment under conditions of mechanical activation and thermal analysis and the keeping in mind of the molar ratio of K/Ca/S/P in starting powder mixtures give us opportunity to expect the following phase composition in ceramic materials presented in Table 1.

Table 1. Possible phase composition of ceramic materials based of powder mixture of β-Ca$_3$(PO$_4$)$_2$ and KHSO$_4$

Molar ratio of Ca$_3$(PO$_4$)$_2$/KHSO$_4$	β-Ca$_3$(PO$_4$)$_2$	K$_2$Ca$_2$(SO$_4$)$_3$	β-Ca$_2$P$_2$O$_7$	K$_2$SO$_4$	Ca$_{10}$K(PO$_4$)$_7$
7/2	+	+	+	-	+
4/2	-	+	+	-	+
1/2	-	+	+	+	-

Fig. 6. XRD data of ceramic samples based on powder mixtures of β-Ca$_3$(PO$_4$)$_2$ and KHSO$_4$ prepared under mechanical activation after firing at 900°C (2 hours).

\# - β-Ca$_2$P$_2$O$_7$, PDF-card 9-346; k - K$_2$SO$_4$, PDF-card 5-613; s - K$_2$Ca$_2$ (SO$_4$)$_3$, PDF-card 20-867;

* - Ca$_{10}$K(PO$_4$)$_7$, PDF-card 45-138; * - β-Ca$_3$(PO$_4$)$_2$, PDF-Card 9-169;

We can see from the table that all ceramic samples could include calciolangbeinite K$_2$Ca$_2$(SO$_4$)$_3$ and β-pyrophosphate β-Ca$_2$P$_2$O$_7$. In ceramic samples based on powder mixtures with the biggest quantity of β-tricalcium phosphate β-Ca$_3$(PO$_4$)$_2$ in the starting powder mixture (Ca$_3$(PO$_4$)$_2$/KHSO$_4$ = 7/2) β-tricalcium phosphate β-Ca$_3$(PO$_4$)$_2$ could be in the phase composition. Potassium substituted tricalcium phosphate could be in the ceramics based on the powder mixtures with Ca$_3$(PO$_4$)$_2$/KHSO$_4$ = 7/2 and 4/2. And potassium sulfate could be in the phase composition of ceramic samples based on powder mixture with Ca$_3$(PO$_4$)$_2$/KHSO$_4$ = 1/2.

XRD data of ceramic samples based on powder mixtures of β-Ca$_3$(PO$_4$)$_2$ and KHSO$_4$ prepared under mechanical activation after firing at 900°C are presented in Fig. 6.

According to XRD data (Fig. 6) calciolangbeinite K$_2$Ca$_2$(SO$_4$)$_3$ was found in the phase composition of all ceramic samples after firing at 900°C. XRD reflexes of β-tricalcium phosphate β-Ca$_3$(PO$_4$)$_2$ and potassium-substituted tricalcium phosphate Ca$_{10}$K(PO$_4$)$_7$ are very close. Those reflexes were found in ceramics based on a powder mixture with molar ratio Ca$_3$(PO$_4$)$_2$/KHSO$_4$ = 7/2 and 4/2. The phase composition of ceramics based on a powder mixture with a molar ratio of Ca$_3$(PO$_4$)$_2$/KHSO$_4$ = 1/2 also included β-pyrophosphate β-Ca$_2$P$_2$O$_7$ and potassium sulfate K$_2$SO$_4$. Phase compositions of ceramic samples found using XRD data are in good correlation with expected phase composition of ceramics suggested in table 1. Only β-pyrophosphate β-Ca$_2$P$_2$O$_7$ was not found by means XRD in ceramic samples based on powder mixture with a molar ratio of Ca$_3$(PO$_4$)$_2$/KHSO$_4$ = 7/2.

Phone photo shows the apparent difference between ceramic samples after firing at 900 °C (Fig. 7).
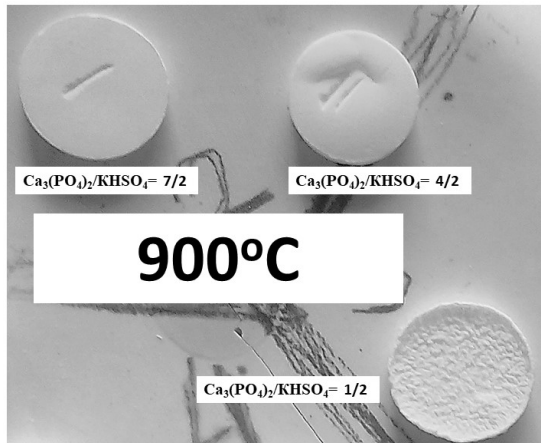
Fig. 7. Phone photo of ceramic samples after firing at 900 °C (2 hours).

The maximum density ($\sim$ 2 g/cm^3) and maximum linear shrinkage (16%) were observed for a sample based on a powder mixture with molar ratio of $Ca_3(PO_4)_2$/KHSO$_4$ = 4/2 (Figs. 8 and 9).
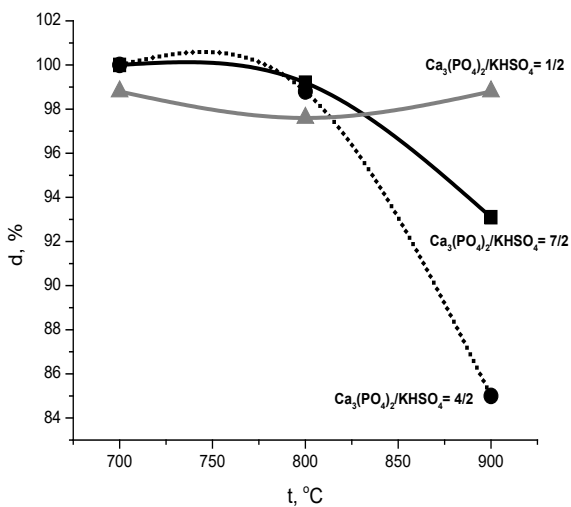
Fig. 8. Dependence of the diameter of ceramic samples obtained from powder mixtures prepared under mechanical activation conditions in acetone at molar ratios $Ca_3(PO_4)_2$/KHSO$_4$ = 7/2, 4/2, 1/2 on firing temperature.

Micrographs of cross-sections and surfaces of ceramic samples after firing at 900°C prepared based on powder mixtures of β-$Ca_3(PO_4)_2$ and KHSO$_4$ mechanically activated in acetone medium at molar ratios of $Ca_3(PO_4)_2$/KHSO$_4$ established as 7/2, 4/2 and 1/2 are presented in Fig. 10.
Microstructure of ceramic sample with a molar ratio of $Ca_3(PO_4)_2$/KHSO$_4$ specified as 7/2 (Fig. 10 a,b)

looks undersintered, the diameter of the sampleremains practically the same as before firing. The grain size can be estimated as 2-4 μm.

The microstructure of a ceramic sample with a molar ratio of $Ca_3(PO_4)_2$/KHSO$_4$ specified as 1/2 also looks undersintered. One can see microcracks in the cross-section. The grain size can be estimated as 0.5-3 μm.

The microstructure of a ceramic sample with a molar ratio of $Ca_3(PO_4)_2$/KHSO$_4$ specified as 4/2 looks better than others. The grain size is preferably in the range of 0.3-1.5 μm.
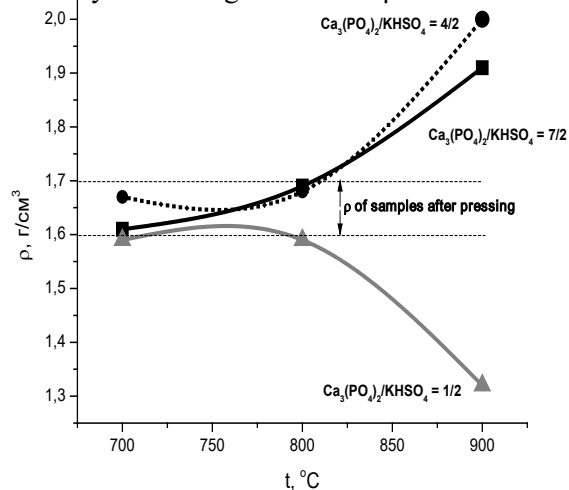
Fig. 9. Dependence of density of ceramic samples obtained from powder mixtures prepared under mechanical activation conditions in acetone at molar ratios $Ca_3(PO_4)_2$/KHSO$_4$ = 7/2, 4/2, 1/2 on firing temperature.

CONCLUSIONS

Powder mixtures of β-tricalcium phosphate β-$Ca_3(PO_4)_2$ and potassium hydrogen sulfate KHSO$_4$ were homogenized in acetone medium under conditions of mechanical activation using a planetary mill at molar ratios established as 7/1, 4/1 and 2/1. β-Tricalcium phosphate β-$Ca_3(PO_4)_2$ was the main phase in all prepared powder mixtures. Only the powder mixture with the highest content of potassium hydrogen sulfate KHSO$_4$ (molar ratio β-$Ca_3(PO_4)_2$/ KHSO$_4$=1/2) additionally had small quantities of potassium hydrogen sulfate phosphates such as $K_8H_9(SO_4)_7PO_4$ and $K_4H_5(SO_4)_3PO_4$. It was the first time when we observed the formation of acidic potassium sulfate phosphates in the powder systems based on β-$Ca_3(PO_4)_2$ and potassium hydrogen sulfate KHSO$_4$ during mechanical activation.

(a) $Ca_3(PO_4)_2/KHSO_4 = 7/2$ cross-section

(b) $Ca_3(PO_4)_2/KHSO_4 = 7/2$ surface

(c) $Ca_3(PO_4)_2/KHSO_4 = 4/2$ cross-section

(d) $Ca_3(PO_4)_2/KHSO_4 = 4/2$ surface

(e) $Ca_3(PO_4)_2/KHSO_4 = 1/2$_cross-section

(f) $Ca_3(PO_4)_2/KHSO_4 = 1/2$_surface
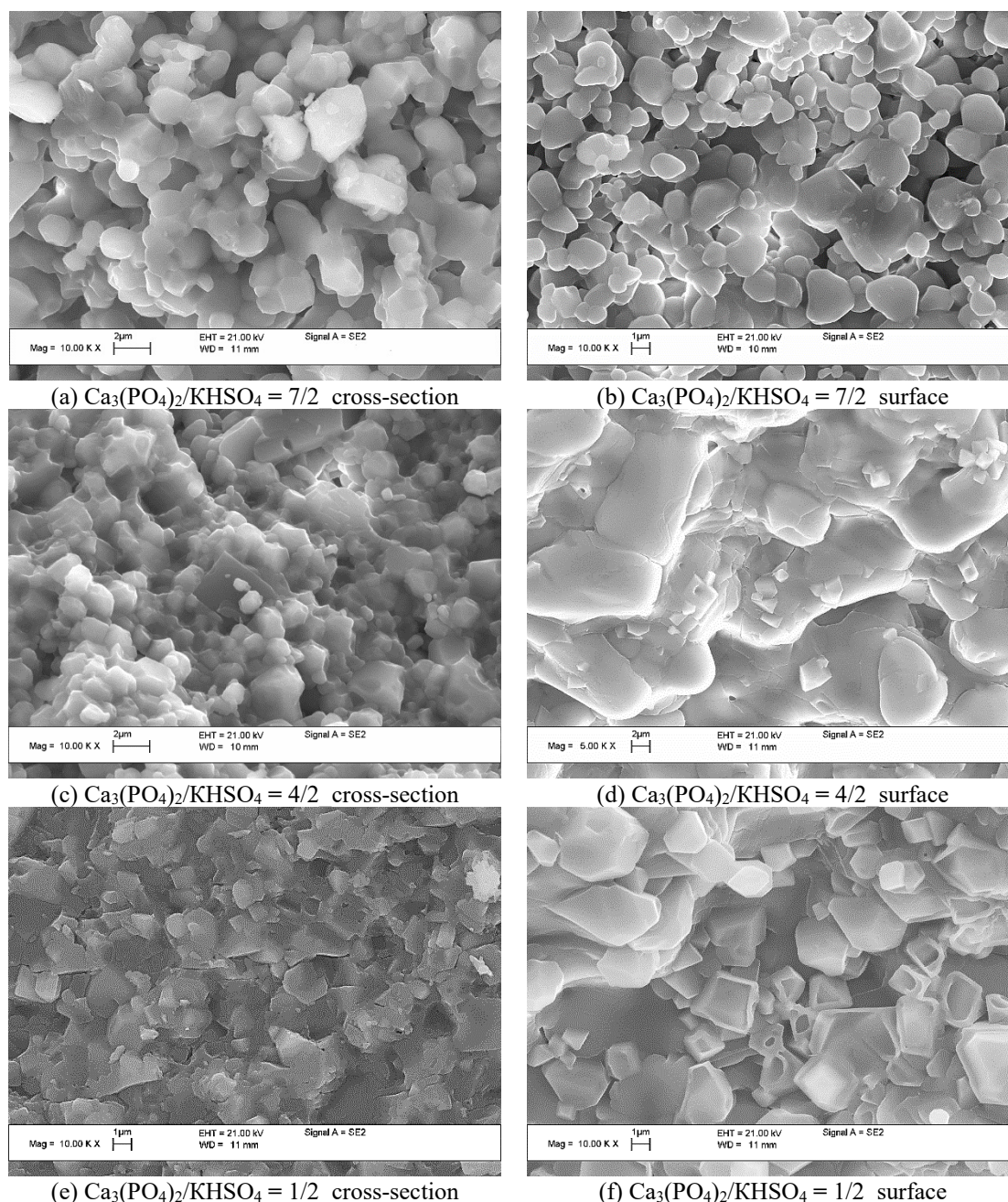
Fig. 10. Micrographs of ceramic samples after firing at 900°C prepared based on powder mixtures of the β-$Ca_3(PO_4)_2$ and $KHSO_4$ mechanically activated in acetone medium at molar ratios of $Ca_3(PO_4)_2/KHSO_4$ established as 7/2 (a, b), 4/2 (c, d) and 1/2 (e, f); cross-sections (a, c, e) and surfaces (b, d, f).

After firing at 900°C the phase composition of all ceramic samples contained phase of calciolangbeinite $K_2Ca_2(SO_4)_3$. Reflexes of β-tricalcium phosphate β-$Ca_3(PO_4)_2$, potassium-substituted tricalcium phosphate $Ca_{10}K(PO_4)_7$ were found in ceramics based on powder mixtures with molar ratios $Ca_3(PO_4)_2/KHSO_4 = 7/2$ and 4/2. The phase composition of ceramics based on a powder mixture with a molar ratio of $Ca_3(PO_4)_2/KHSO_4 = 1/2$ also included β-pyrophosphate β-$Ca_2P_2O_7$ and potassium sulfate K_2SO_4.

The results of this study allow us to consider the possibility of creating new ceramic composite

materials for the treatment of bone tissue defects, which, in addition to calcium phosphate phases such as β-tricalcium phosphate β-$Ca_3(PO_4)_2$ and β-pyrophosphate β-$Ca_2P_2O_7$, include potassium-substituted tricalcium phosphate $Ca_{10}K(PO_4)_7$ and calciolangbeinite $K_2Ca_2(SO_4)_3$ as a possible new resorbable phase of the ceramic material containing β-calcium pyrophosphate β-$Ca_2P_2O_7$.

It should be noted that formation of calciolangbeinite $K_2Ca_2(SO_4)_3$ in the powder system containing calcium phosphate and potassium hydrogen sulfate forced the formation of calcium phosphate during heating with lower calcium to

494

phosphorus ratio than staring calcium phosphate had.

The results of the present investigation can be taken into account when creating resorbable ceramic materials in the K_2O-CaO-SO_3-P_2O_5 system for bone defect treating. with biocompatible and bioresorbable phases such as tricalcium phosphate $Ca_3(PO_4)_2$ and calciolangbeinite (potassium calcium double sulfate) $K_2Ca_2(SO_4)_3$.

REFERENCES

1. S. Pina, V. P. Ribeiro, C. F. Marques, F. R, Maia, T. H. Silva, R. L. Reis, J. M. Oliveira, *Materials*, **12**(11), 1824 (2019).
2. W. Wang, K. W. K. Yeung, *Bioact. Mater.*, **2**(4), 224 (2017).
3. S. Von Euw, Y. Wang, G. Laurent, C. Drouet, F. Babonneau, N. Nassif, T. Azais, *Sci. Rep.,* **9**(1), 8456 (2019).
4. T. V. Safronova, *Inorg. Mater.*, **57**(5), 443 (2021).
5. Z. Yang, D.A. Yang, H. Zhao, *Key Eng. Mater.,* **336** 1635 (2007).
6. T. V. Safronova, M. M. Akhmedov, T. B. Shatalova, S. A. Tikhonova, G. K. Kazakova, *Russ. J. Inorg. Chem.*, **66**(8), 1057 (2021).
7. ICDD (2010). PDF-4+ 2010 (Database), Dr. Soorya Kabekkodu (ed.), International Centre for Diffraction Data, Newtown Square, PA, USA, 2010. http://www.icdd.com/products/pdf2.htm
8. J. J Rowe., G. W. Morey, I. D. Hansen, *J. Inorg. Nucl. Chem.,* **27**(1), 53 (1965).
9. J. T. Kloprogge, Z. Ding, W. N. Martens, R. D. Schuiling, L. V. Duong, R. L. Frost, *Thermochimica Acta,* **417**(1), 143 (2004).

AUTHOR INDEX

SUBJECT INDEX

Instructions about Preparation of Manuscripts

General remarks: Manuscripts are submitted in English by e-mail The text must be typed on A4 format paper using Times New Roman font size 11, normal character spacing. The manuscript should not exceed 15 pages (about 3500 words), including photographs, tables, drawings, formulae, etc. Authors are requested to use margins of 2 cm on all sides

Manuscripts should be subdivided into labelled sections, e.g. **Introduction, Experimental, Results and Discussion**, *etc*. **The title page** comprises headline, author's names and affiliations, abstract and key words. Attention is drawn to the following:

a) **The title** of the manuscript should reflect concisely the purpose and findings of the work. Abbreviations, symbols, chemical formulas, references and footnotes should be avoided. If indispensable, abbreviations and formulas should be givenin parentheses immediately after the respective full form.

b) **The author**'s first and middle name initials and family name in full should be given, followedby the address (or addresses) of the contributing laboratory (laboratories). **The affiliation** of the author(s) should be listed in detail by numers (no abbreviations!). The author to whom correspondence and/or inquiries should be sent should be indicated by asterisk (*) with e-mail address.

The abstract should be self-explanatory and intelligible without any references to the text andcontaining not more than 250 words. It should be followed by key words (not more than six).

References should be numbered sequentially in the order, in which they are cited in the text. The numbers in the text should be enclosed in brackets [2], [5, 6], [9−12], etc., set on the text line. References are to be listed in numerical order on a separate sheet. All references are to be given in Latin letters. The names of the authors are given without inversion. Titles of journals must be abbreviated according to Chemical Abstracts and given in italics, the volume is typed in bold, the initial page is given and the year in parentheses. Attention is drawn to the following conventions:a) The names of all authors of a certainpublications should be given. The use of "*et al*." inthe list of references is not acceptable.b) Only the initials of the first and middle names should be given. In the manuscripts, the reference to author(s) of cited works should be made without giving initials, e.g. "Bush and Smith [7] pioneered...". If the reference carries the names of three or more authors it should be quoted as "Bush *et al*. [7]", if Bush is the first author, or as "Bush and co-workers [7]", if Bush is the senior author.

Footnotes should be reduced to a minimum. Each footnote should be typed double-spaced at thebottom of the page, on which its subject is first mentioned.**Tables** are numbered with Arabic numerals on the left-hand top. Each table should be referred to inthe text. Column headings should be as short as possible but they must define units unambiguously.The units are to be separated from the preceding symbols by a comma or brackets. Note: The following format should be used when figures, equations, *etc*. are referred to the text (followed by the respective numbers): Fig., Eqns., Table, Scheme.

Schemes and figures. Each manuscript should contain or be accompanied by the respective illustrative material as well as by the respective figure captions in a separate file (sheet).As far as presentation of units is concerned, SI units are to be used. However, some non-SI units are also acceptable, such as °C, ml, l, etc.The author(s) name(s), the title of the manuscript, the number of drawings, photographs, diagrams, etc., should be written in black pencil on the back of the illustrative material (hard copies) inaccordance with the list enclosed. Avoid using more than 6 (12 for reviews, respectively) figures in the manuscript. Since most of the illustrative materials are to be presented as 8-cm wide pictures, attention should be paid that all axis titles, numerals, legend(s) and texts are legible.

The authors are required to submit the text with a list of three individuals and their e-mail addresses that can be considered by the Editors as potential reviewers. Please, note that the reviewers should be outside the authors' own institution or organization. The Editorial Board of the journal is not obliged to accept these proposals.

The authors are asked to submit **the final text** (after the manuscript has been accepted for publication) in electronic form by e-mail. The main text, list of references, tables and figure captions should be saved in separate files (as *.rtf or *.doc) with clearly identifiable file names. It is essential that the name and version of the word-processing program and the format of the text files is clearly indicated. It is recommended that the pictures are presented in *.tif, *.jpg, *.cdr or *.bmp format.

The equations are written using "Equation Editor" and chemical reaction schemes are written using ISIS Draw or ChemDraw programme.

EXAMPLES FOR PRESENTATION OF REFERENCES

REFERENCES

1. D. S. Newsome, *Catal. Rev.–Sci. Eng.*, **21**, 275 (1980).
2. C.-H. Lin, C.-Y. Hsu, *J. Chem. Soc. Chem. Commun.*, 1479 (1992).
3. R. G. Parr, W. Yang, Density Functional Theory of Atoms and Molecules, Oxford Univ. Press, New York, 1989.
4. V. Ponec, G. C. Bond, Catalysis by Metals and Alloys (Stud. Surf. Sci. Catal., vol. 95), Elsevier, Amsterdam, 1995.
5. G. Kadinov, S. Todorova, A. Palazov, in: New Frontiers in Catalysis (Proc. 10th Int. Congr. Catal., Budapest,(1992), L. Guczi, F. Solymosi, P. Tetenyi (eds.), Akademiai Kiado, Budapest, 1993, Part C, p. 2817.
6. G. L. C. Maire, F. Garin, in: Catalysis. Science and Technology, J. R. Anderson, M. Boudart (eds), vol. 6, SpringerVerlag, Berlin, 1984, p. 161.
7. D. Pocknell, *GB Patent* 2 207 355 (1949).
8. G. Angelov, PhD Thesis, UCTM, Sofia, 2001, pp. 121-126.
9 JCPDS International Center for Diffraction Data, Power Diffraction File, Swarthmore, PA, 1991.
10. CA **127**, 184 762q (1998).
11. P. Hou, H. Wise, *J. Catal.*, in press.
12. M. Sinev, private communication.
13. http://www.chemweb.com/alchem/articles/1051611477211.html.

Texts with references which do not match these requirements will not be considered for publication!!!

CONTENTS